Relation between molecular structure and ultrafast photoreactivity with application to molecular switches

Artur Iliyanov Nenov

aus

Varna, Bulgarien
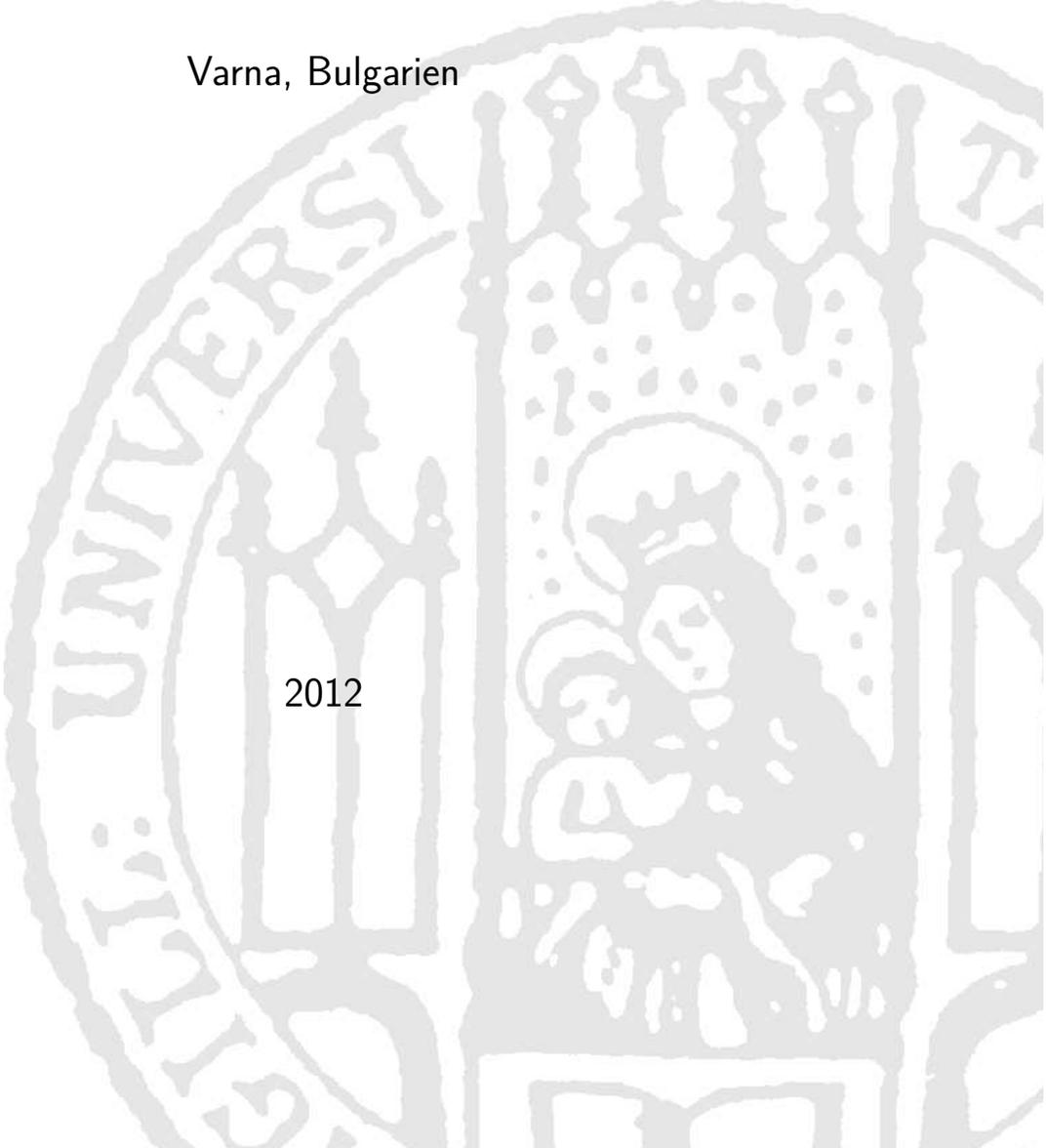
2012

Abstract

Photoinduced ultrafast isomerizations are fundamental reactions in photochemistry and photobiology. This thesis aims for an understanding of the generic forces driving these reactions and a theoretical approach is set up, able to handle realistic systems, whose fast relaxation is mediated by conical intersections. The main focus is on the development of strategies for the prediction and accelerated optimization of conical intersections and their application to artificial compounds with promising physico-chemical properties for technical applications as molecular switches. All calculations are based on advanced quantum chemical methods and mixed quantum-classical dynamics.

In the first part of this thesis the two-electron two-orbital theory by Michl and Bonačić-Koutecký used in its original formulation to rationalize the structure of conical intersections in charged polyene systems is extended by including the interactions of the active pair of electrons with the remaining closed-shell electrons that are present in any realistic system. A set of conditions, called *resonance* and *heterosymmetry* conditions, for the formation of conical intersections in multielectronic systems are derived and verified by calculations on the basic units ethylene, *cis*-butadiene and 1,3-cyclohexadiene at various geometries and functionalizational patterns. The quantitative results help to understand the role of geometrical deformations and substituent effects for the formation of conical intersections and to derive rules of thumb for their qualitative prediction in arbitrary polyenes. An extension of the rules of thumb to conical intersection seams is formulated. The strategy pursued is to divide the molecular system into basic units and into functional groups. Each unit and its intersection space are treated independently, thereby reducing the dimensionality of the search space compared to the complete molecule. Subsequently, the interconnectivity of the intersection spaces of the different units is determined and an initial guess for the complete seam is constructed. This guess is then fed into a quantum chemistry package to finalize the optimization. The strategy is demonstrated for two multi-functionalized systems, hemithioindigo-hemistilbene and trifluoromethyl-pyrrolylfulgide.

In the second part of this thesis state-of-the-art quantum chemical calculations and time-resolved transient and infrared spectroscopy are used to reconstruct the complex multi-channel isomerization mechanisms of hemithioindigo-hemistilbene and trifluoromethyl-indolylfulgide. Both the *cis-trans* isomerization in hemithioindigo-hemistilbene and the electrocyclic ring closure/opening in indolylfulgide are characterized by a charge transfer in the excited state. The ability of each system to stabilize this charge transfer is essential for the returning to the ground state. The relaxation to the ground state through extended regions of the seam is found to be the decisive step determining the reaction speed and the quantum yield.

In the last part of this thesis mixed quantum-classical dynamics simulations at multi-configurational perturbation theory (MS-CASPT2) level, using Tully's fewest switches surface hopping approach, are performed to study the ultrafast photoreactivity of 1,3-cyclohexadiene in the gas-phase. For this purpose a numerical routine for the efficient

calculation of non-adiabatic couplings at MS-CASPT2 level is presented. The major part of the excited molecules are found to circumvent the $1B_2/2A_1$ conical intersection and reach the conical intersection seam between the excited state and the ground state instantaneuosly. Time constants for the evolution of the wavepacket on the bright $1B_2$-state, the relaxation into the $2A_1$-state and the return to the ground state are extracted. It is demonstrated that the accessibility of the conical intersection seam depends on its energetic and spatial relation to the minimum energy path, as well as on the momentum which is accumulated during relaxation on the excited state potential energy surface.

List of Publications

- T. Cordes, S. Malkmus, J. Di Girolamo, W. J. Lees, A. Nenov, R. de Vivie-Riedle, M. Braun and W. Zinth *Accelerated and Efficient Photochemistry from Higher Excited Electronic States in Fulgide Molecules*, J. Phys. Chem. A, **112** (2008) 13364.

- A. Nenov, P. Kölle, M. A. Robb and R. de Vivie-Riedle *Beyond the van der Lugt / Oosterhoff model: When the Conical Intersection Seam and the S_1 Minimum Energy Path do not Cross*, J. Org. Chem., **75** (2010) 123.

- A. Nenov, T. Cordes, T. T. Herzog, W. Zinth and R. de Vivie-Riedle *Molecular Driving Forces for Z/E Isomerization Mediated by Heteroatoms: The Example Hemithioindigo*, J. Phys. Chem. A, **114** (2010) 13016.

- A. Nenov and R. de Vivie-Riedle *Geometrical and Substituent Effects in Conical Intersections: Linking Chemical Structure and Photoreactivity in Polyenes*, J. Chem. Phys., **135** (2011) 034304.

- P. Kölle, A. Nenov, U. Megerle, P. Krok, H. Langhals, R. de Vivie-Riedle and E. Riedle *Ultrafast emission quenching in a perylene diimide by structure rearrangement induced electron transfer from its substituent*, J. Phys. Chem. A, submitted.

- A. Nenov and Regina de Vivie-Riedle *Conical Intersection Seams in Polyenes Derived from Their Chemical Composition*, J. Chem. Phys., **137** (2012) 074101.

- A. Nenov, W. J. Schreier, F. O. Koller, M. Braun, R. de Vivie-Riedle, W. Zinth and I. Pugliesi *Molecular model of the ring-opening and ring-closure reaction of a fluorinated indolylfulgide*, J. Phys. Chem. A, **116** (2012) 10518.

Contents

Introduction

Ever since the finding about the atomic structure of matter it has been our pursuit to cast a glance in chemical, biological and physical processes at atomic resolution, i.e. to follow geometrical deformations like bond breaking and formation in space and time. Tracking the temporal and spatial evolution of a system is the matter of dynamics. As the length scale of molecular bonds is 10^{-10} m (= 1 Ångstrom) and the nuclear speed is in the order of 10^3 m/s a femtosecond temporal resolution is required to achieve a sub-Ångstrom spatial resolution, i.e. to freeze the motion at atomic level. Ultrashort pulses provide a tool to monitor high-speed motion and open the door to femtodynamics. In their pioneering work Zewail and co-workers developed the pump-probe technique[1–3], allowing to take snap shots of the motion of the wavepacket on the excited state potential energy surface by applying a probe pulse at different delay times after triggering an event with a pump pulse. The pump-probe time-resolved spectroscopy allows to address fundamental questions reagarding the time order and time scale of photochemical and photobiological processes. This technique also proves valuable for studying processes in the ground state, e.g. protein folding initiated by an ultrafast molecular deformation induced by the pump pulse[4], thereby establishing a precise zero time reference for determining the time scales of folding. Nowadays, the development of the time-resolved techniques has extended the probing window from the ultraviolet to the near-infrared[5–13], thus permitting to follow the dynamics over extended regions of the excited state surface. A variety of experimental setups like time-resolved transient absorption, fluorescence, photoelectron and infrared spectroscopy have been designed that allow to observe the dynamics from different angles.

The introduction of the pump-probe technique launched a wave of experimental research on a variety of chemical and biological systems. It soon became evident that a number of processes occur much faster than any theoretical model could explain at that time. Exemplarily, prototypical molecules like ethylene[14, 15] and 1,3-cyclohexadiene[16–20], but also bulky systems like retinal[21–23] were found to return to the ground state in a fraction of a picosecond. The efficient ultrafast transfer of population between states could be explained only when real potential energy surface crossings between different electronic states, i.e. conical intersections[24–26], were considered. The development of novel theoretical approaches[27–35] specialized at the optimization of low-energy conical intersections catalyzed the research of photoreactions. These peculiar points on the potential energy surface (called by some authors diabolic points[36]) were quickly recognized as the key factor for the stability of DNA bases[37–42], the initial event in the process of vision[43–46], electrocyclic photoreactions[47–50], photodissociations[51–53], energy and charge trans-

fer processes[54, 55], etc.. As the passage through a conical intersection occurs very rapidly and can not be detected spectroscopically it has become a task for the quantum chemists to shed light on their structure, accessibility and reactivity. In recent years, as new field of research the optimization and characterization of energetically low-lying conical intersection seams, hyperlines of conical intersections allowing for a versatile and effective decay to ground state from extended regions of the excited state potential energy surface, moved into the focus of interest[36, 56–60].

The present work provides an ab-initio treatment of ultrafast photoreactions mediated by conical intersection by means of quantum chemistry and mixed quantum-classical dynamics. In the first section the basic theoretical concepts are outlined. In the second section a theory is presented which allows to derive rules of thumb to predict the structure of single conical intersections and conical intersection seams in arbitrary multifunctionalized polyenes. The method is based on an extension of the two-electron two-orbital model introduced by Michl and Bonačić-Koutecký[61]. It is able to predict structure, topology and energy dependence on the substituent pattern and accelerates the search of conical intersections and conical intersection seam. In three examples this general technique is applied to the photochromic systems 1,3-cyclohexadiene/cZc-hexatriene, hemithioindigo-hemistilbene and trifluoromethyl-indolylfulgide, the latter two being candidates for application as molecular photoswitches in protein folding studies[62] and molecular electronics[63]. Conical intersection seams found in both systems, together with data from time-resolved transient and infrared spectroscopy, are used in the third section to reconstruct the complex multi-channel isomerization mechanism of both chromophores. The relaxation to the ground state through extended regions of the seam is found to be the decisive step determining the reaction speed and the quantum yield of isomerization.

Quantum chemistry gives valuable insights into possible intermediates, barrier heights and ground state products by means of minimum energy paths. However, momentum conservation in vibrational modes drives the systems away from the minimum energy path and can alter the outcome of the reaction. Dynamical simulations are indispensable for answering the following questions: (i) What time constants characterize the individual steps of a reaction? (ii) What is the population distribution in different reaction channels? (iii) Which regions of the conical intersection seam are reached preferentially? (iv) What is the product distribution out of the conical intersection seam? Dynamical simulations on polyatomic systems are very tedious and exact quantum dynamics in full coordinate space is currently out of reach for photoreactions. Quantum dynamics calculations in a reduced coordinate space is an alternative, but the coordinates have to be selected with great care to be physically meaningful. Semi-classical dynamics[64, 65] provide a workaround by focusing on a subset of the system, which is treated quantum mechanically (the electronic degrees of freedom) under the influence of the rest of the system treated classically (the nuclear degrees of freedom). This partitioning allows to mimic the evolution of a quantum dynamical wavepacket by a swarm of classcial trajectories driven by the quantum mechanical electronic potential. In this work the Tully's fewest switches surface hopping approach[66] implemented in the software package for Newtonian

dynamics Newton-X[67] is interlaced with the multi-state complete active space perturbation method[68–70] available in Molpro[71] to simulate non-adiabatic dynamics through conical intersections. In the fourth section of this work the implementation of non-adiabatic couplings at multi-state complete active space perturbation theory level, as well as preliminary results on the dynamics of 1,3-cyclohexadiene are presented. Cyclohexadiene is a prototype for a molecular photoswitch[72] and is the building block of the family of fulgide switches[73]. It is expected that the disclosure of its dynamics will provide valuable information about the accessibility and reactivity of the conical intersection seam[74] beyond the static description.

1. Theoretical background

The present work investigates light-induced ultrafast chemical reactions proceeding on a femtosecond to picosecond time scale by means of *ab initio* quantum chemical methods. The time-independent Schrödinger equation

$$\hat{H}\Psi(r,R) = E(r,R)\Psi(r,R) \tag{1.1}$$

provides the foundation of quantum chemistry. The molecular wavefunction $\Psi(r,R)$ contains the whole information about the nuclear and electronic degrees of freedom of the system and $\hat{H}$ is the Hamiltonian operator

$$\hat{H} = \underbrace{-\sum_\alpha \frac{1}{2m_\alpha}\nabla_\alpha^2}_{\hat{T}^{nuc}} \underbrace{-\sum_i \frac{1}{2}\nabla_i^2 - \sum_{\alpha,i}\frac{Z_\alpha}{R_{\alpha,i}} + \sum_{i,j}\frac{1}{R_{ij}} + \sum_{\alpha,\beta}\frac{Z_\alpha Z_\beta}{R_{\alpha\beta}}}_{\hat{H}^{el}}. \tag{1.2}$$

The first two terms in eq. 1.2 give the kinetic energy of the nuclei (i.e. $\hat{T}^{nuc}$) and of the electrons. The third term gives the electron-nuclei attraction and the last two terms give the electron and nuclear repulsion, respectively. The indices α, β and i, j run over the nuclei and electrons. Solution of eq. 1.1 poses a formidable challenge and is practically impossible for systems with more than three degrees of freedom unless some approximations are introduced. Probably the most significant one is the Born-Oppenheimer (BO) approximation, named after Max Born and Julius Robert Oppenheimer, which allows to treat electronic and nuclear degrees of freedom separately[75, 76]. Its physical justification is provided by the high ratio of the masses of nuclei and electrons, allowing the electrons to quasi-instantaneously adapt to a new nuclear arrangement. Therefore, the electronic motions depend only parametrically on the positions of the nuclei. This dependence allows us to write the total wavefunction $\Psi(r,R)$ in a product form

$$\Psi^{BO}(r,R) = \chi(R)\Psi^{el}(r;R), \tag{1.3}$$

where $\chi(R)$ depends only on the nuclear coordinates and $\Psi^{el}(r;R)$ depends explicitly on the electronic and parametrically on the nuclear coordinates. $\Psi^{el}(r;R)$ is an eigenfunction of the electronic Schrödinger operator $\hat{H}^{el}$

$$\hat{H}^{el}\Psi^{el}(r;R) = V(r;R)\Psi^{el}(r;R), \tag{1.4}$$

with $V(r;R)$ the electronic energy. The ansatz of eq. 1.3 simplfies the solution of eq. 1.1 significantly and is the basis of modern quantum chemistry. The electronic

Schrödinger equation can be solved for a number of fixed nuclear configurations in order to obtain the parametrical dependance of the electronic energy $V(R)$ on the nuclear coordinates. The function $V(R)$ enters the time-independent Schrödinger equation as a potential in which the nuclear wavefunction evolves

$$\left(\hat{T}^{nuc} + V(R)\right)\chi(R) = E(R)\chi(R). \tag{1.5}$$

The BO approximation is well suited for many purposes. However, there are cases where it fails and an explicit treatment of the correlation between molecular and electronic degrees of freedom is indispensable. In sec. 1.1 the circumstances under which the BO approximation breaks down are elaborated and the most prominent example for this break down, the conical intersections, are introduced. Sec. 1.2 provides a detailed insight into the mathematical treatment of conical intersections and conical intersection seams, their optimization and characterization. In sec. 1.3 the multi-configurational nature of photochemical processes, occuring via conical intersections, is elucidated with the help of molecular symmetry. Finally, in sec. 1.4 several quantun chemical methods for treating multi-configurational problems are presented. The following notation is used throughout: vectors are denoted by an arrow (e.g. $\vec{X}$), matrices are given in bold (e.g. $\mathbf{H}$).

1.1. Beyond the Born-Oppenheimer approximation

Going beyond the BO approximation the molecular wavefunction $\Psi(r, R)$ is no longer represented as the simple product from eq. 1.3. A formally exact ansatz is given by expanding the molecular wavefunction in the complete basis of eigenfunctions Ψ_i^{el} of the electronic Schrödinger equation 1.4 at a fixed nuclear geometry R as

$$\Psi(r, R) = \sum_i \chi_i(R)\Psi_i^{el}(r; R). \tag{1.6}$$

Inserting expansion 1.6 into eq. 1.1, multiplying from left with Ψ_j^{el} [1] and integrating over the electronic coordinates gives

$$\sum_i \left\langle \Psi_j^{el}\middle|\hat{T}^{nuc}\middle|\chi_i\Psi_i^{el}\right\rangle + \sum_i \left\langle \Psi_j^{el}\middle|\hat{H}^{el}\middle|\chi_i\Psi_i^{el}\right\rangle = E\sum_i \left\langle \Psi_j^{el}\middle|\chi_i\Psi_i^{el}\right\rangle. \tag{1.7}$$

Using eq. 1.4 and the chain rule for the second derivatives $\hat{T}_{nuc}$ the final form of the time-independent Schrödinger equation for the nuclei is obtained

$$\sum_i \left(\hat{T}^{nuc}\delta_{ij} + V_i\delta_{ij} + \left\langle \Psi_j^{el}\middle|\hat{T}^{nuc}\Psi_i^{el}\right\rangle - 2\sum_\alpha \frac{1}{2m_\alpha}\left\langle \Psi_j^{el}\middle|\nabla_\alpha\Psi_i^{el}\right\rangle\nabla_\alpha\right)\chi_i = E\sum_i \chi_i\delta_{ij} \tag{1.8}$$

---

[1]From here on dependencies on nuclear and electronic degrees of freedom are not denoted explicitly.

or in a matrix notation

$$\left(\hat{T}^{\text{nuc}}\mathbb{1} + \vec{V}^T\mathbb{1} + \mathbf{K}\right)\vec{\chi} = \vec{E}^T\mathbb{1}\vec{\chi}. \tag{1.9}$$

K is the non-adiabatic coupling matrix with elements

$$K_{ij} = -\sum_\alpha \frac{1}{2m_\alpha}(\underbrace{\left\langle\Psi_i^{el}\middle|\nabla_\alpha^2\Psi_j^{el}\right\rangle}_{\text{scalar coupl.}} + 2\cdot\underbrace{\left\langle\Psi_i^{el}\middle|\nabla_\alpha\Psi_j^{el}\right\rangle}_{\text{derivative coupl.}}\cdot\nabla_\alpha). \tag{1.10}$$

It describes the change of the electronic wavefunction with the nuclear displacement, i.e. correlates nuclear and electronic motions. To that point no approximation has been introduced and eqs. 1.8 and 1.9 are formally exact. In most cases the electronic structure changes only slightly with geometrical deformation and electrons can quickly adapt to the new nuclear arrangement. Then, the coupling terms are negligible and the BO approximation is justified. However, there are also cases where the electronic structure changes abruptly over a small geometrical deformation. The electrons can no longer follow the nuclei instantaneuosly and the BO approximation breaks down, giving rise to large couplings K_{ij}. It is therefore a matter of general concern to clarify when the BO approximation is impractical.

The scalar couplings are significantly smaller in magnitude than the dervative couplings. However, they cannot be completely neglected, as the Hamiltonian operator $\hat{H}$ would become Non-Hermitian. The hermeticity can be recovered by considering the non-Hermitian part of the scalar couplings, which can be expressed through the derivative couplings as $\sum_\alpha\nabla_\alpha\cdot\left\langle\Psi_i^{el}\middle|\nabla_\alpha\Psi_j^{el}\right\rangle$[77]. Thus, the non-adiabatic coupling K_{ij} is determined by the properties of the derivative couplings $\left\langle\Psi_i^{el}\middle|\nabla_\alpha\Psi_j^{el}\right\rangle$[2]

$$\left\langle\Psi_i^{el}\middle|\nabla_\alpha\Psi_j^{el}\right\rangle = -\left\langle\Psi_j^{el}\middle|\nabla_\alpha\Psi_i^{el}\right\rangle \quad\text{and}\quad \left\langle\Psi_i^{el}\middle|\nabla_\alpha\Psi_j^{el}\right\rangle = \frac{\left\langle\Psi_i^{el}\middle|\nabla_\alpha\hat{H}\middle|\Psi_j^{el}\right\rangle}{V_j - V_i}. \tag{1.11}$$

The expression on the left states that the derivative coupling couples only vibronic states belonging to different electronic states (for $i = j$ the coupling element is zero). The expression on the right shows that, in general, the derivative coupling between two states increases in magnitude when their Potential–Energy–Surface (PES)s come closer.

Large couplings induce an efficient and rapid change between electronic surfaces. This phenomenon lies beneath the experimental observation that ultrafast photochemical reactions can take less than a few hundred femtoseconds from the moment of excitation of the reactant into an electronically Excited State (ES) to the formation of the product in the Ground State (GS). In order to shed light on the ultrafast molecular mechanisms it is crucial to locate energetically accessible regions where PESs degenerate. These special points, known as Conical Intersection (CoIn), are characterized in the next section.

---

[2]For derivation see Appendix A

1.2. Conical intersections

Although the conditions for potential energy curve crossing had been analyzed mathematically already in the thirties by von Neumann and Wigner[78] another fifty years had to go by before chemists took the concept of CoIns to heart. While CoIns between excited states were recognized as an effective relaxation mechanism from higher ES to the first ES (Kasha's rule[79] is a direct consequence from the instantaneuos relaxation to first ES), radiationless deactivation from the first ES was explained by vibronical coupling of the ES wavefunction to the GS using Fermi's golden rule[72]. It was believed that in molecules the realization of the concept of CoIn between the GS and the first ES demands formidable structural deformations. Hence, CoIns would occur only in high energy regions on the PES and would be irrelevant for the photochemistry. The lifetimes predicted by the Fermi's golden rule reach from nanoseconds down to several hundred picoseconds. Due to the lack of techniques allowing for subnanosecond time resolution the validity of applying the Fermi's golden rule could not be experimentally verified up to the late '80s. Zewail's pioneer works[1, 3] on femtosecond pump-probe gas-phase spectroscopy demonstrated that some photoreactions proceed much faster than anticipated. In the following years the pump-probe technique was successfully transfered to the condensed phase and the ultrafast photoreactivity was confirmed in numerous studies. With the advance of computer technology and the development of affordable methods for treatment of ES the observed ultrafast photoreactivity could be attributed to the presence of low-energy CoIns between the GS and first ES[47, 80–87]. In the next subsections some characteristic properties of CoIns, as well as methods for their localization and characterization are presented.

1.2.1. Adiabatic versus diabatic representation

In sec. 1.1 it was stated that the rapid change of the character of the electronic wavefuncton in the vicinity of a CoIn is responsible for the large non-adiabatic couplings K_{ij}. The calculation of coupling elements is a rather tedious task. Furthermore, their local nature requires to sample the PES around a CoIn in small intervals to recover their correct shape. A possible workaround is to use the diabatic representation[88, 89]. Diabatic wavefunctions are mathematical constructs that diagonalize the coupling matrix $\mathbf{K}$. From a chemical point of view diabatic wavefunctions can be understood as distinct electronic configurations (e.g. covalent or ionic), which behave smoothly, even in the vicinity of a CoIn. However diabatic wavefunctions are not eigenfunctions of the electronic Hamiltonian H^{el} and the coupling between states occurs via the off-diagonal elements in the Hamiltonian matrix. The adiabatic wavefunctions, which are eigenfunctions of the electronic Hamitonian, are allowed to change their character. This happens instantaneously when passing through a CoIn and leads to large non-adiabatic couplings. Then, the leading electronic configuration does not manage to stick with the adiabatic state and follows the diabatic surface, i.e. changes to a different adiabatic surface.

Transformation between a pair of diabatic and adiabatic states is unitary and is given

by the following formula[3]

$$\begin{pmatrix} \Psi_1^d \\ \Psi_2^d \end{pmatrix} = \begin{pmatrix} \cos(\alpha) & -\sin(\alpha) \\ \sin(\alpha) & \cos(\alpha) \end{pmatrix} \begin{pmatrix} \Psi_1^{ad} \\ \Psi_2^{ad} \end{pmatrix}, \tag{1.12}$$

with α the rotational or mixing angle[89] for which the coupling K_{ij} vanishes. The diabatic representation is chemically more intuitive because it follows the energy of a particular electronic configuration along the reaction coordinate and allows for a smooth change of PESs. Therefore, it is used to derive the conditions for CoIn formation.

1.2.2. Conditions for the existence of conical intersections

The adiabatic wavefunction is expanded in the vicinity of a CoIn in the basis of two orthonormalized diabatic states Ψ_1^d and Ψ_2^d[90]

$$\Psi^{ad} = c_1 \Psi_1^d + c_2 \Psi_2^d. \tag{1.13}$$

The eigenstates and energies ε_1 and ε_2 in this basis are obtained by solving the secular problem

$$\begin{pmatrix} H_{11} - \varepsilon & H_{12} \\ H_{12} & H_{22} - \varepsilon \end{pmatrix} \begin{pmatrix} c_1 \\ c_2 \end{pmatrix} = 0, \tag{1.14}$$

with matrix elements H_{ij} of the form $\left\langle \Psi_i^d \middle| \hat{H} \middle| \Psi_j^d \right\rangle$. Diagonalizing eq. 1.14 gives

$$\varepsilon_{1/2} = \frac{H_{11} + H_{22} \pm \sqrt{(H_{11} - H_{22})^2 + 4H_{12}^2}}{2}. \tag{1.15}$$

At a CoIn the two states are isoenergetic, i.e. $\varepsilon_1 = \varepsilon_2$. This requirement provides a set of two independent conditions for the degeneracy

$$H_{11} - H_{22} = 0 \quad \text{and} \quad H_{12} = 0. \tag{1.16}$$

Eqs. 1.16 implicate that two independently variable nuclear coordinates are needed to reach a point of degeneracy. This conclusion is the basis for the non-crossing rule which states that in diatomics real crossings can occur only between states of different (spatial or spin) symmetry, as the coupling term H_{12} is zero. In this special case the condition $H_{11} - H_{22} = 0$ can be fulfilled at a particular internuclear distance. For states of the same symmetry the coupling term has a finit magnitude and no internuclear distance exist where both conditions are fulfilled simultaneously. In polyatomic molecules with $3N - 6$ independently variable coordinates this limitation does not hold. Correspondingly, degeneracy can occur at each point of a $3N - 8$ dimensional hyperspace, known as the Intersection Space (IS)[89].

---

[3]Provided that the two states are well separated everywhere on the PES from the remaining electronic states.
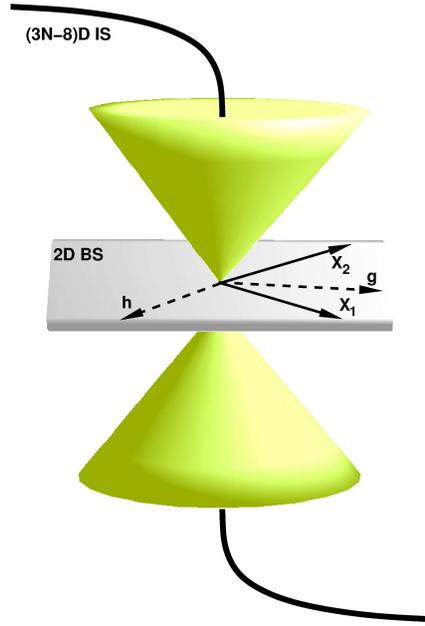
Figure 1.1.: A symmetric CoIn within the two-dimensional BS, which lifts the energetic degeneracy. The 3N-8 dimensional IS, which preserves the degeneracy, lies perpendicular to the BS. The BS vectors in the diabatic (eqs. 1.17) and in the adiabatic (eqs. 1.18) basis do not coincide but span the same plane.

At each point of this space the degeneracy is lifted along two specific vectors derived from the conditions in eq. 1.16

$$\vec{g} = \nabla_R(H_{11} - H_{22}) \tag{1.17a}$$

$$\vec{h} = \nabla_R H_{12} \tag{1.17b}$$

These vectors span the BS[89] perpendicular to the IS (fig. 1.1).

The implementation of algorithms for optimizing CoIns requires the knowledge of the BS. However, while the requirements in eqs. 1.16 are formulated in a diabatic basis, most quantum chemical programs provide adiabatic states and energies. Using the transformation between adiabatic and diabatic states (eq. 1.12) it can be shown that the adiabatic vectors

$$\vec{X}_1 = \nabla_R(V_1 - V_2) \tag{1.18a}$$

$$\vec{X}_2 = (V_2 - V_1)\left\langle \Psi_1^{ad} \middle| \nabla_R \Psi_2^{ad} \right\rangle \tag{1.18b}$$

span the very same plane around a CoIn as $\vec{g}$ and $\vec{h}$ (see Appendix B) (fig. 1.1). Thereby, V_1 and V_2 are the adiabatic energies. Therefore, it suffices to calculate the gradient difference vector $\vec{X}_1$ and the scaled derivative coupling vector $\vec{X}_2$ to obtain the BS in the vicintiy of a CoIn. In reality, the BS is curved in space[91] and the plane

spanned by $\vec{X}_1$ and $\vec{X}_2$ at a CoIn is only tangential to the curved BS. Consequently, also the space spanned by the $3N-8$ vectors perpendicular to $\vec{X}_1$ and $\vec{X}_2$ is tangential to the IS and displacement along them lifts the degeneracy as well. Recovery of the degeneracy is possible by a subsequent displacement along $\vec{X}_1$ and $\vec{X}_2$. With this consideration it becomes possible to formulate a set of curvilinear coordinates, which reproduce the IS energy profile around the CoIn correctly to second order[59, 60]. Differentiating the energy twice with respect to the curvilinear coordinates provides a projection of the Hessian matrix to the IS. Its diagonalization gives frequencies and normal modes characterizing the local curvature of the IS around a CoIn. This analysis allows to search the IS not only for local minima but also for saddle points[92]. It facilitated the optimization of Minimum–Energy–Path (MEP) in the IS, boosting the search of energetically low-lying CoIn seams[74].

1.2.3. Projection method for optimizing minimum energy conical intersections
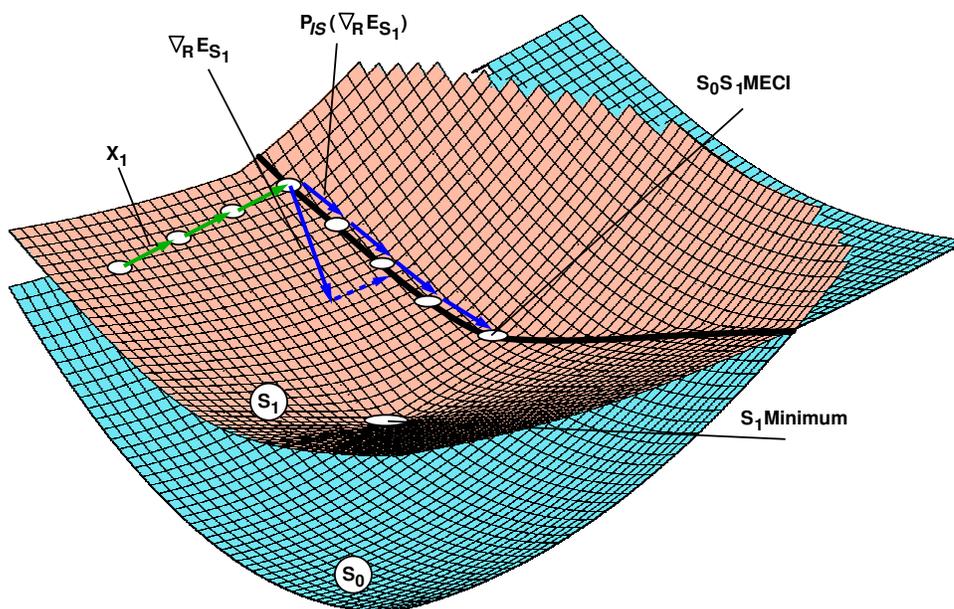
Figure 1.2.: Schematic representation of the algorithm used to optimize minimum energy CoIns (S_0S_1MECI). The effective gradient, which is followed during the optimization, has two contributions. Starting at an arbitrary position in space, displacement along the gradient difference vector $\vec{X}_1$ locates the nearest point of degeneracy between the upper (S_1) and the lower (S_0) states (green arrows). Following the projection of the S_1 gradient onto the orthogonal complement to the plane spanned by the gradient difference ($\vec{X}_1$) and derivative coupling ($\vec{X}_2$) vectors locates a minimum in the IS.

Next, a robust and fast method for locating minimum energy CoIns, proposed originally by Bearpark et al.[31, 92] and currently implemented in software packages like Gaussian[93] and Molpro[71], is outlined. The general idea is to minimize an effective gradient composed of two terms

$$\vec{g} = 2(V_2 - V_1)\frac{\vec{X}_1}{\left\|\vec{X}_1\right\|} + \mathbf{P}_{IS}(\nabla_R V_2). \tag{1.19}$$

Displacement along the gradient difference vector $\vec{X}_1$ drives the algorithm towards the nearest point of degeneracy (green line in fig. 1.2). The multiplication of the normalized gradient difference vector with the energy difference assures that the first term vanishes when both states become degenerate. The second term represents the projection of the ES gradient onto the orthogonal complement to the plane spanned by $\vec{X}_1$ and $\vec{X}_2$ (blue lines in fig. 1.2), accomplished by the projection matrix $\mathbf{P}_{IS} = \mathbf{1} - \mathbf{A}(\mathbf{A}^T\mathbf{A})^{-1}\mathbf{A}^T$ with $\mathbf{A}$ a matrix with columns $\vec{X}_1$ and $\vec{X}_2$. At a point of degeneracy the orthogonal complement to the plane spanned by $\vec{X}_1$ and $\vec{X}_2$ is tangential to the IS. Following the projection of the gradient onto this sub-space ensures that the optimized structure is a minimum in the IS (S_0S_1MECI in fig. 1.2). Consequently, at a minimum energy CoIn the energy of the upper state increases in any of the $3N - 8$ directions of the IS. Then, the energy of the lower state increases as well, as the degeneracy between the upper and the lower state is conserved in the IS. Thus, any information about the GS products accessible directly from the apex of the CoIn is reserved to the BS. A completely symmetric CoIn (a CoIn with a circular base of the cone) as given in fig. 1.1 would implicate an infinite number of relaxation directions in the GS[56]. In practice, there exist preferential relaxation directions associated with steep slopes on the GS PES. These preferential directions can be obtained by performing an unrelaxed scan on a circular cross section around the CoIn in the plane spanned by X_1 and X_2. The number of minima passed through during the scan equals the number of barrierless relaxation pathways in the GS.

By performing an unrelaxed scan one neglects the fact that the plane spanned by X_1 and X_2 coincides with the BS only in infinitesimal displacement from the apex of the cone. An advanced procedure to cope with this issue replaces the scan on the circular cross section by a constrained optimization on a hypersphere around the CoIn[94]. In the present work solely unrelaxed scans around CoIns were performed. It deserves further attention, that the information about the GS relaxation channels gathered in this way is non-dynamical and describes accurately only vibrationally cold ES molecules which relax to the GS through the tip of the CoIn.

1.3. Orbital analysis of photochemical reactions: when to look for conical intersetions

The previous section focused on the mathematical background of CoIns. Up to now a chemical interpretation of the conditions for CoIn formation (eqs. 1.16) has been left out. One goal of this work is to establish a correlation between the chemical composition, the molecular structure and the accessibility of CoIns. For that purpose a Molecular Orbitals (MO) analysis which is used to estimate the energy profile along geometrical deformations is presented. Thereby, the emphasis is on isomerizations. Figure 1.3a presents the valence orbitals of three unsaturated hydrocarbones, which can undergo either a double bond torsion (ethylene, bottom row) or a cyclization (*cis*-butadiene, middle row and cZc-Hexatriene (HT), top row). In the case of ethylene, starting at the Highest Occupied Molecular Orbital (HOMO) a double bond torsion introduces a node in the MO, thereby correlating the HOMO of the one isomer to the Lowest Unoccupied Molecular Orbital (LUMO) of the other isomer. Correspondingly, the configuration with a doubly occupied HOMO of the one isomer correlates to the configuration with a doubly occupied LUMO of the other isomer and vice versa. This correlation diagram (dashed black lines in fig. 1.3a) allows to follow the energy of a particular electronic configuration along a reaction coordinate in analogy to a diabatic representation. The same correlation pattern is encountered for butadiene and HT with respect to the symmetry conserving disrotatory (σ_v mirror plane) and conrotatory (C_2 rotation axis) cyclization (fig. 1.3a). Thus, the correlation diagrams of all three reactions can be described with the same diabatic scheme (green dashed lines fig. 1.3b). By allowing the diabatic states to mix adiabatic states are constructed (red, black and blue solid line in fig 1.3b). Thereby, the diabatic curve crossings become avoided crossings (marked with circles) in the adiabatic representation. Several conclusions can be drawn from the correlation diagram:

a) Geometrical deformations for which the PESs of GS and ES come close can be derived by symmetry considerations.

b) A low-energy CoIn between GS and ES is likely to exist when the valence orbitals of reactant and product are correlated according to fig. 1.3. In fact, this correlation is in the heart of the qualitative rules by Woodward and Hoffmann[95, 96], predicting symmetry "allowed" and "forbidden" photoisomerizations.

c) The non-crossing rule for diatomics[78] holds along the symmetry conserving coordinate. A real CoIn can be reached by an asymmetric deformation.

d) Different isomerization reactions are characterized by a common correlation diagram. Hence, rules for locating CoIns that apply to one of the isomerization reactions outlined above should apply to all three reactions.

The diabatic scheme (fig. 1.3b) shows that in the avoided crossing regions the adiabatic states cannot be represented by a single electronic configuration and become
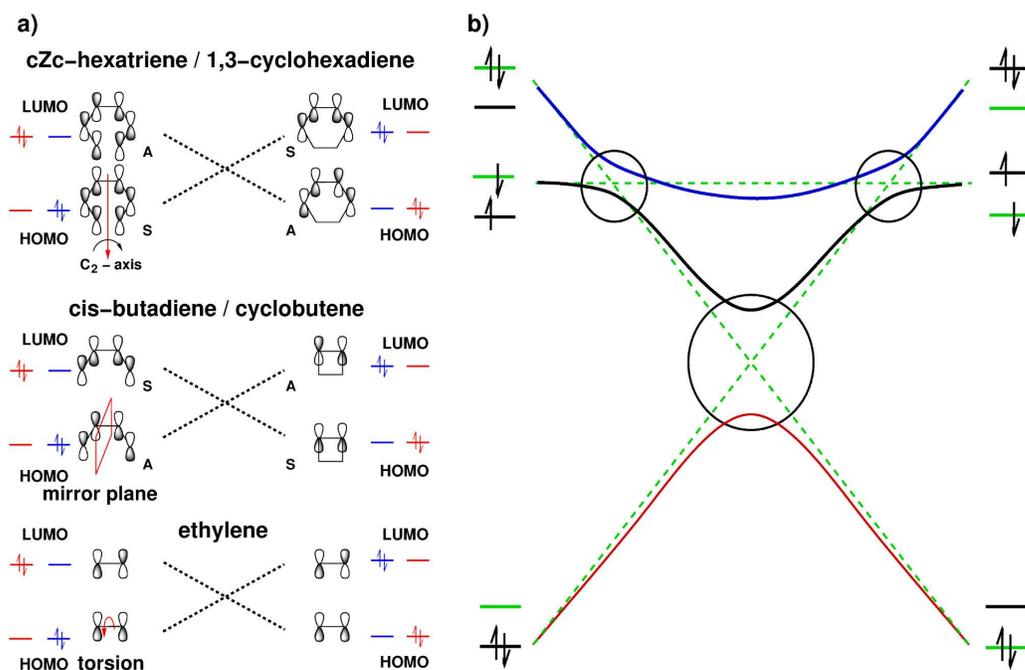
Figure 1.3.: a) Correlation diagrams for ethylene, *cis*-butadiene, cZc-HT along the symmetry conserving reaction coordinates double bond torsion, disrotatory and conrotatory ring opening/closure. b) A unifying diabatic (dashed lines) and adiabatic (solid lines) representation of the correlation diagrams of ethylene, *cis*-butadiene, cZc-HT. The diabatic states cross, the adiabatic states exhibit avoided crossings.

a mixture of configurations. Therefore, for the accurate quantum chemical description of photoisomerization reactions mediated by CoIns it is essential to use methods which can handle multiconfigurational problems. Such methods are in the focus of the next section.

1.4. Solution of the time-independent Schrödinger equation

The electronic wavefunction Ψ^{el} is a many-particle function, depending explicitly on the coordinates of the electrons and parametrically on the coordinates of the nuclei. Each electron is represented in the basis of one-paticle wavefunctions $\tilde{\phi}_i$, also known as spin-orbitals[75], products of the spatial wavefunctions of the electronic coordinates and spin wavefunctions, describing its spin ($\left|\alpha\right\rangle$ or $\left|\beta\right\rangle$)

$$\tilde{\phi}_i = \phi_i\left|\alpha\right\rangle \quad \text{or} \quad \tilde{\phi}_i = \phi_i\left|\beta\right\rangle. \tag{1.20}$$

The total electronic wavefunction can be expanded in the complete basis of one-particle spin-orbitals[75]. If the total electronic wavefunction Ψ^{el} depends only on one variable the expansion reads

$$\Psi^{el}(1) = \sum_i^\infty C_i \; \tilde{\phi}_i(1). \tag{1.21}$$

For two independent variables an expansion in the same one-particle basis reads

$$\Psi^{el}(1,2) = \sum_{i,j}^\infty C_{i,j} \; \tilde{\phi}_i(1)\tilde{\phi}_j(2). \tag{1.22}$$

Correspondingly, for a system of n electrons the exact expansion reads

$$\Psi^{el}(1,2,\ldots,n) = \sum_{i,j,\ldots,m}^\infty C_{i,j,\ldots,m} \; \tilde{\phi}_i(1)\tilde{\phi}_j(2)\ldots\tilde{\phi}_m(n). \tag{1.23}$$

A proper electronic wavefunction must satisfy several conditions. The Pauli exclusion principle postulates that it must change sign when the coordinates of any two electrons are exchanged

$$\Psi^{el}(1,2,\ldots,n) = -\Psi^{el}(2,1,\ldots,n). \tag{1.24}$$

With eq. 1.24 eq. 1.23 is rewritten as a linear combination of Slater determinants, i.e. mathematical construct, which satisfy the Pauli principle

$$\Psi^{el}(1,2,\ldots,n) = \sum_q^\infty C_q\Psi_q^{SD} \quad \text{with} \quad \Psi_q^{SD} = \frac{1}{\sqrt{n!}} \begin{vmatrix} \tilde{\phi}_i(1) & \cdots & \tilde{\phi}_n(1) \\ \vdots & \ddots & \vdots \\ \tilde{\phi}_i(n) & \cdots & \tilde{\phi}_n(n) \end{vmatrix}, \tag{1.25}$$

where the expansion goes over all possible $i,j\ldots,m$ combinations. The expansion coefficients C_q are unknown and an optimization procedure is required (see sec. 1.4.2). The electronic wavefunction Ψ^{el} commutes with the spin and angular momentum operators $\hat{S}^2$, $\hat{S}^z$, $\hat{L}^2$ and $\hat{L}^z$, however, the Slater determinants do not. It is therefore conventional to work with Configuration–State–Function (CSF)s Φ, which are spin- and symmetry adapted linear combination of Slater determinants, to avoids spin-contamination issues[97].
The spatial part ϕ_i of the one-particle wavefunction $\tilde{\phi}_i$ used to construct the Slater determinants are unknown as well and need to be optimized (see sec. 1.4.2). Roothaan proposed to expand each ϕ_i in the complete basis of atomic orbitals Θ_k[98]

$$\phi_i = \sum_{ki}^\infty c_{ki} \; \Theta_k. \tag{1.26}$$

The atomic orbitals can be either of Slater type or Gaussian type, the former being hydrogen-like and thus more accurate, the latter allowing for a fast integral calcu-

lations. With increasing molecular size and number of integrals the STOs quickly become impractical, so that nowadays the GTOs are the functions of choice in quantum chemical calculations. Due to the inaccurate description at very short and large distances from the nuclei each Θ_k is represented as a non-variable contraction of several primitive GTOs

$$\Theta_k = \sum_t d_{kt}\ \chi_t. \tag{1.27}$$

The non-variable nature of the expansion assures the uniformity of quantum chemical calculations. The art and size of the contraction scheme, i.e. the basis set, decide on the quality of the orbital representation. In general, the quality improves with the number of primitive GTOs included in the contraction. The use of finit basis sets represents an error source that must not be underestimated.

The complex nature of the many-particle wavefunction requires a treatment at several levels as summarized in the follwing scheme:

$$\underbrace{\Psi^{el}}_{\text{el. wave fct.}} \rightarrow \underbrace{\Phi}_{\text{conf. state fct.}} \rightarrow \underbrace{\Psi^{SD}}_{\text{Slater det.}} \rightarrow \underbrace{\tilde{\phi}}_{\text{spin orbital}} \rightarrow$$

$$\underbrace{\phi}_{\text{mol. orbital}} \rightarrow \underbrace{\Theta}_{\text{contr. basis fct.}} \rightarrow \underbrace{\chi}_{\text{prim. basis fct.}}$$
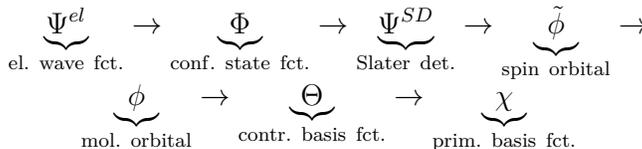
An exact electronic wavefunction Ψ^{el} is completely determined by two infinite sets of expansion coefficients, the CSF (C_q in eq. 1.25) and MO (c_{ki} in eq. 1.26) coefficients. As inifinite expansions are not manageable practically different truncation schemes have been proposed. The crudest approximation is to completely discard the multiconfigurational nature of the electronic wavefunction and only optimize the MO coefficients. This basic approach is known as the Hartree–Fock (HF) Self–Consistent–Field (SCF) method[75, 76]. It constitutes the fundament for all subsequent methods. A significant improvement is achieved by expanding the wavefunction in the basis of all determinants generated via single and double excitations from the HF determinant and finding the optimal solution for the CSF coefficients. Those methods are known as CI with Singles (CIS)[99] and CI with Singles and Doubles (CISD)[100]. Despite discarding higher order excitations, already for CISD the expansion space becomes prohibitively large even for medium-sized molecules and basis sets. A more sophisticated strategy is to optimize the MO and CSF coefficients simultaneously. This ansatz, called the Multi–Configuration SCF (MCSCF) method[101–104], achieves accurate results with a significantly reduced number of determinants/CSFs. However, the additional effort emerging from the complexity of the optimization procedure makes it necessary to restrict the excitations to a subspace of orbitals, referred to as the active space. This modification of the MCSCF ansatz is called the Complete–Active–Space SCF (CASSCF)[101–104]. Normally, the active space is constructed from the valence orbitals. The remaining orbitals are further described at HF level. This shortcomming prevents CASSCF from providing quantitative results. Two improvements have been established, the Multi–Reference–CI (MRCI)[104–106] and the Complete–Active–Space–Perturbation–Theory (CASPT2)[68–70]. Both methods extend the expansion space by including higher order excitations from the CASSCF

wavefunction. The MRCI is a variational approach, similar to CIS and CISD, but using a CASSCF reference function instead of a HF one. CASPT2 treats higher order excitations as perturbation to the CASSCF wavefunction. Both techniques provide almost quantitative results, however, at the expense of immense computatinal effort. CASPT2 is less time-consuming and the method of choice for the systems studied in this work. The next sections provide an overview of the MCSCF and CASPT2 methods. To reduce the mathematical complexity a more practical notation of wavefunctions and operators, known as second quantization, is briefly introduced.

1.4.1. A short introduction to second quantization

Wavefunctions and operators in the standard formulation of quantum mechanics (i.e. first quantization) are defined as functions in the Hilbert space H_n of a fixed number of particles n. Second quantization provides an alternative formulation[75, 107] capable of treating systems with variable number of particles. It extends the expansion space of the wavefunction to the Fock space, constructed as a direct sum over Hilbert spaces H_n ($n = 0 \ldots N$, with N the maximal number of one-particle functions in the system)

$$F_N = H_0 \oplus H_1 \oplus \cdots \oplus H_N. \tag{1.28}$$

Second quantization redefines wavefunctions and operators in the basis of a common set of elementary operators (creation and annihilation operators) and allows for a compact formulation of analytical solutions in multiconfigurational problems.
In second quantization[4] the occupation number vector $\left|k\right\rangle$ is the pendant to a Slater determinant. It gives the occupation of a particular Slater determinant

$$\left|k\right\rangle = \left|k_1, k_2, \cdots, k_N\right\rangle, \tag{1.29}$$

with N the total number of orbitals (occupied and unoccupied) and $k_i = 0, 1$ according to whether the i-th orbital is occupied by an electron or not. In first quantization any multiconfigurational wavefunction can be expanded in the basis of Slater determinants (eq. 1.25). In second quantization the expansion is realized in the basis of occupation number vectors $\left|k\right\rangle$

$$\left|\Psi\right\rangle = \sum_k C_k \left|k\right\rangle. \tag{1.30}$$

The creation and annihilation operators Second quantization allows to formulate operators which shift occupation number vectors between Hilbert spaces. The creation operator $\hat{a}_i^\dagger$

$$\begin{aligned} \hat{a}_i^\dagger \left|k_1, \cdots, 0_i, \cdots, k_N\right\rangle &= (-1)^{\left(\sum_{j=1}^{i-1} k_j\right)} \left|k_1, \cdots, 1_i, \cdots, k_N\right\rangle, \\ \hat{a}_i^\dagger \left|k_1, \cdots, 1_i, \cdots, k_N\right\rangle &= 0 \end{aligned} \tag{1.31}$$

---

[4]This section was written based on the lectures of Jeppe Olsen given at the ESQC 2011[108].

creates an electron in the i-th orbital if it is initially unoccupied and gives zero if this orbital is already occupied. The phase factor $(-1)^{\left(\sum_{j=1}^{k-1} k_j\right)}$ depends on the position of the orbital in the occupation number vector and assures that the Pauli exclusion principle is fulfilled.

The annihilation operator $\hat{a}_i$

$$
\begin{aligned}
\hat{a}_i \big| k_1, \cdots, 1_i, \cdots, k_N \big\rangle &= (-1)^{\left(\sum_{j=1}^{i-1} k_j\right)} \big| k_1, \cdots, 0_i, \cdots, k_N \big\rangle, \\
\hat{a}_i \big| k_1, \cdots, 0_i, \cdots, k_N \big\rangle &= 0
\end{aligned}
\tag{1.32}
$$

annihilates an electron in the i-th orbital if it is occupied and gives zero if this orbital is empty. It can be also defined as the adjoint to the creation operator, i.e. $\hat{a}_i = \left(a_i^\dagger\right)^\dagger$. The product $\hat{a}_j^\dagger \hat{a}_i$ annihilates an electron in the i-th orbital and creates an electron in the j-th orbital j, thus, performing an $i \to j$ single-electron excitation

$$
\hat{a}_j^\dagger \hat{a}_i \big| k_1, \cdots, 1_i, \cdots, 0_j \cdots, k_N \big\rangle = \pm \big| k_1, \cdots, 0_i, \cdots, 1_j \cdots, k_N \big\rangle.
\tag{1.33}
$$

Higher order excitation operators can be defined in analogous way.

Wavefunctions in second quantized form Each occupation number vector $\big| k \big\rangle$ can be expressed as a product of creation operators applied to the vacuum state $\big| \big\rangle$, which is just an empty vector

$$
\big| k \big\rangle = \prod_{i=0}^{N} (\hat{a}_i^\dagger)^{k_i} \big| \big\rangle.
\tag{1.34}
$$

From the above definitions for the elementry operators (eq. 1.31 and 1.32) it follows that the product $a_i^\dagger a_i$ applied to an occupation number vector leaves the vector unchanged and multiplies it with the occupation number of orbital i

$$
\sum_i^N \hat{a}_i^\dagger \hat{a}_i \big| k \big\rangle = \sum_i (k_i) \big| k \big\rangle = n \big| k \big\rangle,
\tag{1.35}
$$

with n being the total number of electrons in the system.

One-and two-electron operators in second quantized form Operators can also be reformulated in second quantized form under the consideration that first and second quantization should give the same result when applied to a wavefunction. Any one-electron operator can be written in a form

$$
\hat{f} = \sum_{ij} f_{ij} \hat{a}_j^\dagger \hat{a}_i = \sum_{ij} \big\langle j \big| \hat{h}(1) \big| i \big\rangle \hat{a}_j^\dagger \hat{a}_i,
\tag{1.36}
$$

where $\hat{h}(1)$ is an arbitrary one-electron operator in its first quantized form. Any two-electron operator can be written in a form

$$\hat{g} = \sum_{ijkl} g_{ijkl} \hat{a}_j^\dagger \hat{a}_l^\dagger \hat{a}_k \hat{a}_i = \sum_{ijkl} \left\langle jl \middle| \hat{h}(1,2) \middle| ki \right\rangle \hat{a}_j^\dagger \hat{a}_l^\dagger \hat{a}_k \hat{a}_i, \tag{1.37}$$

where $\hat{h}(1,2)$ is an arbitrary two-electron operator in its first quantized form.
Formulated in this way both operators are independent of the number of electrons in the system, but depend on the orbital basis.
With the above definitions the electronic Hamilton operator (eq. 1.2) can be reformulated in the scope of second quantization as

$$\hat{H}^{el} = \underbrace{-\sum_i \frac{1}{2m_i} \nabla_i^2 - \sum_{\alpha,i} \frac{Z_\alpha}{R_{\alpha,i}}}_{\sum_i \hat{h}(i)} + \underbrace{\sum_{i,j} \frac{1}{R_{ij}}}_{\frac{1}{2}\sum_{ij} \hat{h}(i,j)} = \sum_{ij} f_{ij} \hat{a}_j^\dagger \hat{a}_i + \frac{1}{2} \sum_{ijkl} g_{ijkl} \hat{a}_j^\dagger \hat{a}_l^\dagger \hat{a}_k \hat{a}_i. \tag{1.38}$$

When the spin of the electron is taken into account eq. 1.38 becomes

$$\hat{H}^{el} = \sum_{ij} f_{ij} \hat{E}_{ji} + \frac{1}{2} \sum_{ijkl} g_{ijkl} \hat{e}_{jilk} \tag{1.39}$$

with the spin-adapted excitation operators $\hat{E}_{ji} = \sum_\sigma^{\alpha,\beta} \hat{a}_{j\sigma}^\dagger \hat{a}_{i\sigma}$ and $\hat{e}_{jilk} = \hat{E}_{ji}\hat{E}_{lk} - \delta_{il}\hat{E}_{jk}$.

Matrix elements in second-quantized form   When the electronic Hamiltonian operator (eq. 1.39) is applied to a wavefunction of the form eq. 1.29 the matrix element $\left\langle \Psi \middle| \hat{H} \middle| \Psi \right\rangle$ becomes

$$\left\langle \Psi \middle| \hat{H} \middle| \Psi \right\rangle = \sum_{ij} f_{ij} \left\langle \Psi \middle| \hat{E}_{ji} \middle| \Psi \right\rangle + \frac{1}{2} \sum_{ijkl} g_{ijkl} \left\langle \Psi \middle| \hat{e}_{jilk} \middle| \Psi \right\rangle = \sum_{ij} f_{ij} D_{ji} + \frac{1}{2} \sum_{ijkl} g_{ijkl} d_{jilk}. \tag{1.40}$$

D_{ji} and d_{jilk} are matrix elements of the one- and two-electron density matrices $\mathbf{D}$ and $\mathbf{d}$

$$D_{ji} = \sum_{rs} C_r C_s \left\langle r \middle| \hat{E}_{ji} \middle| s \right\rangle \quad \text{and} \quad d_{jilk} = \sum_{rs} C_r C_s \left\langle r \middle| \hat{e}_{jilk} \middle| s \right\rangle. \tag{1.41}$$

Eq. 1.40 provides a very compact expression for the energy expectation value of multiconfigurational wavefunctions. The one- and two-electron integrals f_{ij} and g_{ijkl} collect the MO parameters, while the CSF coefficients show up in the density matrices $\mathbf{D}$ and $\mathbf{d}$.

1.4.2. The MCSCF formalism

The MCSCF approach optimizes the MO and CSF coefficients simultaneously. The complexity of the optimization procedure requires either the explicit selection of con-

figurations or restriction of the excitations to an orbital subspace, the active space. CSFs are generated by either performing all possible excitations among the active orbitals (i.e. CASSCF or solely excitations up to a certain order (i.e. Restricted–Active–Space–Self–Consistent–Field (RASSCF)[109]). The MCSCF theory gives a qualitatively correct description of the wavefunction in regions where different electronic configurations interact (static or long-range correlation[110]). In the following two variants of the CASSCF formalism are presented, the Single-State CASSCF (SS-CASSCF) and the State-Average CASSCF (SA-CASSCF)[111, 112].

SS- and SA-CASSCF energies   The MCSCF wavefunction has the form of eq. 1.29 and the total MCSCF energy is given by eq. 1.40. The energy is a function of the MOs $\vec{\phi}$ and the CSF coefficients $\vec{C}$. As the MOs define a real orthonormal basis the optimal solution can be formulated by a unitary transformation of the MO basis

$$\vec{\phi} = \mathbf{U}^T \vec{\phi}^{\,0} \quad \text{with} \quad \mathbf{U}^T \mathbf{U} = \mathbb{1}, \tag{1.42}$$

where $\vec{\phi}^{\,0}$ denotes some initial guess for the MOs. The orthogonal transformation matrix $\mathbf{U}$ contains n^2 optimization parameters (with n the size of the matrix). However, it can be shown (see Appendix C) that the number of linearly independent parameters of an orthogonal matrix is only $n(n-1)/2$. This prohibits the straightforward use of minimizers like Newton-Raphson to find the optimal solution. This problem can be resolved by writing down the transformation matrix in a matrix exponential form

$$\mathbf{U} = e^{\mathbf{K}} = \mathbb{1} + \mathbf{K} + \frac{1}{2}\mathbf{K}^2 + \cdots + \frac{1}{m!}\mathbf{K}^m + \cdots. \tag{1.43}$$

This is possible when $\mathbf{K}$ is a skew-symmetric matrix (i.e. $\mathbf{K}^T = -\mathbf{K}$). Then the matrix exponential is unitary

$$\left(e^{\mathbf{K}}\right)^T e^{\mathbf{K}} = e^{\mathbf{K}^T} e^{\mathbf{K}} = e^{-\mathbf{K}} e^{\mathbf{K}} = \mathbb{1}. \tag{1.44}$$

The lower triangular matrix of $\mathbf{K}$ contains $n(n-1)/2$ linearly independent parameters. In second quantization $\mathbf{K}$ is expressed as the one-electron operator (see Appendix D)

$$\hat{K} = \sum_{pq} k_{pq} E_{pq}, \tag{1.45}$$

with E_{pq} the spin-adapted one-electron excitation operator and k_{pq} the elements of the matrix $\mathbf{K}$, also called the orbital rotation parameters. In the following the entity of rotation parameters is referred to as the set $\vec{k}$. The action of $\mathbf{K}$ (and, hence, of $\hat{K}$) on a trial initial set of MOs transforms each MO as follows

$$\phi_p = \phi_p^0 + \sum_q k_{pq} \phi_q^0 + \frac{1}{2} \sum_{qr} k_{pr} k_{rq} \phi_q^0 + \cdots. \tag{1.46}$$

The CSF-coefficients are parametrized in a similar fashion. Thus, an optimal solution for the MCSCF wavefunction can be generated from a guess wavefunction Ψ_0 (a linear combination of CSFs with initial MO and CSF coefficients $\vec{\phi}^{\,0}$ and $\vec{C^0}$) by applying exponential operators

$$E(\vec{k}, \vec{p}) = \left\langle \Psi \middle| \hat{H} \middle| \Psi \right\rangle = \left\langle \Psi_0 \middle| e^{-\hat{P}} e^{-\hat{K}} \hat{H} e^{\hat{K}} e^{\hat{P}} \middle| \Psi_0 \right\rangle, \tag{1.47}$$

with $\hat{P}$ the operator containing the linearly independent CSF rotational parameters $\vec{p}$.

The optimal parameters can be now obtained via a Newton-Raphson scheme truncated to second order. Therefore the energy is expanded in the space of parameters of $\vec{k}$ and $\vec{p}$ around $\vec{\phi}^{\,0}$ and $\vec{C^0}$

$$\begin{aligned} E(\vec{k}, \vec{p}) &= E^0 + \begin{pmatrix} \vec{k} \\ \vec{p} \end{pmatrix}^T \begin{pmatrix} \vec{g}_k \\ \vec{g}_p \end{pmatrix} + \frac{1}{2} \begin{pmatrix} \vec{k} \\ \vec{p} \end{pmatrix}^T \begin{pmatrix} \mathbf{h}_{kk} & \mathbf{h}_{kp} \\ \mathbf{h}_{kp} & \mathbf{h}_{pp} \end{pmatrix} \begin{pmatrix} \vec{k} \\ \vec{p} \end{pmatrix} \\ &= E^0 + \vec{\boldsymbol{\lambda}}^T \mathbf{G} + \frac{1}{2} \vec{\boldsymbol{\lambda}}^T \mathbf{H} \vec{\boldsymbol{\lambda}}. \end{aligned} \tag{1.48}$$

E^0 is given by eq 1.40, $\vec{\boldsymbol{\lambda}}$ is the supervector containing the optimization parameters, $\vec{\mathbf{G}}$ is the supervector containing gradients of the energy with respect to $\vec{\boldsymbol{\lambda}}$ and $\mathbf{H}$ is the Hessian supermatrix of the second derivatives of the energy. At a stationary point in the parameter space the first derivative of the energy is zero

$$\frac{\partial E(\vec{\boldsymbol{\lambda}})}{\partial \vec{\boldsymbol{\lambda}}} = 0 = \vec{\mathbf{G}} + \frac{1}{2} \mathbf{H} \vec{\boldsymbol{\lambda}} \quad \Rightarrow \quad \vec{\boldsymbol{\lambda}} = -\frac{1}{2} \mathbf{H}^{-1} \vec{\mathbf{G}}. \tag{1.49}$$

The elements of $\vec{\mathbf{G}}$ and $\mathbf{H}$ are obtained by applying the Baker-Campbell-Hausdorff formula (see Appendix E) to eq. 1.47, i.e. by expanding the exponentials according to eq. 1.43

$$\begin{aligned} E(\vec{k}, \vec{p}) = \left\langle \Psi_0 \middle| \hat{H} + [\hat{K}, \hat{H}] + [\hat{P}, \hat{H}] + \frac{1}{2}[\hat{K}, [\hat{K}, \hat{H}]] + \right. \\ \left. [\hat{P}, [\hat{K}, \hat{H}]] + \frac{1}{2}[\hat{P}, [\hat{P}, \hat{H}]] \middle| \Psi_0 \right\rangle. \end{aligned} \tag{1.50}$$

Exemplarily, the gradient of the energy $\vec{g}_k$ with respect to the MO rotations (eq. 1.48), can be derived from eq. 1.50 as

$$\left\langle \Psi_0 \middle| [\hat{K}, \hat{H}] \middle| \Psi_0 \right\rangle = \sum_{pq} k_{pq} \left\langle \Psi_0 \middle| [E_{pq}, \hat{H}] \middle| \Psi_0 \right\rangle = \vec{k} \vec{g}_k, \tag{1.51}$$

where eq. 1.45 was used. The gradient of the energy $\vec{g}_p$ with respect to the CSF rotational parameters and the elements of the Hessian $\mathbf{H}$ (eq. 1.48) can be expressed in a similar fashion in terms of one- and two-electron integrals and density matrices, which allows for their analytic computation.

Eq. 1.49 is evaluated to obtain the rotational parameters $\vec{k}$ and $\vec{p}$. Next, the action

of $e^{\mathbf{K}}$ and $e^{\mathbf{P}}$ on the wavefunction Ψ_0 is computed[104]. This can be readily done by rewriting the exponential according to the Taylor expansion introduced in eq. 1.43. However, this algorithm is quite expensive as it involves multiplications of large matrices. An alternative approach is to diagonalize $\mathbf{K}$ and $\mathbf{P}$ and express the matrix exponential (e.g. $\mathbf{K}$) as

$$e^{\mathbf{K}} = \mathbf{V} e^{i\varepsilon} \mathbf{V}^{\dagger} = \mathbf{V} \left(\cos\left(\boldsymbol{\varepsilon}\right) - i\sin\left(\boldsymbol{\varepsilon}\right) \right) \mathbf{V}^{\dagger} \quad \text{with} \quad \mathbf{KV} = i\boldsymbol{\varepsilon}\mathbf{V}. \tag{1.52}$$

$\mathbf{V}$ is the unitary matrix which diagonalizes the skew-symmetric matrix $\mathbf{K}$ and $\boldsymbol{\varepsilon}$ is a diagonal matrix with real values.

An iterative procedure is applied until the gradient $\vec{\mathbf{G}}$ falls in magnitude below a certain threshold. Then, the rotational parameters $\vec{\boldsymbol{\lambda}}$ become all zero according to eq. 1.49, which corresponds to a multiplication of the MOs with a unit matrix $\mathbf{U} = \mathbb{1}$ and a stationary solution has been found.

As the Hessian (eq. 1.48) is prohibitively large approximative schemes are utilized, where the off-diagonal terms are discarded[113]. In an even cruder approximation also $\mathbf{h}_{pp}$ can be neglected[104]. Furthermore, it is allowed only for rotations between inactive and active orbitals, as inactive-inactive, active-active or virtual-virtual rotations of electron pairs do not change the CASSCF wavefunction.

The energy and orbitals at HF level can be obtained as a special case of the MCSCF procedure where the CSF expansion is truncated to only one Slater determinant. Eq. 1.49 then simplifies to

$$\vec{k} = -\frac{1}{2} \mathbf{h}_{kk}^{-1} \vec{g}_k. \tag{1.53}$$

This procedure for obtaining the HF wavefunction is known as the quadratically converged SCF approach[114].

Eq. 1.49 can be utilized to optimize ES as well, because the n-th ES constitutes a saddle point in the parameter space with $n-1$ negative eigenvalues in the Hessian. However, for ES the state specific variant of CASSCF (i.e. SS-CASSCF) is prone to convergence problems due to root flipping. This happens when the orbitals of the ES under optimization are very different than the orbitals of a lower state. Then, both states may start to continously switch order during the iterative procedure. Root flipping is nearly inevitable when dealing with higher ESs where the state density is large. Furthermore, two SS-CASSCF states of the same spatial symmetry are not orthogonal, which complicates the calculation of transition properties like transition dipole moments, non-adiabatic couplings, etc. Finally, in certain cases a description of two or more states on equal footing is desired, e.g. at CoIns. To deal with these problems a state averaged variant of CASSCF (i.e. SA-CASSCF) was developed. Here the optimization objective is not the energy of a single state, but rather a weighted average of N states of interest

$$\tilde{E} = \sum_i^N w_i E_i^{SA}(\vec{k}, \vec{p}_i) \quad \text{with} \quad 0 \le w_i \le 1 \quad \text{and} \quad \sum_i w_i = 1. \tag{1.54}$$

An average set of MOs, obtained by the set of rotational parameters $\vec{k}$, is optimized for all N states, which are orthonormalized by N sets of SCF parameters $\{\vec{p}_1, \cdots, \vec{p}_N\}$. The variational condition (eq. 1.49) is modified to

$$\frac{\partial \tilde{E}(\vec{\tilde{\lambda}}_{1:N})}{\partial \vec{\tilde{\lambda}}_{1:N}} = \sum_i^N w_i \frac{\partial E_i^{SA}(\vec{\tilde{k}}, \vec{p}_i)}{\partial \vec{\tilde{\lambda}}_{1:N}} = 0, \qquad (1.55)$$

where $\vec{\tilde{\lambda}}_{1:N}$ indicates the energy dependence on an averaged set of MO rotations and on N sets of CSF parameters. SA-CASSCF resolves the shortcomings of SS-CASSCF. However, a disbalance in the quality of the individual state-averaged states can arise when the optimal MOs for the different wavefunctions differ significantly.

SS- and SA-CASSCF Gradients   Differentiating eq. 1.48 with respect to a displacement of an atomic center R_α and truncating to first order gives the general form of the CASSCF energy gradient

$$\frac{\partial E}{\partial R_\alpha} = \frac{\partial E^0}{\partial R_\alpha} + \frac{\partial \vec{\lambda}^T}{\partial R_\alpha} \mathbf{\vec{G}} + \vec{\lambda}^T \frac{\partial \mathbf{\vec{G}}}{\partial R_\alpha}. \qquad (1.56)$$

For optimal MO and CSF-coefficients, as obtained at SS-CASSCF level by the Newton-Raphson procedure outlined in eq. 1.49 $\vec{\lambda}$ and $\mathbf{\vec{G}}$ become zero and the second and third term vanish leaving[104]

$$\frac{\partial E_i^{SS}}{\partial R_\alpha} = \frac{\partial E_i^0}{\partial R_\alpha} = \sum_{ij} \frac{\partial f_{ij}}{\partial R_\alpha} D_{ji} + \frac{1}{2} \sum_{ijkl} \frac{\partial g_{ijkl}}{\partial R_\alpha} d_{jilk} - \sum_{ij} F_{ij} \frac{\partial S_{ij}}{\partial R_\alpha}. \qquad (1.57)$$

with the Fock matrix element

$$F_{ij} = \sum_k f_{ik} D_{kj} + 2 \sum_{klm} g_{iklm} d_{jklm}. \qquad (1.58)$$

The first and the second term in eq. 1.57 follow from differentiating eq. 1.40 with respect to R_α, while the third term contains overlap derivatives and arises from the orthogonality condition for the MOs at all R_α. In the state-averaged case the gradient $\vec{g}_{i\tilde{k}}$ of the i-th averaged state with respect to the MO rotations $\vec{\tilde{k}}$ does not vanish according to eq. 1.55 and the gradient is given by

$$\frac{\partial E_i^{SA}}{\partial R_\alpha} = \frac{\partial \tilde{E}_i^0}{\partial R_\alpha} + \frac{\partial \vec{\tilde{k}}}{\partial R_\alpha} \vec{g}_{i\tilde{k}} = \frac{\partial \tilde{E}_i^0}{\partial R_\alpha} + \frac{\partial \tilde{E}_i^0}{\partial \vec{\tilde{k}}} \frac{\partial \vec{\tilde{k}}}{\partial R_\alpha}. \qquad (1.59)$$

The second term couples the MO coefficients and is obtained by solving the Coupled–Perturbed MCSCF (CPMCSCF) equations[104, 115], obtained by differentiating eq.

1.49 with respect to R_α

$$\frac{\partial \vec{\boldsymbol{\lambda}}}{\partial R_\alpha} = \left(\frac{\partial \vec{k}}{\partial R_\alpha} \ \frac{\partial \vec{p}}{\partial R_\alpha} \right)^T = -\mathbf{H}^{-1} \frac{\partial \mathbf{G}}{\partial R_\alpha}. \tag{1.60}$$

Hence, the computation of state-averaged gradients is associated with the additional effort of calculating the total Hessian.

1.4.3. Second-order perturbation theory

Despite providing a correct description of the wavefunction in asymptotic and state degeneracy regions, CASSCF needs improvement for obtaining quantitative results except for small molecules. As the orbitals outside the active space are further described at HF level short-range correlation effects (dynamic correlation) are not properly treated. Consequently, excitation energies, relative stabilization of stationary geometries, transition state barrier heights, etc. at CASSCF level have often only qualitative character. In the worst scenario CASSCF can predict a wrong ordering of the ES[116] and complicate the interpretation. An improvement could be achieved by adapting the second order Møller–Plesset (MP2) ansatz[117, 118] to ES. The MP2 approach has been shown to successfully resolve the major part of the correlation energy around the GS equilibrium geometry[118, 119], providing almost quantitative results for GS calculations. The CASPT2 generalizes the MP2 ansatz to multi-configurational wavefunctions[68–70]. MP2 and CASPT2 are special applications of the Rayleigh-Schrödinger perturbation theory, which is presented in the next subsection.

Rayleigh-Schrödinger perturbation theory The Rayleigh-Schrödinger perturbation theory assumes that the electronic correlation energy can be recovered by adding a "small" perturbational term to the Hamiltonian for which a solution has been found (e.g. the Fock operator in case of MP2). This assumtion is well justified as the correlation energy contributes less than 5% to the total electronic energy. The exact Hamiltonian reads

$$\hat{H} = \hat{H}^0 + \lambda \hat{H}^1, \tag{1.61}$$

with $\lambda = 0 \ldots 1$ an arbitrary real parameter. Next, the perturbed energy and wavefunction are expressed via power series in the parameter λ around the zeroth-order solution

$$E = E^0 + \lambda E^1 + \lambda^2 E^2 + \cdots, \tag{1.62a}$$

$$\left| \Psi \right\rangle = \left| \Psi^0 \right\rangle + \lambda \left| \Psi^1 \right\rangle + \lambda^2 \left| \Psi^2 \right\rangle + \cdots. \tag{1.62b}$$

Inserting eqs. 1.61, 1.62a and 1.62b into the time-independent Schrödinger equation 1.4 gives

$$\left(\hat{H}^0 + \lambda\hat{H}^1\right)\left(\left|\Psi^0\right\rangle + \lambda\left|\Psi^1\right\rangle + \cdots\right) = \left(E^0 + \lambda E^1 + \cdots\right)\left(\left|\Psi^0\right\rangle + \lambda\left|\Psi^1\right\rangle + \cdots\right). \tag{1.63}$$

Collecting powers of λ gives the zeroth- and higher-order equations

$$\lambda^0 : \hat{H}^0\left|\Psi^0\right\rangle = E^0\Psi^0, \tag{1.64a}$$

$$\lambda^1 : \hat{H}^0\left|\Psi^1\right\rangle + \hat{H}^1\left|\Psi^0\right\rangle = E^0\left|\Psi^1\right\rangle + E^1\left|\Psi^0\right\rangle, \tag{1.64b}$$

$$\lambda^2 : \hat{H}^0\left|\Psi^2\right\rangle + \hat{H}^1\left|\Psi^1\right\rangle = E^0\left|\Psi^2\right\rangle + E^1\left|\Psi^1\right\rangle + E^2\left|\Psi^0\right\rangle. \tag{1.64c}$$

Using the intermediate normalization condition $\left\langle\Psi^0\middle|\Psi^n\right\rangle = 0$ with $n = \{1, 2, \ldots\}$ one obtains an expression for the n-th-order energy

$$E^0 = \left\langle\Psi^0\middle|\hat{H}^0\middle|\Psi^0\right\rangle, \tag{1.65a}$$

$$E^1 = \left\langle\Psi^0\middle|\hat{H}^1\middle|\Psi^0\right\rangle, \tag{1.65b}$$

$$E^2 = \left\langle\Psi^0\middle|\hat{H}^1\middle|\Psi^1\right\rangle. \tag{1.65c}$$

Thus, provided that one has the first-order perturbed wavefunction $\left|\Psi^1\right\rangle$ one can calculate the CASPT2 perturbation energy using eq. 1.65c. The first-order wavefunction is obtained by solving eq. 1.64b. Therefore, the configurational space of the first-order wavefunction and the zeroth-order operator $\hat{H}^0$ have to be defined. Their definition is not unique and different construction schemes have been suggested in the literature. In the following the most common scheme is discussed.

CASPT2 first-order wavefunction The configurational space in which the first-order wavefunction is expanded can be devided into four subspaces $\mathbf{V}_0, \mathbf{V}_\perp, \mathbf{V}_{SD}$ and $\mathbf{V}_{TQ\ldots}$[68]. $\mathbf{V}_0$ is the one-dimensional space spanned by the reference CASSCF wavefunction $\left|\Psi^0\right\rangle$. $\mathbf{V}_\perp$ contains all other wavefunctions which can be obtained with the reference active space. $\mathbf{V}_{SD}$ is generated by single and double excitations from the reference space $\mathbf{V}_0$ (i.e. $\hat{E}_{qp}\hat{E}_{sr}\left|\Psi^0\right\rangle$). The $\mathbf{V}_{TQ\ldots}$ space arises from higher excitations from $\left|\Psi^0\right\rangle$. The $\mathbf{V}_\perp$ and $\mathbf{V}_{TQ\ldots}$ subspaces are per construction orthogonal to the reference CASSCF wavefunction and do not contribute to the correction. Therefore, the first-order wavefunction is spanned in the $\mathbf{V}_{SD}$ space

$$\left|\Psi^1\right\rangle = \sum_i C_i\Psi_i^{\mathbf{V}_{SD}} = \sum_{pqrs} C_{pr}^{qs}\hat{E}_{qp}\hat{E}_{sr}\left|\Psi^0\right\rangle, \tag{1.66}$$

where i runs over each possible $pqrs$ combination. Single excitations from $\left|\Psi^0\right\rangle$ are generated by requiring that either $p = q$ or $r = s$. The generated expansion functions are not orthogonal. It is noted that different $\mathbf{V}_{SD}$ expansion spaces are generated from different reference CASSCF wavefunctions.

CASPT2 zeroth-order Hamiltonian   While at MP2 level the definition of a zeroth-order operator $\hat{H}^0$ is straightforward (i.e. a sum of HF one-electron operators), at CASSCF level a zeroth-order operator does not exist. Here, the zeroth-order Hamiltonian proposed by Andersson, Malmqvist and Roos is discussed[68]. It is defined as a sum of one-electron operators in a way that simplifies to the HF operator in case of a closed-shell reference wavefunction

$$\hat{H}^0 = \hat{P}_0\hat{F}\hat{P}_0 + \hat{P}_\perp\hat{F}\hat{P}_\perp + \hat{P}_{SD}\hat{F}\hat{P}_{SD} + \hat{P}_{TQ...}\hat{F}\hat{P}_{TQ...}. \tag{1.67}$$

$\hat{P}_0, \hat{P}_\perp, \hat{P}_{SD}$ and $\hat{P}_{TQ...}$ are projection operators on the individual configuration subspaces and $\hat{F}$ is the second quantized form of the HF operator constructed from the one- and two-electron matrix elements and the one-electron density matrix (eq. 1.40)

$$\hat{F} = \sum_{pq} f_{pq}^{HF}\hat{E}_{qp} \quad \text{with} \quad f_{pq}^{HF} = f_{pq} + \sum_{rs} D_{rs}\left(g_{pqrs} - \frac{1}{2}g_{prqs}\right). \tag{1.68}$$

With the definition for the first-order wavefunction from eq. 1.66 the action of the zeroth-order Hamiltonian reduces to the action of $\hat{F}$ to the $\mathbf{V}_{SD}$ subspace.

CASPT2 energy   By inserting eq. 1.66 and eq. 1.67 in eq. 1.64b one obtains the following system of linear eqations

$$\sum_{ij} C_i \left\langle \Psi_j^{\mathbf{V}_{SD}} \middle| (\hat{H}^0 + E^0) \middle| \Psi_i^{\mathbf{V}_{SD}} \right\rangle = -\left\langle \Psi_j^{\mathbf{V}_{SD}} \middle| \hat{H}^1 \middle| \Psi^0 \right\rangle, \tag{1.69}$$

or in a matrix form

$$(\mathbf{F} - E^0\mathbf{S})\mathbf{C} = -\mathbf{V}. \tag{1.70}$$

$\mathbf{S}$ is the overlap matrix of the non-orthogonal expansion functions $\Psi_i^{\mathbf{V_{SD}}}$ with elements

$$\mathbf{S}_{ij} = \left\langle \Psi^0 \middle| \hat{E}_{rs}\hat{E}_{pq}\hat{E}_{xv}\hat{E}_{zy} \middle| \Psi^0 \right\rangle, \tag{1.71}$$

where i,j are determined by a given $pqrs,vxyz$ combination, respectively. $\mathbf{F}$ is the zeroth-order Hamiltonian matrix with elements

$$\mathbf{F}_{ij} = \sum_{tu} f_{tu}^{HF}\left\langle \Psi^0 \middle| \hat{E}_{rs}\hat{E}_{pq}\hat{E}_{ut}\hat{E}_{xv}\hat{E}_{zy} \middle| \Psi^0 \right\rangle. \tag{1.72}$$

The matrix elements of $\mathbf{V}$ can be evaluated recalling that $\hat{H}^1 = \hat{H} - \hat{H}^0$ and using eqs. 1.39 and 1.67. Eqs. 1.71 and 1.68 show that higher-order density matrices have to be stored and evaluated. Thus, different contraction schemes have been developed to minimize the computational effort.
Using eq. 1.70 the multi-configurational second-order perturbation energy E^2 (eq. 1.65c) is then obtained as

$$E^2 = \left\langle \Psi^0 \middle| \hat{F}^1 \middle| \Psi^1 \right\rangle = \sum_i C_i \left\langle \Psi^0 \middle| \hat{H}^1 \middle| \Psi_j^{\mathbf{V}_{SD}} \right\rangle = \mathbf{V}^\dagger\mathbf{C} = -\mathbf{V}^\dagger(\mathbf{F} - E^0\mathbf{S})^{-1}\mathbf{V}, \tag{1.73}$$

an expression similar to the one of the MP2 perturbation energy. From eq. 1.73 it follows that configurations from the expansion set $\mathbf{V}_{SD}$ with energies close to the reference energy E^0 will lead to an overestimation or even singularities of the perturbation energy. This is know as the "intruder state" problem[120, 121]. As perturbation theory holds only for small perturbations, such configurations should be included already in the preceeding CASSCF calculation. If this is not practicable a level shift technique can be applied[120, 121]. Thereby a finite shift (normally $0.1 - 0.3$ a.u.) is added to the reference energy E^0, which removes the effect of the intruder state. Caution is required that no new intruder states arise by accidental degeneracy of the shifted reference energy with energies of other configurations.

MS-SR-CASPT2 and MS-MR-CASPT2 The Single-State CASPT2 (SS-CASPT2) ansatz described above has one notable shortcoming arising from the definition of the first-order wavefunction, namely, the static correlation is considered only at the preceeding CASSCF level. While the reference wavefunction $\left|\Psi^0\right\rangle$ is orthogonal to the the wavefunctions from the $\mathbf{V}_\perp$ space, the perturbed wavefunction $\left|\Psi^0\right\rangle+\lambda\left|\Psi^1\right\rangle$ is not. Hence, SS-CASPT2 wavefunctions of different states are no longer orthogonal, although their reference wavefunctions are. A re-orthogonalization is required, i.e. the static correlation between the different states has to be re-evaluated. Two improvements of the SS-CASPT2 alogorithm, the Multi-State Single-Reference CASPT2 (MS-SR-CASPT2)[70] and the Multi-State Multi-Reference CASPT2 (MS-MR-CASPT2)[70] approaches, implement this re-orthogonalization.

In MS-SR-CASPT2 equation 1.70 is solved independently for n states (i.e. n SS-CASPT2 independent calculations are performed), each characterized by its own expansion space $\mathbf{V}_{SD}^n$, generated from the corresponding reference CASSCF wavefunction $\left|\Psi^{0,n}\right\rangle$, and by a zeroth-order Hamiltonian $\hat{H}^{0,n}$, projecting on $\mathbf{V}_{SD}^n$. After the perturbative corrections have been computed independently for all states the couplings between the individual (non-orthogonal) states are calculated. A Hamiltonian matrix of n^2-size is diagonalized to provide a set of eigenfunctions.

In MS-MR-CASPT2 a single expansion space $\mathbf{V}_{SD}$ common to all states is constructed, which constitutes a union of the expansion spaces generated by single and double excitation from all reference wavefunctions. The perturbation corrections for all states are obtained in one cycle. Subsequently, construction and diagonalization of the effective Hamiltonian is performed as in MS-SR-CASPT2 to obtain the eigenfunctions. MS-MR-CASPT2 gives the most accurate results but is more expensive than MS-SR-CASPT2.

2. The extended two-electron two-orbital theory

If the Franck-Condon (FC) point is the doorway to the ES, which determines the initial direction of relaxation, then CoIns are the outlet to the GS, which decide over reaction speed and product distribution. Ever since their importance was recognized[24–26] the general goal of understanding and predicting their structure and energetics has been pursued[50, 122–126]. With the valence bond formalism[127] it could be shown that similar geometrical patterns (-$(CH)_3$-kinks) determine the CoIn geometry of a vast number of conjugated polyenes[123, 128]. Michl and Bonačić-Koutecký presented a two-electron two-orbital model[61] to predict CoIns in strongly polar and charged systems, which was successfully applied to several biological systems containing a protonated Schiff base[129, 130].

Going beyond single CoIns, the ES dynamics is even better accounted for by CoIn seams, the low-lying regions in the IS (sec. 1.2), accessible during a photoreaction[74, 116, 131–133]. In analogy to reaction pathways on potential energy hypersurfaces, the intersection seams can be regarded as the minimum energy connection between stationary CoIns in the IS[92]. The relevance of seams was confirmed by quantum dynamics[77, 134] and semi-classical calculations for various molecular systems[42, 49, 135–139], pointing out the necessity for methods to locate and rationalize them. To the authors's knowledge three different strategies are followed for locating CoIn seams. The straightforward one is based on a constrained optimization out of a minimum energy CoIn[140–142]. It is the most realizable approach for large complex systems, but it fails when the constrained coordinate has an overlap with the BS that lifts the degeneracy between electronic states. More elaborate methods consider the curvature of the IS[143], permitting the application of MEP following algorithms[92]. A further method that locates the lowest seam parallel to the ES MEP has been presented recently[144]. These methods provide a mathematical framework for the optimization of CoIn seams.

In this chapter the two-electron two-orbital ansatz by Michl and Bonačić-Koutecký is extended and its applicability is expanded from unfunctionalized non-polar to multi-functionalized strongly polar polyene systems. In the first section a set of equations for the degeneracy between the GS and the first ES are derived. In the next two sections geometrical and electronical effects, which satisfy these equations, are discussed. Simple rules of thumb for predicting and locating CoIns and CoIn seams from the chemical composition alone are formulated and conceptual strategies for the search of CoIns are outlined. In a series of examples the rules are applied to distinguish low-energy from high-energy CoIns and to reveal the complex branched nature of

the CoIn seam in unfunctionalized non-polar to multi-functionalized strongly polar polyene systems. Parts of this chapter are published in A. Nenov, T. Cordes, T. T. Herzog, W. Zinth and R. de Vivie-Riedle *J. Phys. Chem. A* **2010**, 114, p. 13016, A. Nenov, R. de Vivie Riedle *J. Chem. Phys.* **2011**, 135, p. 034304 and A. Nenov, R. de Vivie-Riedle *J. Chem. Phys.* **2012**, 137, p. 074101.

2.1. Mathematical framework

2.1.1. The two-electron two-orbital model revisited

The two-electron two-orbital model[145, 146] makes the assumption that all states, relevant for the photoreaction, can be constructed by permuting two electrons in the two frontier orbitals of the system (active space). At the equilibrium geometry of a conjugated π-system these orbitals correspond to the highest occupied and the lowest unoccupied MOs π and π^*, respectively. The assumption simplifies the multiconfigurational problem to a full-Configuration-Interaction (CI) calculation in a two-orbital subspace:

$$
\begin{vmatrix}
\left\langle \Phi_1 \middle| \hat{H} \middle| \Phi_1 \right\rangle - E & \left\langle \Phi_1 \middle| \hat{H} \middle| \Phi_2 \right\rangle & \left\langle \Phi_1 \middle| \hat{H} \middle| \Phi_3 \right\rangle \\
\left\langle \Phi_2 \middle| \hat{H} \middle| \Phi_1 \right\rangle & \left\langle \Phi_2 \middle| \hat{H} \middle| \phi_2 \right\rangle - E & \left\langle \Phi_2 \middle| \hat{H} \middle| \Phi_3 \right\rangle \\
\left\langle \Phi_3 \middle| \hat{H} \middle| \Phi_1 \right\rangle & \left\langle \Phi_3 \middle| \hat{H} \middle| \phi_2 \right\rangle & \left\langle \Phi_3 \middle| \hat{H} \middle| \Phi_3 \right\rangle - E
\end{vmatrix} = \mathbf{0} \quad \text{with} \quad
\begin{aligned}
\Phi_1 &= \left| \pi^2 \right\rangle \\
\Phi_2 &= \left| \pi\pi^* \right\rangle \\
\Phi_3 &= \left| \pi^{*2} \right\rangle.
\end{aligned}
\tag{2.1}
$$

In eq. 2.1 $\Phi_{1,2,3}$ are CSFs (sec. 1.4) constructed by permuting two electrons in the active orbitals and $\hat{H} = \hat{h}_1 + \hat{h}_1 + \frac{1}{r_{12}}$ is the Hamiltonian of the two-electron system. It is further assumed that at the equilibrium geometry both active orbitals can be constructed by a unitary transformation from a pair of equivalent MOs A and B, localized at different atomic centers:

$$
\begin{pmatrix} \pi \\ \pi* \end{pmatrix} = \frac{1}{\sqrt{2}} \begin{pmatrix} 1 & 1 \\ 1 & -1 \end{pmatrix} \begin{pmatrix} A \\ B \end{pmatrix}.
\tag{2.2}
$$

In the basis of A and B the 3 x 3 CI determinant eq. 2.1 reads:

$$
\begin{vmatrix}
E_0 + 2h_{AB} + \sum_{i \in A,B} \left\langle AB \middle| ii \right\rangle - E & \frac{1}{\sqrt{2}}(\varepsilon_{AA} - \varepsilon_{BB}) & \Delta J \\
\frac{1}{\sqrt{2}}(\varepsilon_{AA} - \varepsilon_{BB}) & E_0 - 2K_{AB} + \Delta J - E & \frac{1}{\sqrt{2}}(\varepsilon_{AA} - \varepsilon_{BB}) \\
\Delta J & \frac{1}{\sqrt{2}}(\varepsilon_{AA} - \varepsilon_{BB}) & E_0 - 2h_{AB} - \sum_{i \in A,B} \left\langle AB \middle| ii \right\rangle - E
\end{vmatrix},
\tag{2.3}
$$

with

$$E_0 = h_{AA} + h_{BB} + \frac{1}{4}\left(J_{AA} + J_{BB}\right) + \frac{1}{2}J_{AB} + K_{AB},$$

$$\Delta J = \frac{1}{4}\left(J_{AA} + J_{BB}\right) - \frac{1}{2}J_{AB}, \tag{2.4}$$

$$\varepsilon_{AA/BB} = 2h_{AA/BB} + J_{AA/BB},$$

where $h_{AA/BB}$ are the one-electron integrals, h_{AB} the resonance integral and $J_{AA/BB/AB}$ are the two-electron Coulomb repulsion integrals. The exchange integral K_{AB} and the hybrid integrals $\langle AA|AB \rangle$ and $\langle BB|BA \rangle$ are negligible in the basis of the localized MOs A and B due to the vanishing overlap and can be therefore omitted. The required equivalence between A and B at the equilibrium geometry forces the equivalence $\varepsilon_{AA} = \varepsilon_{BB}$ and simplifies the determinant eq. 2.3 to:

$$\begin{vmatrix} E_0 + 2h_{AB} - E & 0 & \Delta J \\ 0 & E_0 - 2K_{AB} + \Delta J - E & 0 \\ \Delta J & 0 & E_0 - 2h_{AB} - E \end{vmatrix}. \tag{2.5}$$

Diagonalization of the determinant eq. 2.5 provides the energies and (unnormalized) wavefunctions of the three roots at the equilibrium:

$$E_{S_0} = E_0 - \sqrt{4h_{AB}^2 + \Delta J^2} \qquad \Psi_1 = -\frac{\Delta J}{\sqrt{4h_{AB}^2 + \Delta J^2} + 2h_{AB}}\Phi_1 + \Phi_3, \quad (2.6\text{a})$$

$$E_{S_1} = E_0 + \Delta J \qquad \Psi_2 = \Phi_2, \tag{2.6b}$$

$$E_{S_2} = E_0 + \sqrt{4h_{AB}^2 + \Delta J^2} \qquad \Psi_3 = \frac{\Delta J}{\sqrt{4h_{AB}^2 + \Delta J^2} - 2h_{AB}}\Phi_1 + \Phi_3, \quad (2.6\text{c})$$

The resonance term h_{AB}, which is negative in magnitude, is responsible for the large energetic stabilization of the GS equilibrium, where $|h_{AB}|^2 \gg \Delta J^2$. Thus, each state is described in good approximation by a single configuration, i.e. $\Psi_1 = \Phi_1, \Psi_2 = \Phi_2, \Psi_3 = \Phi_3$.

Naturally, the first condition for a degeneracy between the GS and first ES would imply the cancelation of the resonance integral h_{AB}:

$$h_{AB} = 0. \tag{2.7}$$

With decreasing magnitude of the resonance integral the condition $|h_{AB}|^2 \gg \Delta J^2$ does not hold anymore. When eq. 2.7 is fulfilled the energies and wavefunctions of

eq. 2.6c become:

$$E_{S_0} = E_0 - \Delta J \qquad\qquad \Psi_1 = \frac{1}{\sqrt{2}}\left(\Phi_1 - \Phi_3\right), \qquad (2.8a)$$

$$E_{S_1} = E_0 + \Delta J + (\varepsilon_{AA} - \varepsilon_{BB}) \qquad \Psi_2 = \frac{1}{2}\left(\Phi_1 + \sqrt{2}\Phi_2 + \Phi_3\right), \qquad (2.8b)$$

$$E_{S_2} = E_0 + \Delta J - (\varepsilon_{AA} - \varepsilon_{BB}) \qquad \Psi_3 = \frac{1}{2}\left(\Phi_1 - \sqrt{2}\Phi_2 + \Phi_3\right). \qquad (2.8c)$$

Eq. 2.8 has a general form as it includes the term $\varepsilon_{AA} - \varepsilon_{BB}$. In the special case when A and B are equienergetic (i.e. $\varepsilon_{AA} - \varepsilon_{BB} = 0$) one speaks about a homosymmetric biradical geometry[61]. In the general case the GS and first ES are separated by a finite gap $E_{S_1} - E_{S_0} = 2\Delta J + (\varepsilon_{AA} - \varepsilon_{BB})$. The reason for the finit gap is understood by analyzing the wavefunctions 2.8. When the resonance integral h_{AB} vanishes the individual electronic states can no longer be approximated by a single configuration as done at the equilibrium geometry. By expressing the wavefunctions in eq. 2.8 in the basis of the localized MOs A and B one obtains:

$$\Psi_1 = \frac{1}{\sqrt{2}}\left(\Phi_1 - \Phi_3\right) = \left|A\alpha(1)B\beta(2)\right\rangle - \left|A\beta(1)B\alpha(2)\right\rangle = \left|A^\bullet B^\bullet\right\rangle, \qquad (2.9a)$$

$$\Psi_2 = \frac{1}{2}\left(\Phi_1 + \sqrt{2}\Phi_2 + \Phi_3\right) = \left|A\alpha(1)A\beta(2)\right\rangle = \left|A^2\right\rangle, \qquad (2.9b)$$

$$\Psi_3 = \frac{1}{2}\left(\Phi_1 - \sqrt{2}\Phi_2 + \Phi_3\right) = \left|B\alpha(1)B\beta(2)\right\rangle = \left|B^2\right\rangle. \qquad (2.9c)$$

The GS is no longer described by a closed shell configuration, it is a singlet biradical. Both ES have the electrons occupying either one of the localized orbitals A and B. These configurations will be refered to as zwitterionic in the following. Due to the localized nature of orbitals A and B both active electrons avoid each other better when occupying different orbitals. Therefore, the biradical configuration lies energetically lower than both zwitterionic configurations. Some additional deformations are needed which can compensate for the stronger Coulomb repulsion in the zwitterionic state. The condition that needs to be satisfied in order to obtain a degeneracy between the GS and first ES reads:

$$J_{AA} - J_{AB} = h_{BB} - h_{AA}. \qquad (2.10)$$

An asymmetric deformation that lifts the equivalence between the energies of the localized orbitals without violating eq. 2.7 is required to reach a CoIn.
Eqs. 2.7 and 2.10 have proved quite handy in the discussion of CoIns in highly polar and charged polyenes[61]. Introduction of polar groups and charges alters the electron-nuclei attraction and, thus, the Right–Hand–Side (RHS) of eq. 2.10 and can be used to fulfill the requirement. In particular, this model found application in the interpretation of the photochemistry of several biological compounds, like retinal[129, 130] and the chromophore of the yellow fluorescing protein[147, 148].

2.1.2. The extended two-electron two-orbital model

During derivation of the conditions eqs. 2.7 and 2.10 the interactions of the two active eletrons with the remaining electrons (present in a realistic system) were completely neglected. In the course of this work the two-electron two-orbital ansatz was refined by including the interactions of the active electrons with a closed-shell of $2n$ electrons (n being the number of closed shell orbitals). For the purpose it is more convinient to work in the biradical/zwitterionic basis (eq. 2.9). Rewriting the 3 x 3 CI problem (eq. 2.1) in this basis gives:

$$
\begin{vmatrix}
E_0 + \sum\limits_{k \in A,B} h_{kk} + J_{AB} + \Delta J_A + \Delta J_B - E & \dfrac{2}{\sqrt{2}}(h_{AB}+D) & \dfrac{2}{\sqrt{2}}(h_{AB}+D) \\[2ex]
\dfrac{2}{\sqrt{2}}(h_{AB}+D) & E_0 + 2h_{AA} + J_{AA} + 2\Delta J_A - E & 0 \\[2ex]
\dfrac{2}{\sqrt{2}}(h_{AB}+D) & 0 & E_0 + 2h_{BB} + J_{BB} + 2\Delta J_B - E
\end{vmatrix} = 0,
$$

(2.11)

with

$$
E_0 = 2 \sum_i^n h_i + \sum_i^n J_{ii} + 4 \sum_i^n \sum_{j>i}^n J_{ij} - 2 \sum_i^n \sum_{j>i}^n K_{ij},
$$

$$
\Delta J_{A/B} = 2 \sum_i^n J_{iA/iB} - \sum_i^n K_{iA/iB},
$$

(2.12)

$$
D = 4 \sum_i^n \left\langle Ai \middle| Bi \right\rangle - 2 \sum_i^n \left\langle AB \middle| ii \right\rangle.
$$

The sums run over the n closed shell orbitals. Inclusion of additional interactions in the model introduces two terms to eq. 2.7:

$$
2h_{AB} + 4 \sum_i^n \left\langle Ai \middle| Bi \right\rangle - 2 \sum_i^n \left\langle AB \middle| ii \right\rangle = 0.
$$

(2.13)

Although the hybrid integrals $\left\langle Ai \middle| Bi \right\rangle$ and $\left\langle AB \middle| ii \right\rangle$ are an order of magnitude smaller than the resonance integral h_{AB} their sum is no longer negligible for the quantification of eq. 2.13.

With eq. 2.13 fulfilled, diagonalizing the determinant 2.11 and requiring that $E_{S_0} \overset{!}{=} E_{S_1}$ provides the extended form of eq. 2.10:

$$
J_{AA} - J_{AB} = \underbrace{(h_{BB} - h_{AA})}_{\mathrm{one-electron\ term}} + \underbrace{\left(2\sum_i^n J_{iB} - 2\sum_i^n J_{iA} \right) - \left(\sum_i^n K_{iB} - \sum_i^n K_{iA} \right)}_{\mathrm{two-electron\ term}} =
$$

$$
= \varepsilon_B - \varepsilon_A.
$$

(2.14)

33

where $\varepsilon_A = h_{AA} + 2\sum_i^n J_{iA} - \sum_i^n K_{iA}$ and $\varepsilon_B = h_{BB} + 2\sum_i^n J_{iB} - \sum_i^n K_{iB}$ are defined as the energies of the singly occupied orbitals A or B in the presence of $2n$ fixed core electrons (not equivalent to ε_{AA} and ε_{BB} introduced earlier). With the two-electron term an additional tool for lowering the GS/ES gap, besides the introduction of polar groups and charges, becomes available. The receipe is to modulate the repulsive interactions of the two active electrons with the remaining $2n$ closed-shell electrons. In the course of this work eqs. 2.13 and 2.14 are referred to as the *resonance* and the *heterosymmetry* conditions, respectively. The *resonance* condition is equivalent to the condition $H_{11} - H_{22} = 0$ in the diabatic representation (eq. 1.16) and the *heterosymmetry* conditions is equivalent to the diabatic condition $H_{12} = 0$ (eq. 1.16). Thus, the *resonance* and the *heterosymmetry* conditions are a re-formulation of the diabatic conditions in terms of adiabatic quantities, obtainable from quantum chemical calculations. A potential application of this relation for the optimization of CoIns without calculating the gradient difference $\vec{X}_1$ and derivative coupling vectors $\vec{X}_2$ (eq. 1.18) is discussed at the end of this chapter.

With the *resonance* and *heterosymmetry* conditions it is possible to classify all essential motions leading to a CoIn. Eqs. 2.13 and 2.14 are very general and allow the description of substituted and unsubstituted polyenes on equal footing and can be used to address the following questions. What is the role of the specific geometric arrangement found at a CoIn? What is the influence of functional groups? Are qualitative predictions on structure and energetic position possible? Eqs. 2.13 and 2.14 have been quantified by SA-CASSCF(2,2) calculations with averaging over three states, which closely resemble the 3 x 3 CI problem 2.1, for several basic units[125]. The quantitative results allow to separate the factors deformation and substituent effects and to derive rules of thumb for qualitative prediction of CoIns and CoIn seams in arbitrary polyenes.

2.2. Rules for finding single conical intersections

In section 1.3 a correlation diagram was presented (fig. 1.3), which generalizes the behaviour of several isomerization reactions: a double bond torsion in a 2π-electronic system (ethylene), a disrotatory electrocyclic ring closure/opening in a $4i$ π-electronic system (*cis*-butadiene) and a conrotatory electrocyclic ring closure/opening in a $(4i + 2)\pi$-electronic system (Cyclohexadiene (CHD)). In diabatic representation the states cross along the reaction coordinate, thereby fulfilling the condition $H_{11} - H_{22} = 0$ (eq. 1.16). Using the equivalence between this diabatic condition and the *resonance* condition, the basic motions which fulfill eq. 2.13 are easily identified: a $90°$ torsion in any double bond sub-unit and a half-way conrotatory or disrotatory ring opening/closure in any $4i\pi$- or $(4i + 2)\pi$-electronic sub-unit, respectively. In correspondence with the Woodward-Hoffmann (WH) rules[95, 96] used to predict the stereochemistry of pericyclic reactions on the basis of orbital symmertry analysis (sec. 1.3) this set of basic motions is labeled as WH-motions. Any of the WH-motions
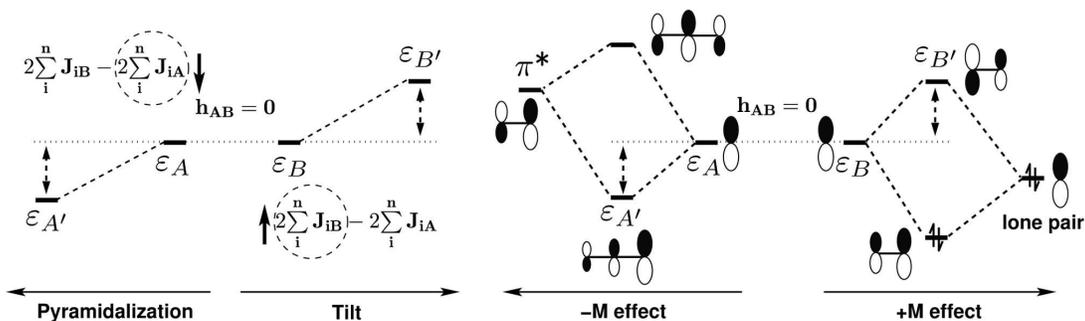
Figure 2.1.: (left) Schematic representation of the energy change of the localized orbitals A and B upon pyramidalization and tilt. Pyramidalization lowers the energy ε_A of orbital A by minimizing the repulsive interactions $\sum_i^n J_{iA}$ of the active electrons therein with the remaining $2n$ closed-shell electrons. Tilt increases the energy ε_B of orbital B by maximizing the repulsive interactions $\sum_i^n J_{iB}$ of the active electrons therein with the remaining $2n$ closed-shell electrons. (right) Schematic representation of the energy change of the localized orbitals A and B upon conjugation to functional groups with mesomeric effect. Negative mesomeric effect induced by low-lying π^*-orbitals has the same net effect as pyramidalization. Positive mesomeric effect possible through the presence of heteroatoms with lone pairs has the same net effect as tilt.

leads to a homosymmetric biradical geometry. Note, that a geometrical deformation is mandatory to fulfill eq. 2.13.

To reach a CoIn from a homosymmetric biradical geometry further deformations are required. Quantifying eqs. 2.13 and 2.14 for various geometrical constellations in several basic molecular systems (ethylene, *cis*-butadiene, $1,3$-CHD, see ref. [125]) helped to extract a set of deformations which satisfy the *heterosymmetry* condition eq. 2.14. These are pyramidalization and tilt. Exemplarily, fig. 2.1, left, sketches the influence of both deformations on the two-electron term of eq. 2.14, tab. 2.1 provides calculated values for all quantities occuring in eqs. 2.13 and 2.14 on the example of the basic unit ethylene.

The homosymmetric biradical geometry Ethylene$_{\text{OBF}}$ is the reference geometry for demonstrating the effect of pyramidalization and tilt. At Ethylene$_{\text{OBF}}$ the resonance term h_{AB} becomes zero and both frontier orbitals A and B degenerate at energy of -0.6378 a.u.. The energetic splitting between the GS and the first ES of 0.1179 a.u. is caused by the Coulomb repulsion in the doubly occupied frontier orbitals of the first ES $\left|A^2\right\rangle - \left|B^2\right\rangle$ given by the expression $1/2(J_{AA} + J_{BB}) = J_{AA} = 0.4428$ a.u.. For comparison, the Coulomb repulsion J_{AB} in the biradical GS is 0.3197 a.u..

The Coulomb repulsion in the zwitterionic state is compensated by applying either pyramidalization or tilt. In fig. 2.1, left and tab. 2.1 the tilt acts exclusively on orbital B and the pyramidalization on orbital A. Generally, tilt is any deformation, which enhances the Coulomb repulsion $2\sum_i^n J_{iB}$ between the active electrons and the remaining $2n$ closed-shell electrons (fig. 2.1, right). In the particular example this

	Ethylene$_{OBF}$	Ethylene$_{pyr}$	Ethylene$_{tilt}$	Ethylene$_{pyr/tilt}$
geometry				
orbital A				
orbital B				
h_{AA}	-6.2543	-6.3186	-6.2178	-6.2683
h_{BB}	-6.2543	-6.3298	-6.2366	-6.3091
h_{AB}	0.0000	-0.0026	0.0000	0.0036
J_{AA}	0.4428	0.4554	0.4546	0.4677
J_{AB}	0.3197	0.3458	0.3168	0.3314
$2\sum_i^n J_{iA}$	5.8137	5.8376	5.7157	5.7549
$2\sum_i^n J_{iB}$	5.8139	5.9649	5.8416	5.9339
$\varepsilon_{A'}{}^a$	-0.6378[b]	-0.6746	-0.7237	-0.7197
$\varepsilon_{B'}{}^a$	-0.6378[b]	-0.5827	-0.6056	-0.5921
$\Delta_{|A\bullet B\bullet\rangle,|A^2\rangle}$	0.1179	0.0136	0.0093	0.0000
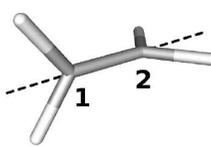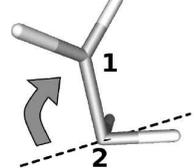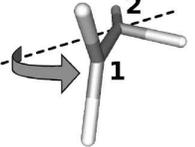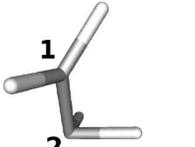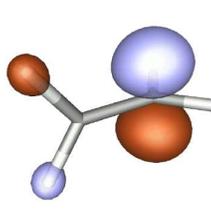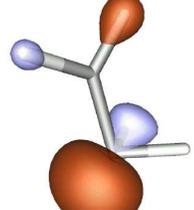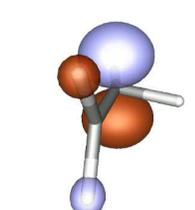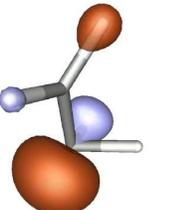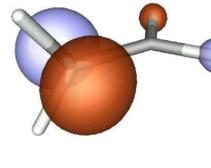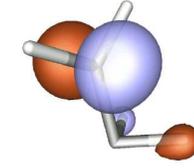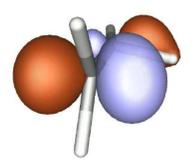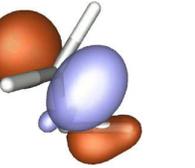
[a] $\varepsilon_{A'/B'} = h_{AA/BB} + 2\sum_i^n J_{iA/iB} - \sum_i^n K_{iA/iB}$
[b] here $\varepsilon_{A'/B'}$ and $\varepsilon_{A/B}$ are identical

Table 2.1.: Quantification of the terms occuring in eqs. 2.13 and 2.14 for a 90° twisted ethylene upon pyramidalization and tilt. At the homosymmetric biradical geometry (Ethylene$_{OBF}$) the orbital energies $\varepsilon_{A/B}$ are equal. Pyramidalization of orbital A (Ethylene$_{pyr}$) shields the active electrons from the remaining $2n$ closed-shell electrons, thus, lowering the Coulomb term $\sum_i^n J_{iA}$ and the orbital energy $\varepsilon_{A'}$. Tilt of orbital B (Ethylene$_{tilt}$) enhances the repulsion $\sum_i^n J_{iB}$ between the active and the closed-shell electrons, thus, increasing the energy $\varepsilon_{B'}$ of orbital B. Together both effects induce the required energetic splitting between ε_A and ε_B to reach a CoIn (Ethylene$_{pyr/tilt}$) without need of geometrical deformations.

enhancement shows by moving C_1 towards one of the hydrogens attached to C_2. A comparison of the homosymmetric biradical Ethylene$_{OBF}$ to the tilted Ethylene$_{tilt}$ indicates that the Coulomb repulsion $2\sum_i^n J_{iB}$ increases by ≈ 0.15 a.u. due to this deformation. The increase of the singly occupied orbital energy ε_B destabilizes the covalent biradical configuration $\left|A^\bullet B^\bullet\right\rangle$ relative to the zwitterionic configuration $\left|A^2\right\rangle$. Pyramidalization is a deformation, which shields the active electrons from the remaining $2n$ electrons (fig. 2.1). In the example this is achieved by pyramidalizing C_2, which changes the hybridization of orbital A from sp^2 to sp^3. As a consequence the term $2\sum_i^n J_{iA}$ decreases by ≈ 0.10 a.u. at Ethylene$_{pyr}$ with respect to Ethylene$_{OBF}$ favoring the zwitterionic state $\left|A^2\right\rangle$.

Tilt and pyramidalization are most effective when acting on different orbitals. A degeneracy between the biradical GS and the zwitterionic ES will be reached upon any of the introduced deformations. Minimum energy CoIns are reached by applying both motions simultaneously, as found for Ethylene$_{pyr/tilt}$. Conceivably, the energetic degeneracy can be preserved along the gradual transformation from the purely pyramidalized to the purely tilted CoIn. This idea is amplified in sec. 2.3.

Geometrical deformations alone do not fully exploit the potential of eq. 2.14. Asymmetric functionalization with polar groups lifts the energetic degeneracy of both localized orbitals A and B by inducing electron density flux. Functionalizing ethylene (tab. 2.2) reveals that mesomeric groups (e.g. -NH$_2$, -COOH, etc.) have the same net effect on eq. 2.14 as geometrical deformations (fig. 2.1, right). Inductive effects were found to be much weaker, as they act along the σ-bond, while the frontier orbitals in polyenes have π-character. A negative mesomeric effect is observed when one of the localized orbitals (e.g. A in fig. 2.1, right) interacts with an energetically low-lying virtual π^*-orbital of a functional group forming the bonding orbital A'. The resulting density flux has two effects. On the one hand, the electron-nuclei attraction h_{AA} (one-electron term in eq. 2.14) increases ($h_{AA} = -11.4571$ a.u. compared to $h_{AA} = -10.6645$ a.u. at Ethylene$_{COOH}$ in tab. 2.2). On the other hand, the delocalization of electron density into the π^*-orbital lowers the repulsion within orbital A' (J_{AA} decreases from 0.4428 a.u. at Ethylene$_{OBF}$ to 0.4039 a.u. at Ethylene$_{COOH}$ in tab. 2.2). Both effects lower the corresponding orbital energy ϵ'_A. A positive mesomeric effect is observed when a lone pair interacts with one of the localized orbitals (e.g. B in fig. 2.1). The new orbital B' is shifted to higher energy ϵ'_B due to the increased Coulomb repulsion $2\sum_i^n J_{iB}$ (two-electron term in eq. 2.14). Comparable to the combined effect of tilt and pyramidalization, the substituent effects are most effective when they act simultaneously on different orbitals. If their electron donating and withdrawing strength is properly chosen, they can stabilize the homosymmetric biradical geometry to a CoIn (Ethylene$_{COOH/NH_2}$ in tab. 2.2).

Based on the quantitative results for the basic units a three-step strategy for the conceptual search of CoIns in functionalized and non-functionalized conjugated polyenes is proposed. The rules of thumb are:

1) Distinguish basic units, which are sterically unimpeded of undergoing a WH-

	Ethylene$_{OBF}$	Ethylene$_{COOH}$	Ethylene$_{NH_2}$	Ethylene$_{COOH/NH_2}$
geometry				
orbital A				
orbital B				
h_{AA}	-6.2543	-11.4571	-8.1794	-13.3561
h_{BB}	-6.2543	-10.6645	-8.5460	-12.8085
h_{AB}	0.0000	0.0000	0.0000	0.0010
J_{AA}	0.4428	0.4039	0.4519	0.4159
J_{AB}	0.3197	0.3079	0.3079	0.2959
$2\sum_i^n J_{iA}$	5.8137	10.7922	7.5484	12.9515
$2\sum_i^n J_{iB}$	5.8139	10.0061	8.0280	12.5480
$\varepsilon_{A'}{}^a$	-0.6378^b	-0.6650	-0.6309	-0.6576
$\varepsilon_{B'}{}^a$	-0.6378^b	-0.6584	-0.5180	-0.5330
$\Delta_{|A\bullet B\bullet\rangle,|A^2\rangle}$	0.1179	0.0864	0.0283	-0.0073

$^a\varepsilon_{A'/B'} = h_{AA/BB} + 2\sum_i^n J_{iA/iB} - \sum_i^n K_{iA/iB}$
^{b}here $\varepsilon_{A'/B'}$ correspond to $\varepsilon_{A/B}$

Table 2.2.: Quantification of the terms occuring in eqs. 2.13 and 2.14 for a 90° twisted ethylene, substituted with a carboxyl group (Ethylene$_{COOH}$), with an amino group (Ethylene$_{NH_2}$) and with both. At the homosymmetric biradical geometry (Ethylene$_{OBF}$) the orbital energies $\varepsilon_{A/B}$ are equal. Groups with a negative mesomeric effect (e.g. -COOH) lower the energy, while groups with a positive mesomeric effect (e.g. -NH$_2$) increase the energy of the localized orbital they are attached to. Together both effects induce the required energetic splitting between ε_A and ε_B to reach a CoIn without need of geometrical deformations.

deformation. There could be more than one basic unit depending on the molecular composition.

2) Fulfill the *resonance* condition: For each basic unit selected in 1) apply the corresponding WH-motion, which cancels the resonance term h_{AB} to form the homosymmetric biradical with localized frontier orbitals A and B.

3) Fulfill the *heterosymmetry* condition, starting from the homosymmetric biradical: Assign geometrical deformations and/or mesomeric effects that tune the relative energies $\varepsilon_{A/B}$ of the localized orbitals. Their energetic splitting has to compensate the electronic repulsion in the doubly occupied zwitterionic configuration.

The predefined geometries can be used as input to finalize the optimization of CoIns by quantum chemical optimizations.

2.3. Rules for finding low-energy conical intersection seams

The two conditions formulated in eqs. 2.13 and 2.14 hold for any point in the IS. In this section it will be demonstrated that with their help the rules of thumb can be extended to predict the position of CoIn seams. The strategy is to divide the IS into segments where the geometry changes linearly, thus, permitting the application of linear interpolation techniques. The *resonance* and *heterosymmetry* conditions are used to estimate supporting points on these segments and to predict the interconnectivity of the individual segments.

In the following it is differentiated between two classes of CoIn seams. The first class includes seams related to one WH-coordinate alone. They arise through variations of the individual terms in eq. 2.14, leaving eq. 2.13 unchanged. The second class includes seams connecting different WH-coordinates, indicating possible loss channels. In this case variations in the integrals of both eqs. 2.13 and 2.14 are needed. As the aim are rules of thumb with qualitative predictive power, the simple form of the *resonance* condition, i.e. eq. 2.7, is used.

Conical intersection seams associated with one Woodward-Hoffmann coordinate
In this class the CoIn seams can be visualized by a plane orthogonal to one particular WH-coordinate ($\vec{g}$) (fig. 2.2). This plane is spanned by geometrical deformations (tilt, pyramidalization) and substituent effects. Each point in the plane fulfills the *resonance* condition. The crossing point with the WH-coordinate corresponds to the homosymmetric biradical. Specific combinations within the plane result in a motion in $\vec{h}$-direction and lead to a point on a CoIn seam. At each point of the seam $\vec{h}$ changes its direction, whereas $\vec{g}$ stays parallel to the WH-coordinate (as indicated in
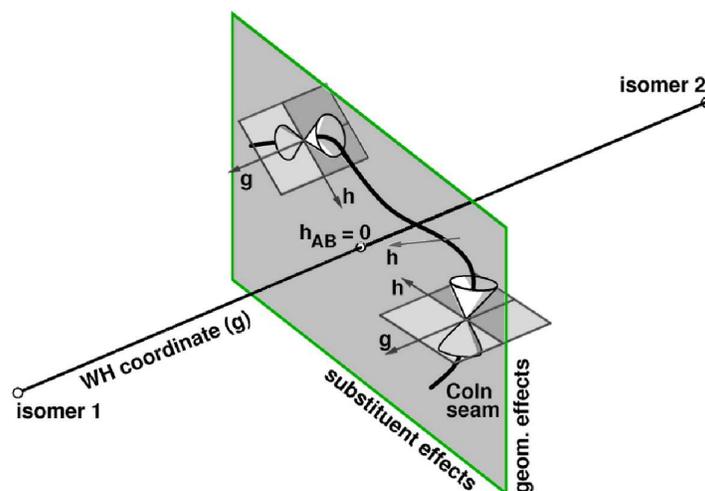
Figure 2.2.: Schematic representation of a CoIn seam related to one WH-coordinate ($\vec{g}$). Eq. 2.7 is fulfilled everywhere on the plane. The heterosymmetry condition (eq. 2.14, $\vec{h}$) for CoIn formation is fulfilled only for particular combinations of geometrical and substituent effects ($\vec{h}$). Single CoIns can be connected by a seam confined to the plane (thick solid line).

fig. 2.2). Such seams connect the two isomers associated with the WH-coordinate in a photoreaction. Within one plane the seam search reduces to a limited number of degrees of freedom. An additional reduction of the degrees of freedom is achieved by considering that the electronic configuration of the ES cannot change along a CoIn seam, i.e. it remains either $\left|A^2\right\rangle$ or $\left|B^2\right\rangle$. If the ES could change its character, this would imply that at some point along the seam orbitals A and B would become degenerate (i.e. as in a homosymmetric biradical) but, then, the *heterosymmetry* condition would not be fulfilled.

If the heterosymmetry condition is fulfilled by geometrical deformations, the CoIn optimization problem reduces to a search in a two-dimensional subspace of the IS, confined to the pyramidalization/tilt plane orthogonal to the WH-coordinate. In the following this concept is demonstrated on the basic unit ethylene. The homosymmetric biradical geometry Ethylene$_{OBF}$ is the reference geometry (tab. 2.1). To obtain supporting points in the pyramidalization/tilt plane the fact that CoIns can be reached either by pure pyramidalization, pure tilt, or by combination of both is used. Then, CoIn$_{pyr/tilt}$ (tab. 2.1) can be regarded as an intermediate point linking purely pyramidalized and purely tilted CoIns. Furthermore, by utilizing the symmetry of ethylene a closed loop seam around the homosymmetric biradical geometry Ethylene$_{OBF}$ (0° pyramidalization, 0° tilt) can be defined (fig. 2.3). This analysis of the topography of the seam allows to compartmentalize it into segments where a linear interpolation routine can be applied. A seam of the general form given in fig. 2.3 is expected to play a role for all non-polar and weakly polar compounds which undergo *cis-trans* isomerization. The magnitude of the geometrical deformations along
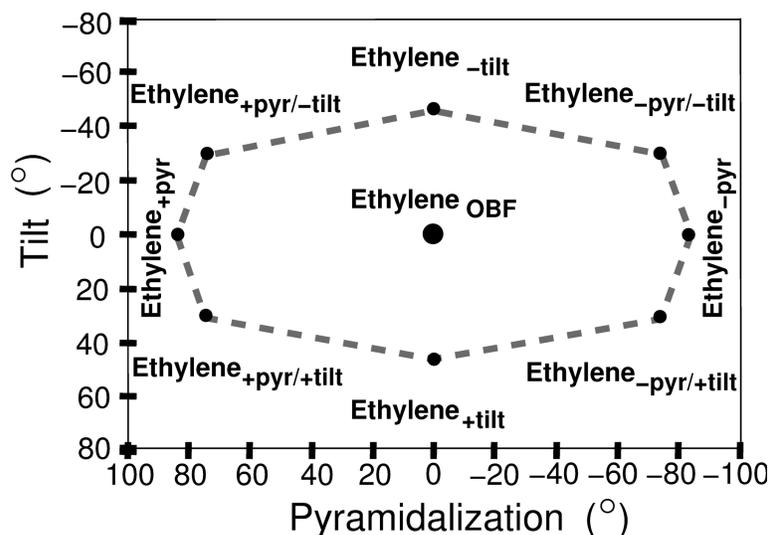
Figure 2.3.: Partitioning scheme of the closed loop CoIn seam around the homosymmetric biradical geometry Ethylene$_{OBF}$ (0° pyramidalization, 0° tilt) into linear segments.

the pyramidalization/tilt coordinates and the energy profile of the seam depend on the specific functionalization pattern. As an example a seam in the Hemithioindigo-Hemistilbene (HTI) system is presented in section 2.4.3.

Conical intersections seams connecting different Woodward-Hoffmann coordinates Depending on the complexity of the molecule several WH-coordinates can exist (e.g. torsion around several double bonds). Each WH-coordinate has a seam associated to it that is located in the corresponding $h_{AB} = 0$ plane (red-, green- and blue-rimmed planes in fig. 2.4). Only seams in one of the planes mediate the desired photoreaction, while the others lead to by-products. The second class of CoIn seams connects the different planes (solid line in fig. 2.4) and thus opens pathways to competing loss channels. The search focuses on the energetically low-lying seams that connect the minimum energy CoIns on the different planes. As these CoIn seams are not restricted to a single WH-coordinate a systematic strategy is required to explore the full $3N - 6$ coordinate space.

For this purpose the *resonance* condition (eq. 2.7) is re-formulated in more intuitive terms going down to the atom-centered basis. The localized MOs A and B (eq. 2.2) are represented as a linear combination of atomic orbitals χ_i:

$$A = \sum_i c_{Ai}\chi_{Ai} \quad \text{and} \quad B = \sum_j c_{Bj}\chi_{Bj}, \tag{2.15}$$
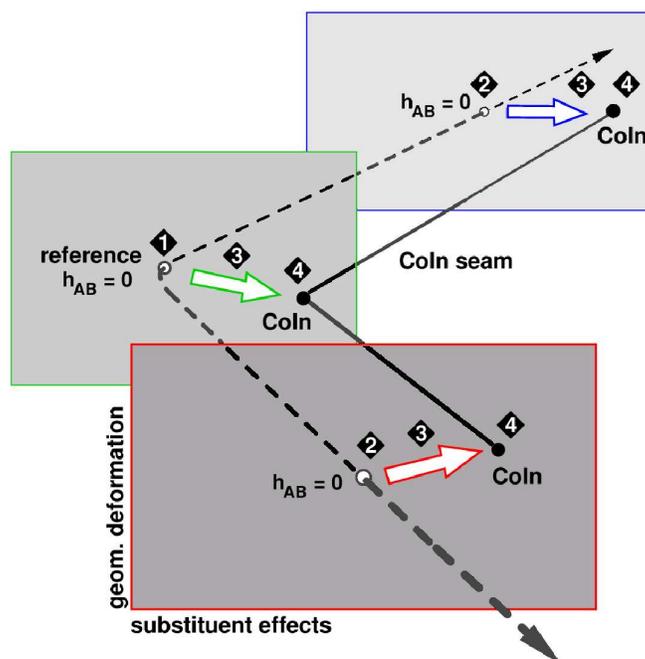
Figure 2.4.: Schematic representation of a CoIn seam connecting planes associated with different WH-coordinates ($\vec{g}$), each fulfilling the *resonance* condition (eq. 2.7). Particular combinations of geometrical and substituent effects on each plane lead to the formation of CoIns by fulfilling the *heterosymmetry* condition (eq. 2.14). The dashed line connects the homosymmetric biradicals, the solid line represents the CoIn seam, connecting different WH-coordinates. The individual steps of the procedure for locating the seam are marked as black diamonds.

where the sums run over different atomic centers i and j. The resonance integral is now written as a sum of two-center integrals:

$$h_{AB} = \sum_i \sum_j c_{Ai} c_{Bj} \left\langle \chi_i \middle| \hat{h} \middle| \chi_j \right\rangle \quad \text{with} \quad c_{Ai/Bj} = \{-1; 1\}. \tag{2.16}$$

Only next neighbor interactions are considered and equal contribution of each center in the linear combination is assumed. The sign of the two-center resonance integrals $\left\langle \chi_i \middle| \hat{h} \middle| \chi_j \right\rangle$ depends on the relative phase of the atomic orbitals in eq. 2.15 and is either positive ($b_{ij} = +\left\langle \chi_i \middle| \hat{h} \middle| \chi_j \right\rangle$) or negative ($a_{ij} = -\left\langle \chi_i \middle| \hat{h} \middle| \chi_j \right\rangle$). According to eq. 2.16 the simplified *resonance* condition (eq. 2.7) is fulfilled only for an equal number of positive and negative contributions, the prerequisite of non-bonding orbitals. Thus, geometrical deformations, which cancel/generate pairwise positive and negative resonance contributions, are required. With the decomposition of eq. 2.16 one can define the homosymmetric biradical structures associated to different WH-coordinates (fig. 2.4) and extract the structural deformations connecting them (dashed line). The in-

dividual homosymmetric biradicals can be reached in two ways. The first one cancels individual two-center resonances $\left\langle \chi_i \middle| \hat{h} \middle| \chi_j \right\rangle$ by spatial separation as realized through torsional motion or bond cleavage. The second one cancels individual expansion coefficients $c_{Ai}c_{Bj}$. This happens only in $2n\pi$-electron subunits, which become structurally decoupled from the remaining π-system by a geometric deformation. Due to their odd number of positive and negative resonance integrals, the subunits also decouple energetically and do not contribute to the active orbitals anymore.

Biradical structures belonging to different WH-coordinates (circles on the dashed line in fig. 2.4) are starting points for a subsequent search of CoIns. For their qualitative prediction the second condition, eq. 2.14, has to be fulfilled. This can be realized by geometrical deformations or substituents effects as formulated in the rules of thumb given in the section 2.2. The individual CoIns found by this strategy serve as supporting points in the IS for the subsequent linear interpolation of the interconnecting seams. The systematic pairwise cancelation/generation of the two-center integrals in eq. 2.16 guarantees that the effects needed to connect two supporting points occur simultaneously, thus the linear interpolation between two supporting points is justified.

Now the rules of thumb for a systematic prediction and optimization of low-lying CoIn seams connecting different WH-coordinates are summarized. The approach is presented graphically in fig. 2.4, the individual rules show as black diamonds. The only knowledge required is the geometry of reactant and product. Rules **1.** and **2.** do not require additional quantum chemical calculations. Rule **3.** and **4.** only need final optimizations of the predicted structures.

1. The WH-coordinate associated with the photochemical reaction under consideration is identified. The resonance integral is formulated in the basis of the atomic orbitals as a sum of two-center integrals (eq. 2.16). The geometry which satisfies eq. 2.7 is determined (labeled as "reference" in fig. 2.4).

2. Different scenarios for the pairwise cancelation/generation of positive and negative resonance integrals, which preserve the simplified *resonance* condition are followed. Each scenario is connected to a different WH-coordinate and leads to the associated homosymmetric biradical structure. The dashed line connects the individual biradical structures.

3. Mesomeric effects of functional groups can fulfill eq. 2.14 (thick arrows in fig. 2.4). For their analysis the localized MOs A and B are best suited and considered at each biradical structure. Geometries without mesomeric stabilization are discarded, as they typically lead to high energy seams. CoIn optimizations are started at the predicted geometries (red-, green- and blue-rimmed arrows). These geometries are not necessarily stationary points in the IS. Therefore, geometrical constraints (available via step **2.**) need to be introduced. The optimized structures serve as supporting points for **4.**

4. By analizing the electronic configuration of the ES it is decided which supporting points can be linked together via a low-energy seam. Only supporting

points with the same ES electronic configuration (either $\left| A^2 \right\rangle$ or $\left| B^2 \right\rangle$) can be interconnected. A linear interpolation scheme with a subsequent constrained CoIn optimization locates the seam (solid line in fig. 2.4) connecting the reference CoIn (green-rimmed arrow) to the CoIns associated with the additional WH-coordinates. The constraints, which must facilitate the stepwise cancelation/generation of pairs of two-center resonance integrals, are taken from step **2.**.

In this work the projection method presented in sec. 1.2.3 was used for the final optimization of the estimated CoIns. When geometrical constraints are applied the projection method converges at geometries with a finite energy gap. This obstacle can be surmounted by a subsequent unconstrained optimization along the gradient difference vector $\vec{X}_1$[142] (eq. 1.18a). It locates the nearest CoIn to the input geometry. This step is usually associated with the energetic destabilization and therefore it is crucial that already the preceding steps locate a geometry in the vicinity of the low-energy CoIn seam. This last step can be omitted when the constraint-adapted gradient projection method[149] for CoIn optimization is used.

2.4. Applications

In this sections the rules of thumb for optimization of CoIns (sec. 2.2) and CoIn seams (sec. 2.3) are applied on realistic conjugated polyene systems. For the purpose photochromic molecules were chosen which undergo photoinduced ultrafast CoIn mediated isomerization: CHD/cZc-HT as a representative of non-polar unfunctionalized polyenes, where CoIns are formed through geometrical deformations, HTI as a representative of weakly polar polyenes, where low-energy CoIns are formed by combining geometrical deformations and substituent effects and trifluoromethyl-pyrrolylfulgide as a representative of multi-functionalized strongly polar polyenes, where the functional groups alone determine the structure of the CoIns[1]. HTI and fulgides have potential application as coherently driven molecular photoswitches. However, representatives of both families are characterized by a relatively low photoswitching quantum yields[116, 126, 150–153]. It is intriguing to pinpoint the reason for the low yield. The rules presented above are well suited to address the question, whether the presence of concurring deactivation channels to the GS is responsible for the low quantum yields.

In sec. 2.4.1 the rules of thumb are benchmarked against known CoIns in the CHD/cZc-HT system. In sec. 2.4.2 low-lying CoIns in the HTI system are identified. In sec. 2.4.3 a seam in the HTI system, associated with the *cis-trans* isomerization coordinate is presented. In sec. 2.4.4 the complex branched structure of the CoIn seam in the fluorinated pyrrolylfulgide system is revealed.

---

[1]The reader is referred to capter 3 for the detailed discussion on the mechanisms of HTI and fulgide isomerization.

2.4.1. Conical intersections in non-polar polyenes: 1,3-cyclohexadiene/cZc-hexatriene

In sec. 2.2 CHD/cZc-HT was identified as a 6π-electronic basic unit, as it is the smallest unit, which can undergo a conrotatory WH-motion. In this regard the system was used in ref. [125] as one of the basic units to quantify the rules of thumb outlined in sec. 2.2 at SA-3-CASSCF(2,2) level of theory. In this section the CHD/cZc-HT system is used to demonstrate the application of these rules for non-polar conjugated polyenes. Several already known CoIn geometries are rationalized[2].

Fig. 2.5 summarizes three local minima in the IS of the CHD/cZc-HT system (bottom row). The global minimum in the intersection space $CoIn_{min}$ was first described by Robb and colleagues[47] and marks one of the pioneering results that demonstrates the crucial role of CoIns in ultrafast photochemistry. The structures of $CoIn_{bu}$ and $CoIn_2$ were reported by Tamura *et al.*[154]. More recently the existence of a low lying accessible CoIn seam connecting $CoIn_{bu}$ and $CoIn_{min}$[74] was reported. All structures exhibit a triangular pattern, denoted in the literature either as a -$(CH)_3$-kink[86, 89, 155] or as a Hula-Twist[123, 156]. Its formation has been recognized as a necessary condition in non-polar polyenes to reach GS/ES degeneracy[80, 86, 157].

The three-step strategy for the conceptual search of CoIn structures is visualized in fig. 2.5 (top to bottom) for $CoIn_{bu}$, $CoIn_2$ and $CoIn_{min}$. The final CoIn optimizations of the predicted structures were performed with an active space of 6 electrons and 6 orbitals and averaging over the GS and the first ES. The electronic wavefunctions at SA-2-CASSCF(6,6) show dominant contributions from the biradical ($\left|A^\bullet B^\bullet\right\rangle$) and zwitterionic ($\left|A^2\right\rangle$ or $\left|B^2\right\rangle$) configurations in support of the practicability of the rules of thumb (see ref. [125]). The basic units in CHD/cZc-HT system are ethylene, *cis*-butadiene and CHD itself. The known CoIn structures can be derived from ethylene and cyclohexadiene. $CoIn_{bu}$ (left column) is associated with a torsion (one-bond flip) around the C_2-C_3 double bond of the ethylene basic unit[3] leading to an asymmetric, though nearly homosymmetric biradical with degenerate localized orbitals $A_{3,5}$ and B_2. Due to the intact σ-bond the torsion is partially hindered. Subsequent pyramidalization at C_3 (denoted by a blue arrow in fig. 2.5) and tilt of C_2 towards C_4 forms the well known -$(CH)_3$-kink arrangement, here between the adjacent centers C_2, C_3 and C_4. In the following, this arrangement is referred to as a 1,3-kink (marked by a dashed blue line in fig. 2.5). In agreement with sec. 2.2 the pyramidalization lowers the energy of orbtial $A'_{3,5}$ while the tilt raises the energy of orbital B'_2.

$CoIn_{min}$ (middle column) is associated with the C_2-symmetry preserving conrotatory rotation in the full 6π-electron space. Along this WH-coordinate the frontier orbitals degenerate and localize either at C_1, C_3 and C_5 or at C_2, C_4 and C_6. These orbitals are labeled $A_{1,3,5}$ and $B_{2,4,6}$. Subsequently, a tilt in the carbon scaffold C_2-C_6 leads to a more flexible 1,5-kink arrangement without pyramidalization. It enhances the

---

[2]For the prediction of further energetically low lying CoIn geometries in the CHD/cZc-HT system see sec. 4.2 and ref. [125].

[3]A torsion around the C_4-C_5 double bond leads to a mirror-symmetric species.
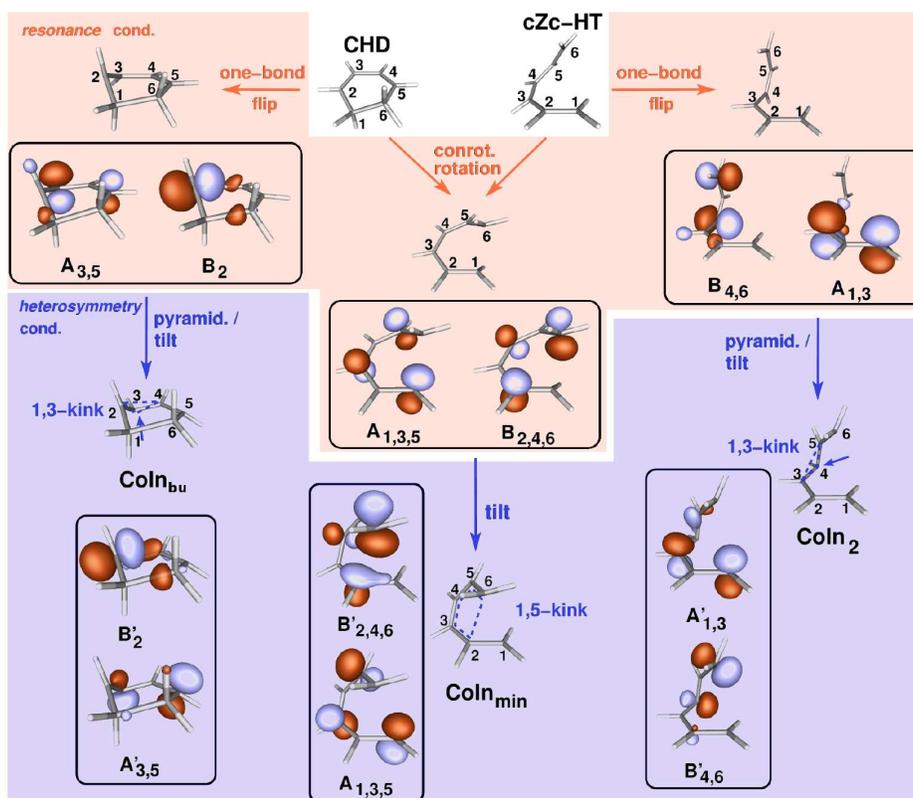
Figure 2.5.: Rationalization of several known CoIn geometries in the CHD/cZc-HT system within the scope of the extended two-electron two-orbital model. Presented are the structures of the homosymmetric biradicals and the CoIns with the corresponding localized orbitals A and B. Red arrows denote the WH allowed motions (*resonance* condition) for the basic units ethylene (one-bond flip, left and right arrow) and CHD itself (conrotatory rotation, middle arrows) leading to the homosymmetric biradicals. Blue arrows indicate the subsequent deformations (*heterosymmetry* condition) leading to the individual CoIn structures. At CoIn geometry dashed blue lines denote the 1,3/1,5-kinks, blue arrows denote the center of pyramidalization.

electronic repulsion within orbital $B'_{2,4,6}$, thus destabilizing the biradical GS $\left|A^{\bullet}B^{\bullet}\right\rangle$ towards a CoIn with the zwitterionic $\left|A^2\right\rangle$ state.

CoIn$_2$ is associated with a one-bond flip within the central ethylene basic unit of cZc-HT (right column). Thereby orbital A localizes at centers C_1 and C_3 and orbital B at centers C_4 and C_6. CoIn$_2$ is reached upon pyramidalization at C_4 and tilt of C_3 towards C_5, which forms a 1,3-kink. This time orbital B is stabilized, while orbital A is destabilized.

Based on this scheme, i.e. making use of the different basic units identifiable in the

CHD/cZc-HT system, further closed ring and open ring low-energy CoIns can be predicted and optimized. A short discussion is presented at the end of sec. 4.2.

2.4.2. Discrimination between low- and high-energy conical intersections: hemithioindigo-hemistilbene
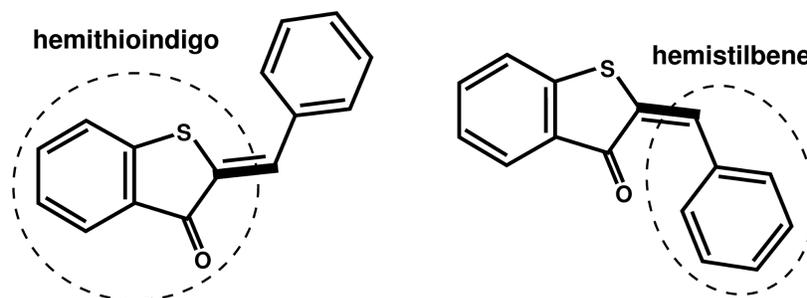
Figure 2.6.: Ground state isomers of Z-HTI (left) and E-HTI (right) in the HTI system. The building blocks hemithioindigo and hemistilbene (encircled) have a common double bond (highlighted).

HTI has two stable GS conformers, Z-HTI and E-HTI (fig. 2.6). Both conformers are interconvertable by visible light. HTI is composed of a hemithioindigo and a hemistilbene moieties sharing a common double bond. For the application of the rules of thumb (sec. 2.2) a separation into a basic unit and functional groups (i.e. sulfur, carbonyl, phenyl) is convenient.

Conical intersections associated with the 2π-electronic basic unit ethylene The most obvious separation of HTI is into an ethylene unit (C_3-C_4 in fig. 2.7) and functional groups. Both π-obitals and π-electrons of the ethylene unit are regarded as the active space for the conceptual discussion. The torsional motion around the double bond (one-bond flip), which connects both HTI isomers, coincides with a WH-motion (sec. 2.2). The *resonance* condition (eq. 2.13) is fulfilled at a 90° twisted geometry (fig. 2.7). There, both subunits, hemithioindigo and hemistilbene, as well as the active orbitals are spatially decoupled (fig. 2.7). The orbital localized at the hemithioindigo is denoted as A_3 while the orbital localized at the hemistilbene is denoted as B_4. Next, the miscelaneous possibilities to satisfy the *heterosymmetry* condition (eq. 2.14) via geometrical deformations and mesomeric effects are discussed. The final CoIn optimizations of the predicted structures were performed with an active space of 10 electron and 9 orbitals and averaging over the GS and the first ES (see Appendix I). The electronic wavefunctions at SA-2-CASSCF(10,9) show dominant contributions from the biradical ($\left| A^\bullet B^\bullet \right\rangle$) and zwitterionic ($\left| A^2 \right\rangle$ or $\left| B^2 \right\rangle$) configurations in support of the practicability of the rules of thumb (see ref. [116]).

From the functional groups attached directly to the ethylene unit only the carbonyl group has a considerable effect on the energies of orbitals A_3 and B_4 due to
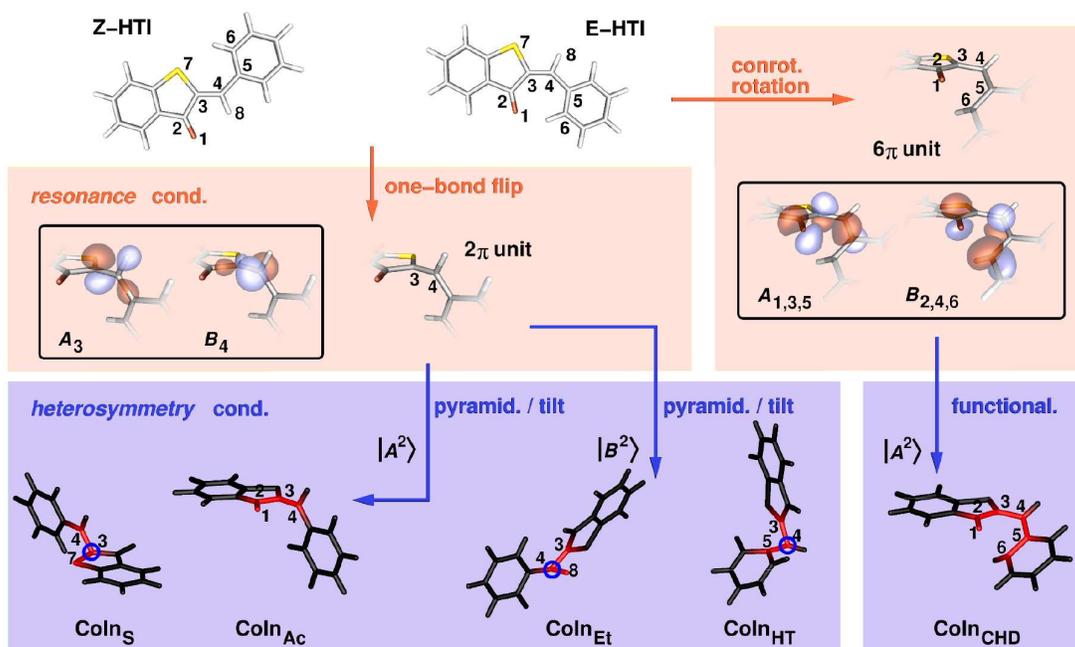
Figure 2.7.: Individual CoIns in the HTI system. The steps performed to fulfill the *resonance* and *heterosymmetry* conditions (eqs. 2.13 and 2.14) are color-coded. The atoms essential for the formation of a particular CoIn (i.e. a minimal model) are colored in red in the bottom panel. A 2π- and a 6π-electronic subunits, associated with the WH-motions *cis-trans* isomerization and conrotatory electrocyclic ring closure, respectively, are identified. Different possibilities for combining pyramidalization and tilt exist for the 2π unit. Correspondingly, four CoIns are obtained: CoIn_S, CoIn_{Ac}, CoIn_{Et} and CoIn_{HT}. The presence of oxygen in the 6π unit provides the asymmetric distortion required to fulfill the *heterosymmetry* condition without additional geomerical deformations giving CoIn_{CHD}. CoIn_{CHD} is the global minimum in the IS of HTI.

its low-lying π^*-orbital. The positive mesomeric effect of sulfur is less pronounced due to the diffusness of its $3p$-orbiatals. Effectively, the negative mesomeric effect of the carbonyl group on orbital A_3 stabilizes the $\left|A^2\right\rangle$ configuration at the 90° twisted geometry. HTI exhibits a charge transfer in the ES from the hemistilbene to the hemithioindigo moiety upon torsion around the central double bond.

The carbonyl group alone cannot stabilize the charge transfer state to a CoIn with the biradical GS (tab. 2.2) and additional geometrical deformations (i.e. pyramidalization and tilt) are required. The asymmetry introduced in the central ethylene unit through the functionalization makes miscellaneous variations possible. According to the rules of thumb (sec. 2.2) CoIns of minimal energy are obtained by simultaneous pyramidalization and tilt ($\text{CoIn}_{\text{pyr/tilt}}$ in tab. 2.1). Furthermore, negative mesomeric effects have the same net effect as pyramidalization, positive mesomeric effects are equivalent to tilting (fig. 2.1). In the current example, the geometrical deformations

can be correlated to the mesomeric effects by taking the pre-stabilization of orbital A_3 by the carbonyl group into account and applying pyramidalization to C_3 from the same orbital. Subsequent tilting of the hemistilbene moiety (and hence orbital B_4) towards the sulfur forms a potential CoIn geometry (CoIn$_S$ in fig. 2.7, the pyramidalized C_3 is marked by a blue circle). CoIn optimization of the predicted structure retains the predefined arrangement. Further CoIns can be obtained for purely pyramidalized or tilted arrangements. In contrast to the unfunctionalized ethylene, where purely pyramidalized and purely tilted CoIns are not minimum energy points in the IS the purely tilted CoIn$_{Ac}$ in HTI (fig. 2.7) with the hemistilbene moiety tilted towards the oxygen is energetically stable (tab. 2.3). The orientation of the oxygen lone pair towards B_4 requires a smaller tilt in contrast to ethylene (CoIn$_{tilt}$ in fig. 2.1) and, thus, facilitates the formation of a minimum energy CoIn.

Despite the $\left|A^2\right\rangle$-configuration being more stable then the $\left|B^2\right\rangle$-configuration at the

	CoIn$_S$	CoIn$_{Ac}$	CoIn$_{Et}$	CoIn$_{HT}$	CoIn$_{CHD}$
ΔE (eV)	0.00	-0.72	0.72	1.36	-0.76
localization pattern	A_3/B_4	A_3/B_4	A_3/B_4	A_3/B_4	$A_{1,3,5}/B_{2,4,6}$
ES configuration	$\left|A^2\right\rangle$	$\left|A^2\right\rangle$	$\left|B^2\right\rangle$	$\left|B^2\right\rangle$	$\left|A^2\right\rangle$
torsion (°)	90.0	90.0	90.0	90.0	154.9
pyramidalization (°)	64.0[1]	0.6[1]	54.1[2]	59.6[2]	3.0[1]
tilt (°)	18.6[3]	-21.7[3]	-28.0[4]	23.3[4]	-[5]

[1]Pyramidalization defined for C_3.
[2]Pyramidalization defined for C_4.
[3]Tilt defined for C_4.
[4]Tilt defined for C_3.
[5]Tilt not defined for angles other than 90°.

Table 2.3.: Relative stabilization ΔE in eV, localized orbital patterns, ES (S_1) electronic configuration and relevant coordinates for the CoIns given in fig. 2.7. Optimization was performed at SA-CASSCF(10,9) level with averaging over two states. The energy of CoIn$_S$ is used as reference for ΔE.

90° twisted geometry the energetic order of both configurations can be changed by applying pyramidalization and tilt in inverse way, i.e. pyramidalization to orbital B_4 and tilt to orbital A_3. Again several possibilities exist. Following the pyramidalization of C_4 a tilt of the hemithioindigo (and hence orbital A_3) can proceed towards C_5 of the phenyl group, leading to CoIn$_{HT}$ (fig. 2.7, the pyramidalized C_4 marked by a blue circle), or towards the hydrogen H_8, leading to CoIn$_{Et}$ (fig. 2.7, the pyramidalized C_4 marked by a blue circle). Both geometrical constellations are very prominent and occur in various unfunctionalized polyenes. The triangular C-C-C or C-C-H arrangements are known as -(CH)$_3$-kinks[86, 155] or Hula-twists[123, 156]. In fact, the C-C-S triangular arrangement at CoIn$_S$ is closely related to the -(CH)$_3$-kink. In HTI the formation of CoIn$_{HT}$ and CoIn$_{Et}$ counteracts the mesomeric effect of the carbonyl group, which is a strong indicator for their irrelevance in the ES dynamics. Indeed,

both $CoIn_{HT}$ and $CoIn_{Et}$ are significantly higher in energy than $CoIn_S$ and $CoIn_{Ac}$ (tab. 2.3).

For the sake of completeness it is noted that $CoIn_S$, $CoIn_{HT}$ and $CoIn_{Et}$ possess diastereomeric structures for 180° torsion around the central double bond (labeled $CoIn_{S*}$, $CoIn_{HT*}$ and $CoIn_{Et*}$ with different characteristics due to the asymmetry in the molecule (see Appendix F). Their formation is readily understood in the context of the above discussion and will not be discussed further. $CoIn_{S*}$ will be revisited in sec. 3.1 when the isomerization mechanism of HTI is investigated.

Conical intersections associated with the 6π-electronic basic unit hexatriene
For HTI a 6π-electronic unit enclosing the oxygen and five carbon atoms C_2 through C_6 can be identified. It can be regarded as a hexatriene basic unit with one carbon atom exchanged by an oxygen. Hexatriene can undergo a cyclization to a CHD solely from a cZc-conformation. Correspondigly, only E-HTI is cyclizable. This observation will be of relevance for the study of the HTI photoreaction mechanism in sec. 3.1. An intermediate geometry with a partially formed C_1-C_6 σ-bond can be located (fig. 2.7) with localized active orbitals $A_{1,3,5}$ and $B_{2,4,6}$. Due to the electronegativity of the oxygen the energy of orbital $A_{1,3,5}$ decreases, leading to the stabilization of the $\left|A^2\right\rangle$-configuration and, thus, the degeneracy is reached along the WH-coordinate without any additional geometrical deformations ($CoIn_{CHD}$). Rather, the exchange of a carbon from the basic unit by an oxygen introduces the asymmetry needed to reach a degeneracy. Correspondingly, this CoIn is notably stable (table 2.3) and must not be neglected during the dicussion of the HTI dynamics, even if it is not associated with the *cis-trans*-isomerization.

2.4.3. Conical intersection seam belonging to a single Woodward-Hoffmann coordinate: hemithioindigo-hemistilbene

In the previous section the rules for obtaining single CoIns (sec. 2.2) were utilized to locate minimum energy CoIns in the HTI system (fig. 2.7). All CoIns with exception of $CoIn_{CHD}$ have in common that they were derived from a 90° twisted geometry by applying pyramidalization and/or tilt. According to the discussion in sec. 2.3, these CoIns belong to a plane orthogonal to the WH-coordinate *cis-trans* isomerization (fig. 2.2). At $CoIn_S$ and $CoIn_{Ac}$ the ES has a $\left|A^2\right\rangle$-configuration, while at $CoIn_{Et}$ and $CoIn_{HT}$ it has a $\left|B^2\right\rangle$-configuration. The *heterosymmetry* condition (eq. 2.14) does not allow for a configuration change along the seam (see also sec. 2.3). Hence, $CoIn_S$ and $CoIn_{Ac}$ are connected by a seam with $\left|A^2\right\rangle$-configuration. $CoIn_{Et}$ and $CoIn_{HT}$ are connected by a seam with a $\left|B^2\right\rangle$-configuration. A connection between both seams does not exist in the scope of the extended two-electron two-orbital theory. In the following, the seam between $CoIn_S$ and $CoIn_{Ac}$ is presented.

Referring to the general form of the seam, derived in fig. 2.3, the $CoIn_S$-$CoIn_{Ac}$ seam
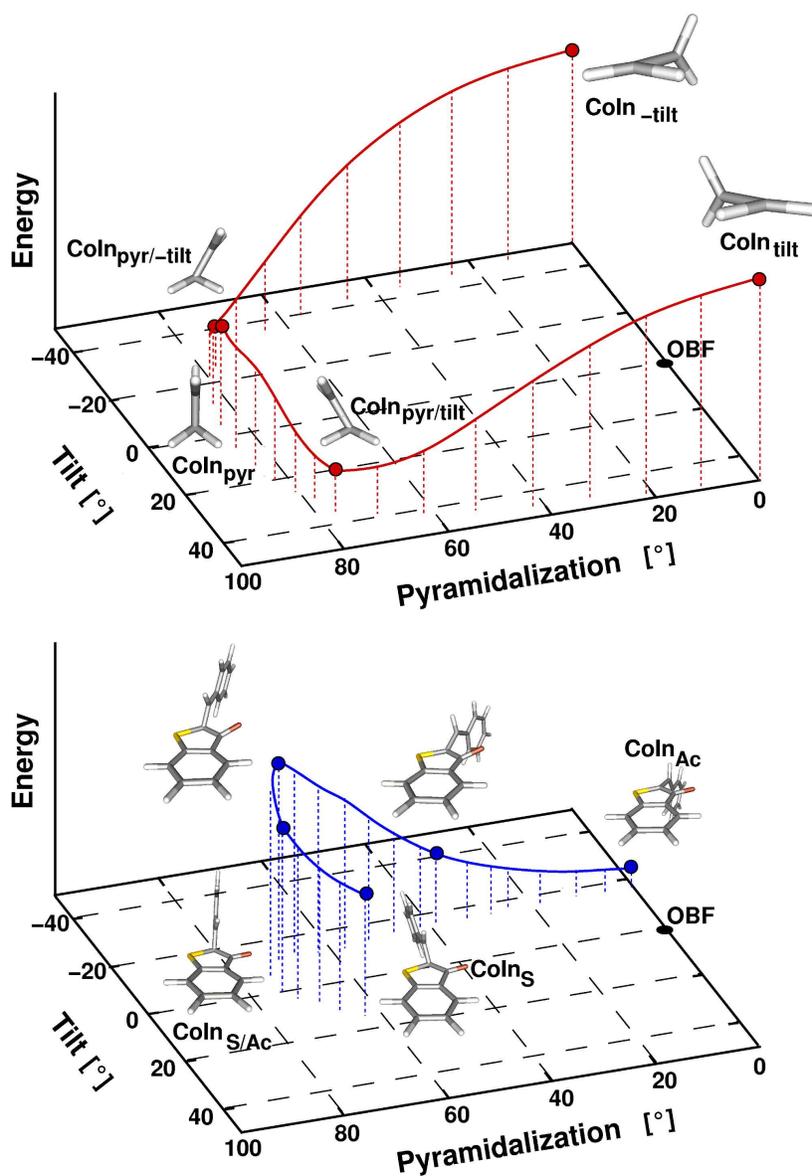
Figure 2.8.: CoIn seams mediating the *cis-trans* isomerization in ethylene (top) and HTI (bottom). Geometries at selected points are given. Dashed lines indicate the projections of calculated points along the seams. Only the seam segment with positive pyramidalization angles is plotted (see fig. 2.3).

has to be curved in the pyramidalization/tilt plane as well. A straightforward linear interpolation gives poor starting structures for the subsequent constrained CoIn optimization. To provide further supporting points, first, a purely pyramidalized intermediate $CoIn_{S/Ac}$ with a pyramidalization angle of 74° was optimized[4]. For negative

---

[4]For definition of the pyramidalization and tilt angles in HTI see Appendix G

tilt angles no local minimum exists for high pyramidalization angles. An intermediate structure with pyramidalization angle of 67° and tilt of $-12°$ was obtained by scanning the tilt coordinate. With this preliminary work the HTI seam between $CoIn_S$ and $CoIn_{Ac}$ was devided into linear segments and the interpolation approach could be applied to finalize the seam (fig. 2.8, bottom). Both pyramidalization and tilt were kept fixed during CoIn optimizations out of the interpolated geometries. For comparison, the corresponding seam segment in ethylene is given in fig. 2.8, top. The supporting points were optimized as follows: $CoIn_{pyr/tilt}$ constitute a minimum in the full $3N-8$ IS, $CoIn_{pyr}$ and $CoIn_{tilt}$ are minimum energy CoIns in C_S-symmetric subspaces.

Indeed, the ehtylene seam and the HTI seam exhibit similar curvature in the IS, however, with differences in the energetic profile and in the magnitude of geometrical displacement. The HTI seam is characterized by weaker pyramidalization and tilt which is attributed to the mesomeric effect of the carbonyl group and the favorable orientation of the lone pairs of the heteroatoms. Furthermore, $CoIn_{Ac}$ constitutes a minimum in the IS. The modest deformation together with the pronounced energetic stability makes the seam segment around $CoIn_{Ac}$ easier accessible than its pendant in the ethylene system and accelerates the relaxation to the GS.

2.4.4. Conical intersection seams connecting different Woodward-Hoffmann coordinates: pyrrolylfulgide
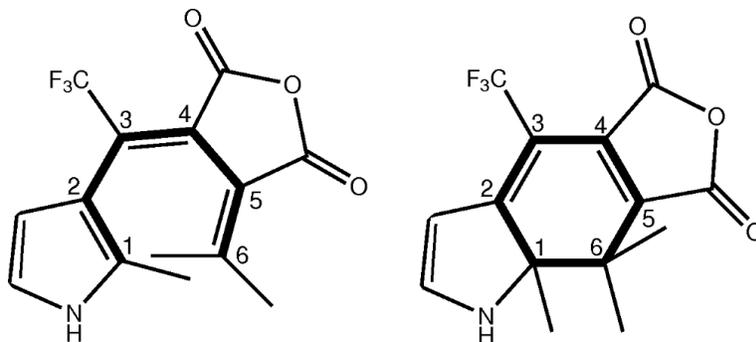
Figure 2.9.: Two GS isomers of trifluoromethyl-pyrrolylfulgide, cZc (left) and C (right). The basic unit $1,3$-CHD/cZc-HT is highlighted.

In the previous section a seam confined to the pyramidalization/tilt subspace of the intersection subspace was presented. In complex systems more than one WH-motion is feasible and concurrent photoprocesses may be initiated simultaneously. In such case the seams connecting planes orthogonal to different WH-coordinates have to be optimized. Rules for achieving this goal were presented in sec. 2.3. In the following, these rules are utilized to find seams associated with competing channels to the electrocyclic isomerization between the open (cZc) and the closed (C) forms of trifluoromethyl-pyrrolylfulgide (fig. 2.9). Three scenarios are discussed
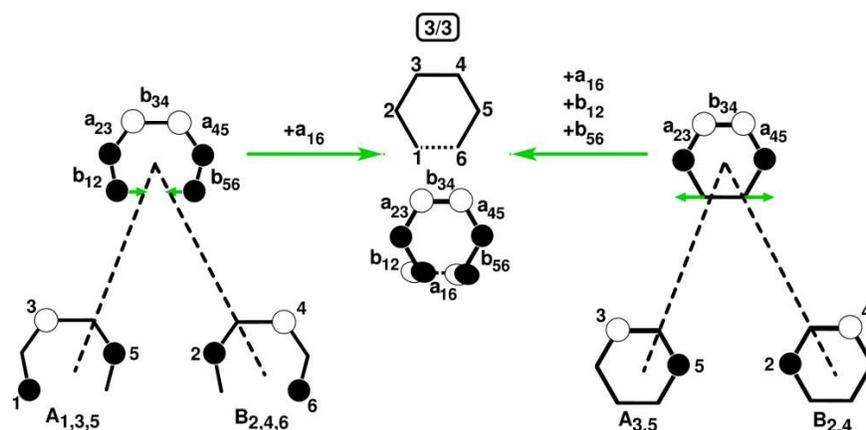
Figure 2.10.: Visualization of the resonance integral h_{AB} by superimposing the localized orbitals A and B along the conrotatory electrocyclic ring closure/opening coordinate (WH-coordinate, green line) of the basic unit 1,3-CHD/cZc-HT. Positive (b_{ij}) and negative (a_{ij}) two-center resonance integrals between neighboring carbon centers are denoted. The requirement of eq. 2.7 is met at the homosymmetric biradical geometry labeled [3/3] with localized active orbitals $A_{1,3,5} = \chi_1 - \chi_3 + \chi_5$ and $B_{2,4,6} = \chi_2 - \chi_4 + \chi_6$ and an equal number of positive and negative two-center resonance integrals.

and a thorough analysis is carried out only for one scenario (for the analysis of the remaining scenarios see Appendix H).

1. The WH-coordinate which guides the cZc↔C isomerization in fulgide is a conrotatory rotation. The basic unit associated with this rotation is the 6π-electron 1, 3-CHD/cZc-HT (given in bold in fig. 2.9). The HOMO and the LUMO at the equilibrium geometries of CHD and cZc-HT are expressed in the basis of equivalent localized MOs A and B according to eq. 2.16. For cZc-HT they read $A_{1,3,5} = \chi_1 - \chi_3 + \chi_5$ and $B_{2,4,6} = \chi_2 - \chi_4 + \chi_6$ (fig. 2.10). For CHD the localized orbitals are $A_{3,5} = \chi_3 - \chi_5$ and $B_{2,4} = \chi_2 - \chi_4$ (fig. 2.10). Along the WH-coordinate the requirement of the simplified *resonance* condition (eq. 2.7) is met at the homosymmetric biradical geometry labeled [3/3] (fig. 2.10), as the resonance intergral h_{AB} is composed of equal number of positive (b_{12}, b_{34}, b_{56}) and negative (a_{16}, a_{23}, a_{45}) resonance integrals

$$h_{AB} = b_{12} + a_{23} + b_{34} + a_{45} + b_{56} + a_{16} = 0. \qquad (2.17)$$

In the following h_{AB} is visualized by superimposing the localized orbitals A and B as shown in fig. 2.10. Then, the sign of the two-center resonance integrals results from the relative phase of the atomic orbitals at neighbouring atoms. Naturally, this representation resembles the nodal structure of the delocalized orbitals.
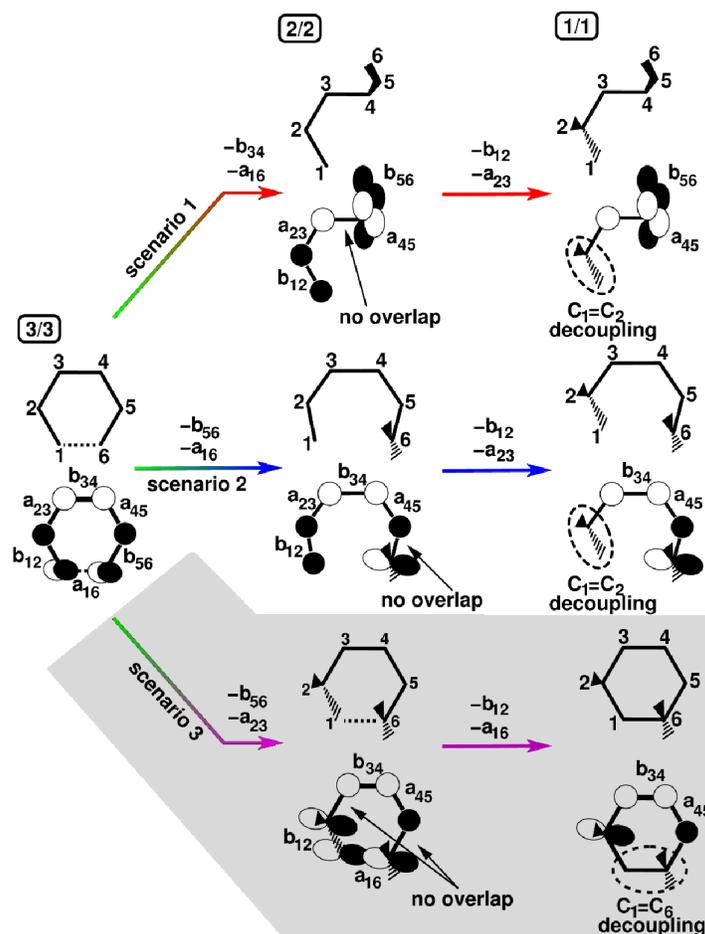
Figure 2.11.: Three scenarios (green→red, green→blue, green→magenta) for geometrical deformations in the basic unit that preserve the *resonance* condition (eq. 2.7). The resonance integral h_{AB} is visualized by superimposing the active orbitals A and B. Positive (b_{ij}) and negative (a_{ij}) two-center resonance integrals between neighboring carbon centers are denoted. The short hand notation [3/3], [2/2] and [1/1] is used to differentiate geometries belonging to different WH-coordinates upon the number of [positive/negative] resonances. Along each scenario the resonance integrals cancel pairwise.

2. Different scenarios for the pairwise cancelation of the two-center resonance integrals are evaluated. Therefore, the active orbitals are presented in terms of their resonance integrals (fig. 2.11). The short hand notation [3/3], [2/2] and [1/1] is used to differentiate geometries upon the number of [positive/negative] resonances. Two additional remarks are made at this point. First, the C_2-symmetry of the basic unit is not conserved for the substituted derivative. Symmetry equivalent motions in the subunit have to be considered. Second, the structure of the substituted derivative introduces several geometrical restrictions that reduce the number of feasible defor-

mations. Center C_1 and C_2, as well as C_4 and C_5 are involved in aromatic rings (pyrrole and maleic anhydride, fig. 2.9) and torsion around these bonds is hindered. With this in mind the following biradical structures can be derived.

- Scenario 1 (green→red in fig. 2.11). Torsion around the C_3-C_4 bond weakens b_{34}. The simultaneous elongation of the C_1-C_6 distance lowers a_{16}. The result is a [2/2] open-ring geometry (fig. 2.11, top row). Additional torsion around the C_2-C_3 bond leads to the [1/1] geometry. The integral a_{23} is weakened and the C_1-C_2 unit ($2n\pi$-unit is decoupled from the π-system ($c_{Ai}c_{Bj} = 0$). At the [1/1] geometry the resonance integral h_{AB} consists only of two terms b_{56} and a_{45}.

- Scenario 2 (green→blue in fig. 2.11). Torsion around the C_5-C_6 bond weakens b_{56}. Simultaneous increase of the C_1-C_6 distance weakens a_{16}. The result is a [2/2] geometry (fig. 2.11, middle row), again an open-ring structure, which is different from scenario 1. Additional torsion around the C_2-C_3 bond cancels a_{23} and decouples the C_1-C_2 unit from the π-system ($c_{Ai}c_{Bj} = 0$), leading again to a [1/1] geometry.

- Scenario 3 (green→magenta in fig. 2.11). Torsion around the C_5-C_6 bond weakens b_{56}. Simultaneous torsion around C_2-C_3 (fig. 2.11, bottom row) weakens a_{23} and yields a [2/2] geometry. Increase of the C_1-C_6 distance decouples the C_1-C_2 unit from the π-system and ultimately leads to the [1/1] geometry from scenario 2. Decrease of the C_1-C_6 distance (i.e. formation of a σ-bond) decouples the C_1-C_6 unit to yield a new [1/1] closed ring geometry with only b_{34} and a_{45} contributing to the resonance h_{AB}.

In principle CoIn seams can connect each pair of homosymmetric biradicals. In the current example the interest is on seams reachable from the reference structure [3/3]. Which seam is energeticly favorable is decided by the mesomeric effects, i.e. the interaction of the basic unit with the substituents.

3. The discussion of the mesomeric effects is limited to scenario 3. The remaining scenarios are shown in the Appendix H. For the analysis the localized molecular basis at each biradical geometry is considered. The geometrical deformations in 2. divide the original π-system in subunits as indicated by the dashed lines in fig. 2.12. Only non-bonding subunits contribute to the final MOs, i.e. subunits that undergo bonding and antibonding interactions with the remaining π-orbitals can be discarded (red crosses). Such subunits typically have no amplitudes in the terminal position. The resulting localized active orbitals are $A_{3,5}$ and $B_{2,6}$ for the [2/2] geometry and $A_{3,5}$ and B_2 for the [1/1] geometry.
 For these orbitals the influence of the functional groups to satisfy the *heterosymmetry* condition (eq. 2.14) is investigated. Two mesomeric groups are present in the fulgide, an anhydride moiety with negative mesomeric effect (-M) conjugated to the basic unit at C_4 and C_5 and an amino moiety with positive mesomeric effect (+M) conjugated

at C_1 and C_2. Exemplarily, fig. 2.13 shows the interaction of the functional groups at the geometries [3/3] and [1/1]. The energetic position of the resulting functionalized orbitals is indicated.

[3/3] geometry. Each substituent can act on both orbitals $A_{1,3,5}$ and $B_{2,4,6}$ (fig. 2.13 green-rimmed arrows). By appropriate combination of the mesomeric effects either the electronic configuration $\left|A^2\right\rangle$ or $\left|B^2\right\rangle$ is stabilized. In each case a CoIn with the GS is reached simply by adjusting bond lengths as shown in fig. 2.13.

[1/1] geometry. Each substituent can act only on one orbital. The anhydride conjugates to center C_5 from orbital $A_{3,5}$, the amino group to center C_2 from orbital B_2 (fig. 2.13 violet-rimmed arrow). Both effects stabilize exclusively $\left|A^2\right\rangle$ the configuration.

From these predicted geometries low-lying CoIns were optimized by quantum chemical methods. The final CoIn optimizations of the predicted structures were performed with an active space of 8 electron and 8 orbitals and averaging over the GS and the first ES. The electronic wavefunctions at SA-2-CASSCF(8,8) show dominant contributions from the biradical ($\left|A^\bullet B^\bullet\right\rangle$) and zwitterionic ($\left|A^2\right\rangle$ or $\left|B^2\right\rangle$) configurations in support of the practicability of the rules of thumb[126]. These structures are the supporting points for the subsequent linear interpolation of the seam. In table 2.4 selected low-lying CoIns from scenarios 1-3 are presented. In the first row the geometries of the CoIns and the structures of the homosymmetric biradical basic units are superimposed. Latter were obtained by constrained optimization at CASSCF(2,2) level, whereby the constraints originate from rule **2**. Their optimization is not required for the seam, but advantageous for testing different substitution patterns. The comparison shows that the CoIns retain to a great extent the geometries of the biradicals. The interactions of the substituents with the π-system manifest in bond
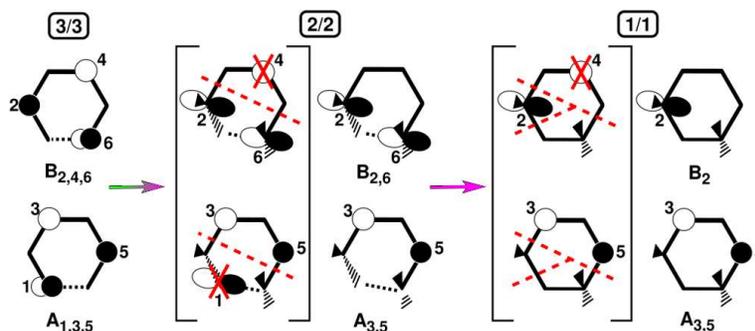
Figure 2.12.: Localized MOs at the [3/3], [2/2] and [1/1] biradical geometries for scenario 3 (green→magenta). Dashed red lines indicate the spatial separation of the π-system into subunits. Red crosses mark atomic centers which do not contribute to the final MOs.
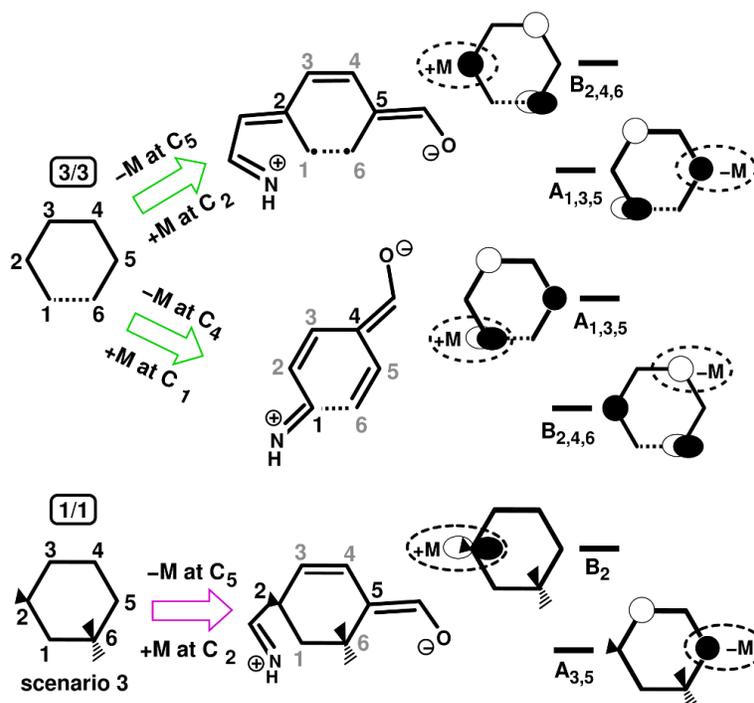
Figure 2.13.: Conjugation of the amino group (+M effect) and anhydride group (-M effect) to the π-system of the basic unit in the fulgide. The energetic order of the active orbitals is shown on the right side. For the reference geometry [3/3] two conjugation patterns that stabilize either the $\left|A^2\right\rangle$ or $\left|B^2\right\rangle$ configuration (upper and lower green-rimmed arrows) can be formulated. For the [1/1] geometry of scenario 3 only one conjugation pattern is possible, stabilizing the $\left|A^2\right\rangle$ configuration.

length rearrangements (table 2.4) rather than in structural deformations. As a general rule mesomerically stabilized CoIns are more stable then CoIns formed by pyramidalization or tilt alone. CoIn$_A$ and CoIn$_B$ are associated with the reference biradical [3/3] (upper and lower branch in fig. 2.13) and thus with the WH-coordinate of the electrocyclic reaction. CoIn$_C$, CoIn$_D$ and CoIn$_E$ are associated with WH-coordinates leading to by-products and result from scenarios 1, 2 and 3, respectively.

4. The CoIn seams between the supporting points are now obtained by linear interpolation. Thereby, the focus is on seams that either include CoIn$_A$ or CoIn$_B$. These seams constitute loss channels for the main photoreaction. The *resonance* and *heterosymmetry* conditions (eqs. 2.13 and 2.14) do not allow for configuration change along the seam. Hence, only CoIn structures with the same electronic configuration, either $\left|A^2\right\rangle$ or $\left|B^2\right\rangle$ can be connected, resulting in two low-lying seam branches (CoIn$_B$-CoIn$_D$, CoIn$_B$-CoIn$_E$) arising from CoIn$_B$. Only one seam branch (CoIn$_A$-CoIn$_C$) arises from CoIn$_A$. The necessary constraints for the optimization of

	$CoIn_A$	$CoIn_B$	$CoIn_C$	$CoIn_D$	$CoIn_E$
ΔE	1.0	0.2	0.0	0.7	0.4
geometry	[3/3]	[3/3]	[2/2]	[1/1]	[1/1]
local. pattern	$A_{1,3,5}/B_{2,4,6}$	$A_{1,3,5}/B_{2,4,6}$	$A_{1,3}/B_{4,6}$	$A_{3,5}/B_6$	$A_{3,5}/B_2$
ES config.	$\left\vert B^2 \right\rangle$	$\left\vert A^2 \right\rangle$	$\left\vert B^2 \right\rangle$	$\left\vert A^2 \right\rangle$	$\left\vert A^2 \right\rangle$
+M/-M	C_1/C_4	C_2/C_5	C_1/C_4	-/C_5	C_2/C_5
C_1-C_6 (Å)	2.42	2.03	4.38	3.20	1.76
C_4-$C_{(=O)}$ (Å)	1.40	1.50	1.39	1.51	1.50
C_5-$C_{(=O)}$ (Å)	1.53	1.43	1.51	1.39	1.45
N-C_1 (Å)	1.30	1.41	1.29	1.37	1.43
N-$C_{(-C2)}$ (Å)	1.45	1.32	1.42	1.38	1.32

Table 2.4.: Structures, relative stabilization ΔE in eV, localized orbitals A and B, ES electronic configuration of the extended two-electron two-orbital model, relevant mesomeric effects and distances for selected low-lying CoIns from scenarios 1-3. The energy of $CoIn_C$ is used as reference for ΔE. Optimization was done at SA-CASSCF(8,8)/6-31G* level with averaging over three states. For comparison the structures of the homosymmetric biradical basic units (red-colored), optimized at SA-CASSCF(2,2)/6-31G* level with averaging over three states, are superimposed.

the intermediate points along each seam can directly be obtained from **2**. For the $CoIn_A$-$CoIn_C$ seam, the torsion around C_3-C_4 and the distance C_1-C_6 were kept fixed. For the $CoIn_B$-$CoIn_D$ seam, torsions around C_2-C_3 and C_5-C_6 as well as the distance C_1-C_6 were kept fixed. For the $CoIn_B$-$CoIn_E$ seam, the torsion around C_2-C_3 and the distance C_1-C_6 were kept fixed. The seams are plotted in fig. 2.14 against the C_1-C_6 coordinate, which all seams have in common.

The findings are summarized in fig. 2.15, where the spatial and energetic relation of the reactive CoIns and the competing CoIn seams (dashed lines) between the GS and the ES is sketched. The reactive regions are shown in green, the competing loss regions are shown in red, blue and magenta, according to the color code used in fig. 2.14. The desired photoreaction connects isomer C and cZc via $CoIn_A$ and $CoIn_B$. The substituent effects that allow for the fast dynamics in these complex fulgides, simultaneously reduce the selectivity of the reaction as can be seen from fig. 2.15. Thus, also the competing channels are easily accessible from the FC regions of both isomers. They can either photostabilize the system or lead to by-products.
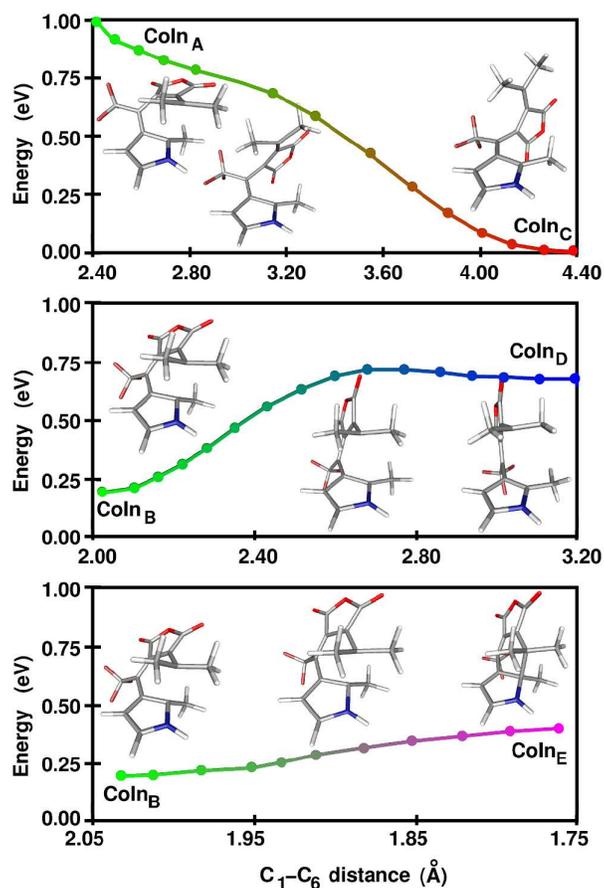
Figure 2.14.: CoIn seams obtained with a linear interpolation scheme between pairs of CoIns from table 2.4. The seams CoIn$_A$-CoIn$_C$ (top), CoIn$_B$-CoIn$_D$ (middle) and CoIn$_B$-CoIn$_E$ (bottom) are shown.

2.5. Summary and perspectives

In this chapter an extension of the two-electron two-orbital theory, originally introduced by Michl and Bonačić-Koutecký, was presented. The extension takes into account the interactions of the active pair of electrons with the remaining closed-shell electrons that are present in any realistic systems. Based on the equations derived within the extended model a set of simple rules of thumb to guide the search for low-energy CoIns and CoIn seams were formulated. Thereby, the only necessary knowledge is the chemical composition of the system.

The strategy pursued is to divide the molecular system into basic units, which behave according to the correlation diagram in fig. 1.3, and into functional groups. Each unit and its IS are treated independently, thereby reducing the dimensionality of the search space compared to the complete molecule. Subsequently, the interconnectivity of the IS of the different units is determined and an initial guess for the seam in the
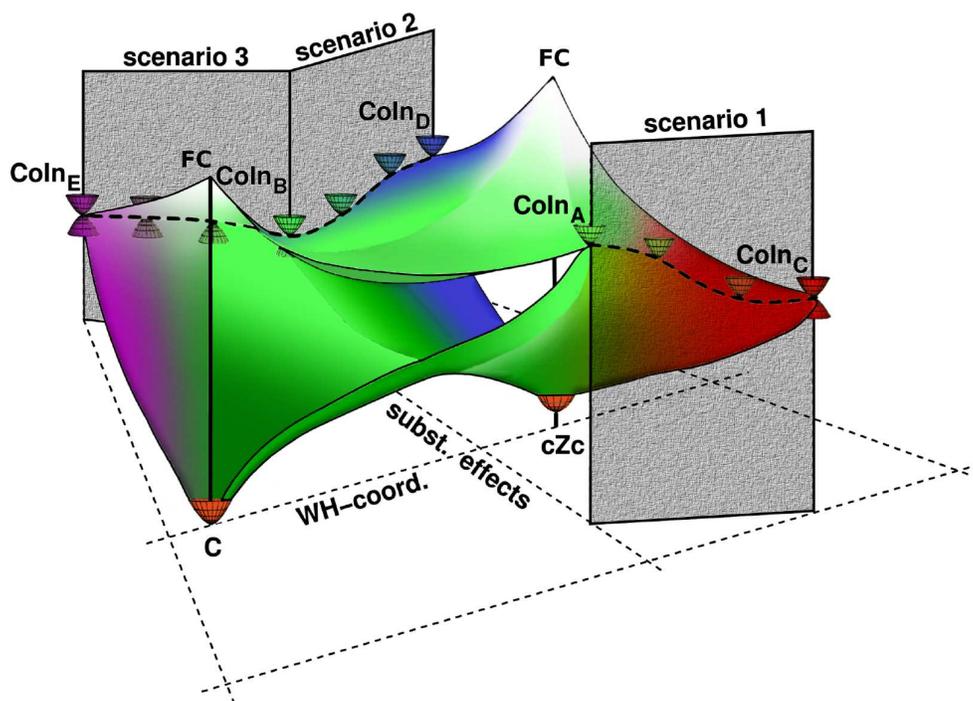
Figure 2.15.: Graphical summary for the electrocyclic photoreaction of trifluoromethyl-pyrrolfulgide. Sketched is the spatial and energetic relation of the reactive and the competing CoIn seams between ES and GS. $CoIn_A$ and $CoIn_B$ mediate the C$\leftrightarrow$cZc isomerization, the associated reactive regions are shown in green. The competing loss channels, leading either back to the reactant or to by-products are mediated by the low-energy seams $CoIn_A$-$CoIn_C$, $CoIn_B$-$CoIn_D$ and $CoIn_B$-$CoIn_E$ (dashed lines). The associated regions are shown in red, blue and magenta, according to the color code introduced in fig. 2.14. Both CoIn seams are reachable from the FC points on the ES.

complete IS is constructed. This guess is then fed into quantum chemistry package to finalize the CoIn optimization. The strategy was demonstrated for three systems, CHD/cZc-HT, HTI and pyrrolylfulgide, revealing a number of low-lying CoIns and extended CoIn seams. Accessible seams promote not only the desired reaction but also formation of by-products or act photostabilizing. These aspects have to be considered in order to design efficient molecular photoswitches. The predictive power of the rules of thumb can be exploited in the process of modeling molecular switches with tailored properties. Proper functionalization can be utilized to selectively stabilize the photoreactive parts of the IS and destabilize concurring channels. This will introduce the required selectivity without sacrifying reaction speed.
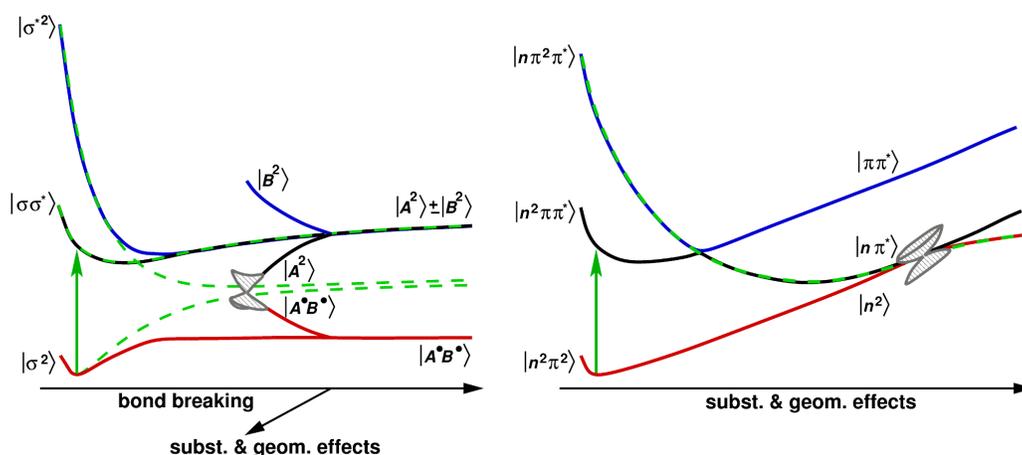
Figure 2.16.: Adiabatic (solid lines) and diabatic (dashed) potential energy curves for the photodissociation of a symmetric σ-bond (left) and for a hole transfer process (right). Electronic configurations are denoted. During photodissociation the *resonance* condition is fulfilled along the bond-breaking coordinate, the *heterosymmetry* condition along an asymmetric distortion. Latter can be introduced through a functionalization or a geometrical deformation. In hole transfer processes both active orbitals are decoupled, thus, the *resonance* condition is fulfilled already at the FC point. Functionalizations and geometrical deformations aim to stabilize the $\left|n\pi^*\right\rangle$-state and to destabilize the $\left|n^2\right\rangle$-state.

2.5.1. Application to photodissociation and hole transfer processes

So far the rules of thumb have been discussed in connection with photochemical isomerization reactions in conjugated polyenes, where the photoreactivity is determined by the interaction of the two active electrons in the highest occupied π and lowest unoccupied π^* orbitals (fig. 1.3). However, the rules have a much more general scope of application, e.g. for photodissociation (fig. 2.16, left) and for hole transfer processes (fig. 2.16, right).

To describe a photodissociation the active space has to be composed of the σ and σ^* orbitals of the dissociating bond. Starting from a symmetric σ-bond (the basic unit) the *resonance* condition is fulfilled along the bond-breaking coordinate (fig. 2.16, left). Along this coordinate the GS aquires a covalent biradical character ($\left|A^\bullet B^\bullet\right\rangle$, with A and B localized at either side of the bond), while the two ionic ES degenerate ($\left|A^2\right\rangle \pm \left|B^2\right\rangle$). To satisfy the *heterosymmetry* condition asymmetric substitutions or geometrical deformations can be introduced.

Hole transfer processes are associated with an electron transfer between two spatially separeated MOs. An examples hereof is the population of a dark $n\pi^*$ state out of a bright $\pi\pi^*$ state (fig. 2.16, right)[55]. Thereby, the n-orbital is centered at a heteroatom somewhere in the system. CoIns between the $n\pi^*$ state and the closed-shell

GS can be understood in the scope of the extended two-electron two-orbital theory by spanning the active space over the π^*-orbital, the n-orbital and the electron lone pair therein. Then, again, a two-electron two-orbital active space can be constructed. Due to the spatial separation of the n- and π^*-orbitals, the *resonance* condition is fulfilled already at the FC point. Then, in the spirit of the two-electron two-orbital theory the n-orbital can be labeled as A and the π^*-orbital as B. The closed shell GS $\left|n^2\right\rangle$ is equivalent to $\left|A^2\right\rangle$, the $\left|n\pi^*\right\rangle$-state to $\left|A^{\bullet}B^{\bullet}\right\rangle$. Note, that in contrast to conjugated polyenes the energetic order of both configurations is reversed. Geometrical (pyramidalization, tilt) and substituent (mesomeric) effects have to be applied to stabilize the $\left|n\pi^*\right\rangle$-state and destabilize the closed-shell $\left|n^2\right\rangle$-state in order to satisfy the *heterosymmetry* condition.

Through the appropriate choice of the active pair of orbitals, not necessarily being the highest occupied and lowest virtual orbitals in the system, it becomes possible to understand and predict CoIns for various types of photoreactions.

2.5.2. Pre-optimization of conical intersections at Hartree-Fock level

The extended two-electron two-orbital theory allows to express the diabatic conditions for CoIn formation via adiabatic quantities, which can be obtained from quantum chemical calculations. It is possible to formulate a CoIn optimization algorithm, based on the *resonance* and *heterosymmetry* conditions (eqs. 2.13 and 2.14). Here an algorithm for locating minimum energy CoIns similar to the projection method by Bearpark and co-workers (sec. 1.2.3) is presented. The general goal is to minimize an effective gradient composed of three terms

$$\vec{g} = \vec{f_1} + \vec{f_2} + \mathbf{P}_{IS}\left(\nabla_R E_1\right) \tag{2.18}$$

The first and the second terms are the scaled gradients with respect to the nuclear coordinates

$$\vec{f_1} = \left|V_1\right| \cdot \frac{\nabla_R V_1}{\left\|\nabla_R \vec{V_1}\right\|} \quad \text{and} \quad \vec{f_2} = \left|V_2\right| \cdot \frac{\nabla_R V_2}{\left\|\nabla_R V_2\right\|} \tag{2.19}$$

of the diabatic quantities

$$
\begin{aligned}
V_1 &= 2h_{AB} + 4\sum_i^n \left\langle Ai\middle|Bi\right\rangle - 2\sum_i^n \left\langle AB\middle|ii\right\rangle \\
V_2 &= J_{AA} - J_{AB} - \varepsilon_B + \varepsilon_A.
\end{aligned} \tag{2.20}
$$

V_1 and V_2 are obtained from eqs. 2.13 and 2.14. Multiplication with the absolute values of V_1 and V_2 assures that the corresponding gradient vanishes at the CoIn. The last term represents the projection of the GS energy gradient onto the orthogonal complement to the BS. This operator acts similarly to the operator used in the projection method (eq. 1.19) with the only difference that the BS is defined by the

vectors $\vec{f_1}$ and $\vec{f_2}$ instead of $\vec{X}_1$ and $\vec{X}_2$.

The presented method locates the lowest point on the GS PES for which the *resonance* and *heterosymmetry* conditions are fulfilled. There is no need of calculating ES properties or non-adiabatic coupling vectors. In principle all quantities can be collected from a HF calculation by working in a localized basis for the HOMO and the LUMO. Of course, as the electronic correlation is not properly described at HF level the obtained geometries can serve only as reference points for a precise CoIn optimization. Nevertheless, this approach can be valuable for a fast pre-computing of CoIns in large molecular systems.

3. Molecular switches

Molecular switches are molecules which can be reversibly transformed between two or more stable forms[73]. Transformation may be induced by variation of temperature, of the pH level, by interaction with electric or magnetic field. Molecules with photochromic properties, i.e. which can switch between stable forms upon interaction with light, are promising candidates for technical applications as molecular switches[158]. Applications in the fileds of biology for studying ultrafast processes in protein folding[4], of medicine for targeted drug delivery[159] and for photoregulation of enzyme activity[160–163], of molecular electronics for developing data storage devices[63, 158, 164, 165], logic gates[166] and optomechanical devices[167, 168] were proposed. For the practical use as photochromic switches molecules have to possess several properties, e. g. designable absorption spectra and solubility, very high environmental and photochemical fatigue resistance, high switching efficiency with respect to the amount of absorbed light, thermal stability and low production costs. A variety of molecular classes, which satisfy the above requirements, azobenzenes[73], diarylethenes[73], spyropyranes[73] to name a few, have been brought up for discussion. In the course of this work HTI, a chromophore designed by linking stilbene and thioindigo, and trifluoromethyl-indolylfulgide, a representative of the fulgide family[73], were investigated. Switches based on the HTI chromophore undergo a *cis-trans* isomerization after irradiation with near-Ultraviolet (UV) light. They are more suitable for in-vivo applications than azobenzenes, which are currently in use despite of their limited stability in cellular environments[169] and the need to use UV radiation to excite their $\pi\pi^*$ transitions. The decisive photochromic properties of fulgides switches rely on the pericyclic ring-opening and ring-closure reaction based on the embedded 1,3-CHD/cZc-hexatriene motif. The closed form absorbs in the visible spectral range and the open form shows absorption exclusively in the UV and blue. Thus, the ring-opening and ring-closure reaction can be selectively initiated with the appropriate wavelength. In a joint experimental-theoretical work the complex photoisomerization mechanisms of both compounds were elucidated by time-resolved spectroscopy and state-of-the-art quantum chemical calculations. Time-resolved absorption spectroscopy was performed at HTI by T. Herzog and T. Cordes. Time-resolved Infrared (IR)-spectroscopy was performed at trifluoromethyl-indolylfulgide by F. O. Koller, W. J. Schreier and I. Pugliesi. Parts of this chapter are published in A. Nenov, T. Cordes, T. T. Herzog, W. Zinth and R. de Vivie-Riedle *J. Phys. Chem. A* **2010**, 114, p. 13016 and A. Nenov, W. J. Schreier, F. O. Koller, M. Braun, R. de Vivie-Riedle, W. Zinth and I. Pugliesi, **2012**, 116, p. 10518.

3.1. Photoisomerization of hemithioindigo-hemistilbene

The molecular system under study, HTI, belongs to a fairly new class of photochromic molecules[170–173]. The molecular structure of HTI (fig. 2.6) is based on two well-known organic compounds, namely thioindigo and stilbene. HTI exists in two different stereoisomers (fig. 2.6, Z and E), which can be interconverted by near-UV and Visible (Vis) light (fig. 3.1). HTI can be regarded as a minimal model for isomerization comprising the following key features: (i) photochromism (see spectra in fig. 3.1); (ii) the possibility of studying the light-induced isomerization with high time-resolution; (iii) composition from two different parent molecules with well-known properties; (iv) the possibility to study the role of heteroatoms in the photoreaction; (v) moderate size, which allows state-of-the-art quantum chemical calculations.
Recently, different experimental studies for differently substituted HTI molecules in
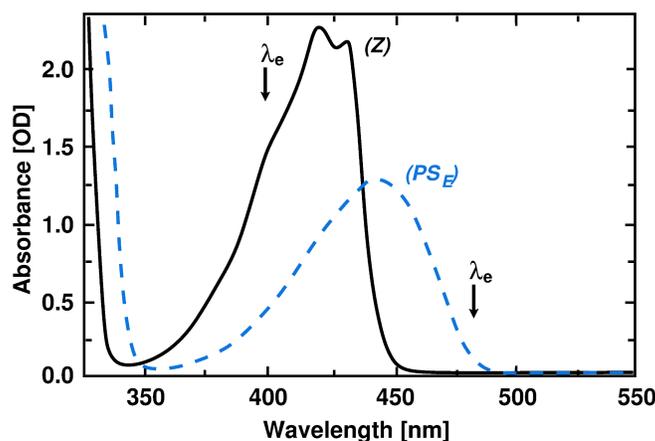
Figure 3.1.: UV/Vis spectra of HTI. The absorption of the Z-isomer (black solid line) and the photostationary state PS_E containing the isomer E at high ($> 70\%$) concentration PS_E (blue dashed line) are shown for the non-polar solvent cyclohexane. The arrows indicate the excitation wavelength λ_e in the time resolved experiments.

polar solvents have been performed and a qualitative picture of both photoreactions Z→E and E→Z have been published[150, 151, 174, 175]. HTI derivatives have been used as ultrafast molecular switches in biomolecules to initiate structural changes at reasonably high quantum efficiencies[150, 175, 176]. Forward and backward processes in HTI showed significant differences in the reaction dynamics, and there is a strong and systematic dependence on substitution[151, 174]. Recently a theoretical study of HTI was published[177]. Surprisingly, the authors reported fluorescence decay as the dominant pathway contrary to the interpretation given in the context of the experimental investigations.
HTI is investigated as a complex prototype for Z/E isomerization providing several

heteroatoms steering the electron flux by their withdrawing and donating charac-
ters. The complexity of experiments and calculations is reduced by focusing on the
photochemistry of the simplest possible HTI compounds without any substituents
in a nonpolar environment, i.e., in cyclohexane. Results are obtained from ultrafast
absorption spectroscopy combined with state-of-the-art quantum chemical methods
(CASSCF/CASPT2 for unsolvated molecules, for details on the quantum-chemical
methods see Appendix I) to answer the following questions: (i) What are the reac-
tion coordinates for the isomerization process? (ii) What is the exact geometric and
electronic structure of the intermediates along the reaction pathway? (iii) What are
the driving forces for isomerization? (iv) Do the heteroatoms influence the choice
between the polar and nonpolar reaction pathways? (v) Why do both isomers, Z and
E, show such a different isomerization speed?

3.1.1. Experimental results: stationary and time-resolved absorption spectroscopy

In order to allow ready comparison with the results from solvent-free theoretical
investigations, the experiments were performed in the nonpolar solvent cyclohexane.

Z→E photoreaction (400 nm excitation). Exciting the Z-isomer with near-
ultraviolet light at 400 nm immediately results in strong absorption changes. In
fig. 3.2a the time dependence of the absorption change is plotted as a function of
time delay between pump and probe pulses for λ_{pr}) 437 and 573 nm. At time zero
there is a strong rise of the absorption at 573 nm. A weak decay on the time scale
of 2 ps is followed by a strong decrease in absorption on the 10 ps time scale. At
437 nm a rise in absorption is found on the time scale of 600 ps. At 573 nm a very
weak absorption decrease is found at late delay times. Absorption spectra taken at
different delay times are shown in fig. 3.2b. They are important for the molecular
interpretation of the observed transients. At early times, one observes the formation
of a broad and structured absorption change throughout the investigated spectral
range (fig. 3.2b, 0.2 ps). The absorbance change is characterized by peaks at 450
and 550 nm, and a minimum at 425 nm. The absorption increase can be assigned
to ES absorption, which is overlapped by negative signal contributions arising from
GS bleaching (centered at 425 nm) and stimulated emission centered at 490 nm.
The spectral positions, from both GS bleaching and stimulated emission, are in good
agreement with stationary spectra of HTI in the nonpolar solvent cyclohexane (fig.
3.1 and refs. [171] and [173]). On the time scale of a few picoseconds minor changes of
the peak positions and the oscillator strength of ES absorption/stimulated emission
can be observed (fig. 3.2b, 0.2 ps vs 2.0 ps). The dominant decay of the induced
absorption signal is seen on the time scale of 10 ps (fig. 3.2b, 2.0 ps vs 12 ps). After
this decay a broad absorption band with a slight maximum at 450 nm and bleaching
at 425 nm can be observed (fig. 3.2b, 25 ps). It is only after hundreds of picoseconds
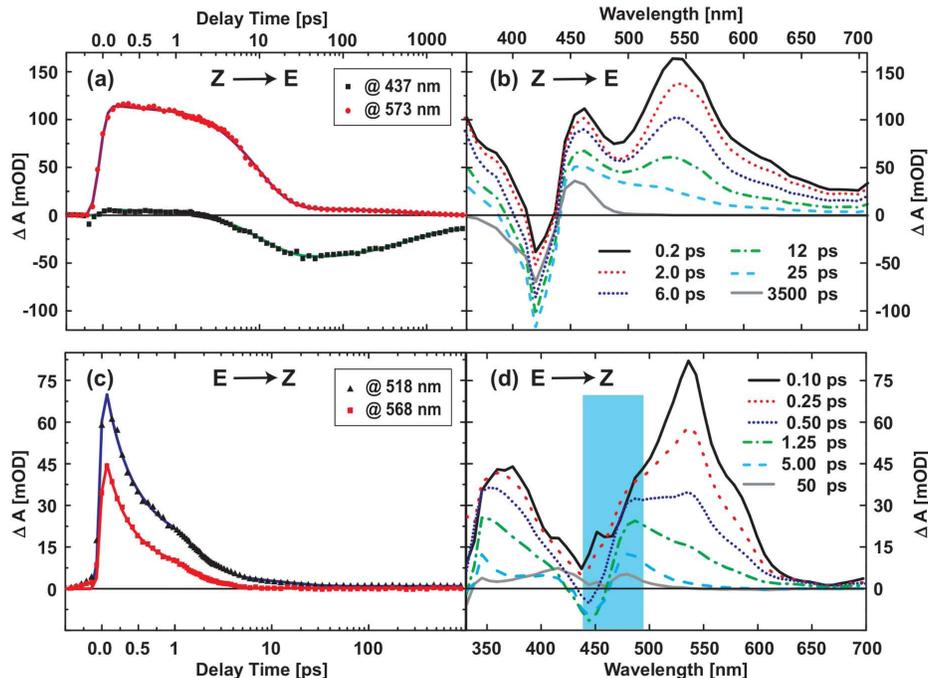
Figure 3.2.: Results from transient absorption spectroscopy. (a and b) Z→E isomerization after 400 nm excitation. (a) Time-dependent absorption change measured as a function of delay time for probing at 437 and 573 nm. (b) Transient spectra at certain delay times between pump and probe pulse. (c and d) E→Z isomerization after 485 nm excitation. (c) Time-dependent absorption change recorded as a function of delay time for probing at 518 and 568 nm. (d) Transient spectra at certain delay times between pump and probe pulse. In the range of probing wavelengths marked in blue the accuracy of the absorption measurement is reduced due to stray light from the excitation pulse.

that most of the remaining induced absorption (>450 nm) decays and reveals the difference spectrum expected from the formation of the E-isomer. Global fitting of the data set by a multiexponential model (using three time constants together with an offset) and the inspection of the transient spectra (see fig. 3.2b) allow interpretation of the data with the scope of recently established reaction models[178]. There is a first kinetic component ($\tau_0 = 2.0 \pm 0.8$ ps) connected with weak absorption changes. The small changes in absorption indicate that this kinetic component may be caused by reactions in the excited electronic state. Interestingly, changes of the stimulated emission during this first reaction are much weaker than the ones observed recently for HTI in more polar solvents such as dichloromethane[151] or methanol[150, 176]. Subsequently, one finds the second kinetic component (time constant of $\tau_1 = 10 \pm 1$ ps) with a much stronger absorption signal representing the decay of the ES and the transition into the GS (of the educt Z-HTI and the product E-HTI). This interpre-

tation is supported by the observed decay of ES absorption and stimulated emission and the appearance of the absorption peak at 450 nm corresponding to the product isomer. At late delay times a very slow component $\tau_2 = 650 \pm 200$ ps is found, which is related to the decay of a broad absorption band extending from 400 to 600 nm and the superimposed recovery of GS bleach at 425 nm. This transition is tentatively assigned to the decay of a short-lived triplet state. The photochemical conversion efficiency $\phi_{pc,Z}$ of the Z→E process was measured in stationary experiments in the weakly polar solvent dichloromethane and was found to be $\phi_{pc,Z} = 0.230 \pm 0.035$. An alternative assignment of the 650 ps kinetic component to the decay of the excited electronic singlet state can be ruled out by the following observations. One finds a very small fluorescence quantum yield of HTI in cyclohexane of $\phi_{fl} = 0.0003$ and a rather long radiative lifetime of $\tau_{rad} = 15$ ns (obtained from the Strickler-Berg relation[179]). As a consequence, the fluorescing excited electronic state should have a livetime τ_{S1} in the range of $\tau_{S1} \approx \tau_{rad} phi_{fl} = 4.5$ ps. This finding gives clear evidence that the slow kinetic component $\tau_2 = 650 \pm 200$ ps is not associated with a (fluorescent) singlet state populated for the major fraction of the molecules.

E→Z photoreaction. The transient absorption changes induced by excitation at 480 nm of the E isomer are shown in fig. 3.2c,d. The time dependence observed at two probing wavelengths (518 and 568 nm, fig. 3.2c) reveals very fast reaction dynamics. This increased reaction speed is also visible in the transient spectra shown in fig. 3.2d. Immediately after excitation there are features from ES absorption and GS bleaching (fig. 3.2d). First absorption transients occur on the 100 fs time scale (see fig. 3.2c) and are followed by a 1 ps process. Subsequently, a weak absorption change is visible on the 10 ps time scale. No indication for a transient in the 100 ps range have been found. A multiexponential modeling of the transients yields time constants of $\tau_0 = 260 \pm 80$ fs, $\tau_1 = 1.2 \pm 0.4$ ps, and $\tau_2 = 13 \pm 6$ ps. With the molecular model proposed for other HTI molecules[178] the 260 fs process is assigned to the initial motion on the excited electronic potential surface, the 1.2 ps transient to the transition from the ES to the GS of educt and product, and the 13 ps process to vibrational cooling of the reformed E isomer. The photochemical yield for Z-product formation was determined in dichloromethane to be only $\phi_{pc,E} = 0.053 \pm 0.016$. In the following sections the combination of the experimental data on the minimal molecular models HTI in an nonpolar solvents with state-of-the-art quantum chemical calculations allows a detailed insight into the pure molecular driving forces for Z/E isomerization.

3.1.2. Theoretical results: reaction pathways in the excited state

Vertical excitation from the ground state isomers. The GS equilibrium structures of both isomers characterize the initial and the final states of the photoreaction and were optimized using density functional theory with the B3LYP hybrid functional[180–182], which has proved to be reliable for GS problems. Both isomers

		SS-CASSCF(14,13)			SS-CASPT2(14,13)			exp.
		$\Delta E_{S_N S_0}$	$\langle S_N|\mu|S_0\rangle$		$\Delta E_{S_1 S_0}$	$\langle S_N|\mu|S_0\rangle$	$\Delta E_{S_1 S_0}$	
		(eV)	(D)	character	(eV)	(D)	character	(eV)
Z	S_1	3.75	0.00	$n\pi^*$	3.48	2.75	$\pi\pi^*$	2.92
	S_2	4.67	2.39	$\pi\pi^*$	3.72	0.00	$n\pi^*$	-
E	S_1	3.57	0.00	$n\pi^*$	3.27	2.44	$\pi\pi^*$	2.76
	S_2	4.39	2.10	$\pi\pi^*$	3.60	0.00	$n\pi^*$	-

Table 3.1.: Vertical excitation energy $\Delta E_{S_N S_0}$, transition dipole moment and ES electronic character at the equilibrium geometries of Z-HTI and E-HTI optimized at B3LYP/6-31G* level. Transition dipole moments obtained from the oscillator strength f, according to $\langle S_1|\mu|S_0\rangle = [3f/2\Delta_{S_0-S_1}^{CASPT2}]$.

were found to be planar, i.e. of C$_S$-symmetry. At SS-CASSCF(14/13) level the lowest excited electronic state corresponds to a $n \rightarrow \pi^*$ excitation from the oxygen lone pair into the aromatic system (tab. 3.1). In C$_S$-symmetry this state has no oscillator strength. Only by symmetry breaking motions some oscillator strength may be borrowed. The second ES is a $\pi \rightarrow \pi^*$ transition with a transition dipole moment of 2.39 Debye for Z-HTI and of 2.10 Debye for E-HTI. The excitation energies for the $\pi \rightarrow \pi^*$ transition of 4.67 eV (Z-isomer) and 4.39 eV (E-isomer) deviate significantly from the experimental values (see absorption spectra in fig. 3.1) with maxima at 2.92 eV and 2.76 eV, respectively. Perturbative correction recovers most of the missing dynamic electron correlation energy of the $\pi\pi^*$ state, which becomes the lowest ES at SS-CASPT2 level with excitation energies corrected to 3.48 eV and 3.27 eV. Comparable calculations at time-dependent density functional theory level confirm this energetic order[177]. However, the shortcomings of time-dependent density functional theory in describing double excitations, as well as the overestimation of charge transfer states, which gain in importance away from the FC region, prevents from its use for the description of the complete ES reaction path. Based on the state order predicted by SS-CASPT2 and on the magnitude of the transition moments the assumtion is made that upon laser irradiation the electron is excited into a S$_1$ state of $\pi\pi^*$ character. Furthermore, the $\pi\pi^*$ and $n\pi^*$ states are very close in the FC region (energy separation ≈ 0.3 eV) and one can speculate on a partial excitation of the $n\pi^*$ state by femtosecond pulses opening reaction channels, which compete to the direct S$_1$-relaxation pathway. Experimental indications are found in the long time constant $\tau_2 = (650 \pm 200)$ ps, tentatively attributed to triplet contributions. Preliminary calculations support the existence of a side channel trapping the molecule in a dark $n\pi^*$ region on S$_1$ from where it can decay via intersystem crossing.

Conical intersection seam. The isomerization of HTI is a typical example of an ultrafast photoreaction proceeding on a picosecond time scale. Its ES decay cannot be explained by means of the avoided crossing model applying Fermi's golden rule[72]. Furthermore, a radiative decay can be excluded as a major decay path to the GS due

to the low fluorescence quantum yield $\phi_{\text{fl}} = 0.0003$) (sec. 3.1.1). It is therefore obvious to assume a CoIn gated decay model that manages to explain both the ultrafast time scale and the suppressed fluorescence.

Using the rules of thumb for predicting and optimizing CoIns presented in sec. 2.2 and 2.3 a number of low-lying minimum energy CoIns could be obtained systematically (sec. 2.4.2). Moreover, several of them could be connected via a low energy CoIn seam (sec. 2.4.3). With the knowledge about the energetic position of the FC points the accessibility of the individual CoIns can now be discussed in more detail. CoIn_{HT}, $\text{CoIn}_{\text{HT}*}$, CoIn_{Et} and $\text{CoIn}_{\text{Et}*}$ lie above the FC limit (tab. 3.2). The strong deformations needed to counteract the mesomeric effect of the carbonyl group render them inaccessible from the FC region. These four CoIn are not further considered.

CoIn_{S}, $\text{CoIn}_{\text{S}*}$, CoIn_{Ac} and CoIn_{CHD} are energetically accessible from the FC point. Of all four, $\text{CoIn}_{\text{S}*}$ is the energetically highest one due to the sterically unfavorable alignment of the hemistilbene and the hemithioindigo moieties. CoIn_{S} lies about 0.5 eV below $\text{CoIn}_{\text{S}*}$. CoIn_{CHD} is the global minimum. The energetic position of CoIn_{Ac} is very sensitive to dynamic correlation effects due to the notable $n\pi^*$ contribution to the ES wavefunction[183]. While SA-CASSCF(10,9) predicts energy in the range of CoIn_{CHD}, at MS-SR-CASPT2(14,13) level CoIn_{Ac} lies in the range of CoIn_{S}. Hence, insufficient description of dynamic correlation effects falsely overestimates the weight of CoIn_{Ac} (and, hence, of the seam region around CoIn_{Ac}, fig. 2.8) in the decay process to the GS.

Perturbative treatment was applied to check the relative energies along the seam
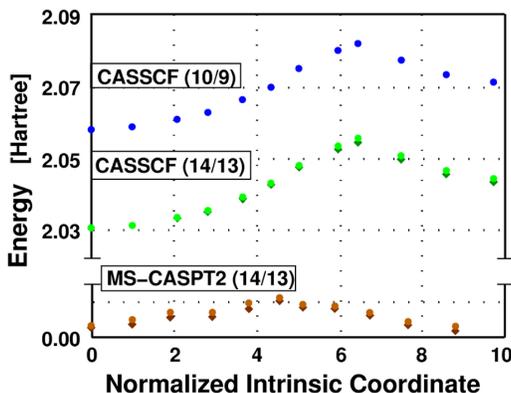
Figure 3.3.: SA-CASSCF(10,9), SA-CASSCF(14/13) and MS-SR-CASPT2(14/13) energies (averaging over two states) for selected points along the CoIn seam between CoIn_{Ac} and CoIn_{S}, plotted against the normalized length of the seam in the full Cartesian space. The blue and the green dots follow the CASSCF seam, the brown dots follow the CASPT2 corrected seam.

between CoIn_{S} and CoIn_{Ac} (fig. 2.8). At MS-SR-CASPT2(14,13) level with averaging over the lowest two states the dynamic correlation lifts the degeneracy up to maximally 0.5 eV. However, a MS-SR-CASPT2(14,13) scan in the pyramidalization/tilt

plane could reduce the energy gap to less than 0.1 eV confirming the existence of a low-lying $CoIn_S/CoIn_{Ac}$ seam also at CASPT2 level. In fig. 3.3 the energetic profile of the seam at different levels of theory is plotted against the normalized length of the intrinsic seam coordinate. Latter was obtained by adding up the absolute distances in space between subsequent points on the seam. Thereby, the absolute distances were rescaled with respect to the normalized distance between $CoIn_{Ac}$ and the next point on the seam. The blue and the green dots in fig. 3.3 follow the seam optimized at SA-CASSCF(10,9) level, the brown dots follow the MS-SR-CASPT2(14/13) corrected geometries. When perturbative correction is applied the region of pure $\pi\pi^*$ character (around $CoIn_S$) is stabilized significantly and the seam flattens. Comparison of the energies of the FC points (tab. 3.2) with the CASPT2 corrected CoIn seam indicates that it is energetically accessible during the photoreaction.

Once the CoIn seam is reached the decay to the GS becomes possible. Information about the GS products, accessible from the tip of the CoIn, can be obtained from a first order Taylor expansion in the BS around a CoIn (sec. 1.2.3). Therefore, a scan was performed on a circular grid around each of the minimum energy CoIns $CoIn_S$, $CoIn_{Ac}$ and $CoIn_{CHD}$. The resulting topologies are presented in fig. 3.4. Optimization from various initial points on the GS PES around $CoIn_S$ led exclusively to Z-HTI. No gradient towards E-HTI emerges directly from the CoIn tip. Both E-HTI and Z-HTI can be formed with equal probability from $CoIn_{Ac}$. Both gradients remain indistinguishable as they are overlapped by a large gradient in the direction of increasing C-S distance. For this reason no preferential formation of either isomer out of $CoIn_{Ac}$ is expected. For the sake of completeness, the possible formation of a metastable byproduct, containing an oxetene ring is noted. However its formation is unlikely due to the tilted form of $CoIn_{Ac}$. The GS PES around $CoIn_{CHD}$ exhibits a pronounced gradient towards E-HTI. The possible formation of a closed-ring chromene derivative introduces a side reaction. The chromene is metastable and relaxes rapidly to E-HTI. No Z-HTI formation is possible from $CoIn_{CHD}$. An important conclusion from the aforementioned analysis is that for neither of the two reactants an exclusive decay to the corresponding product can be observed from the accessible regions of the IS. $CoIn_S$ and $CoIn_{CHD}$ photostabilize Z-HTI and E-HTI, respectively. Neither isomer is preferentially formed out of $CoIn_{Ac}$, in agreement with the measured quantum yields of less than 50%.
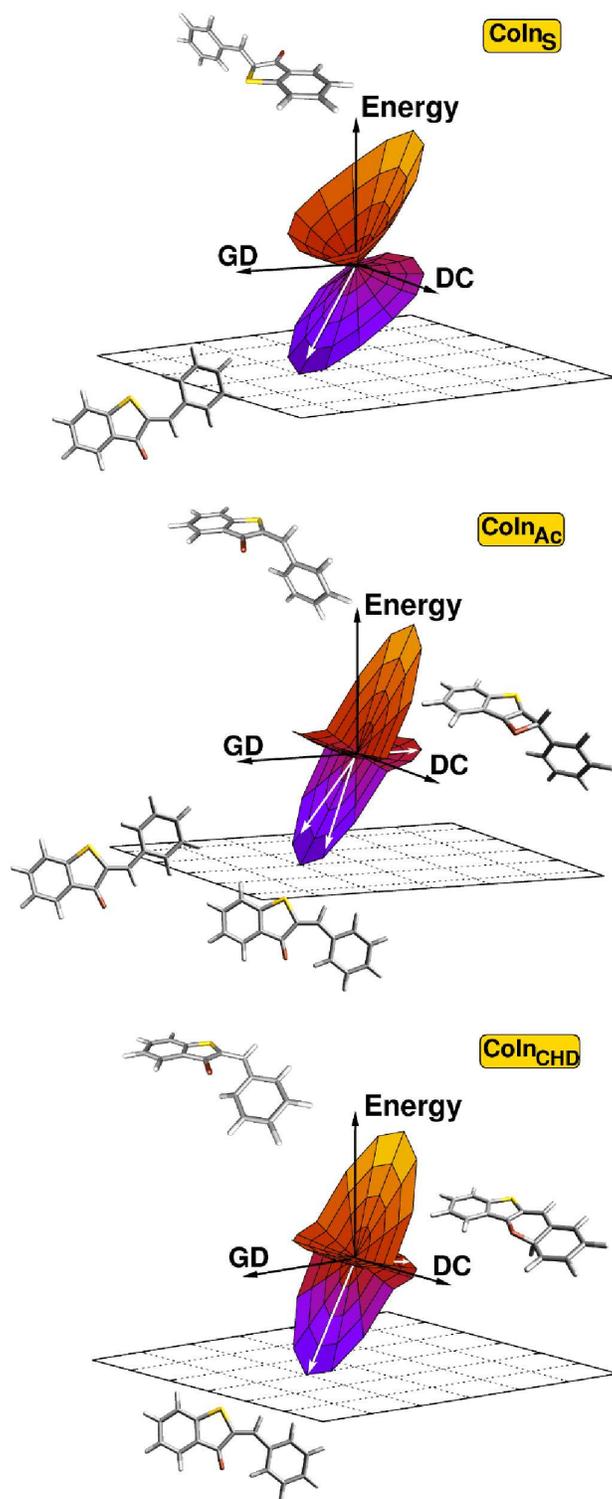
Figure 3.4.: Topologies of CoIn$_S$, CoIn$_{Ac}$ and CoIn$_{CHD}$ together with GS products accessible from the CoIn tip.

structure	SA-2-CASSCF(10,9)			MS-2-CASPT2(14,13)			reactive coordinantes				dipole moments	
	Δ_{S_0} (eV)	Δ_{S_1} (eV)	$\Delta_{S_0-S_1}$ (eV)	Δ_{S_0} (eV)	Δ_{S_1} (eV)	$\Delta_{S_0-S_1}$ (eV)	C=C (Å)	torsion (°)	pyramid. (°)	tilt (°)	$\langle S_1\vert\mu\vert S_0\rangle$ (D)	$\langle S_1\vert\mu\vert S_1\rangle$ (D)
FC$_Z$	0.00	0.00	4.79	0.00	0.00	3.59	1.35	0.0	0.0	-	2.75	6.23
FC$_{Z^*}$	0.36	-0.41	4.02	0.50	0.04	3.13	1.41	0.0	0.0	-	1.88	7.30
Min$_{S1Z}$	0.70	-0.43	3.65	0.78	0.02	2.84	1.42	29.4	13.1	-	1.76	6.84
TS$_{S1Z}$	1.15	-0.43	3.19	1.21	0.04	2.42	1.44	43.0	21.3	-	1.87	6.03
CoIn$_S$	3.80	-0.99	0.00	3.44	-0.15	0.49	1.44	90.0	64.0[1]	18.6[2]	-	5.76
CoIn$_{S^*}$	4.58	-0.49	0.00	3.83	0.24	0.31	1.45	90.0	-59.0[1]	21.7[2]	-	4.26
CoIn$_{Ac}$	3.07	-1.71	0.00	3.37	-0.22	0.03	1.48	90.0	0.6[1]	-19.1[2]	-	1.49
CoIn$_{CHD}$	3.03	-1.75	0.00	2.93	-0.66	0.48	1.44	154.9	3.0[1]	-	-	1.50
CoIn$_{HT}$	5.16	0.37	0.00	5.13	1.53	0.07	1.46	90.0	59.6[3]	23.3[4]	-	2.27
CoIn$_{HT^*}$	5.60	0.81	0.00	5.15	1.56	0.21	1.44	90.0	-57.0[3]	19.4[4]	-	3.61
CoIn$_{Et}$	4.52	-0.27	0.00	4.86	1.26	0.06	1.39	90.0	54.1[3]	-28.0[4]	-	3.62
CoIn$_{Et^*}$	4.60	-0.19	0.00	4.96	1.36	0.04	1.39	90.0	-52.5[3]	-28.5[4]	-	4.85
TS$_{S1E}$	1.36	-0.36	3.00	1.39	0.03	2.24	1.45	136.4	-15.4	-	2.13	4.02
Min$_{S1E}$	0.61	-0.44	3.74	0.70	0.01	2.91	1.42	180.0	0.0	-	1.69	7.44
FC$_E$	0.24	-0.03	4.51	0.22	-0.03	3.34	1.36	180.0	0.0	-	2.37	6.30

[a] Pyramidalization defined for C$_3$.
[b] Tilt defined for C$_4$.
[c] Pyramidalization defined for C$_4$.
[d] Tilt defined for C$_3$.

Table 3.2.: Relative GS and ES energies Δ_{S_0} and Δ_{S_1}, vertical energy gap $\Delta_{S_0-S_1}$ at SA-CASSCF(10,9) and MS-SR-CASPT2(14,13) level (averaging over two states), selected coordinates, transition and ES permanent dipole moments for all points of interest in the HTI system. Optimization was done at SA-CASSCF(10,9) level. The energy of the GS equilibrium geometry Z-HTI is used as reference for Δ_{S_0}. The energy of the FC point of Z-HTI is used as reference for Δ_{S_1}. Transition dipole moments obtained from $\langle S_1\vert\mu\vert S_0\rangle = [3f/2\Delta_{S_0-S_1}^{CASPT2}]$.

Figure 3.5.: Reactive coordinates for the Z-HTI/E-HTI isomerization. (left) Out-of-plane torsion in the range [0°:360°]; (middle) Pyramidalization (shown for a torsional angle of 90°) in the range [-90°:90°]; (right) Tilt (shown for a torsional angle of 90°and pyramidalization of 60°) in the range [-90°:90°].

Relaxed scan on the excited state potential energy surface. The reactive coordinates, suited to describe the relaxation from the FC point to the energetically reachable degeneracy region, are torsion, pyramidalization and tilt (fig. 3.5). Naturally, these coordinates fufill the *resonance* (torsion) and *heterosymmetry* (pyramidalization, tilt) conditions for CoIn formation derived in sec. 2.2[1].

The torsion constitutes the main reaction coordinate, facilitating the isomerization. The pyramidalization and the tilt gain in significance as the CoIn seam is approached. Due to the heteroatoms involved in the CoIns along the seam (sec. 2.4.2) the tilt deformation is less pronounced (fig. 2.8 and tab. 3.2). Therefore, torsion and pyramidalization were chosen for a relaxed scan to obtain preliminary information about potential relaxation channels from the FC region to the seam. The scan was performed at SA-CASSCF(10,9)/6-31G level. The obtained PES, shown in fig. 3.6, is solely of qualitative nature as the fairly small basis set 6-31G has been used and dynamic correlation effects were not considered. Another issue was the construction of the active space. CASSCF favors the $n\pi^*$ state compared to the $\pi\pi^*$ state, which leads to an inverted energetic order in the FC-region (tab. 3.2) and prevents a balanced description at CASSCF level. However, non-negligible contributions from the $n\pi^*$-configuration are responsible for the stabilization of CoIn$_{Ac}$. They make the inclusion of the oxygen lone pair in the active space necessary in the vicinity of the seam. In principle the unbalanced description of the electron correlation could be remedied by CASPT2. However, this is not affordable for a two-dimensional scan. A consistent picture of the PES can be obtained on CASSCF level by excluding the oxygen lone pair from the active space and afterwards rescaling the energy of the region around CoIn$_{Ac}$ to reflect the energetic position obtained at CASPT2 level (tab. 3.2). Selected geometries on the two-dimensional PES were re-optimized at SS-CASSCF(10,9)/6-31G* level to assess the quality of the scan.

Z→E potential energy surface. Optimization on the $\pi\pi^*$ state induces bond length

---

[1]For details on their construction in HTI see Appendix G
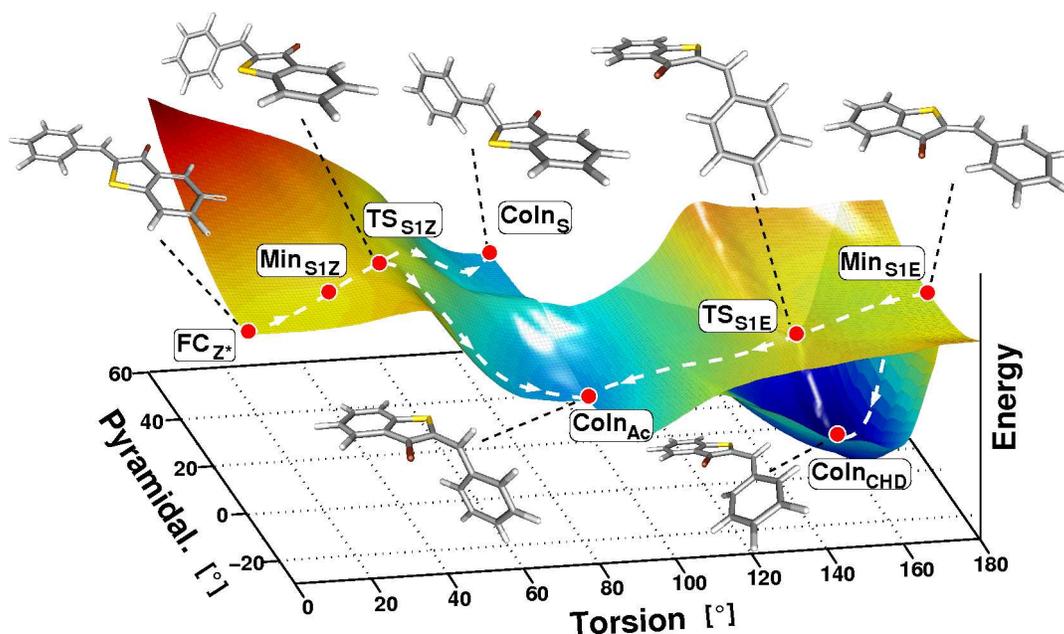
Figure 3.6.: ES PES for the Z↔E reaction obtained from a two-dimensional relaxed scan in the region 0°and 180° torsion and between −30°and 60°pyramidalization. Two surfaces arise on the E-HTI side between 110° and 170° torsion for different residual deformations. The upper surface is optimized starting at the FC point, the lower surface starting at CoIn$_{CHD}$. Approximate ES reaction pathways are derived from the topography of the PES (dashed white lines).

rearrangements which drive the system out of the FC region (FC$_{Z^*}$, 0° torsion, 0° pyramidalization). Thereby, the central C-C double bond is elongated in response to the partial promotion of electron density into the π^*-orbital. The relaxed scan suggests the existence of a local minimum in the region around 20° torsion and 20° pyramidalization. Unconstrained optimization yields a local minimum at 29.4° torsion and 13.1° pyramidalization (Min$_{S1Z}$, see tab. 3.2). It turns out, that pyramidalization is initiated immediately after the FC point is left. Next, a transition state search was carried out in the region around 40° torsion and 20° pyramidalization. The transition state (TS$_{S1Z}$) is shifted with respect to Min$_{S1Z}$ to larger torsion (43.0°) and pyramidalization angles (21.3°). TS$_{S1Z}$ is characterized by an imaginary frequency of -43.73 cm^{-1}, whose eigenvector activates the tilt and drives the system towards CoIn$_S$. The barrier height is calculated to be less than 1.0 kJ/mol at CASSCF level and about 1.5 kJ/mol at CASPT2 level. The two-dimensional scan reveals a second possibility to reach the seam in the surrounding of CoIn$_{Ac}$ by backward pyramidalization after TS$_{S1Z}$ is passed. Hence, two main relaxation pathways towards the seam are postulated (denoted by white arrow in fig. 3.6).

E→Z potential energy surface. Optimization on the $\pi\pi^*$ state induces bond length rearrangements which drive the system out of the FC region. The 180° torsion/0°

pyramidalization point coincides with a local minimum on the E-HTI side (Min_{S1E}). The relaxed scan suggests a preferable initial pyramidalization of opposite sign as compared to the Z→E isomerization. Correspondingly, this deformation is expected to lead towards $\text{CoIn}_{\text{S*}}$, while CoIn_{S} is inaccessible from the E-HTI side. However, due to the unfavorable alignment of the hemithioindigo and hemistilbene moieties at $\text{CoIn}_{\text{S*}}$ this CoIn is destabilized notably (tab. 3.2). Its formation is possible, but seems highly unlikely. Hence, the relaxation channel through $\text{CoIn}_{\text{S*}}$ was discarted and the two-dimensional scan was restricted to the interval between -30° – 30° pyramidalization, revealing a relaxation pathway towards CoIn_{Ac} (upper white arrow in fig. 3.6).

In sec. 2.2 it was discussed that E-HTI contains a cyclizable C_5O moiety which can undergo an electrocyclic ring-closure. If CoIn_{CHD}, the CoIn associated with the cyclization, is taken as starting point for performing a relaxed two-dimenisonal scan in the torsion/pyramidalization plane a broad energetically low lying valley (lower surface in fig. 3.6) is found to characterize the S_1 PES. The existence of multiple solutions to the constrained optimization problem implies that further coordinates (here an electrocyclic ring-closure coordinate) are necessary for the unique construction of the E→Z surface. Nevertheless, even in the reduced coordinate space of fig. 3.6 it is obvious that already at 10° torsion a rapid relaxation to the region around CoIn_{CHD} is feasible. This channel is associated with a low ES barrier, which renders it easily accessible from the FC point (lower white arrow in fig. 3.6).

3.1.3. Connecting theory and experiment

The results provided from experiment and theory demonstrate that the *cis-trans* isomerization of HTI conceals a complex reaction mechanism, offering several decay channels through an extended, low lying, accessible CoIn seam. As a schematic representation fig. 3.7 shows the energetic profile of the ES reaction pathways. The out-of-plane torsion as the main reaction coordinate is displayed in the transparent plane connecting Z and E. The most left and right segments of that plane visualize the effect of bond length rearrangement in the planar structures. The elongation of the central carbon-carbon bond was found to give the major initial energetic stabilization. The diagonal light-gray plane, crossing the torsional plane at 90°, combines pyramidalization and tilt for a constant torsional angle of 90° [2] and contains a projection of the CoIn seam connecting CoIn_{S} and $\text{CoIn}_{\text{S*}}$ via CoIn_{Ac} (red dashed line). Based on the arguments derived for the optimized seam segment $\text{CoIn}_{\text{S}}/\text{CoIn}_{\text{Ac}}$ (positive pyramidalization, fig. 2.8), the seam can be readily extrapolated to the region of $\text{CoIn}_{\text{S*}}$ (negative pyramidalization). This extension is expected to lie energetically high due to the unfavorable orientation of the fragments. In support of this speculation an intermediate geometry on the seam $\text{CoIn}_{\text{S*/Ac}}$, which is the analogue to $\text{CoIn}_{\text{S/Ac}}$, was optimized. It was found to lie energetically above the E-HTI FC point.

---

[2]The tilt/pyramidalization plane lies orthogonal to the torsional plane. For a comprehensible visualization, both planes were drawn at an angle of 45°.
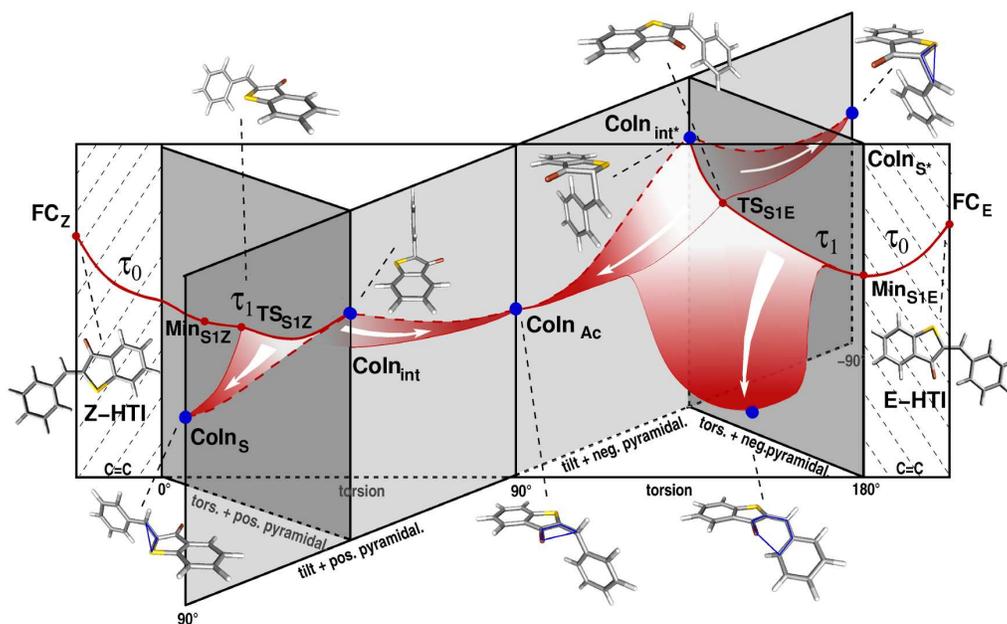
Figure 3.7.: Schematic representation of the reaction pathways on the ES PES. The out-of-plane torsion is symbolized by a transparent plane connecting Z and E. The shaded planes sketch the effect of bond length rearrangement within the planar geometries. The diagonal light-gray plane combines pyramidalization and tilt for a constant torsional angle of 90° and contains a projection of the CoIn seam connecting CoIn$_S$ and CoIn$_{S*}$ via CoIn$_{Ac}$ (red dashed line). Both dark-gray surfaces connecting the torsional plane and the CoIn$_S$/CoIn$_{S*}$ seam plane symbolize modes of contrariwise pyramidalization and torsion.

Evolution from the FC regions of Z-HTI and E-HTI is driven by pyramidalization and torsion of opposite sign (see fig. 3.6). This is indicated by the two dark-gray surfaces connecting the torsional plane to the seam plane.

The Z→E reaction . After excitation of the Z-isomer the initial S$_1$-relaxation is dominated by rapid bond length rearrangement, mainly of the central C-C double bond, accompanied by solvent adjustment to the altered electron density distribution. Both processes contribute to the experimental signal. The reaction then proceeds in a flat region of the ES where gradual redistribution of the energy into torsion and pyramidalization drives the molecule into the local minimum Min$_{S1Z}$. Evidence for the existence of such a local minimum is provided by the detected weak fluorescence. As the $\pi\pi^*$ and the dark $n\pi^*$ states (tab. 3.1) in the FC region are nearly of the same energy, an additional relaxation pathway via a singlet ($n\pi^*$)-triplet ($\pi\pi^*$)-singlet (π^2) cascade is assumed. Both pathways contribute to the reaction rate k$_0$ = 1/τ_0 with τ_0 = (2.0 ± 0.8) ps, observed experimentally. From the absorption changes in the
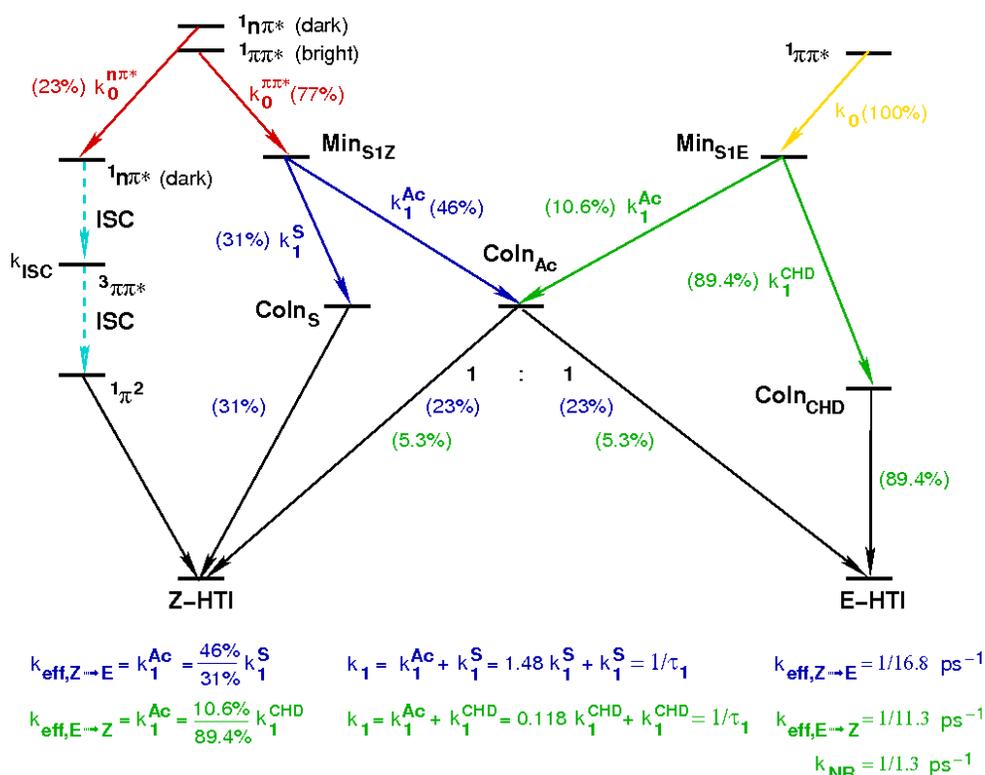
Figure 3.8.: Rate model illustrating the photochemical behavior of HTI, based on the experimental data (time constants, rates) and quantum-chemically extracted decay pathways, including the non-reactive and the possible triplet channels. The color code distinguishes between processes associated with the different rate constants: processes contributing to the rate constant $k_0 = 1/\tau_0$ are marked in red (Z→E) and yellow (E→Z), processes contributing to the rate constant $k_1 = 1/\tau_1$ are marked in blue (Z→E) and green (E→Z). The triplet-singlet-triplet cascade responsible for the long time constant $\tau_2 = (650 \pm 250)$ ps on the Z-HTI side is colored in cyan. The distribution in the individual channels is estimated from the quantum yields $\phi_{\text{pc,Z/E}}$ and ϕ_{isc}. The rate constant k_1^{Ac} of the decay towards the reactive CoIn$_{\text{Ac}}$ is assigned to the effective reaction rate constants for the Z→E ($k_{\text{eff,E→Z}}$) and E→Z ($k_{\text{eff,Z→E}}$) isomerization. The rate constant k_1^{CHD} of the decay towards CoIn$_{\text{CHD}}$ is assigned to the non-reactive rate constant k_{NR}.

range of the GS band at 425 nm the yield ϕ_{isc} of triplet formation is estimated in the order of the isomerization yield $\phi_{\text{pc,Z}}$, i.e. $\phi_{\text{isc}} \approx 23\%$. This value is deduced from the observation that the amplitude of the bleach recovery and the final offset spectrum at 435 nm (representing the photochemical conversion Z to E) are similar. Consequently, approximately 77% of the molecules proceed along the singlet pathway.

The second time constant $\tau_1 = (10 \pm 1)$ ps is attributed to the overcoming of the

shallow ES barrier and relaxing towards the seam. Two main relaxation channels contributing to the overall rate $k_1 = 1/\tau_1$ were identified, a reactive channel mediated by $CoIn_{Ac}$ and a photostabilizing channel via $CoIn_S$. Dynamic simulations are indispensable for recovering the population of the individual channels. Without this information the experimental quantum yields are used to estimate the distribution and reconstruct the time constants of the individual relaxation processes (fig. 3.8). Thereby, following assumptions are made: a) deactivation pathways through the regions around the reactive $CoIn_{Ac}$ and the photostabilizing $CoIn_S$ are each described by one effective time constant giving the collective decay in this region; b) a 1:1 bifurcation in the GS is assumed for the reactive seam segment around $CoIn_{Ac}$, i.e. the exact topology of the seam and effects coming from momentum conservation are neglected; c) the region in the vicinity of $CoIn_S$ is completely non-reactive, i.e. an insurmountable GS barrier towards E-HTI is assumed; d) deactivation through fluorescence is neglected. With the estimated population of the siglet state of 77% and the quantum yield for the Z→E isomerization $\phi_{pc,Z} \approx 23\%$ the population distribution into the reactive and non-reactive channel is estimated to be 46%(reactive):31%(nonreactive). Based on these considerations the effective reaction rate $k_{eff,Z \to E}$ from Min_{S1Z} to the E-isomer can be estimated to be $k_{eff,Z \to E} = 1/(16.8 \pm 1.6)$ ps^{-1} (fig. 3.8).

The E→Z reaction . The initial relaxation process from the FC point of E-HTI is comparable to the one on the Z-side and leads to the planar minimum Min_{S1E}. There are no experimental indications of possible triplet contributions, i.e. 100% of the molecules proceed via the singlet relaxation pathway. During the first several hundred femtoseconds ($\tau_0 = (260 \pm 80)$ ps) only bond relaxation takes place. Two pathways emerge from Min_{S1E}. One proceeds primarily along the torsion coordinate towards $CoIn_{Ac}$. A second one, involving the electrocyclic ring-closure of the C_5O fragment, opens the valley to $CoIn_{CHD}$. The first pathway is the photoreactive pathway and is mechanistically comparable to the one discussed for the Z→E isomerization. Applying the assumptions outlined above and considering that no Z-HTI can be formed after relaxation through $CoIn_{CHD}$ the time constants of the individual relaxation processes are reconstructed (fig. 3.8). Taking again the low quantum yield of $\phi_{pc,E} \approx 5.3\%$ as a basis only 10.6% of all molecules follow this path. The remaining 89.4% evolve along the second pathway, the rapid non-reactive deactivation via $CoIn_{CHD}$. With the specific values for τ_1 the effective reaction rate $k_{eff,E \to Z}$ for Z-HTI formation from Min_{S1E} can be determined $k_{eff,E \to Z} = 1/(11.3 \pm 3.7)$ ps^{-1} (fig. 3.8). This value which is close to the one obtained for the reactive segment of the Z→E reaction and is much slower than the direct non-reactive decay rate $k_{NR} \approx 1/(1.3 \pm 0.4)$ ps^{-1} via $CoIn_{CHD}$ (fig. 3.8). The observed high rate of the non-reactive decay is explained well by the calculations. The two-dimensional scan scan reveals that E-HTI can relax into the $CoIn_{CHD}$ valley already at 10° torsion. The substantial differences observed for the Z→E and E→Z reactions for time constants and quantum yields can be explained by the existence of an efficient photostabilizing channel accessible only from E-HTI and not to differences in the isomerization mechanism itself.

3.1.4. Summary: charge transfer formation and charge balance recovery mediated by heteroatoms drive the isomerization
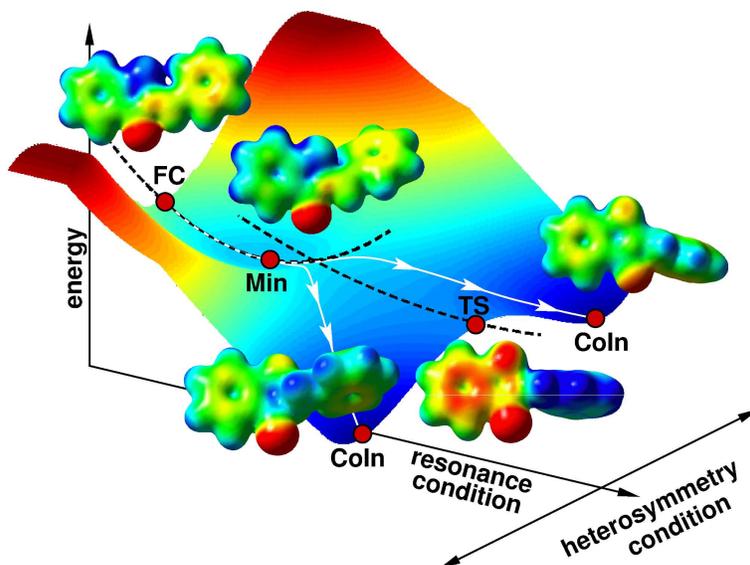
Figure 3.9.: Idealized ES PES segment from FC_Z to the CoIn seam with electrostatic potentials for selected points. The electrostatic potentials were projected on the 0.01 electron bohr^{-3} isodensity surface. Regions with high proton affinity show in red, regions with low proton affinity show in blue. For optimal contrast ratio a minimum value of -0.05 a.u. and a maximum value of 0.15 a.u. were used. The charge transfer state formed with increasing torsion cannot be stabilized in the gas-phase and becomes a transition state on the ES.

The driving force for the isomerization is the flux of electron density in the π-system of HTI. Upon excitation density is transfered from the lone pair of the sulfur into the π-system of hemistilbene (fig. 3.9, FC). This process weakens the cental double bond and activates torsion. The isomerization is initiated. With ongoing torsion a continous decoupling of both sub-units is observed until the delocalization of the π-orbitals breaks down (fig. 3.9, transition state). At the twisted geometry the carbonyl group causes the stabilization of a charge transfer state with the frontier electrons localized at the hemithioindigo. Yet, in gas-phase and unpolar solvents the charge transfer geometry is unstable and is not formed. Additional deformations, which lead to the CoIn seam (fig. 3.9, CoIn), restore charge balance. The CoIns transfer back electron density to the hemistilbene via the lone pairs of the heteroatoms. Therefore, in gas-phase and in unpolar solvents $CoIn_S$ and $CoIn_{Ac}$ coincide with local minima on the ES, i.e. the CoIn seam crosses the ES MEP and allows for a fast relaxation to the GS. The picture is expected to change when polar solvents come into play.

In summary, the electron density flux is governed by the heteroatoms. They initiate charge transfer at the FC, thereby facilitating the isomerization, and restore charge

neutrality at the seam. Their presence opens new possibilities to stabilize the reaction pathway by adjustment of the electrostatic interactions. On one hand, this new diversity comes at the expense of additional loss channels. In the presented model such a loss channel opens on the side of E-HTI and acts as a very efficient trap. On the other hand, the new diversity allows for fast photochemical switching, even in bulky systems such as HTI. Slow skeletal deformations are replaced by fast charge redistributions using substituent effects in heterocycles.

3.2. Photoisomeriaztion of trifluoromethyl-indolylfulgide
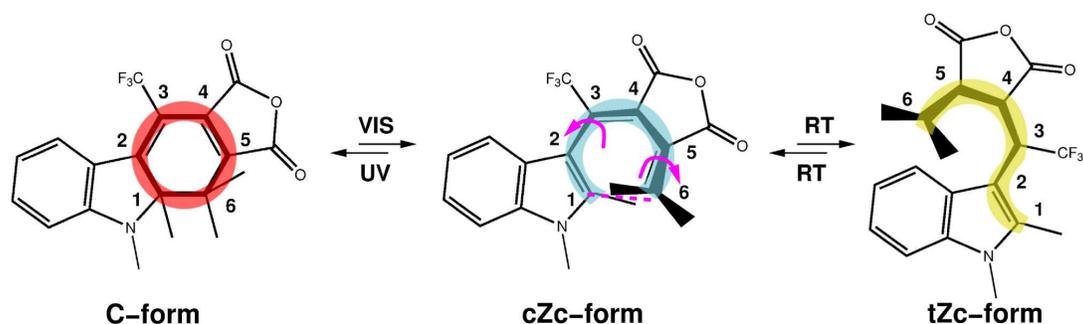
Figure 3.10.: Isomers of the trifluoromethyl-indolylfulgide. Notation refers to the configuration of the 1,3-CHD/HT central unit, C denotes closed-, Z open-ring configuration. In the open-ring structures c = *cis* and t = *trans* describe the orientation of the functional groups with respect to the single bonds C_2-C_3 in the hexatriene unit. Coordinates relevant for the subsequent discussion are denoted: the C_1-C_6 distance and the torsion angles around the C_2-C_3 and around the C_5-C_6 bond.

The molecular system under study, trifluoromethyl-indolylfulgide, belongs to the class of fulgides[73]. It exists in one closed-ring form denoted as C-form in fig. 3.10 and several open-ring forms. Figure 3.10 shows the Z-form (with respect to the orientation of the functional groups to double bond C_3-C_4), which exists in two stable conformers, denoted as cZc- and tZc-form, indicating the different orientation of the functional groups with respect to the single bond C_2-C_3 in the hexatriene subunit (c = *cis*, t = *trans*). Illumination with visible light (fig. 3.11) induces the electrocyclic ring-opening of the C-form. Only the cZc-form is cyclizable, the electrocyclic ring-closure is initiated by UV light (fig. 3.11). Further non-cyclizable open-ring conformers (e.g. cEc, tEc, not shown) are accessible from the Z-form. The isomerization from and into the E-form is not addressed the present study as the Z/E ratio in every photostationary state was found to be less than 2%[184].

The ultrafast kinetics of ring-opening and closure have been investigated with
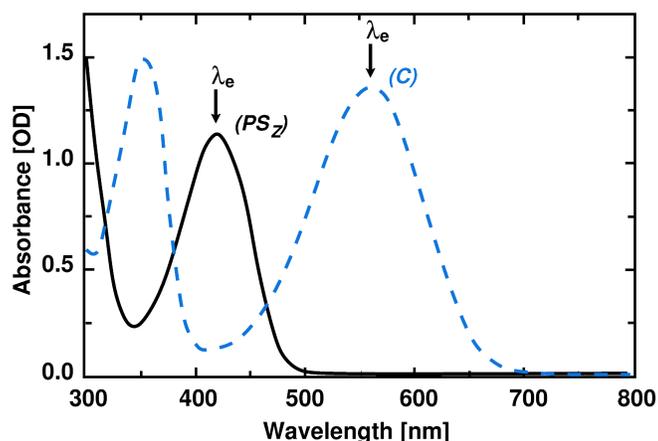
Figure 3.11.: UV/Vis spectra of trifluoromethyl-indolylfulgide. The absorption of the C-isomer (blue, dashed) and the photostationary state PS_Z (black, solid) containing a mixture of the cZc- and tZc-isomers) are shown for the non-polar solvent 1,4-dioxane. The arrows indicate the excitation wavelength λ_e in the time resolved experiments.

UV/Vis transient absorption experiments and time-resolved fluorescence studies[152, 153, 185–200]. In the indolylfulgides and related indolylfulgimides the ring-opening occurs with a reaction time in the range between 2 and 20 ps and a quantum efficiency between 0.1% and 50% depending on sample temperature[152, 196–198, 200]. The ring-closure proceeds on a sub-picosecond time scale (0.2-0.5 ps) with quantum yields between 10% and 17% and is not influenced by thermal or optical excess energy[153, 199]. These experiments performed in the UV/Vis range have given important information. However, questions on the detailed molecular reaction mechanism could not be answered. Time-resolved spectroscopy in the mid-IR as complementary probe for structural and vibrational dynamics can fill this gap. First time resolved IR-probe experiments on indolylfulgimides in the groundstates have been carried out by Braun and co-workers[63, 201, 202].

In this work the dynamics of both the ring-opening and the ring-closure reaction of trifluoromethyl-substituted indolylfulgide, dissolved in tetrachloroethylene, is explored by means of time resolved UV/Vis-pump IR-probe spectroscopy, characterizing the reaction in the excited and in the ground state. The sensitivity of this spectroscopic technique towards structural and vibrational dynamics will allow to investigate the interactions of the functional groups with the photochromic core. A comparison to the previously studied indolylfulgimides will aid the design of photochromic switches with tailored properties like high quantum yields[125, 126, 193]. State-of-the-art ab inito quantum chemical calculations (for details on the quantum-chemical methods see Appendix J) resolve the missing structural resolution at the atomic level and permit the interpretation of the observed time constants in terms of electronic and structural changes.

3.2.1. Photoinduced dynamics probed in the IR

Time-resolved infrared difference spectra for the ring-opening and ring-closure reactions were recorded between 1200 cm^{-1} to 1900 cm^{-1}. For the interpretation the region of the carbonyl-modes between 1650 cm^{-1} and 1875 cm^{-1} shown in fig. 3.12 is analyzed closely. The contour plots (fig. 3.12b,e) provide a two-dimensional representation of the experimental data. Negative absorption changes are marked in blue, positive absorption changes are indicated in red. In support of the spectral interpretation, the IR steady state absorption spectra of the isomerically pure samples of C and Z isomers are shown (gray area in fig. 3.12c,f) together with transient spectra at selected pump-probe delays.

For both the ring-opening (fig. 3.12, left) and the ring-closure (fig. 3.12, right)
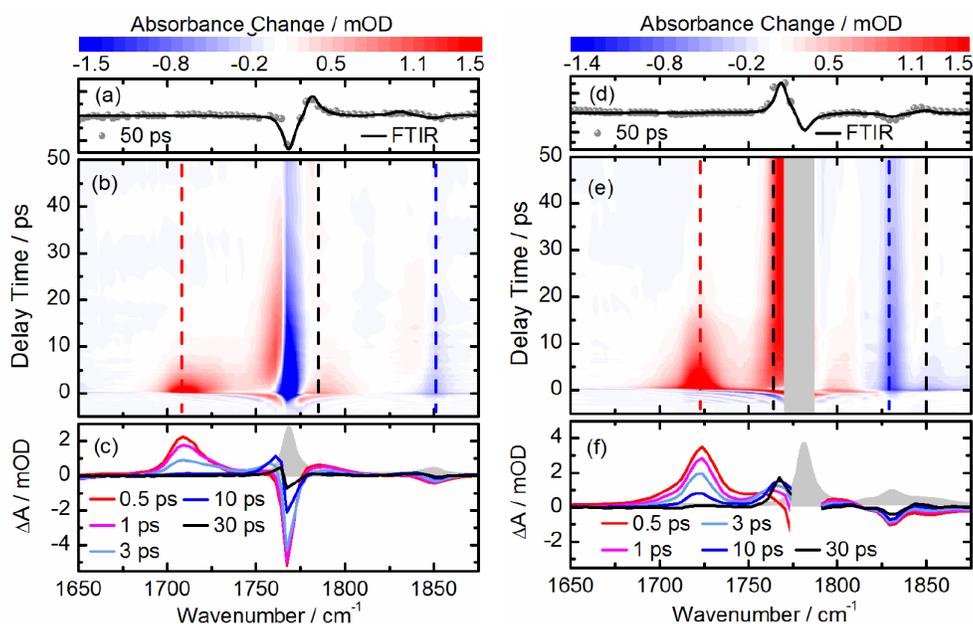
Figure 3.12.: Time resolved IR data for the C→Z reaction (left) and the Z→C reaction (right). a) and d) Comparison of the difference spectra obtained in a steady state experiment (solid black line) with the transient spectra after 50 ps (gray circles). b) and e) Contour plot representation of the data. Dashed lines indicate the frequency position of transients shown in fig. 3.13. c) and f) Transient spectra at the indicated delay times. The GS absorption spectrum is given as gray area for comparison. Due to technical reasons the expected bleach signal around 1781 cm^{-1} could not be recorded

GS bleach signals of the initial isomers are overlaid with excitation induced absorption bands. The most prominent features can be observed in the range of the CO stretching vibrations between 1700 cm^{-1} and 1850 cm^{-1} (asymmetric and symmetric CO stretch). Excitation induced absorption bands appear to both sides of the CO

stretch bleach signals and indicate that the photoinduced reaction is associated with a substantial change in bond character of the CO groups on the maleic anhydride. Although a complex temporal evolution of the transient signals is observed, relevant time-scales of the C→Z and Z→C reactions can be identified. For both, the ring-opening and the ring-closure reaction, transient spectra recorded at a delay time of 50 ps agree well with the scaled steady-state difference spectra of the isomerically pure C and Z isomers (fig. 3.12a,d) For delay times larger than 50 ps the signals remain constant (data not shown). Thus, both the C→Z ring opening and the Z→C ring-closure reactions are completed within 50 ps. At early delay times, before and around time-zero up to $\approx$ 0.4 ps, the dominant signal contributions are due to perturbed free induction decay and cross-phase modulation[203, 204]. Furthermore, the solvent tetrachloroethylene shows signal contributions up to 0.4 ps. Thus, the time range containing information exclusively on the dynamics of the ring-opening and ring-closure reaction lies between 0.4 and 50 ps. The observed absorption changes can be classified into three groups according to their spectral signature: (i) recovery and cooling of reactant GS (blue dashed lines in fig. 3.12b,e), (ii) decay of singlet ES (red dashed lines in fig. 3.12b,e) (iii) formation and cooling of product states (black dashed lines in fig. 3.12b,e).

  (i) In the transient data one finds instantaneous bleaching that recovers on a time scale of 20 ps. Bands of this category can be found at 1768 cm^{-1} and 1851 cm^{-1} for the ring-opening and at 1829 cm^{-1} for the ring-closure reaction. The expected bleaching signal around 1781 cm^{-1} for the ring-closure reaction could not be recorded due to technical reasons. All bands correspond to the GS absorption of the carbonyl stretching vibrations. The bleach recovery is accompanied by an induced absorption on the lower frequency side, which undergoes a blue-shift of several wavenumbers. This signature includes ES relaxation and hot GS formation[205, 206].

 (ii) Positive, instantaneous absorption changes decay predominantly on the 0.5 to 10 ps time scale. Bands of this category can be found around 1708 cm^{-1} and 1785 cm^{-1} for the ring-opening reaction and at 1723 cm^{-1} and 1800 cm^{-1} for the ring-closure reaction. These bands are assigned to the asymmetric and symmetric carbonyl vibrations of the electronically ES.

(iii) The characteristic changes for product formation following the decay of the ES absorption bands (ii) can be clearly observed at 1785 cm^{-1} and 1831 cm^{-1} for ring-opening and at 1764 cm^{-1} and 1850 cm^{-1} for the ring opening reaction. They show a delayed rise combined with a decay on the 10 to 20 ps time scale to match the offset value found in the steady state difference spectra (solid line in fig. 3.12a,d).

A global analysis of the transient data using exponential functions shows that both the ring-opening and the ring-closure reactions proceed with a complex temporal evolution in the ps range with deviations from simple exponential behavior. It has to be

ν (cm^{-1})	τ_1 (ps)	τ_2 (ps)	τ_3 (ps)
1851 (i)	2.9	17	∞
1785 (iii)	2.6	—	∞
1708 (ii)	2.9	—	∞

Table 3.3.: Time constants and amplitudes of the ring-opening reaction. Data have been analysed by a sum of exponential functions convoluted with the instrumental response function. The Roman numbers in brackets refer to the category assignment described in the text

ν (cm^{-1})	τ_1 (ps)	τ_2 (ps)	τ_3 (ps)	τ_4 (ps)
1850 (iii)	0.7	11	—	∞
1829 (i)	0.5	—	24	∞
1764 (iii)	0.5	3.9	24	∞
1723 (ii)	0.8	7.8	—	∞
1555	0.5	—	23	∞

Table 3.4.: Time constants and amplitudes of the ring-closure reaction. Data have been analysed by a sum of exponential functions convoluted with the instrumental response function. The Roman numbers in brackets refer to the category assignment described in the text

noted that the decay associated difference spectra derived from a global fit using a sum of exponential functions partly compensate each other to mimic band shifts and thus have to be interpreted with care. These deviations are due to cooling of vibrationally hot molecules[205]. The transient traces of different spectral positions representative for GS recovery, ES decay and product formation are depicted in figs. 3.13 and 3.14. Fits on the data at single selected probing wavelength using a sum of exponentials are given as solid black lines. The resulting time constants are summarized in tabs. 3.3 and 3.4.

Ring-opening (C→Z) kinetics Time transients are given in fig. 3.13. At the position of the GS absorption at 1851 cm^{-1} instantaneous bleaching is observed (i). The recovery of the bleach signals can be described by two time constants of 2.9 ps and 17 ps (blue). At 1708 cm^{-1} the decay of the ES can be followed (ii). The decay can be described by a single time constant of 2.9 ps (red). Product formation is observed at 1785 cm^{-1} together with the decay of the ES absorption (iii). The kinetics are well reproduced by one time constants of 2.6 ps (black).
From the experimental data the following picture for the ring-opening reaction is obtained. The initially ES decays with about 3 ps. With this time constant recovery of the reactant GS via internal conversion and product formation is observed. Cooling of the hot reactant molecules to the solvent surrounding occurs within 10-20 ps.
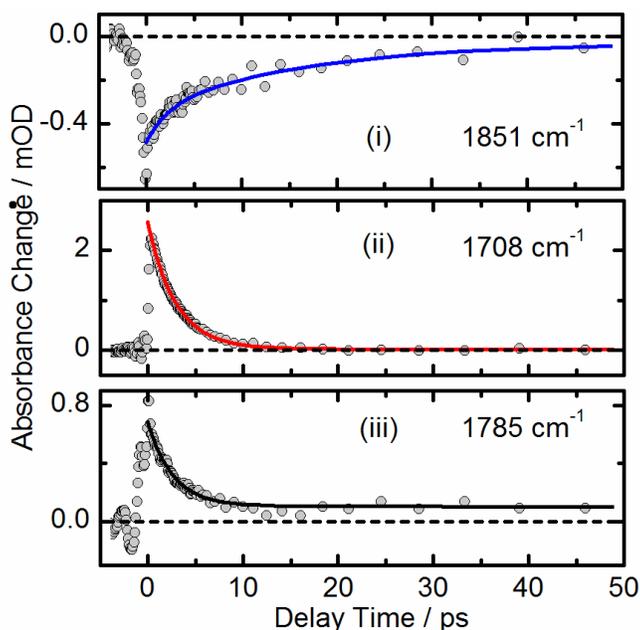
Figure 3.13.: Transient data for the C→Z reaction at the indicated frequencies. Fits on the data are given as solid lines with the color matching the respective category of the underlying molecular process. The resulting time constants are summarized in table 3.3.

These findings are in line with recent UV/Vis transient absorption experiments in cyclohexane, where a time constant of 2.2 ps was found for the ES decay and the cooling was associated with a 7 ps time constant[196].

Ring-closure (Z→C) kinetics   Time traces are shown in fig. 3.14. The GS bleach recovery at 1829 cm^{-1} (i) can be described by a fast 0.5 ps and a slower 24 ps time constant (blue). At around 1723 cm^{-1} one finds a spectrally broad induced absorption that can be assigned to the singlet ES (ii). In contrast to the ring-opening reaction the kinetics of the ES decay cannot be described mono-exponentially. A good representation of the decay can be obtained by using two time constants of about 1 ps and 8 ps (red). Similar time constants are observed for the time trace at 1850 cm^{-1} which represents product formation together with GS recovery of the reactant (iii). The product band at 1764 cm^{-1} (iii) can be modeled using three time constants of 0.5 ps, 4 ps and 24 ps (black). Here the transient behavior is partly overlaid by signals due to cooling of neighboring GS absorption bands.

The data can be interpreted with the following reaction scheme. After photoexcitation a decay of the ES on a sub-picosecond and on a 10 ps time scale is observed. Additionally, vibrational cooling of hot reactant GS molecules occurs within 30 ps. These findings are comparable to the ring-closure dynamics observed in the UV/Vis transient absorption experiments of ref. [199]. The appearance of the product state,
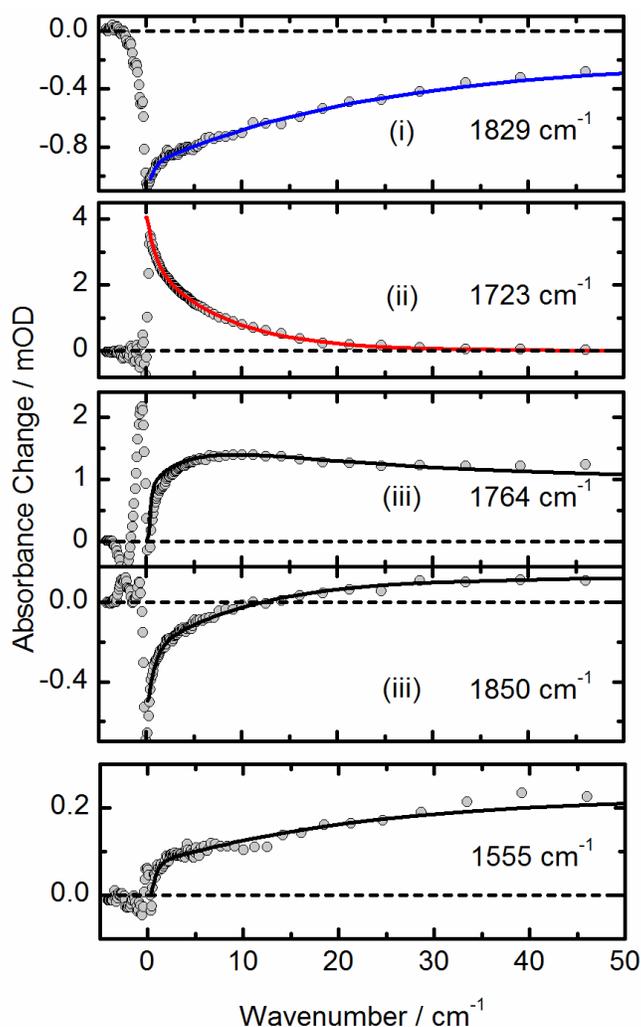
Figure 3.14.: Transient data for the the Z→C reaction at the indicated frequencies. Fits on the data are given as solid lines with the color matching the respective category of the underlying molecular process. The resulting time constants are summarized in Table 3.4.

observable at 1764 cm^{-1} and 1850 cm^{-1}, cannot be clearly assigned to either the 0.5 or 10 ps time constant if only these bands are taken into account. To resolve this ambiguity the product band at 1555 cm^{-1} (outside the spectral range of fig. 3.12e) can be used. This band does not overlap with the spectral signatures of the reactant and can be described by a fast 0.5 ps and a slower 24 ps time constant, confirming product formation with the 0.5 ps time constant and subsequent cooling of the hot product within 24 ps. The 10 ps time constant observed at other frequencies cannot be clearly assigned to either of these processes. It will be discussed below in sec. 3.2.3.

Quantum yields   The quantum yield η of the photo-reaction was determined by comparing the maximum bleach amplitudes with the remaining absorption losses at delay times later than 50 ps. For the C→Z ring opening reaction it is estimated to $\eta = 10\%$, while for the Z→C ring closure reaction $\eta = 20\%$, in good agreement with steady state measurements in the visible spectral range[152, 199].

3.2.2. Structural, electronic and vibrational analysis from ab-initio calculations and vibrational spectra

The complex temporal evolution of the transient spectral signatures of the two C→Z and Z→C together with the moderate quantum yields are a strong indication that after excitation the fulgide evolves along a complex ES PES with different competing pathways. To obtain a mechanistic insight into the nature of the ES and the structural deformations involved in the ultrafast dynamics, ab initio quantum chemical calculations have been carried out together with a vibrational analysis of the GS and first singlet ES.

Ground state geometries   Three stable GS isomers are relevant for the subsequent discussion of the ES dynamics, the closed-ring C-form and two open-ring forms tZc and cZc (see fig. 3.10). The C-form is planar, with a completely delocalized π-system. The open-ring isomers are nearly isoenergetic and lie 0.26 eV higher than the C-form. Torsion around the C2-C3 single bond (63.5° and 120.5° for cZc and tZc, respectively, table 3.5) weakens the conjugation in the Ï-system. As a consequence the π-orbitals localize either at the indole or at the anhydride. Only the cZc-form is photochemically cyclizable.

Due to the sterical interactions of the methyl groups at C_1 and C_6 the C↔cZc electrocyclic reaction proceeds in the GS via a conrotatory motion, contrary to the WH rules[95, 96]. The resulting high activation barrier (C↔cZc: 1.95 eV, cZc↔C: 1.86 eV) makes thermal isomerization practically impossible at room temperature. As the cZc↔tZc isomerization proceedes along a single bond torsion (fig. 3.10) the barrier associated therewith is only 0.33 eV. Using the Eyring formula

$$k = \frac{k_B T}{h} e^{-\frac{\Delta G}{RT}}, \tag{3.1}$$

with k_B, h and R the Boltzmann, Planck and ideal gas constants and ΔG the Gibbs free activation energy an isomerization rate constant $k = 107$ s^{-1} is estimated, corresponding to an isomerization time of several tens of ns. Thus, at room temperature both open-ring forms exist in a thermal equilibrium. Their ratio is estimated using Boltzmann distribution

$$\frac{P_{\text{cZc}}}{P_{\text{tZc}}} = e^{-\frac{\Delta G}{k_B T}} \tag{3.2}$$

to 60%(cZc):40%(tZc). When the pump pulse is applied to a thermal equilibrium of a cZc/tZc mixture only 60% of all open-ring fulgides are in a cyclizable form.

Excited state geometries   The lowest excited electronic singlet states of C, cZc and tZc are of $\pi\pi^*$-character. The transition is spectroscopically allowed, with an oscillator strength of approximately 0.10. The theoretically predicted excitation energies ($\Delta E_{S_1 S_0}$ in tab. 3.5) are in a fair agreement with the experimentally determined absorption maxima of 2.20 eV (C-form) and 2.98 eV (Z-form)[199]. The overestimation of the blue shift by approximately 0.65 eV is attributed to the limited basis set and the omission of solvent effects in the gas-phase calculations. The ES permanent dipole moments are larger by a factor of 2 compared to the GS dipole moments. The solvent tetrachloroethylene is expected to lower the excitation energy. The bathochromic shift of the closed-ring isomer absorption is attributed to the intact π-system. Both open-ring isomers absorb at the same wavelength, which renders them spectroscopically indistinguishable.

Optimization on the spectroscopically accessible first ES from the C-form converges to a local minimum (Min$_C$) lying approx. 0.5 eV below the FC point (ΔE_{S_1} in tab. 3.5). It is reachable solely by bond length rearrangements (partial double bond/single bond inversion) in the aromatic system. Noticeable is the asymmetric change of the $C_{4/5}$-$C_{(=O)}$ bond lengths in the anhydride, as well as the re-hybridization of the nitrogen from sp^3 to sp^2 (tab. 3.5).

Optimization on the spectroscopically accessible first ES from the open-ring cZc- and tZc-forms yields local minima (Min$_{cZc}$ and Min$_{tZc}$) with more pronounced structural changes and a stabilization of 0.5-0.6 eV with respect to the associated FC points (ΔE_{S_1} in tab. 3.5). Bond rearrangements in the π-system are now accompanied by torsion around the C_2-C_3 bond (fig. 3.10). For cZc the torsional angle increases by approx 10° to 74°, while for tZc it decreases by approx. 15° to 106°. The vertical energy gaps at Min$_{cZc}$ and Min$_{tZc}$ ($\Delta E_{S_1 S_0}$ in tab. 3.5) indicate that the fluorescence bands overlap.

Remarkably, the ES gradient accelerates the cyclizable cZc-form towards increasing torsion around the C_2-C_3 bond, and, thus, towards further ring-opening, rather than along the ring closure coordinate. However, this gradient is very sensitive to the angle between the indole and the anhydride. Starting from a slightly less twisted initial geometry a barrierless pathway along the ring-closure coordinate towards a low-lying CoIn CoIn$_{C/cZc}$ is encountered, which facilitates fast radiationless decay to the GS. Its geometry is shown in fig. 3.17, top.

	MS-3-CASPT2(14,13)		coordinates							dipole moments	
	ΔE_{S_1} (eV)	$\Delta E_{S_1S_0}$ (eV)	C_1-C_6 (Å)	$\angle_{C_2=C_3}$ (°)	$\angle_{C_5=C_6}$ (°)	C_4-$C=O$ (Å)	C_5-$C=O$ (Å)	N-C_1 (Å)	N-C_{C-C_2} (Å)	$\langle S_1|\mu|S_0\rangle$ (D)	$\langle S_1|\mu|S_1\rangle$ (D)
FC_C	0.00	2.86	1.60	1.0	58.0	1.49	1.49	1.46	1.40	3.51	12.08
FC_{cZc}	1.30	3.64	3.70	63.5	7.0	1.51	1.49	1.37	1.38	2.52	17.23
FC_{tZc}	1.25	3.61	4.22	120.5	172.0	1.51	1.49	1.37	1.38	2.72	17.85
Min_C	-0.51	1.96	1.63	13.0	53.5	1.50	1.44	1.46	1.31	5.67	14.62
Min_{cZc}	0.68	2.44	3.90	74.0	19.5	1.47	1.49	1.32	1.40	2.62	17.17
Min_{tZc}	0.72	2.48	4.07	106.0	164.5	1.47	1.49	1.32	1.40	2.35	17.98
$Coln_{C/cZc}$	-0.59	0.00	2.03	41.5	46.0	1.50	1.43	1.41	1.33	-	16.26
$Coln_{cZc/tZc}$	-0.14	0.00	3.20	89.0	88.0	1.50	1.45	1.34	1.40	-	16.39
$Coln_C$	-0.44	0.00	1.76	69.0	70.0	1.50	1.45	1.44	1.32	-	17.11

Table 3.5.: Relative stabilization on the ES ΔE_{S_1} in eV, vertical energy gap $\Delta E_{S_1S_0}$ between GS and ES in eV, relevant coordinates, ES permanent and transition dipole moments for all relevant geometries. Optimization was done at SA-CASSCF(14,13) level with averaging over three states. Perturbative treatment (i.e. MS-SR-CASPT2(14,13) with averaging over three states) was performed at the optimized geometries. The energy of FC_C is used as reference for ΔE_{S_1}.
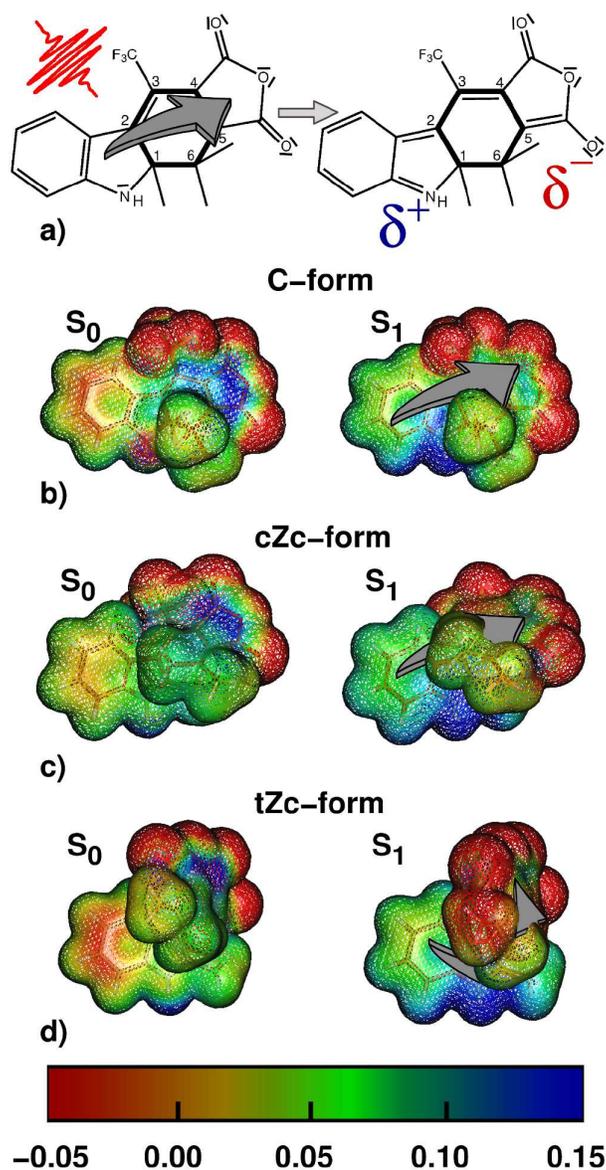
Figure 3.15.: a) Schematic representation of the electronic charge transfer from the indole to the anhydride induced upon photoexcitation and the change in the conjugation pattern associated with the charge transfer. b) - d) Electrostatic potentials (range [-0.05:0.15] a.u.) on a density isosurface with a value of 0.003 electron/bohr^3 for the GS (left column) and ES (right column) equilibrium geometries of C, cZc and tZc. Negative potentials with high electron density are given in red. Positive potentials with low electron density are given in blue.

Excited state charge transfer and vibrational spectra Recently, it has been shown[50] that the formation of CoIns is driven by charge transfer. In the present case the first ES has a partial charge transfer character already in the FC-region. A

comparison of the electrostatic potentials of the GS equilibrium geometries to the potentials of the ES intermediates (fig. 3.15) demonstrates this charge transfer from the indole to the anhydride. Remarkably, the asymmetric shortening of the $C_{4/5}$-$C_{(=O)}$ and N-C bonds (table 3.5), identified as an essential prerequisite for CoIn formation (sec. 2.4.4), is initiated simultaneously. Thus, the system feels an ES gradient towards the CoIns already in the FC-region. The calculated electrostatic potentials (fig. 3.15) indicate that the carbonyl groups are suitable markers to track charge fluctuation, as the IR-bands associated with CO stretching vibrations are well separated from the remaining signal. The increase of the charge density in the carbonyl bonds upon excitation will induce a bathochromic shift in the IR-signal of the ES intermediates, an indicator for the charge transfer formation. To verify the charge transfer character in the FC-region of the closed-ring and open-ring isomers, ES vibrational spectra, extracted from the transient data and calculated with quantum chemical methods, were compared against each other and to the steady-state spectra of the GS.

The extraction of ES vibrational spectra from the transient absorption data follows a procedure similar to that described in ref. [207]. The analysis of the temporal evolution of the absorption changes (sec. 3.2.1) shows that the transient signal at early delay times (about 0.5 ps) consists predominantly of the negative GS bleach and the induced ES absorption of the reactant. Signal contributions from (hot) product molecules can be neglected. The sum of the transient absorption spectrum at 0.5 ps and the scaled steady-state GS absorption spectrum was calculated to remove the contributions from the GS bleach and to reconstruct the IR-spectrum. Furthermore, it was verified that the obtained absorption bands show a transient decay behavior with time constants of the ES lifetimes (group (ii) signals, sec. 3.2.1). Seven absorption bands could be identified for the excited C-form (1785, 1708, 1440, 1390, 1340, 1265, 1195 cm^{-1}) and the cZc/tZc-mixture (1800, 1723, 1515, 1470, 1385, 1245, 1195 cm^{-1}), respectively. The spectral positions and intensities were determined by a fit to a sum of Lorentzians with a width of 5 cm^{-1}. The results are shown in fig. 3.16c and d as black traces.

CASSCF normal mode analysis were carried out for the GS and ES minima of C, cZc and tZc isomers and the calculated intensities were convoluted with Lorentzians with again a width of 5 cm^{-1}. The spectra are shown in fig. 3.16 as colored traces. Normal modes in the region from 1150 cm^{-1} to 1950 cm^{-1} are provided in the supplementary information. The peaks at 1708 cm^{-1}, 1785 cm^{-1}, 1723 cm^{-1} and 1800 cm^{-1} can be confidently assigned to the symmetric and antisymmetric CO stretching modes of the closed- and open-ring forms in the ES, respectively. Both the scaled calculated spectra and the experimental data show the bathochromic shift of the CO bands caused by the charge transfer. The shift is indicated by the colored areas in fig. 3.16. An unambiguous assignment of the remaining peaks is not possible due to the high density of modes in the spectral region between 1200 cm^{-1} and 1400 cm^{-1}, however, some general features can be identified. Stretching vibrations of bonds, having a double bond character in the GS are red-shifted from 1450-1550 cm^{-1} to 1250-1450 cm^{-1} due to double bond / single bond rearrangement (bathochromic shift in tab. 3.6). Stretching vibrations of bonds that have acquired partial double bond character
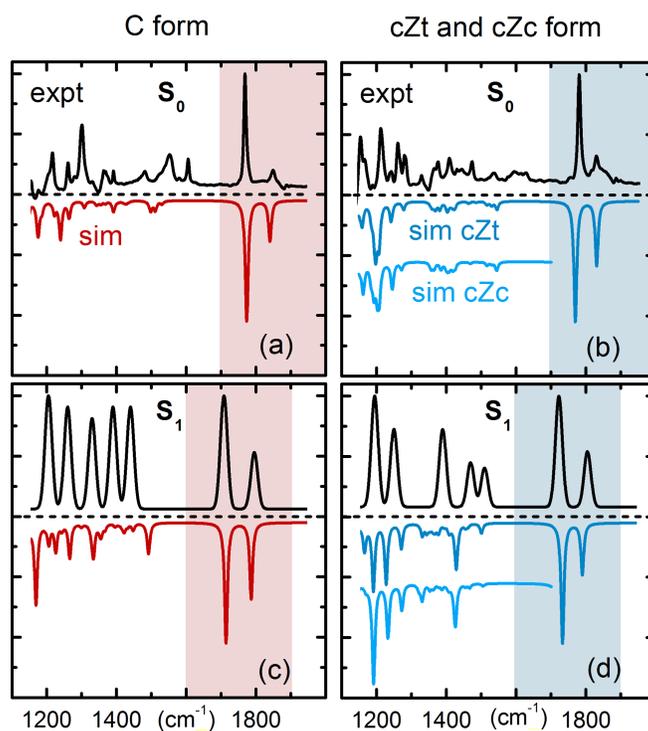
Figure 3.16.: Comparison between experimentally obtained and calculated GS and ES vibrational spectra for the C-form (a,c) and the cZc/tZc-forms (b,d). Experimental ES spectra (c,d) are extracted from the transient absorption data at 0.5 ps delay time according to a procedure similar to that described in [207] (black traces). Theoretical spectra are obtained from a frequency analysis at the local minima in the ES Min_C, Min_{cZc} and Min_{tZc} (color traces). Calculations were performed at SS-CASSCF(14/13) level with a scaling factor of 0.86.

exhibit a blue shift (hypsochromic shift in tab. 3.6). The red and blue shifts are again a consequence of the charge transfer. Similar vibrational bands are observed in the measured ES vibrational spectra.

Conical intersections   To obtain first information about potentially accessible products from the CoIn, a two dimensional scan around $CoIn_{C/cZc}$ in the branching plane was performed (fig. 3.17)[208, 209]. Following the gradient in the GS revealed that $CoIn_{C/cZc}$ facilitates the electrocyclic isomerization in both directions. In fact $CoIn_{C/cZc}$ is a point on an extended low-energy ES/GS degeneracy region, known as CoIn seam. The location and analysis of this seam is of vital importance for deciphering the ultrafast dynamics of fulgides. In sec. 2.4.4 a low-lying CoIn seam, spreading from the closed-ring to the open-ring side, was reported for the related compound trifluoromethyl-pyrrolylfulgide. Although the indole was replaced by a pyrrole, this substitution does not influence the topography of the seam, as it is determined by the

spectral shift	C-form			
	S_0	bond	S_1	bond
bathochromic	1840	CO(s)	1785	CO(s)
	1773	CO(a)	1713	CO(a)
	1530	C_2-C_3,C_4-C_5 (s)	1448	C_4-C_5
	1497	C_2-C_3,C_4-C_5 (a)	1266	C_2-C_3
	1488	indole	1355	indole
hypsochromic	1308	C_3-C_4	1329	C_3-C_4

spectral shift	cZc-form			
	S_0	bond	S_1	bond
bathochromic	1832	CO(s)	1790	CO(s)
	1770	CO(a)	1731	CO(a)
	1544	C_5-C_6	1330	C_5-C_6
	1516	C_3-C_4	1426	C_3-C_4
	1495/1469	indole,C_1-C_2	1321	C_1-C_2
hypsochromic	1208	C_4-C_5,C_5-$C_{=O}$	1232	C_4-C_5,C_5-$C_{=O}$

spectral shift	tZc-form			
	S_0	bond	S_1	bond
bathochromic	1831	CO(s)	1787	CO(s)
	1770	CO(a)	1730	CO(a)
	1546	C_5-C_6	1344	C_5-C_6
	1517	C_3-C_4	1428	C_3-C_4
	1486/1465	indole,C_1-C_2	1330	C_1-C_2
hypsochromic	1207	C_4-C_5,C_5-$C_{=O}$	1227	C_4-C_5,C_5-$C_{=O}$

Table 3.6.: Assignment of bands in the calculated ES IR-spectra to bands of the GS IR-spectra for C-, cZc- and tZc-fulgide. Bonds from the aromatic system with significant contributions to the normal mode associated with each band are listed. Bands are sorted according to their spectral shift.

interactions of the 1,3-CHD/cZc-HT core with the anhydride group and the nitrogen lone pair (see sec. 2.3). Correspondingly, the results from the pyrrolylfulgide seam can be used to locate critical geometries for the indolylfulgide. $\text{CoIn}_{C/cZc}$ is the counterpart of CoIn_B in the indolylfulgide system (tab. 2.4). Next, the role of the seam is elucidated by focusing on the energetic and structural characteristics of two further CoIns from the indolylfulgide seam, one in the closed-ring region (the counterpart to CoIn_E in the pyrrolylfulgide system, tab. 2.4) and one in the open-ring region (the

counterpart to $CoIn_D$ in the pyrrolylfulgide system, tab. 2.4).

  $CoIn_C$ (fig. 3.17, middle) is characterized by a pronounced twist of the C_2-C_3 bond and an initiated cleavage of the C_1-C_6 σ-bond (1.79 Å, tab. 3.5). Its geometry can be rationalized with the rules of thumb derived in sec. 2.2. It is an example of a strongly polar ethylene derivative[61] (C_2-C_3 fragment) functionalized with an electron withdrawing (anhydride) and an electron donating (nitrogen lone pair) group. As for other strongly polar ethylene derivatives degeneracy with the GS is reached only for a significantly large torsional angle. The structure and gradients indicate that $CoIn_C$ does not mediate the electrocyclic reaction between the C- and the cZc-form. Indeed, even though the C_1-C_6 σ-bond is elongated by 0.16 Åcompared to the GS closed-ring geometry, a scan in the branching plane reveals that $CoIn_C$ permits a barrierless relaxation only to the C-form (fig. 3.17, middle).

A similar constellation is found at the open-ring side, where $CoIn_{cZc/tZc}$ could be located (gig. 3.17, bottom). It also exhibits a pronounced twist of the C_2-C_3 bond, this time accompanied by a complete cleavage of the C_1-C_6 σ-bond (3.01 Å, tab. 3.5). Another structural feature of $CoIn_{cZc/tZc}$ is the large twist of the C_5-C_6 bond. This structure can be rationalized as a weakly polar ethylene derivative (C_5-C_6 fragment) with an electron withdrawing carbonyl group conjugated to C_5. The nitrogen lone pair is structurally decoupled and not conjugated to the ethylene fragment. The insufficient ES stabilization via functionalization requires additional geometrical deformations to reach a CoIn lie the shortening of the C_2-C_6 distance. The geometrical deformations shift $CoIn_{cZc/tZc}$ energetically above $CoIn_{C/cZc}$ and $CoIn_C$. The topographic analysis (fig. 3.17, bottom) reveals that $CoIn_{cZc/tZc}$ facilitates a radiationless cZc$\leftrightarrow$tZc isomerization via a combined motion of torsion around the C_2-C_3 and the C_5-C_6 bonds and shortening of the C_2-C_6 distance, accompanied by bond rearrangements in the π-system. Ring-closure cannot be initiated from this CoIn. For comparison the thermal cZc$\leftrightarrow$tZc isomerization is carried out solely by torsion around the C_2-C_3 bond. As a consequence the thermal and photochemical isomerization (via $TS_{cZc/tZc}$ and $CoIn_{cZc/tZc}$, fig. 3.18) result in different conformers in the GS with respect to the substituents at C_6. Thus, labeling one of the methyl groups can be utilized to confirm the passage through $CoIn_{cZc/tZc}$ upon photoexcitation.

3.2.3. Reaction mechanism

Based on the spectroscopical and theoretical findings a detailed mechanism for the ring-opening and closure dynamics is proposed, which explain the observed quantum yields and helps to assign the extracted time constants (fig. 3.18).

Ring-opening (C→Z)   Excitation at 560 nm populates the bright $\pi\pi^*$ first ES. Instantaneous relaxation from the FC-region, dominated by bond rearrangements in the π-system, occurs within the first 100 fs and drives the system into a local minimum Min_C with an intact C_1-C_6 σ-bond. This fast initial process is below the time resolution of the experiment. However, evidence for the population of an intermediate in the ES on a sub-picosecond scale is provided by time-resolved UV/Vis
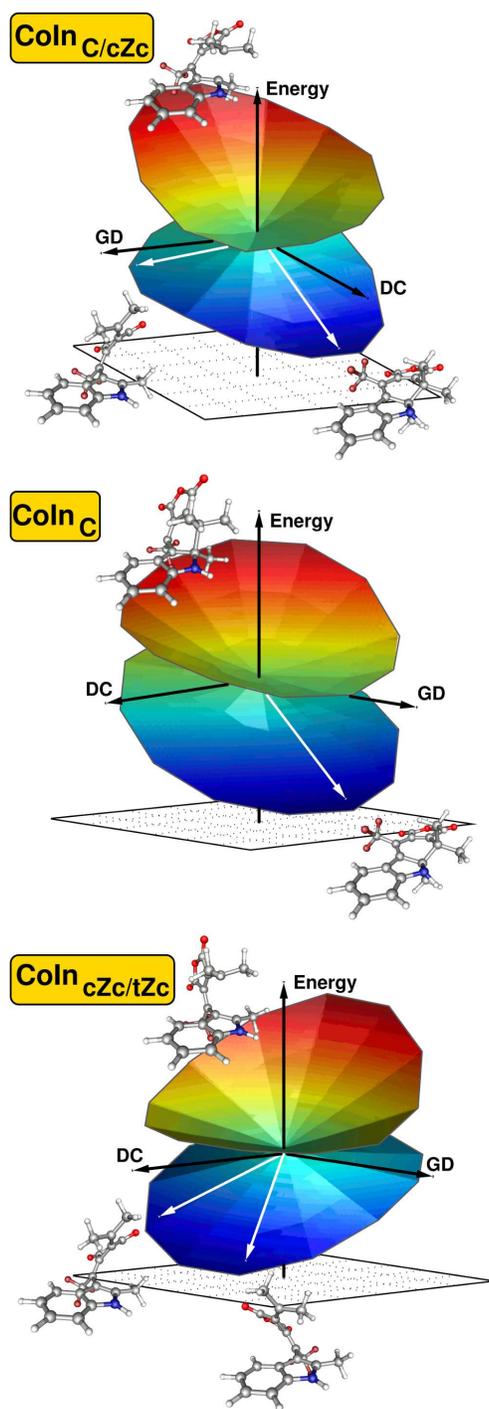
Figure 3.17.: CoIn topologies of CoIn$_{C/cZc}$, CoIn$_C$, CoIn$_{cZc/tZc}$ with associated GS products.
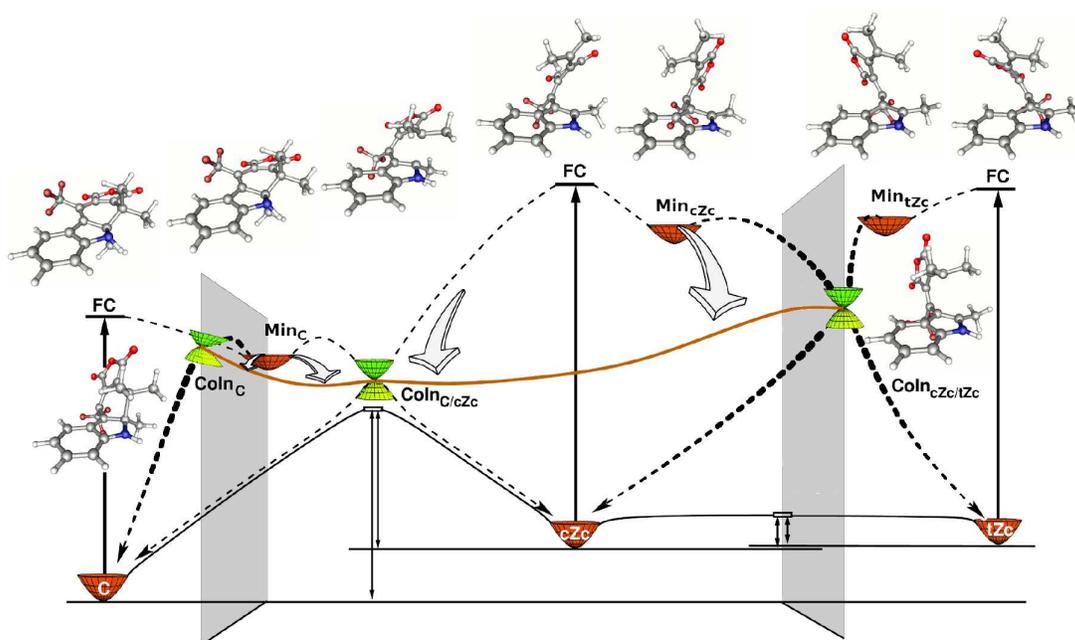
Figure 3.18.: Schematic reaction scheme with relevant geometries and ES relaxation channels. The coordinate for the ring-closure/opening and the cZc/tZc GS isomerization lies in the drawing plane. The coordinates for the internal conversion through $CoIn_C$ and for the cZc/tZc photoisomerization through $CoIn_{cZc/tZc}$ lie perpendicular to the drawing plane as indicated by the gray panels.

experiments[199]. Two radiationless decay mechanisms from Min_C exist, a photoreactive and a photostabilizing one. The photoreactive mechanism involves cleavage of the C_1-C_6 σ-bond and passes through $CoIn_{C/cZc}$. Here, a rapid decay to the GS with bifurcation towards either the C- or the cZc-form is possible. The photostabilizing mechanism involves a torsion around the C_2-C_3 double bond and drives the system towards $CoIn_C$ and finally to the C-form. In fact, effective radiationless decay occurs at all intermediate geometries along the low-lying seam connecting $CoIn_{C/cZc}$ and $CoIn_C$. Scans in the BS of selected geometries along the corresponding seam segment in the related compound pyrrolylfulgide (fig. 2.14b and c, seam $CoIn_D$-$CoIn_B$-$CoIn_E$) indicates that bifurcation in the GS occurs only in the vicinity of $CoIn_{C/cZc}$ (green line in fig. 3.19) while at large parts of the seam relaxation to the C-form is favored. The time constant of $\tau_1 = 2.6\text{-}2.9$ ps provides an effective description for the collective decay process from the ES intermediate Min_C through the CoIn seam. Dynamic simulations are indispensable for recovering the population of the individual channels. Without this information the experimental quantum yields are used to estimate the distribution and reconstruct the time constants of the individual relaxation processes. Thereby, the following assumptions are made: a) deactivation pathways through the reactive and the nonreactive seam segments are each described by one effective time constant giving the collective decay along the segment; b) a 1:1 bifurcation in the GS

is assumed for the reactive seam segment around $CoIn_{C/cZc}$, i.e. the exact topology of the seam and effects coming from momentum conservation are neglected; c) the region in the vicinity of $CoIn_C$ is completely nonreactive, i.e. an insurmountable GS barrier towards cZc is assumed; d) deactivation through fluorescence is neglected. Using the quantum yield for the ring-opening $\eta = 10\%$ a population distribution of 20%:80% into the reactive and nonreactive channels is estimated. Consequently, a ratio between the time constants $\tau_{C\rightarrow cZc}$ for the reactive and τ_{deact} for the stabilizing photoprocesses of 4:1 is obtained. Using this relation and an effective time constant τ_1 of about 3.0 ps in the rate equation

$$\frac{1}{\tau_1} = \sum_i \frac{1}{\tau_i}, \tag{3.3}$$

where the sum runs over the individual processes, the time constants $\tau_{C\rightarrow cZc}$ and τ_{deact} are calculated to be 15.0 ps and 3.8 ps, respectively.

The presence of an intermediate MinC prevents the C-form from immediately reaching $CoIn_{C/cZc}$ and provides the necessary time window for energy redistribution into modes, which drive the system towards the nonreactive region on the seam. Analysis of experimental data from the temperature dependence of the ring-opening reaction point in the same direction[197, 198].

Ring-closure (Z→C) At room temperature about 60% of the open-ring molecules exist in the cyclizable cZc-form, while 40% are in the tZc-form. The mixture is excited at 420 nm to the first bright ES of $\pi\pi^*$-character. Two competing processes occur in the FC-region of the cZc-isomer. A barrierless relaxation towards $CoIn_{C/cZc}$ facilitates the ring-closure, the main reaction path, with a time constant $\tau_{cZc\rightarrow C}$. The recorded short time constant $\tau_1 = 0.5$-0.8 ps is assigned to $\tau_{cZc\rightarrow C}$.

Concurrent torsional motion around the C_2-C_3 bond drives the system to the local minimum Min_{cZc}. From the non-cyclizable tZc-isomer a corresponding local minimum Min_{tZc} can be reached. The longer time constant $\tau_2 = 3.9$-11.0 ps is attributed to the passage from the intermediate minima Min_{cZc} and Min_{tZc} to the GS of both open forms passing through $CoIn_{cZc/tZc}$ and the closed by seam segment connecting to $CoIn_{C/cZc}$ (fig. 3.19). Photoisomerization between the cZc- and the tZc-forms occurs exclusively by this process.

In summary, the ring-closure of the cZc-form proceeds on a sub-picosecond time scale, thereby being an order of magnitude faster than the ring-opening. The ring-closure is very efficient as the system has no time to redistribute the energy and follows the gradient on the excited surface in a ballistic fashion towards $CoIn_{C/cZc}$. From the ring-closure quatum yield of 20% and the 1:1 product distribution out of $CoIn_{C/cZc}$ it follows that two of every three molecules in the cyclizable cZc-form follow the ring-closure coordinate. The moderate quantum yield is attributed to the high percentage of non-cyclizable tZc molecules in the initial equilibrium mixture.
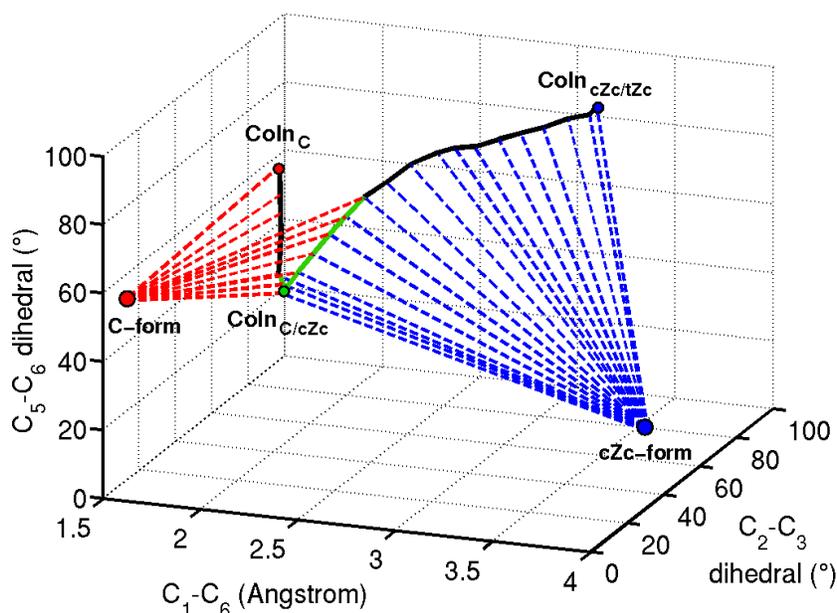
Figure 3.19.: Ground state product accessibility from the CoIn seam, plotted in the coordinate space of the C_1-C_6 bond and the torsional angles around the C_2-C_3 and the C_5-C_6 bonds. The region around CoIn$_C$ facilitates a relaxation solely to the C-form (red dashed lines). The region around CoIn$_{cZc/tZc}$ facilitates a relaxation solely to the cZc-form (blue dashed lines). In the region around CoIn$_{C/cZc}$ (green solid line) both channels can be accessed.

3.2.4. Summary: ultrafast photoreactivity at the expense of selectivity

From a joint experimental-theoretical study important information is obtained on the photoinduced ring-opening/closure of trifluoromethyl-indolylfulgide. Time resolved IR measurements provide mode-specific dynamics on the few picosecond time scale which can be related to ES and GS processes. Quantum chemical calculations reveal a complex potential energy landscape in the excited electronic state with pathways for ring-opening and closure reactions as well as for competing side-reactions such as internal conversion to local minimia and the GS.

The existence and the spectral signatures of an additional time constant found during the ring-closure reaction and the molecular modeling convincingly shows that the ensemble of open-ring fulgides contains conformers (tZc) which cannot undergo cyclization and react via internal conversion back to the GS within about 10 ps. The cyclizable cZc conformers react much faster on the 500 fs time scale via the CoIn$_{C/cZc}$. The existence of two conformers also answers the long standing question, whether ring-opening and ring-closure occur via a common CoIn. It has been argued that both reactions proceed via different CoIns as the quantum yields do not sum up to 100%[199, 210]. The present study indicates that both the ring-closure of the cy-

clizable conformer and the ring-opening proceed in the vicinity of the CoIn$_{C/cZc}$ with high yield. The loss in reaction yield is due to the bifurcation at CoIn$_C$ during ring-opening and to the presence of the non-reactive conformers tZc upon ring-closure. Furthermore, this study sheds light on the electronic nature of the ultrafast photore-activity of fulgides. Upon photoexcitation a charge transfer from the indole to the anhydride is initiated already in the FC region. This facilitates bond rearrangements and drives the system towards reactive and non-reactive regions on the energetically low-lying CoIn seam. Since the functionalization pattern of the fulgide may stabilize the charge transfer state in certain geometrical arrangements, substitution may be used to tune and optimize the photochemical properties. With the acquired knowl-edge it should become possible to develop strategies for the selective stabilization of regions on the CoIn seam and for the suppression of undesired side-reactions. This can be done by introducing sterical constraints to prevent torsion about the C_2-C_3 bond, but also by new functionalization patterns, which aim at stabilizing CoIn$_{C/cZc}$. Then, selectivity can be significantly enhanced without sacrifying speed. The rules derived in secs. 2.2 and 2.3 provide a systematic way to pursue this ultimate goal.

4. Mixed quantum-classical dynamics

The previous chapters provided a deep insight into the quantum chemical treatment of photoreactive molecular systems. Using the information provided by stationary quantum chemical calculations (i.e. electronic structure and geometries, MEPs, analysis of their curvature) reaction mechanisms were formulated and experimental findings could be rationalized. However, these reaction mechanisms apply only to slow reactions, where the system can dissipate the excess energy to the environment and follows closely the MEP. At room temperature or when a high amount of energy is pumped into the system by an intense ultrashort laser pulse the system may deviate strongly from the stationary path and a dynamical treatment is indispensable. Dynamical simulations consider momentum conservation in active modes which drive the system towards non-stationary regions on the PES. This chapter sets the focus on the dynamics at the CoIn seam, i.e. the region on the PES, which mediates the ultrafast relaxation to a lower state. As the seam does not constitute a stationary point on the PES its accessibility is a question, which can be addressed only by dynamical calculations.

The fundamental formula of quantum dynamics is the time dependent Schrödinger equation:

$$i\frac{\partial \Psi(r, R, t)}{\partial t} = \hat{H}\Psi(r, R, t).$$ (4.1)

A wavefunction ansatz for solving eq. 4.1 performs an expansion of the total wavefunction in the complete basis of electronic states:

$$\Psi(r, R, t) = \sum_i \chi_i(R, t)\Psi_i^{el}(r; R),$$ (4.2)

with χ_i the time-dependent nuclear wavefunctions. Inserting eq. 4.2 into eq. 4.1, multiplying with Ψ_j^* and integrating over the electronic coordinates gives:

$$i\frac{\partial \chi_j}{\partial t} = \sum_i \left(\hat{T}^{\mathrm{nuc}}\delta_{ij} + V_i\delta_{ij} + \left\langle \Psi_j^{el} \middle| \hat{T}^{\mathrm{nuc}}\Psi_i^{el} \right\rangle - \sum_\alpha \frac{1}{m_\alpha} \left\langle \Psi_j^{el} \middle| \nabla_\alpha \Psi_i^{el} \right\rangle \nabla_\alpha \right) \chi_i.$$ (4.3)

So far no approximation has been introduced. Quantum dynamical treatment is the only rigorous approach for solving the equation. It accounts for all quantum mechanical phenomena without performing any approximations. Solution requires the precomputation of certain quantities like multidimensional potentials for all states of interest and nonadiabatic couplings between them. The effort scales exponentially with the size of the system, which makes quantum dynamics very demanding[211]. Different approximation schemes have been proposed to deal with the complexity of

eq. 4.3. Mixed quantum-classical dynamics embrace a classical limit for the nuclear degrees of freedom while treating the electronic degrees of freedom on a quantum mechanical level along the classical path of the nuclei.

4.1. Mixed quantum-classical dynamics

Depending on the choice of formulation of the quantum dynamical problem and the way the classical limit is reached one differentiates between Ehrenfest[212, 213] and surface hopping[66, 214, 215] (both arising from a wavefunction formulation to eq. 4.3), quantum-classical Liouville[216] (arising at the classical limit of the Liouville equation), Pechukas'[217] (path-integral formulation), Bohmian[218, 219] (hydrodynamical formulation) dynamics, etc. In this section the Ehrenfest and surface hopping approaches are presented. The discussion follows the derivation outlined in ref. [65]. Based on eq. 4.3 the necessary approximations are introduced and their significance is discussed.

1. Neglect of the second derivative of the nuclear wavefunctions $\hat{T}_{nuc}\chi_j$ with respect to the nuclear coordinates. This term is responsible for the spatial correlation of a wavepacket at a certain time. Neglecting this correlation allows for treating the dynamics of a wavepacket by a swarm of independent trajectories. This appoximation localizes the wavepacket entirely at a classical trajectory path $\overline{R}$:

$$\chi_j = c_j(t)\xi_j(R - \overline{R}), \tag{4.4}$$

   where $\xi_j(R - \overline{R})^1$ is a peaked function centered at each trajectory coordinate $\overline{R}$.

2. Neglect of the second derivative of the electronic wavefunctions Ψ_j^{el} with respect to the nuclear coordinates $\sum_i \left\langle \Psi_j^{el} \middle| \hat{T}_{nuc}\Psi_i^{el} \right\rangle$. This term affects the transition probability between states i and j. Normally, it is small and its neglect is justified.
   Thus, neglecting the first and third term on the RHS of eq. 4.3, inserting the expression 4.4, multiplying from left with ξ_j^* and integrating over the nuclear coordinates leads to

$$i\frac{\partial c_j(t)}{\partial t} = \sum_i \left(\left\langle \xi_j \middle| V_i \delta_{ij} \middle| \xi_i \right\rangle - i \left\langle \xi_j \middle| \vec{F}_{ij} \cdot \hat{v} \middle| \xi_i \right\rangle \right) c_i(t), \tag{4.5}$$

   where the short-hand notations

$$\vec{F}_{ij} = \sum_\alpha \left\langle \Psi_j^{el} \middle| \nabla_\alpha \Psi_i^{el} \right\rangle \quad \text{and} \quad \hat{v} = -i\sum_\alpha \frac{\nabla_\alpha}{m_\alpha} \tag{4.6}$$

   were introduced.

---

[1]From here on the dependency of ξ_j on the nuclear coordinates is not denoted explicitly.

3. Classical limit for the momentum operator. The non-local quantum mechanical velocity operator is substitued by a classical velocity function

$$\hat{v}_\alpha \approx \vec{v}_\alpha(R), \tag{4.7}$$

which introduces a small error to the transition probability.

4. Saddle-point approximation[220]. The local nature of the classical nuclear wavepacket (eq. 4.4) allows to approximate the integrals in eq. 4.5 by applying first-order saddle point approximation

$$\left\langle \xi_i \middle| f(R) \middle| \xi_j \right\rangle = \left\langle \xi_i \middle| \left(f(\overline{R}) + (R - \overline{R})f'(\overline{R}) + (R - \overline{R})^2 \frac{f''(\overline{R})}{2} + \cdots \right) \middle| \xi_j \right\rangle \approx$$
$$\approx \left\langle \xi_i \middle| \xi_j \right\rangle f(\overline{R}), \tag{4.8}$$

thereby requiring the knowledge of $f(R)$ only at the maximum of the product of both peaked functions ξ_i and ξ_j evolving on different PES, i.e. at the center of the trajectory coordinate $\overline{R}$.

5. A unity overlap of the nuclear wavefunctions. The assumption that the overlap between classical nuclear wavepackets evolving on different PES is unit

$$\left\langle \xi_i \middle| \xi_j \right\rangle = 1 \tag{4.9}$$

implies that they are always correlated and no quantum decoherence can occur[221, 222].

Applying the above approximations to eq. 4.5 gives the final expression for the evolution of the expansion coefficients $c_j(t)$

$$i\frac{\partial c_j(t)}{\partial t} = \sum_i (V_i \delta_{ij} - i\vec{F}_{ij} \cdot \vec{v})c_i(t). \tag{4.10}$$

4.1.1. Mean field approach

Using the Ehrenfest theorem[223]

$$\frac{d\langle \hat{O} \rangle}{dt} = \frac{i}{\hbar} \left\langle [\hat{O}, \hat{H}] \right\rangle + \left\langle \frac{\partial \hat{O}}{\partial t} \right\rangle, \tag{4.11}$$

which establishes the correspondence between quantum and classical dynamics one can obtain the Newton's equation of motion for the center of the wavepacket

$$m_\alpha \frac{d^2 R_\alpha}{dt^2} = \frac{d\langle \hat{p}_\alpha \rangle}{dt} = -\left\langle \Psi \middle| \nabla_\alpha \hat{H}^{el} \middle| \Psi \right\rangle = \mathfrak{F}_\alpha. \tag{4.12}$$

Using the expansions 4.2 and 4.4 the force acting on the nuclei α can be expressed as

$$\mathfrak{F}_\alpha = -\sum_j \left|c_j\right|^2 \nabla_\alpha V_j + \sum_{ij} c_i c_j^* (V_i - V_j) F_{ij,\alpha}. \tag{4.13}$$

Eq. 4.10 and 4.13 define the Ehrenfest or mean-field method[213]. Here the evolution of the classical wavepacket occurs on an average PES. The unity overlap assumption does not allow wavepackets evolving on different PES to decohere even in regions where the non-adiabatic coupling is small and the quantum wavepackets would travel independently on each surface. Thus, the mean-field approch performs good only in regions of large coupling.

4.1.2. Surface hopping approach

Surface hopping is a related method which aims at recovering the decoherence. Here a trajectory evolves at each instance in time on a single adiabatic PES, although, according to eq. 4.10 there is non-zero population in each state. The force is then given by the gradient of a single surface

$$\mathfrak{F}_\alpha = -\nabla_\alpha V_j. \tag{4.14}$$

To account for the non-adiabaticity the classical wavepacket is allowed to instantly change the surface it is evolving on, an event called a surface hop. The decision whether a hop will occur or not is taken stochastically after calculating the population on each state $a_{jj} = c_j^* c_j$ according to eq. 4.10. There are multiple ways to determine whether a hop should occur. The most simple approach forces a hop as soon as the population of a certain state exceeds a predefined threshold[44]. Another approach relies on the evaluation of Landau-Zener transition probabilities[224, 225]. The probably most popular formulation is the "fewest switches" approach by Tully[66]. During a time step the change of population of a particular state j is expressed as

$$\Delta a_{jj} = -\sum_i p_{j\to i} a_{jj} + \sum_i p_{i\to j} a_{ii}, \tag{4.15}$$

with $p_{j\to i}$ the transition probability from state j to state i. According to eq. 4.15 at every time step there is non-zero probability for population transfer from j to i and backwards. Tully's ansatz looks for the fewest number of switches to set up the final population in all states at the end of the time step. Naturally, this can be achieved if population transfer is allowed in only one direction. This assumption implies that either one of the sums on the right hand side of eq. 4.15 is kept, depending on whether the population in state j increases or decreases. For a two-state case the transition probability is given by the expression

$$p_{j\to i} = -\frac{\Delta a_{jj}}{a_{jj}}. \tag{4.16}$$

By introducing a sufficiently short time step Δt for which the change of the population Δa_{jj} can be approximated via a first order Taylor expansion

$$\Delta a_{jj} = \frac{\partial a_{jj}}{\partial t} \Delta t \tag{4.17}$$

and using eq. 4.10 the final expression for the "fewest switches" transition probability is obtained as

$$p_{j \to i} = -\frac{2\Re(a_{ij})\vec{F}_{ij} \cdot \vec{v}}{a_{jj} \Delta t}. \tag{4.18}$$

The presented approach can be extended to more than two electronic states.

A hop can occur at any instance in time if two conditions are fulfilled. The transition probability to a certain state must be higher in magnitude than a randomly chosen number in the [0,1] interval and the total energy of the system must be conserved. To achieve energy conservation the velocity of the system needs to be readjusted to compensate the instant change in the potential energy. Usually, the adjustment is performed along the non-adiabatic vector $\vec{F}_{ij}$[226], however adjustment along the energy difference gradient or along the velocity vector itself can be applied. A hop to a higher PES is rejected if the velocity reduction is higher than the component of the velocity in direction of $\vec{F}_{ij}$[227], although eq. 4.10 suggests an electronic transition. These classically forbidden electronic transitions are the result of the deficiency of the classical description of a quantum mechanical property as the non-adiabaticity.

The quality of the surface hopping approach is reflected in its ability to reproduce the averaged occupation $\bar{a}_{jj}(t)$ of state j at time t (quantum mechanical quantity)

$$\bar{a}_{jj}(t) = \frac{\sum_j \left| c_j(t) \right|^2}{N_{\text{tot}}} \tag{4.19}$$

by the fraction of trajectories $N_j(t)$ evolving on state j (classical quantity)

$$f_j(t) = \frac{N_j(t)}{N_{\text{tot}}}. \tag{4.20}$$

With increasing number of classically forbidden transitions the quality deteriorates. In mixed quantum-classical dynamics there is no rigorous way to surpass this problem. The simplest solution is to just ignore forbidden hops, although other suggestions like reversing the velocity component in the direction of the non-adiabatic coupling have been proposed.

4.1.3. Integration the Newton's equation

The integration of the Newton's equation of motion 4.12 is performed with the Velocity Verlet algorithm[228]. This is a modified version of the Verlet algorithm which allows to calculate both position and velocity in each time step of a classical dynamics simulation. As elucidated in the previous section the velocity is required for calculat-

ing the transition probability $p_{j \rightarrow i}$ (eq. 4.18) and for monitoring the conservation of total energy during surface switching. The Velocity Verlet algorithm has an accuracy of the order of Δt^3 for positions and velocities. The position $\vec{R}(t + \Delta t)$ and velocity $\vec{v}(t + \Delta t)$ are expanded in Taylor series, truncated to second order

$$\vec{R}(t + \Delta t) = \vec{R}(t) + \vec{v}(t)\Delta t + \frac{1}{2}\vec{a}(t)\Delta t^2 + O(\Delta t^3) \tag{4.21a}$$

$$\vec{v}(t + \Delta t) = \vec{v}(t) + \vec{a}(t)\Delta t + \frac{1}{2}\vec{j}(t)\Delta t^2 + O(\Delta t^3), \tag{4.21b}$$

with velocity $\vec{v}(t)$, acceleration $\vec{a}(t)$ and jerk $\vec{j}(t)$ the first, second and third derivative with respect to the nuclear position at time t, respectively. Next, the jerk at time t is expressend in a forward difference approximation via the accelerations at times t and $t + \Delta t$

$$\vec{j}(t) = \frac{1}{\Delta t}\left(\vec{a}(t + \Delta t) - \vec{a}(t) + O(\Delta t^2)\right). \tag{4.22}$$

Inserting eq. 4.22 into eq. 4.21b gives

$$\vec{v}(t + \Delta t) = \vec{v}(t) + \frac{\vec{a}(t + \Delta t) + \vec{a}(t)}{2}\Delta t + O(\Delta t^3). \tag{4.23}$$

Eq. 4.21a and 4.23 are the working equations in the Velocity Verlet algorithm. Starting at position R at time t first the new position $R(t + \Delta t)$ is obtained using eq. 4.21a. At $R(t + \Delta t)$ the new acceleration is calculated using eq. 4.14. It is then used to calculate the velocity at $R(t + \Delta t)$ via eq. 4.23.

4.1.4. Sampling of initial conditions

An important factor in the quasiclassical dynamics is the definition of the initial conditions for the swarm of trajectories. One needs to correctly account for the distribution of the GS wavepacket in phase space. Wigner's quasi-probability distribution[229] provides the probability distribution for a quantum mechanical wavefunction in phase space and encodes all expectation values. Phase space distribution is given by the Wigner distribution function

$$P_w(\vec{q}, \vec{p}) = (2\pi\hbar)^{-1}\int \chi^*(\vec{q} + \frac{\vec{s}}{2})\chi(\vec{q} - \frac{\vec{s}}{2})\exp\left(\frac{i}{\hbar}\vec{s}\vec{p}\right)d\vec{s}. \tag{4.24}$$

It can be shown that this representation gives a correct expression for the probability of a quantum mechanical wavefunction in phase space.
Asumming a quadratic approximation for the GS potential the GS wavefunction $\chi(\vec{q})$ can be spanned in the basis of eigenfunctions $\chi(\vec{q_i})$ of the $3N - 6$ one-dimensional harmonic oscillators along the normal modes $q_1 \ldots q_{3N-6}$ with reduced masses μ_i and

harmonic frequencies ω_i

$$\chi(\vec{q_i}) = \left(\frac{2\alpha}{\pi}\right)^{\frac{1}{4}} \exp\left(-\alpha\vec{q_i}^2 + \frac{i}{\hbar}\vec{p_i}\vec{q_i} + \frac{i}{\hbar}\gamma\right) \quad \text{with} \quad \alpha = \frac{\mu_i\omega_i}{2\hbar}. \qquad (4.25)$$

Inserting the expression 4.25 in the Wigner distribution 4.24 and evaluating the integral gives

$$P_w(\vec{q_i}, \vec{p_i}) = (\pi\hbar)^{-1} \exp\left(-\frac{\mu_i\omega_i}{\hbar}\vec{q_i}^2\right) \exp\left(-\frac{1}{\mu_i\omega_i\hbar}\vec{p_i}^2\right). \qquad (4.26)$$

Eq. 4.26 gives the distribution of a quantum mechanical wavepacket in phase space. It can be utilized to sample the phase space and to reproduce the quantum dynamical distribution for quasiclassical trajectory runs.

An independent distribution sampling in coordinate space is performed for each mode. As GS vibrational wavefunctions are used, the maximal imposed displacement along a normal mode corresponds to a conversion of the zero-point energy $E_i^{ZVP} = \frac{1}{2}\omega_i$ into potential energy. Subsequently, the conjugated momentum is evaluated for each displacement and a stochastic alogrithm decides on the sign of the momentum. Thereby, it is assured, that each trajectory has a total energy of

$$E_{ZPE} = \frac{1}{2}\sum_i \omega_i, \qquad (4.27)$$

corresonding to the zero-point energy of the system. This procedure assures that the distribution of the quantum mechanical wavefunction is reproduced, asumming a sufficient number of initial conditions are generated.

4.1.5. On-the-fly dynamics

As already outlined in the previous sections the mixed quantum-classical dynamics assume that a quantum wavepacket can be approximated by a swarm of classical (i.e. localized) uncorrelated trajectories (the swarm). A large number of trajectories is needed to obtain meaningful results. On the one hand a large set of initial conditions is required to reproduce the quantum mechanical distribution in the GS. On the other hand the stochastic nature of the surface hopping routine makes a single trajectory physically meaningless and only a statistical average over all trajectories can be interpreted.

The local nature of each classical wavefuntion makes the precomputation of PES unnecessary as the gradient obtained at each time step suffices to determine the subsequent position and velocity of the system. The feature of supplying almost no initial information in advance (all necessary quantities are calculated "on-the-fly") and the possibility for a full dimensional treatment are responsible for the attention mixed quantum-classical approaches received in the past years (Selected reviews and applications can be found in refs. [43, 65, 148, 219, 230–232]). Since the gradient contains only local information about the PES short time steps are required. As a rule of thumb one takes one tenth of the oscillation period of the highest frequency modes

(normally hydrogen stretching vibrations at 3000 cm^{-1}) for the time step. A standard value is 0.5 fs. This limitation, together with the necessity of running a relatively big number of trajectories restricts the application of surface hopping dynamics to molecules with a limited number of non-hydrogen atoms and time windows of several hundred femtoseconds if highly correlated ab-initio quantum chemical approaches are used.

The possibility to solve the electronic problem and perform the nuclear dynamics separately allows to interlace the surface hopping code practically with any quantum chemical software and to profit from the variety of software packages available. Newton-X[67], a package for Newtonian dynamics, freely distributed by Mario Barbatti and colleagues, offers a flexible framework allowing to write interfaces to quantum chemical software. Part of the present work was connected to the development of an interface for Newton-X to the software package Molpro[71] with focus on the implementation of non-adiabatic couplings at MS-MR-CASPT2 level.

4.1.6. MS-MR-CASPT2 on-the-fly mixed quantum-classical dynamics

A fast and accurate calculation of gradients and non-adiabatic couplings is a key aspect in performing non-adiabatic dynamics. While analytic gradients are nowadays implemented for a variety of methods, analytic non-adiabatic couplings are reserved to multiconfigurational methods like CASSCF[65, 104] (sec. 1.4.2) and MRCI[65, 104]. Due to its deficient description of dynamic correlation[110] the CASSCF method can serve merely for qualitative predictions regarding barrier heights and relative stabilites of intermediates and products. MRCI is very costly and is currently applicable to molecules with a few non-hydrogen atoms. Another approach with a comparable accuracy as MRCI but considerably cheaper is CASPT2[68–70] (sec. 1.4.3). Nowadays, this has become the method of choice for systems with tens of non-hydrogen atoms. In the last years CASPT2 energy calculations has been interlaced with quasi-classical dynamics codes to correct energies and gradients obtained at CASSCF level[43]. The aim of this work is to develop surface hopping dynamics entirely at CASPT2 level. This objective became feasible with the recent implementation of analytic MS-MR-CASPT2 gradients[233] in the quantum chemistry package Molpro. A drawback, though, is the lack of analytical non-adiabatic couplings. Fortunatelly, as seen from eq. 4.10 only the projection of the non-adiabatic coupling on the velocity $\vec{F}_{ij} \cdot \vec{v}$ is needed for the surface hopping dynamics. This observation simpfies the numerical calculation of the coupling term significantly as it allows to obtain the desired quantity at the price of one additional energy calculation in direction of the velocity vector. This idea was originally exploited by Martínez and colleagues to interlace their multiple spawning dynamics code with MS-MR-CASPT2[234, 235]. The dot product of the non-adiabatic coupling and the velocity can be reformulated as

$$\vec{F}_{ij} \cdot \vec{v} = \left\langle \Psi_i^{MS}(R) \middle| \nabla_{\vec{v}} \Psi_j^{MS}(R) \right\rangle, \tag{4.28}$$

where the superscript MS denotes that MS-MR-CASPT2 wavefunctions are used. In a forward difference approximation the derivative can be written as

$$\left\langle \Psi_i^{MS}(R)\middle|\nabla_{\vec{v}}\Psi_j^{MS}(R)\right\rangle = \frac{1}{\varepsilon}\left(\left\langle \Psi_i^{MS}(R)\middle|\Psi_j^{MS}(R+\varepsilon\vec{v})\right\rangle - \left\langle \Psi_i^{MS}(R)\middle|\Psi_j^{MS}(R)\right\rangle\right)+O((\varepsilon\vec{v})^2).$$
(4.29)

Due to the orthogonality of the MS-MR-CASPT2 eigenstates the overlap between the j-th and i-th states at R vanishes, simplifying the expression for the projection $\vec{F}_{ij}\cdot\vec{v}$. Eq. 4.29 can be evaluated, provided the MS-MR-CASPT2 wavefunctions at two different geometries can be stored. For technical reasons this simple solution is yet not practicable with Molpro and a detour is needed. Therefore, two alternative approaches for evaluating eq. 4.28 with quantities obtainable from Molpro are discussed.

One can express each MS-MR-CASPT2 wavefunction in the basis of the SS-CASPT2 wavefunctions Ψ^{SS}. Then, eq. 4.29 becomes

$$\left\langle \Psi_i^{MS}(\vec{R})\middle|\nabla_{\vec{v}}\Psi_j^{MS}(\vec{R})\right\rangle = \frac{1}{\varepsilon}\sum_{m,n}c_{mi}c_{nj}\left\langle \Psi_m^{SS}(\vec{R})\middle|\Psi_n^{SS}(\vec{R}+\varepsilon\vec{v})\right\rangle,$$
(4.30)

or in a matrix notation providing all coupling terms at one glance

$$\begin{pmatrix} 0 & \vec{F}_{1,2}\cdot\vec{v} & \cdots & \vec{F}_{1,n}\cdot\vec{v} \\ -\vec{F}_{1,2}\cdot\vec{v} & 0 & \cdots & \vec{F}_{2,n}\cdot\vec{v} \\ \vdots & \vdots & \ddots & \vdots \\ -\vec{F}_{1,n}\cdot\vec{v} & -\vec{F}_{2,n}\cdot\vec{v} & \cdots & 0 \end{pmatrix} \equiv \mathbf{F}\cdot\vec{v} = \frac{1}{\varepsilon}\mathbf{C}_R\mathbf{S}_{R|R+\varepsilon\vec{v}}\mathbf{C}_{R+\varepsilon\vec{v}}^T,$$
(4.31)

where $\mathbf{C}$ is the matrix of the expansion coefficients and $\mathbf{S}_{R|R+\varepsilon\vec{v}}$ the overlap matrix of the SS-CASPT2 wavefunctions at R and $R+\varepsilon\vec{v}$. The subscript denotes whether the quantities are obtained at $\vec{R}$ or at $\vec{R}+\varepsilon\vec{v}$.

As the overlap between CASPT2 wavefunctions at different positions is not directly available in Molpro the wavefunctions at $\vec{R}+\varepsilon\vec{v}$ is expressed through the wavefunctions at $\vec{R}$ by the following unitary transformation

$$\Psi_i^{SS}(R+\varepsilon\vec{v}) = \sum_k u_{ki}\Psi_k^{SS}(R).$$
(4.32)

The transformation matrix $\mathbf{U}$ with elements u_{ki} is obtained by maximizing the overlap between the states at both geometries. $\mathbf{U}$ is then used to rewrite eq. 4.31 as

$$\mathbf{F}\cdot\vec{v} = \frac{1}{\varepsilon}\mathbf{C}_R\mathbf{S}_{R|R}\mathbf{U}\mathbf{C}_{R+\varepsilon\vec{v}}^T.$$
(4.33)

All quantities in eq. 4.33 are available in Molpro using the RS2[236] and the DDR[237] routines.

An alternative expression for the couplings is obtained by recalling that according to

eq. 1.11 the nonadiabatic coupling can be written as

$$\left\langle \Psi_i^{MS} \middle| \nabla_{\vec{v}} \Psi_j^{MS} \right\rangle = \frac{\left\langle \Psi_i^{MS} \middle| \nabla_{\vec{v}} \hat{H} \middle| \Psi_j^{MS} \right\rangle}{V_j - V_i}. \tag{4.34}$$

Expressing the MS-MR-CASPT2 wavefunctions in the basis of the SS-CASPT2 wave-functions Ψ^{SS} and resorting to forward difference approximation eq. 4.34 becomes

$$\left\langle \Psi_i^{MS} \middle| \nabla_{\vec{v}} \Psi_j^{MS} \right\rangle = \frac{\sum_{m,n} c_{mi} c_{nj} \left\langle \Psi_i^{SS}(R) \middle| \hat{H}(R + \varepsilon \vec{v}) \middle| \Psi_j^{SS}(R) \right\rangle}{\varepsilon(V_j - V_i)}. \tag{4.35}$$

Applying the unitary transformation of eq. 4.32 allows to write

$$\left\langle \Psi_i^{SS}(R) \middle| \hat{H}(R + \varepsilon \vec{v}) \middle| \Psi_j^{SS}(R) \right\rangle = \sum_{k,l} u_{ki} u_{lj} \left\langle \Psi_k^{SS}(R + \varepsilon \vec{v}) \middle| \hat{H}(R + \varepsilon \vec{v}) \middle| \Psi_l^{SS}(R + \varepsilon \vec{v}) \right\rangle$$
$$= \mathbf{U}^T \mathbf{H}_{R+\varepsilon\vec{v}} \mathbf{U}, \tag{4.36}$$

giving the final expression for the couplings

$$\mathbf{F} \cdot \vec{v} = \frac{\mathbf{C}_R \mathbf{U}^T \mathbf{H}_{R+\varepsilon\vec{v}} \mathbf{U} \mathbf{C}_R^T}{\varepsilon(V_j - V_i)}. \tag{4.37}$$

Eq. 4.37 has been chosen for the implementation of the MS-MR-CASPT2 surface hopping dynamics as it correctly reproduces the anti-symmetry of the non-adiabatic coupling matrix $\mathbf{F}$.

In the next section the implementation is used to study the photodynamics of the ring-opening of 1,3-cyclohexadiene.

4.2. Application: dynamics of cyclohexadiene

The photoinduced isomerization of 1,3-CHD to cZc-HT is a text book example for a WH allowed electrocyclic reaction[72]. The desire to follow the ultrafast isomerization dynamics in real time and decipher all electronic and structural changes involved initiated the development of novel experimental setups providing sub-picosecond temporal resolution[239] and theoretical concepts like the radiationless relaxation via CoIn seams[240].

In the original treatment of photochemical reactions obeying the WH rules[95, 96], as devised by van der Lugt and Oosterhoff[241, 242], it was assumed that both the GS and ES reactions evolve along a common symmetry conserving reaction coordinate. In the CHD↔HT isomerization this is a C_2-symmetry conserving conrotatory torsion (fig. 4.1, left). Non-adiabaticity was explained by introducing the concept of the avoided crossing coinciding with the pericyclic minimum on the ES[242]. It arises from the correlation of the potentials of the reactant GS and the product ES
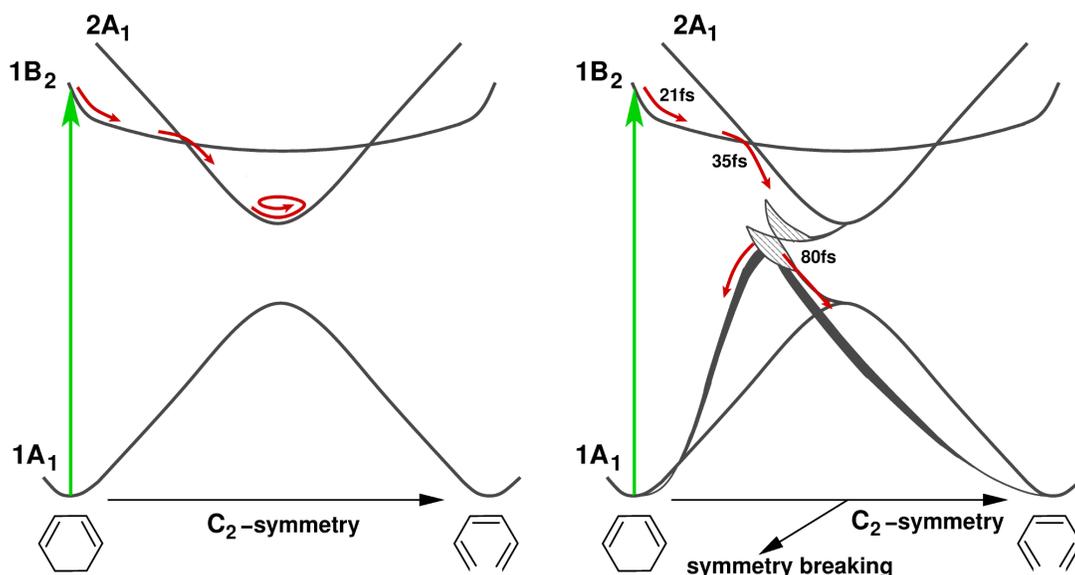
Figure 4.1.: Models for the 1,3-CHD/cZc-HT conrotatory photoisomerization with assignment of state symmetry. (left) The C_2-symmetry preserving isomerization according to van der Lugt and Oosterhoff leads to an avoided crossing where the wavepacket stays before decaying non-adiabatically to the GS. (right) In the asymmetric model a low-energy CoIn (lying out of the drawing plane) is reached by symmetry-breaking deformations. The system accumulates momentum in symmetry-breaking modes already at the $1B_2/2A_1$-crossing. Experimental time constants taken from ref. [238] are denoted.

along the common coordinate (fig. 4.1, left, see also fig. 1.3). According to Fermi's golden rule[72] the non-adiabatic coupling of the vibronical levels of the electronically ES with a continuum of vibronical levels in the GS in the vicinity of an avoided crossing allows for a nonradiative decay. This treatment applies only to "slow" photochemical processes. For the CHD/HT system, the energy gap between both correlated states remains so large along the symmetry-conserving path that an effective and fast non-adiabatic transition is impossible, in contradiction to what is observed experimentally[16–20, 238, 243]. In this case, the role of real crossings displaced from the symmetry-conserving path is indispensable and the avoided crossing of the van der Lugt/Oosterhoff picture becomes a real crossing (i.e. CoIn) away from the minimum energy reaction path (fig. 4.1, right).

Robb et al. first reported on the existence of a low-lying asymmetric $CoIn_{min}$[47] in the CHD/HT system in the vicinity of the pericyclic minimum. Based on this finding Fuss et al. proposed a symmetry breaking ballistic model[240] of the wavepacket motion towards the CoIn and assigned time constants to the underlying processes (fig. 4.1, right). Quantum dynamical simulations confirmed that the sub-picosecond dynamics can be simulated only when a CoIn is explicitly considered[244, 245]. A study by Garavelli and co-workers documented an energetically low-lying CoIn seam

connecting $CoIn_{min}$ to a C_2-symmetric open-ring $CoIn_{C_2}$[240]. Quantum dynamical simulations by Hofmann et al. suggested that $CoIn_{C_2}$ is the dominant relaxation pathway during ring-opening[77]. A thorough search in the IS, inspired by this finding, extended the CoIn seam to the closed-ring region[74], providing an outlet towards the GS from large part of the conrotatory ES MEP.

Unlike other prototypical ultrafast reactions such as the *cis-trans* photoisomerization of retinal[45, 46] where the ES relaxation is strongly directed toward the minimum on the crossing seam ("sand-in-the-funnel" picture), previous studies demonstrated that in the CHD/HT system the ES MEP and the accessible CoIn seam do not intersect[74]. Rather, they are quasi-parallel in the $3N - 6$ coordinate space, i.e. evolve along similar geometrical deformations.

In this section the question, which regions of the extended low-lying CoIn seam are accessed during the ring-opening, is addressed by means of mixed quantum-classical non-adiabatic dynamics at MS-MR-CASPT2(2,2)/6-31+G* level and averaging over the lowest three states of the system. Before presenting the results of the simulations the extended CoIn seam is characterized and compared (energetically and geometrically) to the MEP in the ES. The MEP was optimized at the same theoretical level used in the dynamical simulations. As currently a CoIn seam optimization at MS-MR-CASPT2 level is not feasible the CoIn seam between the GS and the first ES was optimized at CASSCF(6,6)/6-31G* level.
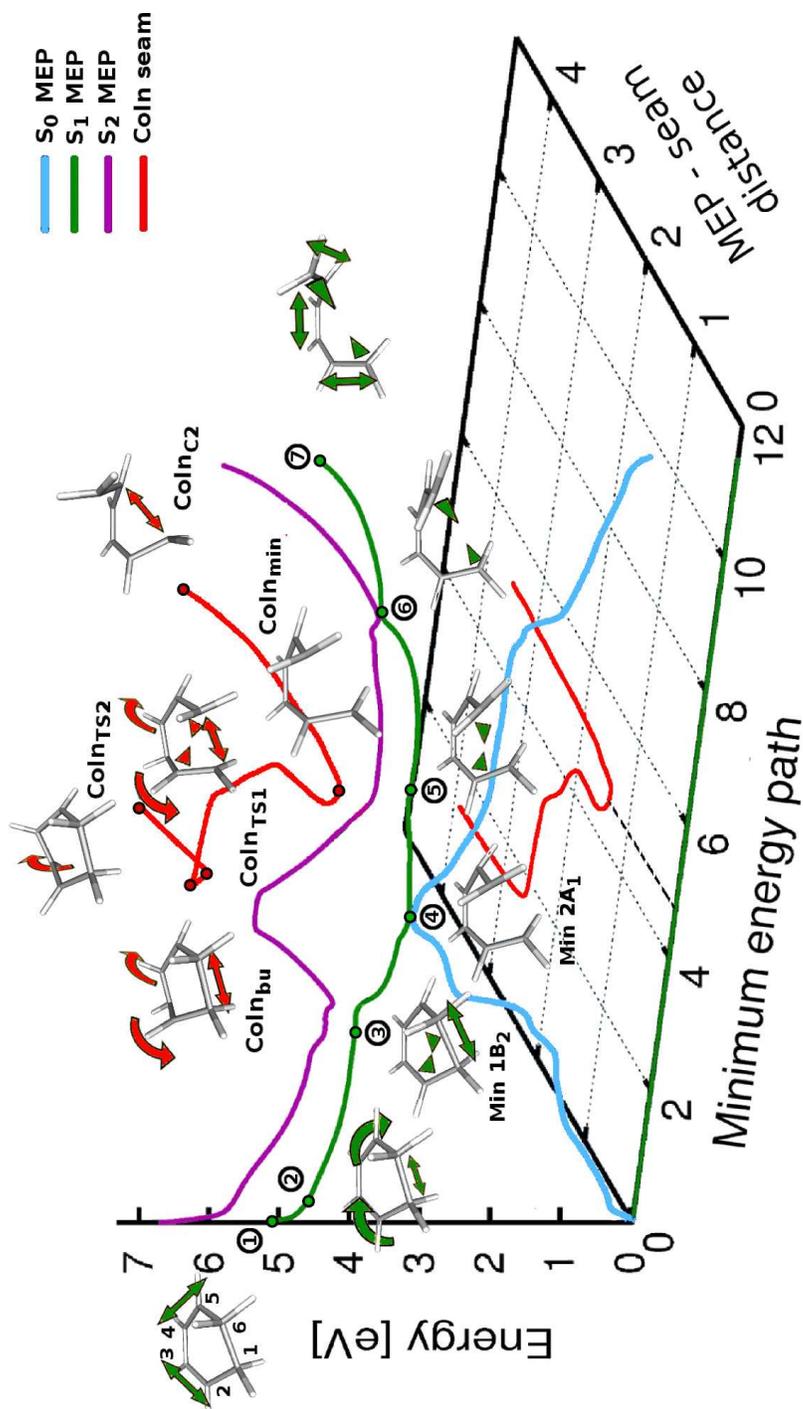
Figure 4.2.: Potential energy curves for the lowest three electronic states along the MEP on the first ES, obtained at MS-MR-CASPT2(2,2) level. The spatial relation to the extended CoIn seam (absolute distance in space) is visualized by drawing each point on the seam opposite to the nearest point from the MEP. For the energetic comparison the minimum energy CoIn (CoIn$_{min}$) was put on a level with the global minimum on the first ES. Selected geometries together with leading deformations are shown.

4.2.1. Statical view: Conical intersection seam and excited state minimum energy path

The first ES of CHD has a $\pi\pi^*$-configuration (B_2-symmetry) and is spectroscopically accessible (tab. 4.1). The second ES is a doubly excited dark state with A_1-symmetry. It is a well-known fact that CASSCF(6,6) including the π-orbitals in the active space underestimates the stabilization of the $1B_2$-state and predicts a false state order in the FC-region (Table 4.1)[244]. CASPT2(6,6) corrects the behavior and improves the excitation energy to match the experimental value of 4.96 eV (Table 4.1). A trimmed-down CASPT2(2,2) calculation including only two electrons and two orbitals in the active space of the underlying CASSCF calculation gives an excitation energy into the $1B_2$-state of 5.23 eV, not too far from the value obtained with the larger active space. The second ES of A_1-symmetry is underestimated by over 0.6 eV (Table 4.1) because HOMO-1→LUMO and HOMO→LUMO+1 excitations have significant contribution to its wavefunction in the FC-region. Their contributions cannot be fully recovered by perturbational treatment. Possible consequences for the quasi-classical dynamics are discussed in the next section.

	CASSCF(2,2)		CASPT2(2,2)	CASSCF(6,6)		CASPT2(6,6)	exp.
	ΔE	ES config.	ΔE	ΔE	ES config.	ΔE	
$1B_2$	5.92	$\pi_3\pi_4$ (1.00)	5.23	7.15	$\pi_3\pi_4$ (1.00) π_4^2 (0.38)	5.04	4.96
$2A_1$	9.97	π_4^2 (1.00)	6.86	6.54	$\pi_2\pi_4$(0.25) $\pi_3\pi_5$ (0.15)	6.25	-

Table 4.1.: Vertical excitation energies to $1B_2$ and $2A_1$ states from the GS equilibrium of CHD. The 6-31+G* basis set was used throughout. The major configurations, contributing to the ES wavefunctions, are denoted. The experimental value corresponds to the maximum of the longest wavelength band from the gas-phase UV spectrum in ref. [238].

The ES MEP[2] connecting the FC points of CHD and HT is shown in fig. 4.2 (green line). To check the quality of the MEP a comparison of selected geometries along the MEP to geometries optimized at MS-MR-CASPT2(6,6)/6-31G* level is made. Latter are taken from ref. [246]

Starting from the closed-ring side (C_1-C_6 distance of 1.56 Å) the FC point ① of the $1B_2$ state is left by double-bond/single-bond rearrangment in the 4π butadiene moiety, associated with a strong decrease of energy (segment ①-②). The weakening of the double bonds facilitates wagging deformations of the hydrogens attached to C_2

---

[2]The MEP was approximated in a series of geometry optimizations with a maximal step size of 0.015 Bohr. The segments ①-③ and ⑦-⑤ were obtained through optimizations from the associated FC points ① and ⑦. The transition states in the segments ③-④ and ⑤-④ were estimated by linear interpolation. Backward and forward optimization from the energetically highest point along the interpolated line completed the MEP.

| | CASPT2(2,2) | | | | CASPT2(6,6) | | | |
	$\Delta E_{S_0 S_1}$	ΔE_{S_1}	C_1-C_6	C_2-C_6	$\Delta E_{S_0 S_1}$	ΔE_{S_1}	C_1-C_6	C_2-C_6
Min $1B_2$	2.86	-0.97	1.754	2.535	3.02	-0.87	1.727	-
Min $2A_1$	0.09	-1.49	2.092	2.375	0.00^1	-1.63	2.137	2.394

[1] Global minimum coincides with the minimum energy CoIn.

Table 4.2.: Structural and energetic comparison between stationary points along the MEP obtained at MS-MR-CASPT2(2,2)/6-31+G* level and geometries from ref. [246] optimized at MS-MR-CASPT2(6,6)/6-31G* level.

and C_5. These deformations gradually induce interactions between the π-electrons of the butadiene moiety and the electron pair in the C_1-C_6 σ-bond and start the electrocyclic ring-opening (segment ②-③). The σ-bond elongate until a shallow minimum ③ on the first ES PES with C_2-symmetry is reached at approx. 1.75 Å. Optimization at MS-MR-CASPT2(6,6) level finds an intermediate with a very similar structure (table 4.2). Further elongation of the σ-bond combined with an asymmetric distortion, a shortening of the C_6-C_2 distance, stabilizes the $2A_1$ state below the $1B_2$ state. The asymmetric deformation allows the molecule to circumvent the apex of the CoIn between the $2A_1$- and $1B_2$-states. It proceeds on the lower PES towards the global minimum of the first ES ④[3] and towards the CoIn seam. The existence of an intermediate minimum ③ is discussed controversially in literature and depends on the quantum chemical method used to obtain the MEP[244]. In any case, due to the large potential energy decrease from the FC point of nearly 0.95 eV the barrier height of solely 0.05 eV is not expected to impact the dynamics.

Starting at the FC point ⑦ on the open-ring side (C_1-C_6 distance of 3.47 Å) double-bond/single-bond rearrangment in the 6π hexatriene triggers immediately the ring-closure. No asymmetric deformation is induced on crossing through the $1B_2/2A_1$ CoIn ⑥ at 2.73 Å. Further relaxation on the $2A_1$-state leads to a shallow minimum ⑤ at 2.21 Å. An asymmetric deformation, shortening of the C_2-C_6-distance, drives the system towards the global minimum ④ and towards the CoIn seam. The calculated barrier of 0.02 eV can be neglected due to the preceeding decrease of the potential energy of nearly 2.10 eV.

The C_2-symmetry is preserved on the major part of the ES MEP in the segments ①-③ and ⑦-⑤. Only in the region around the global minimum ④ asymmetric distortion is observed. However, exactly this asymmetric deformation drives the system towards the seam and accelerates the isomerization dynamics by several orders of magnitude.

Calculations at CASSCF(6,6) level predict energy gaps at the global minimum of nearly 1.0 eV, demanding strong geometrical deformations to reach the CoIn seam[47, 240]. On MS-MR-CASPT2(2,2) the global minimum exhibits a much smaller energy gap of solely 0.09 eV. Accordingly, only minimal deformations are required to

[3]There exist two equivalent mirror-symmetric minima in whose vicinity the C_2-symmetric region becomes a potential ridge[47, 240].
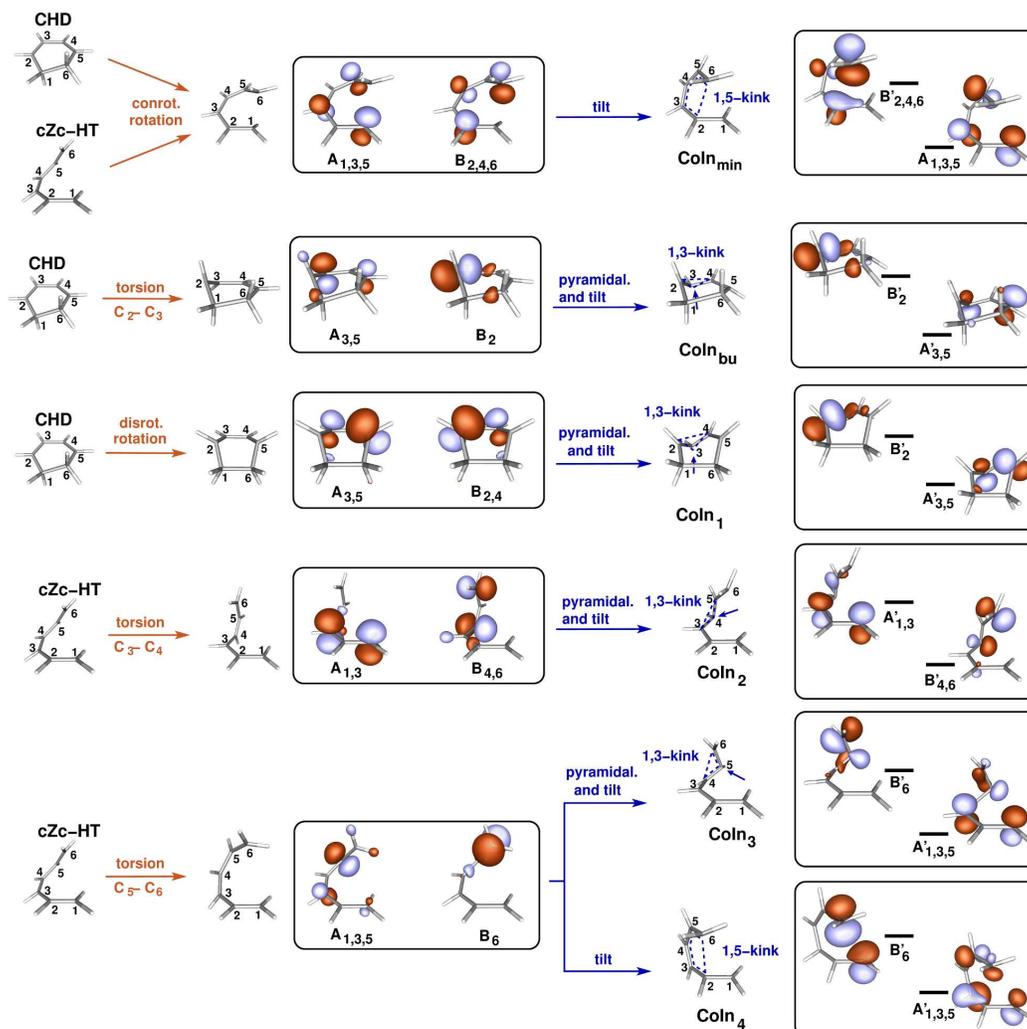
Figure 4.3.: CoIns, predicted with the rules of thumb given in sec. 2.2 and optimized at CASSCF(6,6)/6-31G* level. Red arrows denote the WH-coordinate (see sec. 2.2). Motion along this coordinate fulfills the *resonance* condition eq. 2.13 leading to the homosymmetric biradicals (middle column). Blue arrows indicate the subsequent deformations (pyramidalization, tilt), which fulfill the *heterosymmetry* condition (eq. 2.14) and lead to the individual CoIns (right column). For each CoIn, dashed blue lines denote the characteristic 1,3/1,5-kinks, blue arrows denote the center of pyramidalization.

access the CoIn seam. This is confirmed by comparing the structure of the global minimum ④ to the $CoIn_{min}$ optimized on MS-MR-CASPT2(6,6) level (tab. 4.2). The distance between the MEP and the CoIn seam is very sensitive to the dynamic correlation. At CASSCF level they are further apart than at CASPT2 level.

Next, the CoIn seam, is characterized. It was optimized in a colaboration with the
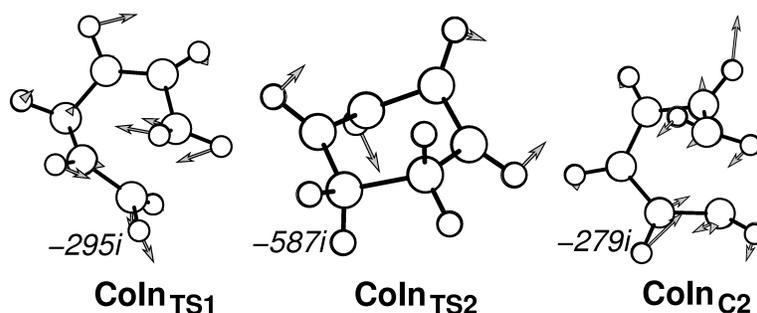
Figure 4.4.: Normal modes to the imaginary frequencies for the transition state geometries along the CoIn seam.

group of Michael A. Robb using their algorithm implemented in a development version of Gaussian[93] and described in ref. [92].

In the scope of the extended two-electron two-orbital model (sec. 2.1.1) the lowest point on the seam $CoIn_{min}$ can be rationalized (see sec. 2.4.1) by realizing that it is connected to the C_2-symmetry conserving conrotatory rotation. Along this WH-coordinate (sec. 2.2) the frontier orbitals degenerate (at the pericyclic minimum), thus fulfilling the *resonance* condition (eq. 2.13), and localize at C_1, C_3, C_5 and at C_2, C_4, and C_6, respectively (fig. 4.3, top). These orbitals are labeled $A_{1,3,5}$ and $B_{2,4,6}$. Subsequently, a tilt of C_6 towards C_2 leads to an arrangement which enhances the electronic repulsion in orbital $B_{2,4,6}$. Thereby the biradical GS $\left| A^\bullet B^\bullet \right\rangle$ is destabilized toward a CoIn with the $\left| A^2 \right\rangle$ ES (fig. 4.3, top).

Starting from $CoIn_{min}$ seam extensions in ring-closing and ring-opening directions were optimized (red curve in fig. 4.2). In ring-closing direction the formation of the C_1-C_6 σ-bond is accompanied by a twist around the C_2-C_3 bond (fig. 4.2) and a local minimum in the IS $CoIn_{bu}$ emerges. Its structure can be also elucidated with the rules of thumb given in sec. 2.2 (see sec. 2.4.1). $CoIn_{bu}$ formation is associated with a torsion around the C_2-C_3 double bond of the ethylene sub-unit of CHD (WH-coordinate) leading to a homosymmetric biradical with localized orbitals $A_{3,5}$ and B_2 (fig. 4.3). Pyramidalization at C_3 (denoted by a blue arrow in fig. 4.3) and tilt of C_2 towards C_4 forms a triangular arrangement between the adjacent centers C_2, C_3, and C_4. The pyramidalization lowers the energy of orbtial $A_{3,5}$ while the tilt raises the energy of orbital B_2. In the following, this arrangement is referred to as a 1,3-kink (marked by a dashed blue line in fig. 4.3).

A transition state on the CoIn seam $CoIn_{TS1}$ connecting $CoIn_{bu}$ to $CoIn_{min}$ was located. Its stationary nature was verified by a frequency analysis in the IS[59, 60], revealing one imaginary mode (fig. 4.4). $CoIn_{TS1}$ has an interesting chemical relevance since it resembles a bond-breaking/making transition state along the seam. In the region between $CoIn_{bu}$ and $CoIn_{TS1}$ only relaxation towards CHD is possible, at $CoIn_{TS1}$ a concurring channel towards HT opens. In the closed-ring region the seam was further extended to a C_2-symmetric $CoIn_{TS2}$ (fig. 4.2). Frequency analysis (fig. 4.4) revealed that $CoIn_{TS2}$ is a transition state in the IS connecting two equivalent

119

asymmetric minima $CoIn_{bu}$.

In ring-opening direction the CoIn seam extends to a C_2-symmetric $CoIn_{C2}$ (fig. 4.2) which is also a transition state in the IS (fig. 4.4), connecting two equivalent asymmetric minima $CoIn_{min}$. In fact, the optimized CoIn seam constitutes a closed loop in the IS:

$$\ldots\text{-}CoIn^*_{bu}\text{-}CoIn_{TS2}\text{-}CoIn_{bu}\text{-}CoIn_{TS1}\text{-}CoIn_{min}\text{-}CoIn_{C2}\text{-}CoIn^*_{min}\text{-}CoIn^*_{TS1}\text{-}CoIn^*_{bu}\text{-}\ldots$$

where the * denotes mirror-symmetry.

Symmetric CoIns (e.g. $CoIn_{TS2}$ and $CoIn_{C2}$) cannot be explained with the extended two-electron two-orbital theory (sec. 2.1.1) because they preserve the degeneracy of the two localized active orbitals *A* and *B*, while fulfillment of the *heterosymmetry* condition eq. 2.14 requires asymmetric deformations which lift the degeneracy. In fact, formation of symmetric CoIns can be attributed to the interactions of *A* and *B* with energetically higher lying virtual orbitals. These interactions are missing in the extended two-electron two-orbital theory. Nevertheless, due to the additional requirement of symmetry conservation symmetric CoIns lie typically energetically higher than asymmetric CoIns (e.g. $CoIn_{min}$ and $CoIn_{bu}$).

Next, the geometrical relation between the MEP and the CoIn seam is addressed. Fig. 4.2 visualizes the absolute distance (y-axis) in space. Each point on the CoIn seam is only related to its nearest point on the MEP. The result demonstrates that the MEP and the CoIn seam are not parallel in space. Rather, they are curved with respect to each other. Partially differing motions can occur along both paths which affect their absolute distance and differ from region to region. The MEP and the CoIn seam approach each other in the vicinity of the global minimum where also $CoIn_{min}$ is found. In the region between $CoIn_{min}$ and $CoIn_{TS1}$ MEP and seam are dominated by similar deformations, the shortening/elongation of the C_1-C_6 and C_2-C_6-distances. In the closed-ring and open-ring regions the MEP and the seam develop different deformations. Strong torsions in the 4π moiety along the $CoIn_{TS1}$-$CoIn_{bu}$-segment and shortening of the C_1-C_5-distance along the $CoIn_{min}$-$CoIn_{C2}$-segment are observed, which are essentially different from the motions along the MEP. Correspondingly, the distance between the MEP and the CoIn seam is large in the FC-regions. This complex relationship is subsumed in the expression quasi-parallel.

A consequence of the quasi-parallelism is that there is no unique seam associated with the MEP. Rather, multiple CoIn seam segments can arise in the $3N-8$ dimensional IS. This idea initiated the search for further CoIns using the predictive power of the rules of thumb, formulated in sec. 2.2[125]. Selected CoIns are presented with their localized orbitals in fig. 4.3. All CoIns have been obtained by starting either from the closed- or the open-ring isomer, selecting 2π- or 4π-subunits and then following the associated WH-coordinate (e.g. double bond torsions for 2π-subunits). By this operation homosymmetric biradical geometries were reached where both frontier orbitals become degenerate (fig. 4.3, middle column). Subsequent pyramidalization and tilt at selected centers led to different geometrical arrangements, which served as starting geometries for the actual quantum chemical optimization. Statical calculations render all located CoIns accessible from the FC point. However, they have

a different geometrical and energetic relation to the MEP. It is therefore an open question which CoIns actually play role in the photoisomerization. This question is addressed by mixed quantum-classical CASPT2 dynamics.

4.2.2. Absorption spectra

The MS-MR-CASPT2(2,2) calculations limits the description to the energetically lowest two states with A_1-symmetry and one state with B_2-symmetry. While the energetic profile of the $1B_2$ is correctly reproduced along the MEP, the energy of the $2A_1$ state is underestimated in the FC-region (tab. 4.1). Therefore, one concern is whether this inconsistency could affect the simulations. It needs verifications, whether low-frequency asymmetric vibrational modes induce oscillator strength in the excitation to the $2A_1$-state, which is dark at the C_2-symmetric GS equilibrium geometry and whether this excitation is correctly described at CASPT2(2,2) level.
For this purpose the absorption spectrum of CHD was calculated starting from Wigner distribution around the equilibrium geometry of the GS. A set of 1000 samples was used and the calculated signals were convoluted with Gaussians of a Full Width at Half Maximum (FWHM) of 2.5 nm. Figure 4.5a shows a reference absorption spectrum at MS-SR-CASPT2(6,6)/cc-pVDZ level averaging over the GS and lowest three ES ($1B_2$, $2A_1$ and $3A_1$), figure 4.5b shows the spectrum at MS-SR-CASPT2(2,2)/6-31+G* level (used for the subsequent dynamics simulations) averaging over the GS and the lowest two ES ($1B_2$ and $2A_1$). Vertical excitation energies from the equlibrium geometry is denoted with bars whose (normed) height is proportional to the oscillator strength of the transition. Contributions to the absorption signal coming from excitation to the $1B_2$-, $2A_1$- and $3A_1$-states are coded in red, blue and green, respectively.
The reference absorption spectrum consists of a low-energy band (290-210 nm) from the excitation to the $1B_2$ state, a high-energy band (180-130 nm) from excitation to the $3A_1$ state and a weak band from excitation to the $2A_1$ state (220-160 nm). The spectrum reproduces well the steady state absorption spectra published in the literature[238, 240, 247]. Apparently, the $1B_2$ transition dominates the low-energy window. The absorption spectrum obtained with the smaller active space reproduces well the low-energy absorption region. For comparison, the spectrum resulting by omitting the perturbative correction (i.e. at CASSCF(2,2)/6-31+G* level, fig. 4.5, bottom) exhibits a strong hypsochromic shift. Naturally, the intensive absorption band in the high-enegry region is missing. The contribution of the excitation to the $2A_1$-state is underestimated in the spectrum.
In summary, the experimental setup of Fuss et. al which use pulses around 270 nm[238] is best suited for comparison with the presented simulations. The incomplete description of the $2A_1$ state in the FC-region will not interfere with the initial dynamics.
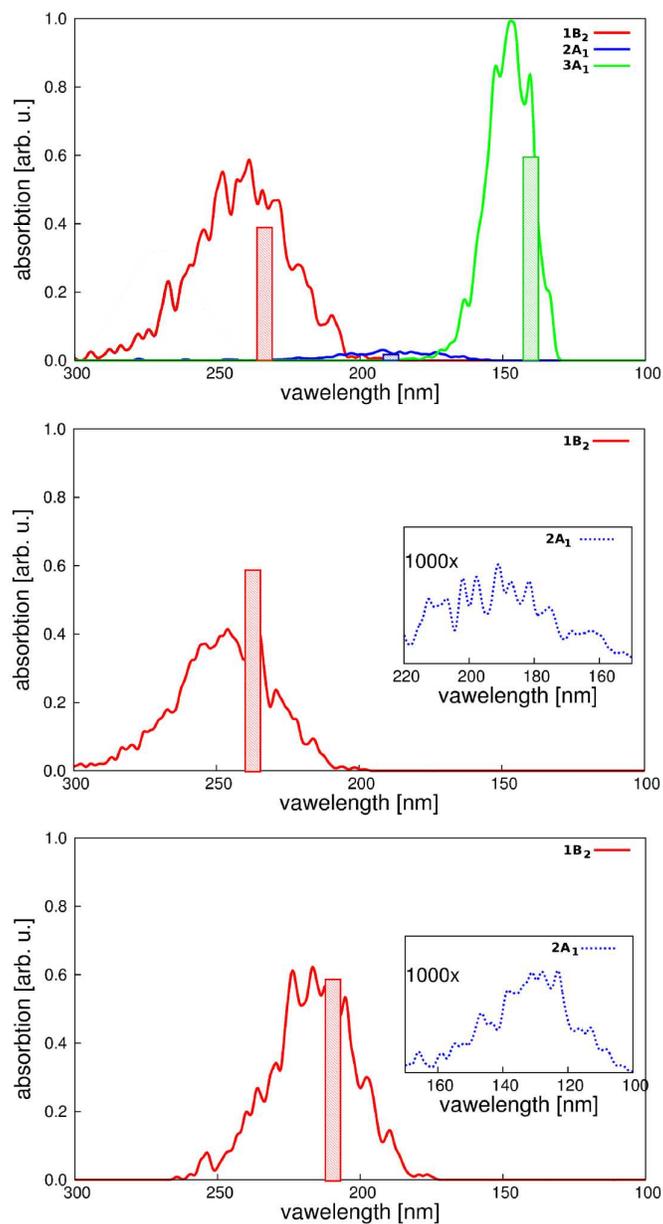
Figure 4.5.: Calculated absorption spectra of CHD at MS-SR-CASPT2(6,6)/cc-pVDZ (top), MS-MR-CASPT2(2,2)/6-31+G* (middle) and CASSCF(2,2)/6-31+G* (bottom). Contributions to the absorption signal coming from excitation to the $1B_2$-, $2A_1$- and $3A_1$-states are coded in red, blue and green, respectively. Vertical excitation energies from the GS equlibrium geometry are denoted with color bars.
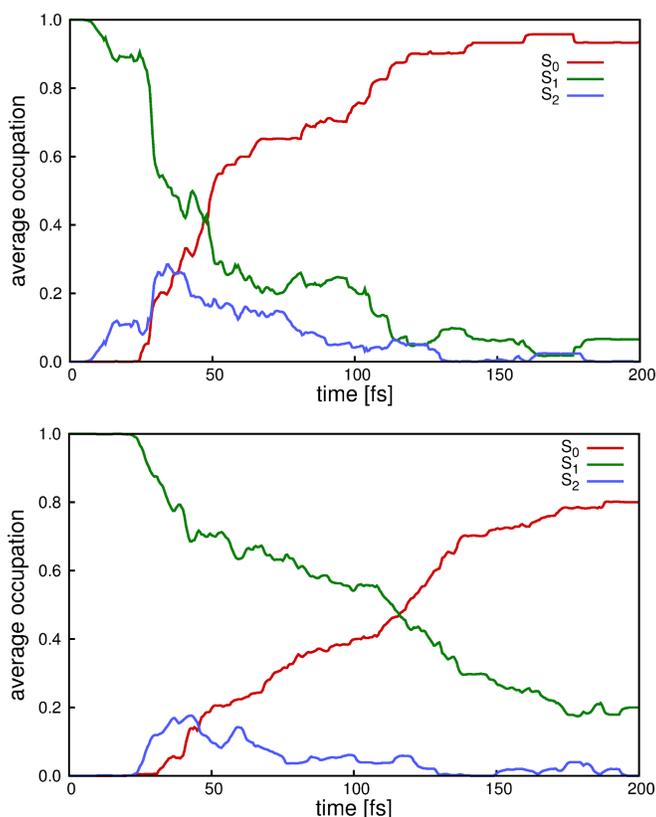
Figure 4.6.: Time evolution of the average population in the electronic states included in the dynamic simulation performed at MS-MR-CASPT2(2,2)/6-31+G* (top) and CASSCF(2,2)/6-31+G* (bottom).

4.2.3. Dynamical view: The accessibility of the conical intersection seam

A set of 50 trajectories was run with the modified version of Newton-X for 200 fs with a time step of 0.5 fs starting in the first ES with $1B_2$-symmetry. The quantum chemical calculations were performed at MS-SR-CASPT2(2,2)/6-31+G* level averaging over three states. Hopping probabilities were obtained in each step by calculating the projection of the non-adiabatic couplings onto the velocity vector (sec. 4.1.6). After a successful hopping event the velocity was adjusted along the gradient difference vector. A comparative simulation over 50 trajectories was run at CASSCF(2,2)/6-31+G* level with analytical non-adiabatic couplings.

Figure 4.6, top gives the average occupation $\overline{a}_{jj}(t)$ (eq. 4.19) of the individual states during the CASPT2 simulation. In the beginning only the first ES is occupied (green line). Initial decay at approx. 5 fs is accompanied by population increase in the second ES which lasts until 35-40 fs. Thereafter a slow decrease of the population of the second ES within 100 fs occurs. A rapid population of the GS begins only after

25 fs. Within 50 fs half of the population is transferred to the GS, after 150-200 fs the transfer is almost quantitative.

Relying on the MEP (fig. 4.2) the following mechanism for the depopulation of the ES is derived. After excitation to the bright $1B_2$-state initial relaxation occurs within 5-6 fs (τ_1) and drives the system towards the $1B_2/2A_1$-crossing region. The occupation increase in the second ES manifests the approching of the $1B_2/2A_1$ CoIn. Approximately two-thirds of the molecules circumvent the CoIn apex and evolve further on the first ES, which has now adopted a $2A_1$ character. To obtain information about the kinetics of this process the evolution of the average transition dipole moment μ_{10} between the GS and the first ES was tracked with time (fig. 4.7, middle). Thereby the fact was utilized that the dipole moment μ_{10} decreases rapidly with enhancing $2A_1$ character (fig. 4.7, top, approx. 2.5 units). Hence, it constitutes a suitable observable to determine an approximate time constant for the ES character change. By a monoexponential fit of the average dipole moment decay a time constant $\tau_2 = 17.5 \pm 0.3$ fs was obtained. The molecules that go around the $1B_2/2A_1$ CoIn quickly apporach the GS/ES CoIn seam and give rise to the initial rapid occupation increase of the GS within the first 50 fs. One-third of the molecules switch into the second ES by conserving momentum along the C_2-symmetric coordinate, i.e. going through the $1B_2/2A_1$ CoIn. Their return to the first ES within the next 100 fs is responsible for the slower occupation increase at later times. An effective time constant $\tau_3 = 45.5 \pm 0.9$ fs was obtained for the overall process by fitting the total occupation decay of both ES $\bar{a}_{11} + \bar{a}_{22}$. In the end, the overall time needed to return to the GS is obtained as the sum of the three time constants as approx. $5.5 + 17.5 + 45 = 68$ fs. The propposed mechanism agrees with experimental findings. It confirms the ballistic model proposed by Fuss et al.[240] as two-thirds of all molecules are found to circumvent the $1B_2/2A_1$ CoIn and reach the GS/ES seam instantaneuosly. The time constants, associated with the individual processes, are, though, shorter than the constants recorded experimentally ($\tau_1 = 21$ fs, $\tau_2 = 35$ fs, $\tau_3 = 80$ fs)[238]. To analyze this discrepancy a closer look at the hopping events between the GS and ES during the CASPT2 simulations (fig. 4.8 green bars) is required. While the majority of hops occur for gaps between 0.1 and 0.5 eV energy gap one out of four hops occurs at an energy gap larger than 1.0 eV, i.e. in regions with small non-adiabatic couplings. The comparative CASSCF(2,2) simulations undergo hops in a more limited energy window (fig. 4.8 red bars) and, consequently, show a considerably slower dynamics (fig. 4.6, bottom). Thereby, the return to the GS takes approximately twice as long (125 fs) as obtained from the CASPT2 dynamics.

Next, the relaxation to the GS via the GS/ES CoIn seam is analyzed in detail. A spatial correlation between hopping geometries and the CoIn seam is established and dynamically accessible regions on the seam are extracted. Hopping events at large energy gaps occur away from the CoIn seam and are not considered in the evaluation. They have no physical meaning and arise due to the stochastical nature of the dynamics. For a total of 41 hopping geometries the spatial overlap with stationary CoIns from the seam (fig. 4.2) and the CoIns obtained with the extended two-eletron two-orbital theory (fig. 4.3) was calculated. As all CoIns are available
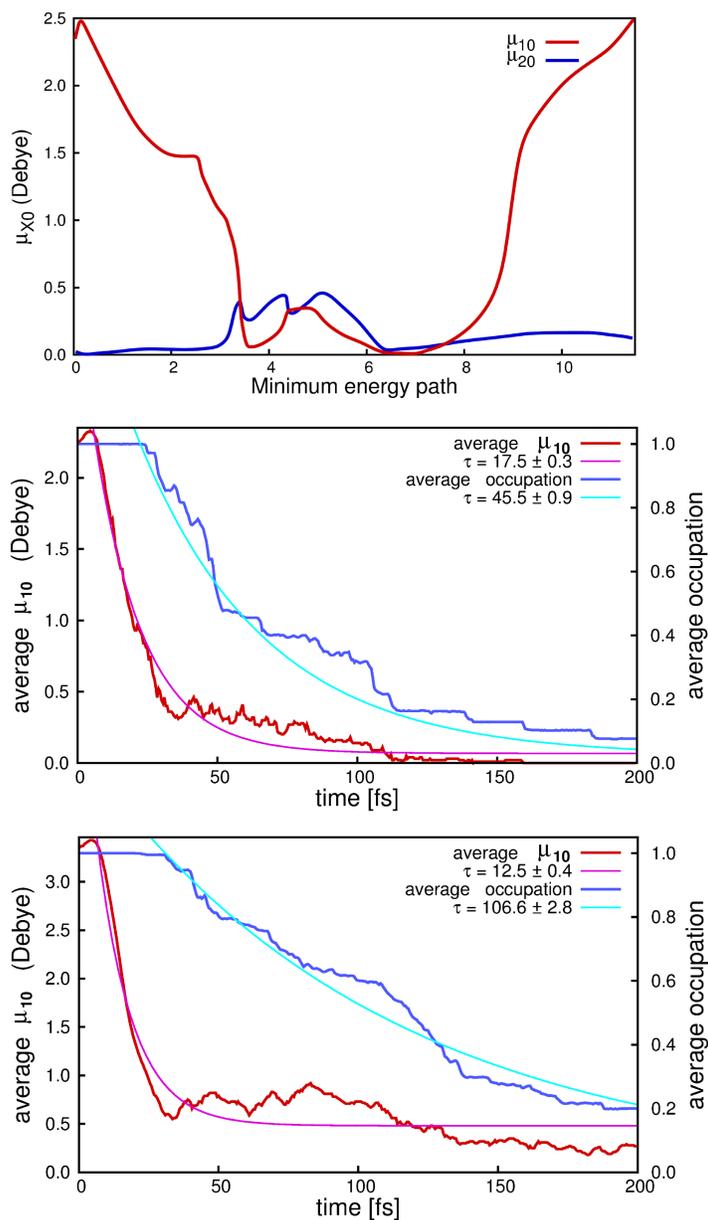
Figure 4.7.: (top) Evolution of the transition dipole moments μ_{10} (GS $\rightarrow$ first ES) and μ_{20} (GS $\rightarrow$ second ES) along the MEP; (middle, bottom) Time evolution of the transition dipole moment μ_{01} (red line) and of the average total population in the first and second electronic ES (blue line) from MS-MR-CASPT2(2,2)/6-31+G* (middle) and CASSCF(2,2)/6-31+G* (bottom) simulations. Monoexponential fits are also shown.
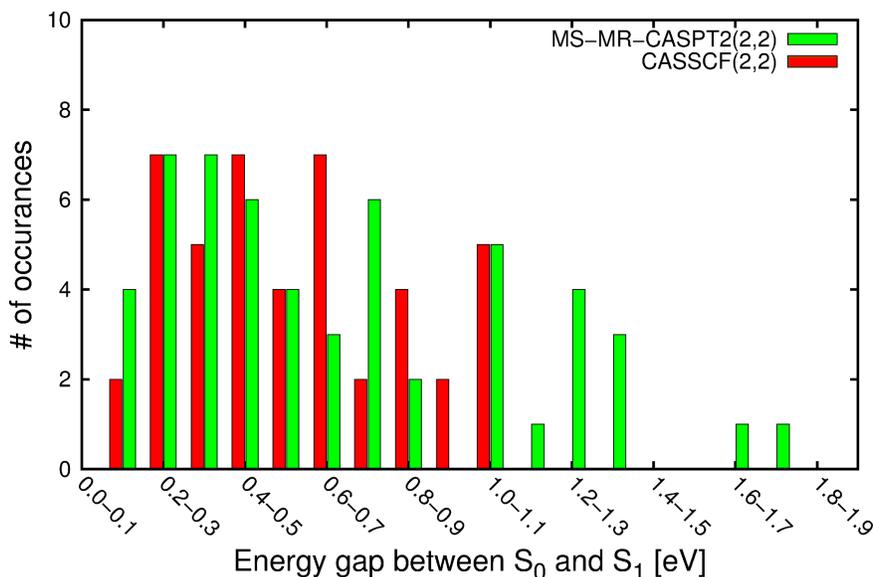
Figure 4.8.: Hopping occurances against the energy gap between the GS (S_0) and the first ES (S_1) during the MS-MR-CASPT2(2,2)/6-31+G* (green bars) and the CASSCF(2,2)/6-31+G* (red bars) simulations.

only at CASSCF(6,6)/6-31G* level it was approximated that the basic geometrical features, characterizing each CoIn (1,3-, 1,5-kink, etc.) are independent of the dynamic correlation. It turns out that the hopping geometries exhibit large resemblance to either $CoIn_{min}$ or $CoIn_{TS1}$ and two-thirds of the hopping events occur in the spatial proximity of $CoIn_{min}$. Among the 41 samples there were no geometries close to any of the stationary CoIns given in fig. 4.3. In fig. 4.9 the correlation between hops, MEP and CoIn seam is visualized in the reduced space of three reactive coordinates, suitable for descriminating the deformations along the MEP and the seam. The C_1-C_4-C_3-C_6 dihedral angle describes the symmetry conserving ring-opening and, thus, the major part of the MEP, except for the region around the perycyclic minimum, where asymmetric deformations towards the seam are initiated (fig. 4.2). These asymmetric deformations are described by the C_2-C_6 coordinate. In addition a third coordinate, the dihedral angle between the normals through C_2 and C_3, perpendicular to the first substituents of C_2 and C_3, respectively, describes the wagging deformations of the hydrogen atoms along MEP and seam. They are essential for both the coupling of the π-system to the σ-bond and for the formation of the 1,3-kink around $CoIn_{bu}$ (fig. 4.2).

In the reduced coordinate space the MEP (green line in fig. 4.9) and CoIn seam (red line in fig. 4.9) exhibit regions which are spatially close and others that are far apart, in agreement with the representation in fig. 4.2. Hoppings (blue and magenta dots) are confined to the region between the MEP and the CoIn seam. Now, further details can be added to the isomerization mechanism. The FC (CHD in fig. 4.9) point is left by wagging deformations in the butadiene moiety, leading to an increase of the N_{C_2}-
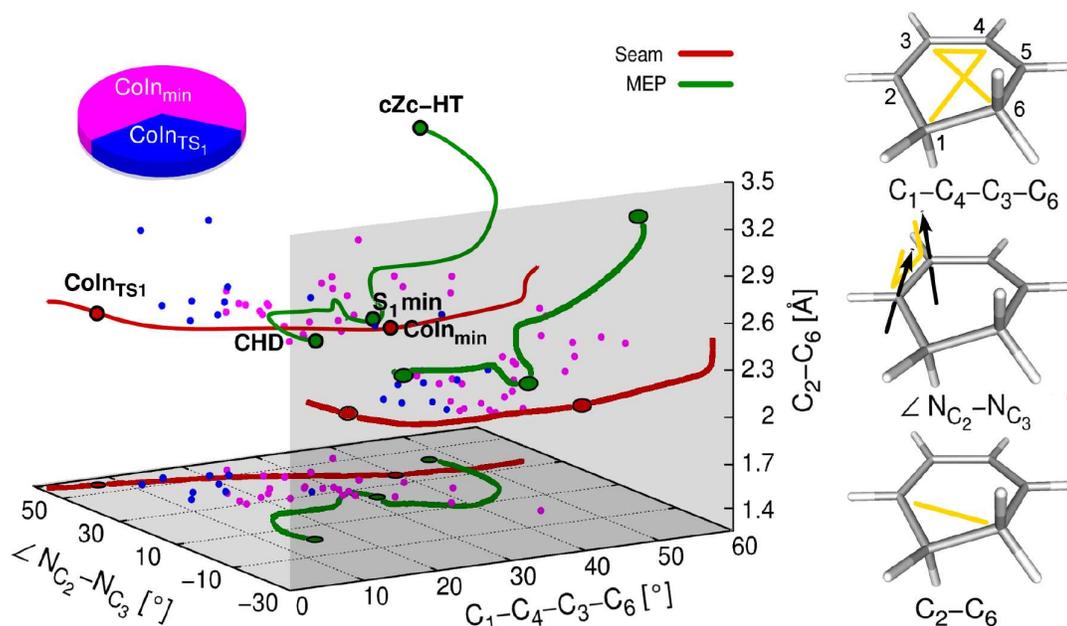
Figure 4.9.: Correlation between hops (blue and magenta dots), MEP (green curve) and CoIn seam (red curve) visualized in the reduced space of three reactive coordinates: the dihedral angle C_1-C_4-C_3-C_6, the dihedral angle between the normals through C_2 and C_3, perpendicular to the first substituents of C_2 and C_3, respectively, and the distance C_2-C_6. Two-dimensional projections are also shown. The pie chart shows the ratio of hops closer either to $CoIn_{min}$ or to $CoIn_{TS_1}$.

N_{C_3} angle. As a result the system accumulates momentum in the direction towards the seam. Correspondingly, a significant number of hopping events is observed in the region equally far from $CoIn_{min}$ and $CoIn_{TS1}$. Plotting the hoppings against time (fig. 4.10) shows that the relaxation through this region of the seam occurs within a time window of 20-60 fs (Note, that almost all hopping events close to $CoIn_{TS1}$ occur in this time window.). Bifurcation in the GS towards reactant and product is observed with no preferential formation of either isomer. This is reasonable since the breaking of the σ-bond is initiated at $CoIn_{TS1}$, thus, all hoppings occur in a region with a partially broken σ-bond. The remaining molecules which do not accumulate enough momentum towards the seam follow the MEP before hitting the seam in the region around $CoIn_{min}$. Its surrounding constitutes the most effective relaxation channel. Again, no preferential formation of either isomers is observed (fig. 4.2).

To sum up, the isomerization of CHD on MS-MR-CASPT2(2,2) level occurs along an extended region of CoIn seam and the relaxation is not confined to the very vicinity of $CoIn_{min}$. On the other hand, not the entire CoIn seam is equiprobably accessible. The closed-ring segment around $CoIn_{bu}$ and the open-ring segment around $CoIn_{C2}$ seem hardly reachable. Furthermore, the seam segment accessed preferentially in-

127
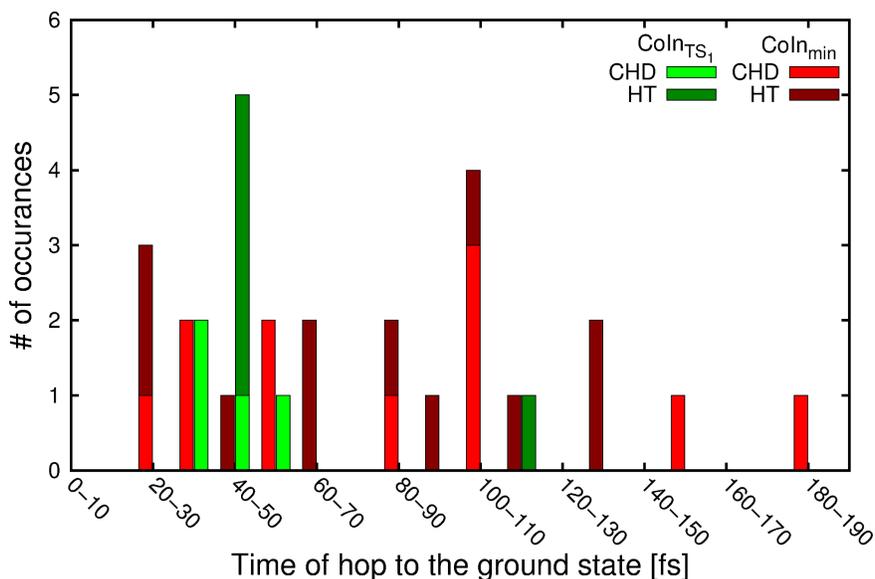
Figure 4.10.: Hopping occurances with time during the CASPT2(2,2)/6-31+G*
simulations. Hopping geometries closer to $CoIn_{TS_1}$ are denoted in green, hopping
geometries closer to $CoIn_{min}$ are denoted in red. Formation of CHD after hopping
is encoded with darker colors, formation of HT with lighter color.

duces a bifurcation in the GS, which results in an isomerization quantum yield of
55%. This value, however, overrates the experimentally measured yield of 40%.
As already mentioned earlier, $CoIn_{C2}$ and $CoIn_{TS2}$ are not properly described at
CASPT2(2,2) level due to the limited size of the active space. Thus, relaxation
through these channels, as observed in the quantum dynamical simulations on
CASSCF(6,6) level, could have been underestimated in the quasi-classical simula-
tions in their current form. Simulations with larger active spaces are required to
address this question.

4.2.4. Summary and perspectives

Mixed quantum-classical dynamics simulations at MS-MR-CASPT2 level, using
Tully's surface hopping routine, were performed to study the ultrafast photoreac-
tivity of CHD in gas-phase. An interface of the package for Newtonian dynamics
Newton-X to the quantum chemistry package Molpro was designed and a numerical
rountine for the efficient calculation of non-adiabatic couplings at MS-MR-CASPT2
level was implemented.
The results confirm the ballistic model, proposed by Fuss and co-workers[240]. About
two-thirds of all excited molecules are found to circumvent the $1B_2/2A_1$ CoIn and
reach an extended region of the GS/ES seam instantaneuosly. Consequently, the iso-
merization proceeds on a femtosecond timescale. It was demonstrated that not the
entire low-energy seam is equiprobably reachable, rather, the accessibility depends

on the energetic and spatial relation between MEP and CoIn seam, as well as on the momentum which is accumulated during relaxation on the ES PES. The possibility to reach both isomers from each point on the accessible CoIn seam is responsible for the high quantum yield of $\approx 50\%$.

Although the present study sheds light into the isomerization mechanism, a quantitative agreement with the experimental observations is still out of reach. An improvement is expected by increasing the number of trajectories and the size of the active space. Including further π-orbitals in the active space will allow for a realistic description of the $2A_1$-state in the FC-region and for an accurate description of the relaxation through the symmetric CoIns $CoIn_{TS2}$ and $CoIn_{C2}$. This work is currently in progress.

Several questions, which were not addressed in this work, but are subject to future research, are: i) What is the role of the Rydberg states in the isomerization dynamics[240, 248]? ii) Can higher lying regions of the seam be reached by exciting CHD to higher vibrational levels of the ES? iii) It has been shown that complex laser pulses are required to control the isomerizational process[154, 249–253]. It is intriguing whether this complexity can be reduced by combining coherent control with chemical modeling of the CoIn seam.

5. Conclusion

The presented work explored with the help of state-of-the-art quantum chemical calculations and quasi-classical dynamics simulations how the chemical composition influences the photoreactivity of molecules. A relation between the molecular structure and the topography of the intersection space, the 3N-8 dimensional space where the degeneracy between the ground state and the excited state is preserved, was found. By exploiting this relation a systematic analysis of the intersection space becomes available. Benefits with regard to the optimization of conical intersections, molecular modeling and deciphering complex excited state dynamics were discussed. In this context quasi-classical dynamics simulations were used to explore the accessibility of the encountered energetically low lying regions of the intersection space, thereby providing detailed information about the spatial and temporal evolution of the photoreactions.

In the first part of this thesis the two-electron two-orbital theory introduced by Michl and Bonačić-Koutecký to rationalize the structure of conical intersections in charged polyene systems was extended by including the interactions of the active pair of electrons with the remaining closed-shell electrons that are present in any realistic system. A set of conditions, the *resonance* and the *heterosymmetry* conditions, for the formation of conical intersections in multielectronic systems were derived. The extended two-electron two-orbital model directly translates into a SA-3-CASSCF(2,2) set up with two active electrons in two localized active molecular orbitals. The molecular system is separated into basic units and units reflecting the actual substitution pattern. Calculations on this theoretical level were performed for the basic units ethylene, *cis*-butadiene and 1,3-cyclohexadiene at various geometries and functionalizational patterns. The quantitative results demonstrated that geometrical deformations and substituent effects constitute different mechanisms for achieving the same goal, namely, the formation of conical intersections. Based on this finding rules of thumb for their qualitative prediction in arbitrary polyenes were derived. Essentially, no other information besides the chemical composition of the system is necessary. An extension of the rules of thumb to conical intersection seams was also formulated. The general idea is to divide the intersection space into subspaces according to the following criteria:

(i) association with different Woodward-Hoffmann coordinates: for each basic unit identified in the system (e.g. different double bonds, *cis*-butadiene sub-units, etc.) a plane, orthogonal to the corresponding Woodward-Hoffmann motion, exists, which contains a fraction of the intersection space;

(ii) electronic structure of the excited state: the *heterosymmetry* condition forbids the change of the electronic configuration along the seam;

(iii) geometrical deformations and substituent effects which satisfy the *heterosymmetry* condition: when both are possible, geometrical deformations are discarded for energetical reasons;

(iv) connection to the reaction of interest: only subspaces are considered which contain conical intersections associated with the Woodward-Hoffmann motion of interest.

The dimensionality of the individual subspaces is reduced to a few degrees of freedom, which allows for the location of supporting points in each subspace. Individual subspaces are then connected by a linear interpolation scheme, which provides the initial guess for the conical intersection seam. This guess is then fed into a quantum chemistry package to finalize the conical intersection optimization.

The strategy was demonstrated for three polyene systems: CHD/cZc-HT as a representative of non-polar unfunctionalized polyenes, where CoIns are formed through geometrical deformations, HTI as a representative of weakly polar polyenes, where low-energy CoIns are formed by combining geometrical deformations and substituent effects and trifluoromethyl-pyrrolylfulgide as a representative of multi-functionalized strongly polar polyenes, where the functional groups alone determine the structure of the CoIns. The rules for optimizing single conical intersections were utilized to systematically scan the intersection space for minimum energy conical intersections and differentiate between high- and low-energy ones. Further, a seam connecting conical intersections associated with the *cis-trans* isomerization (i.e. the Woodward-Hoffmann motion) in hemithioindigo-hemistilbene was optimized. It was demonstrated by comparison with the basic unit ethylene that a similar seam exists in every compound capable of performing a *cis-trans* isomerization. The energetics and topography of the seam depend on the specific functionalization pattern. For pyrrolylfulgide, parts of the seam that either photostabilize the system or lead to by-prodcuts were found to compete with the reactive parts of the seam.

Understanding the mechanisms and requirements for formation of conical intersections provides the foundation needed to derive control schemes for quantum yield enhancement based on a combination of chemical synthesis and light control as proposed in ref. [254]. The performance of molecular switches and photostabilizers could be improved by opening or closing channels selectively by suitable chemical substitutions. The introduced rules of thumb provide already two strategies how this can be achieved: by either hindering the motions needed for the *resonance* condition or by weakening the mesomeric effects responsible for the formation of a distinct conical intersection. An intriguing perspectives lie in the utilization of polar solvents to tune the accessibility of conical intersections[255] and in the coherent laser control schemes[256] that address specific electronic effects by vibrational mode coupling and induce directed ultrafast decay through selected regions of the designed intersection space.

In the second part of this thesis the theoretical studies on hemithioindigo-hemistilbene and trifluoromethyl-indolylfulgide were deepened to obtain a detailed static picture of the isomerizational mechanisms. Experimentally determined rate constants could be assigned and processes, which cannot be distinguished spectroscopically were revealed. The proposed reaction mechanisms explain the observed differences in the dynamics of the forward and the backward reactions and are in good agreement with the measured quantum yields. Both the *cis-trans* isomerization in hemithioindigo-hemistilbene and the electrocyclic ring closure/opening in indolylfulgide are characterized by the formation of a charge transfer in the excited state. The ability of each system to stabilize this charge transfer is essential for the returning to the ground state. In the indolylfulgide the functional groups stabilze the charge transfer to a conical intersection with the ground state along the main reaction coordinate. The presence of functional groups opens a range of possibilities to stabilize the charge transfer by adjustment of the electrostatic interactions, rather then by geometrical deformations. Consequently, broad degeneracy regions between the ground and the excited state emerge, which allow for a fast return to the ground state. However, also loss channels become easily accessible and the selectivity of the isomerization is lost. In hemithioindigo-hemistilbene pyramidalization and tilt orient the molecule in an appropriate way for a charge balance recovery to take place via interactions of the π-system with the lone pairs of the heteroatoms.

In the last part of this thesis mixed quantum-classical dynamics simulations at multi-state multi-reference complete active space perturbation theory level, using Tully's fewest switches surface hopping approach, were performed to study the ultrafast photoreactivity of 1,3-cyclohexadiene in the gas-phase. The results confirm the ballistic model, proposed by Fuss and co-workers, as the major part of the excited molecules are found to circumvent the $1B_2/2A_1$ conical intersection and reach the conical intersection seam between the excited state and the ground state instantaneuosly. Time constants for the evolution of the wavepacket on the bright $1B_2$-state, the relaxation into the $2A_1$-state and the return to the ground state could be extracted, resulting in an overall reaction time of ≈ 70 fs. It was demonstrated that, effectively, only the part of the intersection space, facilitating relaxation to both the closed and the open ring structures, is used for the return to the ground state. The accessibility depends on the energetic and spatial relation between minimum energy path and accessible conical intersection seam, as well as on the momentum which is accumulated during relaxation on the excited state potential energy surface.

The incorporation of multi-configurational perturbation theory into the mixed quantum-classical dynamics allows for a nearly quantitative description of the electronic correlation. Consequently, time-resolved spectroscopic data can be reproduced with high accuracy from first principles. Recently, promising results have been published for ethylene[257]. With the approach outlined in this thesis prototypical and biologically relevant molecules like 1,3-cyclohexadiene and the DNA bases thymine and cytosine are now within reach. Furthermore, by incorporating environmental effects into the mixed quantum-classical dynamics scheme[258] this technique can be used as a powerful tool to test the applicability of the rules of thumb for molecular

modeling by sampling the accessibility of the designed conical intersection seam under realistic conditions. Finally, by comparing the results of the mixed quantum-classical dynamics to multi-dimensional quantum dynamics simulations (available for example within the multi-configurational time-dependent Hartee formalism[259]) the challenging question about the role of pure quantum effects in the molecular dynamics can be addressed[260].

A. Properties of the derivative couplings

To derive the left expression in eq. 1.11 we make use of the orthogonality of eigenfunctions of a hermitian operator

$$\left\langle \Psi_i^{\text{el}} \middle| \Psi_j^{\text{el}} \right\rangle = 0. \tag{A.1}$$

As the overlap A.1 remains zero for all values of α the derivative with respect to the nuclear coordinates is also zero

$$\nabla_\alpha \left\langle \Psi_i^{\text{el}} \middle| \Psi_j^{\text{el}} \right\rangle = \left\langle \nabla_\alpha \Psi_i^{\text{el}} \middle| \Psi_j^{\text{el}} \right\rangle + \left\langle \Psi_i^{\text{el}} \middle| \nabla_\alpha \Psi_j^{\text{el}} \right\rangle = 0. \tag{A.2}$$

From the above relation it immediately follows that the derivative coupling matrix is antihermitian, whose diagonal entries are zero

$$\left\langle \Psi_j^{\text{el}} \middle| \nabla_\alpha \Psi_i^{\text{el}} \right\rangle = -\left\langle \Psi_i^{\text{el}} \middle| \nabla_\alpha \Psi_j^{\text{el}} \right\rangle \quad \text{and} \quad \left\langle \Psi_i^{\text{el}} \middle| \nabla_\alpha \Psi_i^{\text{el}} \right\rangle = 0. \tag{A.3}$$

The right expression in eq. 1.11 is obtained by differentiating the electronic Schrödinger equation 1.4 with respect to each nuclear coordinate α and subsequently multiplying from left with Ψ_j^{el} and integrating over the electronic coordinates.

$$\begin{aligned}
\nabla_\alpha(\hat{H}^{el}\Psi_i^{\text{el}}) &= \nabla_\alpha(V_i\Psi_i^{\text{el}}) \\
(\nabla_\alpha\hat{H}^{el})\Psi_i^{\text{el}} + \hat{H}^{el}(\nabla_\alpha\Psi_i^{\text{el}}) &= (\nabla_\alpha V_i)\Psi_i^{\text{el}} + V_i(\nabla_\alpha\Psi_i^{\text{el}}) \quad | \quad \left\langle \Psi_j^{\text{el}} \middle| \right. \\
\left\langle \Psi_j^{\text{el}} \middle| \nabla_\alpha\hat{H}^{el} \middle| \Psi_i^{\text{el}} \right\rangle + \left\langle \Psi_j^{\text{el}} \middle| \hat{H}^{el} \middle| \nabla_\alpha\Psi_i^{\text{el}} \right\rangle &= V_i\left\langle \Psi_j^{\text{el}} \middle| \nabla_\alpha\Psi_i^{\text{el}} \right\rangle \\
\left\langle \Psi_j^{\text{el}} \middle| \nabla_\alpha\hat{H}^{el} \middle| \Psi_i^{\text{el}} \right\rangle &= V_i\left\langle \Psi_j^{\text{el}} \middle| \nabla_\alpha\Psi_i^{\text{el}} \right\rangle - V_j\left\langle \nabla_\alpha\Psi_i^{\text{el}} \middle| \Psi_j^{\text{el}} \right\rangle.
\end{aligned} \tag{A.4}$$

In the last line the hermiticity of the electronic hamiltonian was used. The above equation states that the derivative coupling between the states i and j is reciprocally proportional to their energy gap

$$\left\langle \Psi_j^{\text{el}} \middle| \nabla_\alpha\Psi_i^{\text{el}} \right\rangle = \frac{\left\langle \Psi_j^{\text{el}} \middle| \nabla_\alpha\hat{H}^{el} \middle| \Psi_i^{\text{el}} \right\rangle}{V_i - V_j} \quad \text{and} \quad \left\langle \Psi_i^{\text{el}} \middle| \nabla_\alpha\Psi_j^{\text{el}} \right\rangle = \frac{\left\langle \Psi_j^{\text{el}} \middle| \nabla_\alpha\hat{H}^{el} \middle| \Psi_i^{\text{el}} \right\rangle}{V_j - V_i} \tag{A.5}$$

B. Relation between the adiabatic vectors and the diabatic vectors

By using the two-state adiabatic to diabatic transformation (eq. 1.12) the gradient difference vector $\vec{X}_1$ (eq. 1.18) can be expressed as

$$
\begin{aligned}
\vec{X}_1 &= \nabla_R(V_1 - V_2) = \nabla_R(\left\langle \Psi_2^{\mathrm{ad}} \middle| \hat{H}^{el} \middle| \Psi_2^{\mathrm{ad}} \right\rangle - \left\langle \Psi_1^{\mathrm{ad}} \middle| \hat{H}^{el} \middle| \Psi_1^{\mathrm{ad}} \right\rangle) = \\
&\quad \nabla_R(\left\langle -\sin(\alpha)\Psi_1^{\mathrm{d}} + \cos(\alpha)\Psi_2^{\mathrm{d}} \middle| \hat{H}^{el} \middle| -\sin(\alpha)\Psi_1^{\mathrm{d}} + \cos(\alpha)\Psi_2^{\mathrm{d}} \right\rangle - \\
&\quad \left\langle \cos(\alpha)\Psi_1^{\mathrm{d}} + \sin(\alpha)\Psi_2^{\mathrm{d}} \middle| \hat{H}^{el} \middle| \cos(\alpha)\Psi_1^{\mathrm{d}} + \sin(\alpha)\Psi_2^{\mathrm{d}} \right\rangle) = \\
&\quad \nabla_R(\sin^2(\alpha)H_{11} - 2\sin(\alpha)\cos(\alpha)H_{12} + \cos^2(\alpha)H_{22} - \\
&\quad \cos^2(\alpha)H_{11} - 2\sin(\alpha)\cos(\alpha)H_{12} - \sin^2(\alpha)H_{22}) = \\
&\quad \cos(2\alpha)\nabla_R(H_{22} - H_{11}) - 2\sin(2\alpha)\nabla_R H_{12} = \cos(2\alpha)\vec{g} - 2\sin(2\alpha)\vec{h},
\end{aligned}
\tag{B.1}
$$

hence, $\vec{X}_1$ can be represented as a linear combination of the $\vec{g}$ and $\vec{h}$ vectors 1.17. The scaled derivative coupling vector $\vec{X}_2$ (eq. 1.18) can be expressed as

$$
\begin{aligned}
\vec{X}_2 &= (V_1 - V_2)\left\langle \Psi_1^{\mathrm{el}} \middle| \nabla_R \Psi_2^{\mathrm{el}} \right\rangle = \left\langle \Psi_1^{\mathrm{ad}} \middle| \nabla_R \hat{H}^{el} \middle| \Psi_2^{\mathrm{ad}} \right\rangle = \\
&\quad \left\langle -\sin(\alpha)\Psi_1^{\mathrm{d}} + \cos(\alpha)\Psi_2^{\mathrm{d}} \middle| \nabla_R \hat{H}^{el} \middle| \cos(\alpha)\Psi_1^{\mathrm{d}} + \sin(\alpha)\Psi_2^{\mathrm{d}} \right\rangle = \\
&\quad \nabla_R(-\sin(\alpha)\cos(\alpha)H_{11} - \sin^2(\alpha)H_{12} + \cos^2(\alpha)H_{12} + \sin(\alpha)\cos(\alpha)H_{22}) = \\
&\quad \frac{1}{2}\sin(2\alpha)\nabla_R(H_{22} - H_{11}) + \cos(2\alpha)\nabla_R H_{12} = \frac{1}{2}\sin(2\alpha)\vec{g} + \cos(2\alpha)\vec{h}.
\end{aligned}
\tag{B.2}
$$

In the above derivation eq. A.5 was used. Further, as diabatic functions change slowly with the nuclear coordinates their derivatives were neglected, i.e. $\left\langle \Psi_i^{\mathrm{d}} \middle| \nabla_R \hat{H}^{el} \middle| \Psi_j^{\mathrm{d}} \right\rangle \approx \nabla_R \left\langle \Psi_i^{\mathrm{d}} \middle| \hat{H}^{el} \middle| \Psi_j^{\mathrm{d}} \right\rangle$.

C. Number of linearly independent paramenters in an orthogonal matrix

An orthogonal matrix is a square matrix with real entries whose columns and rows are orthonormal. Thus, if we have an nxn matrix, the first column (or row) would have $n-1$ independent parameters, as the only condition it needs to satisfy is to be normalized. The second column would have $n-2$ independent paramenters, as it must be orthogonal to the first column and normalized as well. The third column would have $n-3$ independent paramenters, the fourth $n-4$ and so on. The last column would have no independent parameters, i.e. will be predefined by the entries in the previous $n-1$ columns. Therefore the number of independent coefficients equals:

$$\#of parameters = \sum_{1}^{n-1} = \frac{n-1+1}{2} \cdot (n-1) = \frac{n(n-1)}{2}, \tag{C.1}$$

where the fact was used that the sum of n consequtive numbers starting at 1 is given by the mean value $(n+1)/2$ multiplied by the number of elelments (i.e. n).

D. Rotational matrix as a one-electron operator in second quantization

By applying $\mathbf{U}$ on a trial wavefunction $\vec{\phi^0}$ transforms a spin-orbital according to

$$\phi_p = \sum_q U_{qp} \phi_q^0 = \sum_q (e^{\mathbf{K}})_{qp} \phi_q^0, \tag{D.1}$$

where eq. 1.43 was used. In second quantization this transformation corresponds to the action of a creation operator $\tilde{a}_p^\dagger$ of the form

$$\tilde{a}_p^\dagger = \sum_q U_{qp} a_q^\dagger = \sum_q (e^{\mathbf{K}})_{qp} a_q^\dagger \tag{D.2}$$

on the vacuum state $\big| \big\rangle$. Thereby, $a_q^\dagger$ is the creation operator which creates an electron in the q-th orbital of the trial wavefunction. The new wavefunction is obtained by applying a complete set of creation operators on the vacuum state

$$\tilde{a}_{p_1}^\dagger \tilde{a}_{p_1}^\dagger \ldots \big| \big\rangle = \sum_{q_1, q_2 \ldots} U_{q_2 p_2} U_{q_1 p_1} \ldots a_{q_1}^\dagger a_{q_1}^\dagger \ldots \big| \big\rangle. \tag{D.3}$$

Essentially, the above equation generates the new occupation number vector in the basis of trial occupation number vectors (sec. 1.4.1).
Using eq. 1.43 eq. D.1 can be rewritten as

$$
\begin{aligned}
\tilde{a}_p^\dagger = \sum_q (e^{\mathbf{K}})_{qp} a_q^\dagger &= \sum_q (\mathbb{1} + \mathbf{K} + \frac{1}{2}\mathbf{K^2} + \ldots)_{qp} a_q^\dagger \\
&= a_p^\dagger + \sum_q (\mathbf{K})_{qp} a_q^\dagger + \frac{1}{2} \sum_q (\mathbf{K}^2)_{qp} a_q^\dagger,
\end{aligned}
\tag{D.4}
$$

where k_{qp} are the coefficients of the rotational matrix $\mathbf{K}$. It can be shown that the above equation is equivalent to

$$
\begin{aligned}
\tilde{a}_p^\dagger &= a_p^\dagger + \sum_q (\mathbf{K})_{qp} a_q^\dagger + \frac{1}{2} \sum_q (\mathbf{K}^2)_{qp} a_q^\dagger \\
&= a_p^\dagger + [a_p^\dagger, \hat{K}] + \frac{1}{2}[[a_p^\dagger, \hat{K}], \hat{K}] + \ldots \\
&= e^{-\hat{K}} a_p^\dagger e^{\hat{K}},
\end{aligned}
\tag{D.5}
$$

where the Baker-Cambell-Hausdorff formula was used (see Appendix E). $\hat{K}$ is the operator of eq. 1.45. Inserting the final expression of eq. D.5 into eq. D.3 gives the final expression for the new occupation number vectors

$$
e^{-\hat{K}} a_{p_1}^\dagger e^{\hat{K}} e^{-\hat{K}} a_{p_2}^\dagger e^{\hat{K}} \ldots e^{-\hat{K}} a_{p_N}^\dagger e^{\hat{K}} \big| \big\rangle = e^{-\hat{K}} a_{p_1}^\dagger a_{p_2}^\dagger \ldots a_{p_N}^\dagger e^{\hat{K}} \big| \big\rangle = e^{-\hat{K}} \vec{\phi}^0
\tag{D.6}
$$

In the last expression the fact that matrix exponential is unitary was used. The action of $e^{\hat{K}}$ on the vacuum state $\big| \big\rangle$ gives

$$
e^{\hat{K}} \big| \big\rangle = (\mathbb{1} + \hat{K} + \frac{1}{2}\hat{K}^2 + \ldots) \big| \big\rangle = \big| \big\rangle
\tag{D.7}
$$

as the operator $\hat{K}$ first annihilates an electron from the occupation number vector. Eq. D.6 states that all MO coefficients can be rotated/transformed simultaneously by applying the exponential operator $e^{-\hat{K}}$

E. Baker-Campbell-Hausdorff expansion of the MCSCF matrix element

The Baker-Campbell-Hausdorff expansion reads:

$$
\begin{aligned}
e^{\mathbf{K}}\hat{H}e^{-\mathbf{K}} =& (\mathbb{1} + \mathbf{K} + \frac{1}{2}\mathbf{K^2} + \cdots)\hat{H}(\mathbb{1} - \mathbf{K} + \frac{1}{2}\mathbf{K^2}\dots) = \\
& \hat{H} + \mathbf{K}\hat{H} - \hat{H}\mathbf{K} + \frac{1}{2}\mathbf{K^2}\hat{H} - \mathbf{K}\hat{H}\mathbf{K} + \frac{1}{2}\hat{H}\mathbf{K^2} + \cdots = \\
& \hat{H} + [\mathbf{K}, \hat{H}] + \frac{1}{2}[\mathbf{K}, [\mathbf{K}, \hat{H}]] + \dots,
\end{aligned} \tag{E.1}
$$

where the Taylor expansion 1.43 for the matrix exponential $e^{\mathbf{K}}$ was used. The above expression is correct up to second order. It can be used to rewrite the operator in the expectation value eq. 1.47

$$
\begin{aligned}
e^{\mathbf{P}}e^{\mathbf{K}}\hat{H}e^{-\mathbf{K}}e^{-\mathbf{P}} =& e^{\mathbf{P}}(\hat{H} + [\mathbf{K}, \hat{H}] + \frac{1}{2}[\mathbf{K}, [\mathbf{K}, \hat{H}]] + \dots)e^{-\mathbf{P}} = \\
\hat{H} + [\mathbf{K}, \hat{H}] + \frac{1}{2}[\mathbf{K}, [\mathbf{K}, \hat{H}]] &+ [\mathbf{P}, \hat{H}] + [\mathbf{P}, [\mathbf{K}, \hat{H}]] + \frac{1}{2}[\mathbf{P}, [\mathbf{P}, \hat{H}]] + \dots.
\end{aligned} \tag{E.2}
$$

Again, this expression is correct up to second order. It gives a perscript for calculating the energy gradients with respect to the rotation coefficients $\vec{k}$ and $\vec{p}$.

F. Diastereomeric pairs of CoIns in HTI
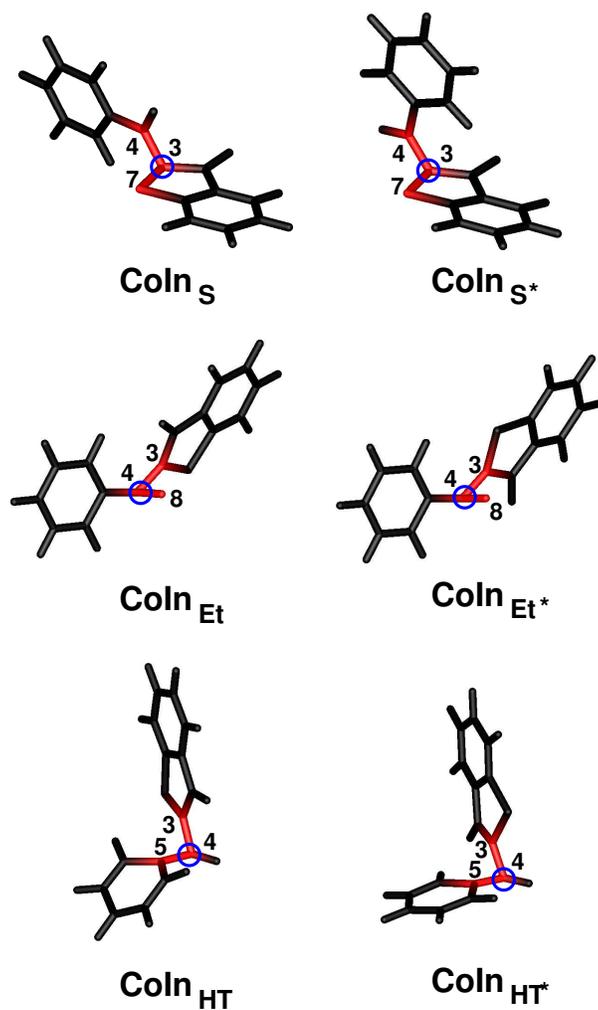
Figure F.1.: Diastereomeric pairs of CoIns: top) $CoIn_S/CoIn_{S*}$: middle) $CoIn_{Et}/CoIn_{Et*}$; bottom) $CoIn_{HT}/CoIn_{HT*}$. The atoms essential for the formation of a particular CoIn are colored in red. The center of pyramidalization is denoted by a blue circle.

G. Definition of the reactive coordinates torsion, pyramidalization and tilt in HTI

A set of reactive coordinates, well suited to describe the relaxation from the FC point to the energetically reachable degeneracy region, consists of torsion, pyramidalization and tilt. Naturally, these coordinates fulfill the *resonance* (torsion) and *heterosymmetry* (pyramidalization, tilt) conditions for CoIn formation derived in sec. 2.2. The torsion of the hemistilbene with respect to the hemithioindigo (fig. G.1, left) is the main reaction coordinate (WH-coordinate). For the quantitative evaluation the GS equilibrium structure of the Z-HTI isomer was chosen as reference geometry with a torsional angle of 0°. With this definition the Z→E isomerization runs clockwise (0°→ 180°), the E→Z isomerization counterclockwise (180°→ 0°). The pyramidalization is defined as the out-of-plane bending of the hemistilbene. In fig. G.1, middle, the pyramidalization is visualized for a torsional angle of 90°. At 0° pyramidalization the bridging carbon atom lies in the plane of the hemithioindigo. The third coordinate is the tilt of the hemistilbene either toward the carbonyl group (negative tilt) or toward the sulfur (positive tilt). Exemplarily, in fig. G.1, right, the tilt is visualized for a geometry with a torsional angle of 90° and pyramidalization of 60°. The purely pyramidalized $CoIn_{S/Ac}$ (fig. 2.8) is used as a 0° reference to determine the tilt.
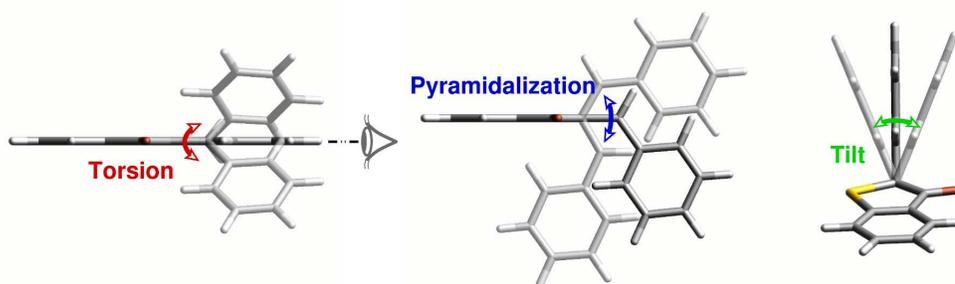
Figure G.1.: Reactive coordinates for the Z/E isomerization. (left) Out-of-plane torsion with Z-HTI as a zero-point reference in the range [0°:360°]; (middle) Pyramidalization (shown for a torsional angle of 90°) in the range [-90°:90°]; (right) Tilt (shown for a torsional angle of 90°and pyramidalization of 60Â°) in the range [-90°:90°].

According to this definition pyramidalization and tilt can be evaluated as shown in the sketch G.2 for an arbitrary pyramidalized and tilted geometry (given in black). To simplify the visualization HTI was truncated to the central double bond (①-②) and its first substituents. As both coordinates are not directly obtainable from a regular Z-matrix two dummy atoms were introduced (blue dots), so that the plane defined by ①, X_2 and X_1 (red-rimmed plane) divides the angle ③-①-④ in half. With the help of the dummy atoms the angle between the green-rimmed plane (defined via ②-①-X_2) and the red plane is adjusted to 90°. When this is achieved, the pyramidalization can be calculated by substracting the angle X_1-①-X_2 from 90°. The tilt is given through the angle ②-①-X_2, i.e. X_2 is the projection of ② in the red-rimmed plane. Furthermore, it is assumed, that the torsional angle at every CoIn is 90°. In the sketch G.2 this assumption implies that centers ⑤ and ⑥ adjust in order to preserve orthogonality between the two part of the π-system.
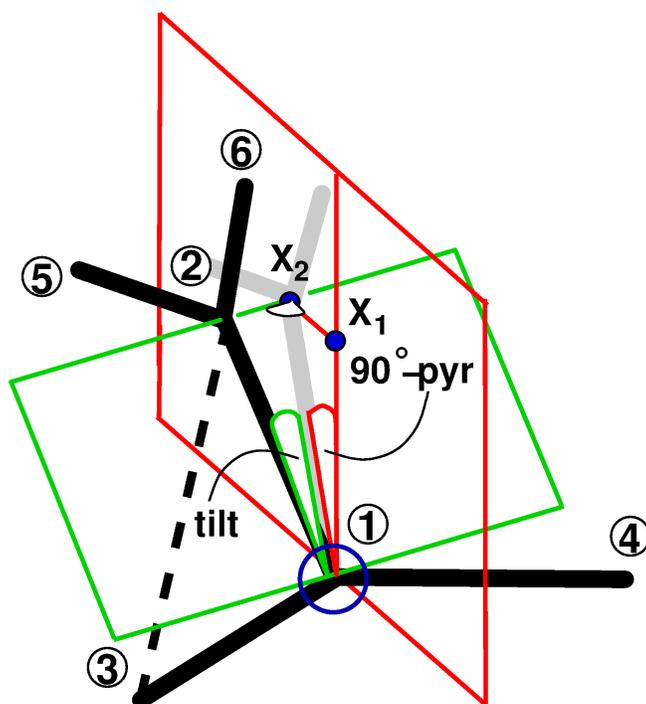
Figure G.2.: Sketch of the construction utilized to read-off pyramidalization and tilt from an arbitrary geometry (given in black). For this purpose two dummy atoms are introduced (blue dots). The pyramidalization is calculated by substracting the angle X_1-①-X_2 from 90° and the tilt is given via the angle ②-①-X_2. The center of pyramidalization is denoted by an blue circle.

H. Localized molecular orbitals and effects of the functional groups for scenario 1. and 2. in trifluoromethyl-pyrrolylfulgide
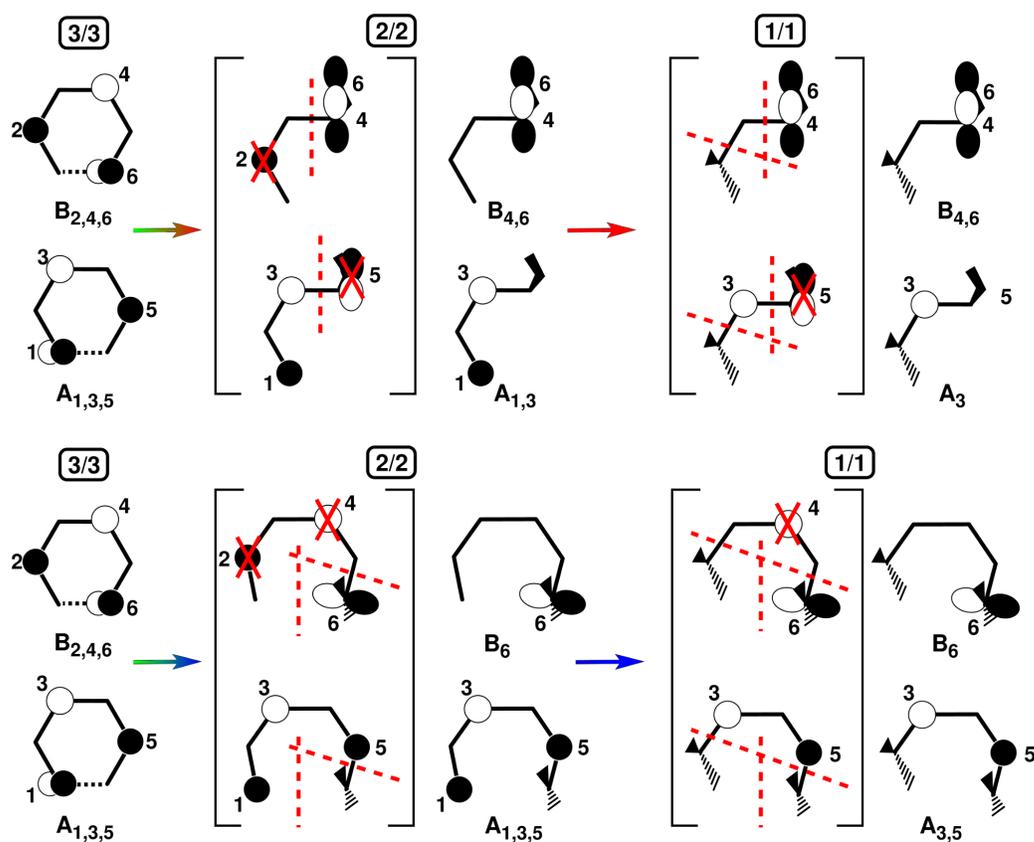
Figure H.1.: Localized molecular orbitals at the [2/2] and [1/1] homosymmetric biradicals in scenario 1 (top) and scenario 2 (bottom) (fig. 2.11 sec. 2.4.4). Dashed red lines indicate the spatial separation of the π-system into subunits. Red crosses mark atomic centers which do not contribute to the final molecular orbitals.
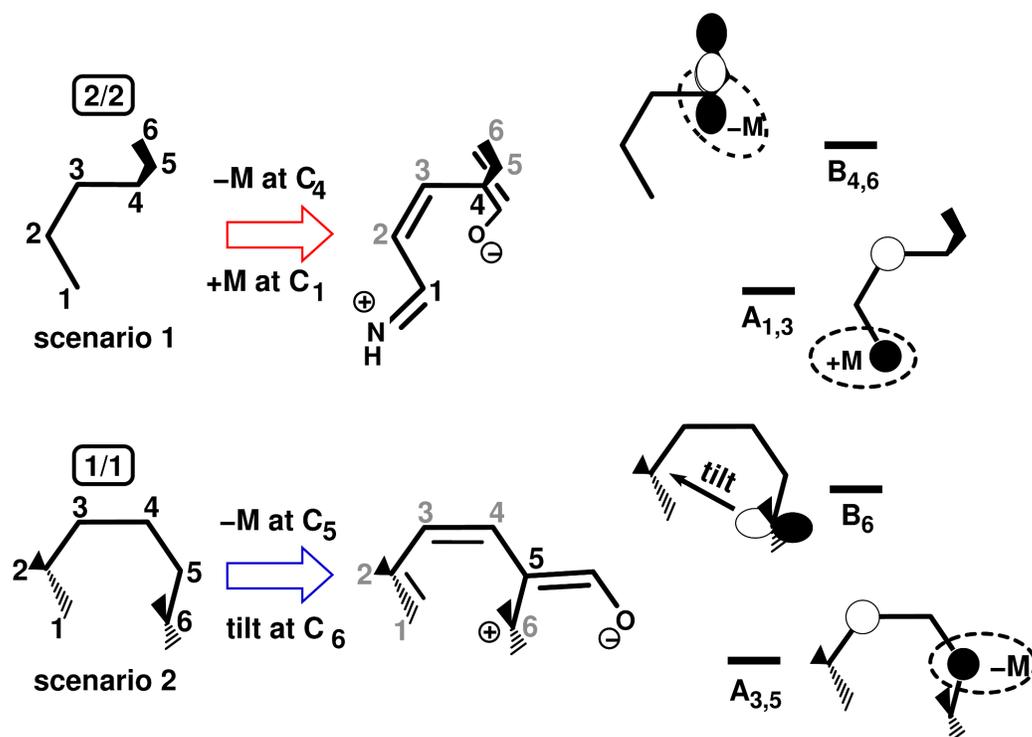
Figure H.2.: Conjugation of the functional groups -NHR (+M effect) and -CHO (-M effect) to the π-system of the basic unit for the [2/2] homosymmetric biradical in scenario 1 (top) and for the [1/1] homosymmetric biradical in scenario 2 (bottom) (fig. 2.11 in sec. 2.4.4). The alignment of the orbitals reflects their energetic order.

I. Quantum chemical methods utilized in the study of HTI

The quantum chemical studies were performed with the software packages Molpro[71], Molcas[261] and Gaussian[93]. Excited state structural optimizations were done on the CASSCF level including up to 10 electrons and nine orbitals in the active space. For points of interest CASPT2 was carried out, utilizing 14 electrons and 13 orbitals in the active space. Transition dipole moments were obtained with the CASSCF State-Interaction mathod (RASSI) method[262] as implemented in Molcas. Electrostatic potentials[263] were used to visualize the charge distribution along the reaction path in the ES. For the ES calculations the nomenclature SA-n and MS-n for averaging over n states in CASSCF and in CASPT2, respectively.

The size of HTI does not allow the inclusion of all π-orbitals in the active space. All first neighbors to the central double bond and one set of bonding and antibonding orbitals per benzene ring were considered (fig. I.1). Critical is the role of the oxygen lone pair, which can interact with the π-system depending on the structural arrangement and in principle must be considered in the active space. However, the simultaneous description of $n\pi^*$ and $\pi\pi^*$ states leads to problems due to the unbalanced description of the electron correlation for both states at CASSCF level (see dicussion in sec. 3.1.2). Therefore, the lone pair of the oxygene was included in the active space only in the single point calculations at the FC point and in the optimization of CoIn_{Ac}, which is very sensitive to dynamic correlation effects due to the notable $n\pi^*$ contribution to the ES wavefunction[183] (see discussion in sec. 3.1.2). As the character of the electronic states and thereby the amount of electronic correlation change along the MEP CASSCF can often only provide a qualitative description of the ES topography. Therefore, comparative single point CASPT2(14,13) calculations with Molcas, using an ionization potential-electron affinity (IPEA) modified zero order Hamiltonian[264] with an IPEA shift parameter of 0.25 a.u. and a real denominator shift of 0.30 a.u.[120, 121] were performed at all optimized stationary structures to incorporate the missing electron correlation. The active space was extended by an additional set of bonding and antibonding orbitals per benzene ring.

The stationary structures (minima, transition states, CoIns) were optimized on the CASSCF level with the standard Pople basis set 6-31G*[265, 266] and their characters were verified by frequency analysis. A relaxed state-averaged scan at CASSCF level along two reactive coordinates was performed for the construction of the two-dimensional ES PES, using the smaller basis set 6-31G[265]. Minimum energy CoIns were optimized with the projection method as implemented in Molpro (see sec. 1.2.3).
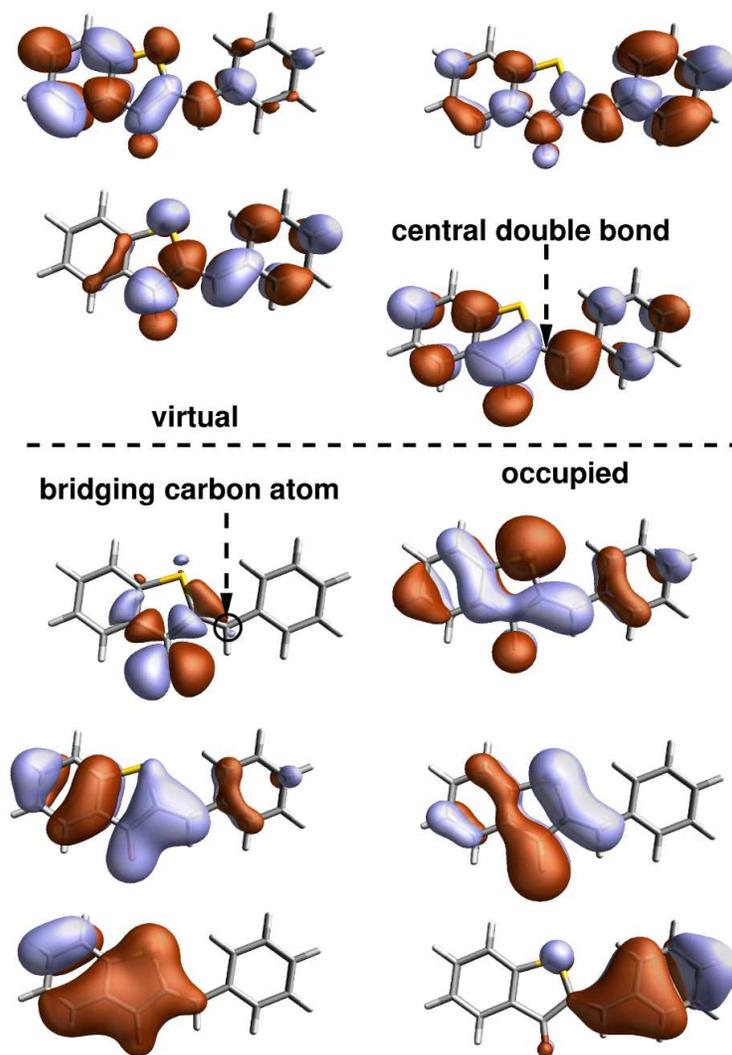
Figure I.1.: (10 electrons/9 orbitals) active space of HTI plus the oxygen lone pair. Exemplarily, the active orbitals of the Z-HTI are presented.

J. Quantum chemical methods utilized in the study of trifluoromethyl-indolylfulgide

The compound with a de-methylated nitrogen was used in the quantum chemical calculations. Geometry optimizations were performed with the software packages Molpro[71] and Gaussian[93]. CASSCF and the time-dependent density functional theory[267, 268] with the CAM-B3LYP functional[269] were utilized. The complete π-spaces of the indole and cyclohexadiene/hexatriene subunits were included in a (14 electrons/13 orbitals) large active space (fig. J.1). Averaging over the three lowest states for the chosen active space was applied (i.e. SA-3-CASSCF). At each stationary point the missing dynamic correlation was recovered using multistate MS-SR-CASPT2, correlating the three CASSCF states (denoted as MS-3-CASPT2) as implemented in Molcas[261]. Thereby, a default ionization potential-electronic affinity (IPEA) shift of 0.25 a.u.[264], as well as a real shift of 0.1 a.u.[120, 121] were used for the energy calculations. Transition dipole moments were obtained with the CASSCF State-Interaction (RASSI) method[262] as implemented in Molcas. Frequency calculations at SS-CASSCF level were performed for ground state equilibrium geometries, as well as for the excited state local minima in the vicinity of the FC-regions. Normal modes, frequencies and IR-intensities were calculated from analytical first derivatives and dipole moments obtained via a parallelized numerical procedure. To verify the CASSCF results, IR-spectra were also calculated at time-dependent density functional theory level. For comparison with experimental spectra the SS-CASSCF frequencies were scaled by a factor of 0.86, the CAM-B3LYP frequencies by a factor of 0.94. The standard Pople 6-31G*[265, 266] basis set was used for the atoms included in the π-system, whereas the 6-31G[265] basis set was used for the methyl- and trifluoromethyl-groups. Ground state and excited state topologies around CoIns have been obtained by performing an unrelaxed scan in the two-dimensional plane defined by the gradient difference and derivative coupling vectors. They lift the degeneracy between electronic states and define the branching space in a first order approximation (see sec. 1.2). The scan was performed at equidistant displacements (scaling factors: 0.05, 0.10, 0.15) from the CoIn along the orthonormalized gradient difference and derivative coupling vectors. Electrostatic potentials at selected geometries were generated and visualized with Molden[270].

148
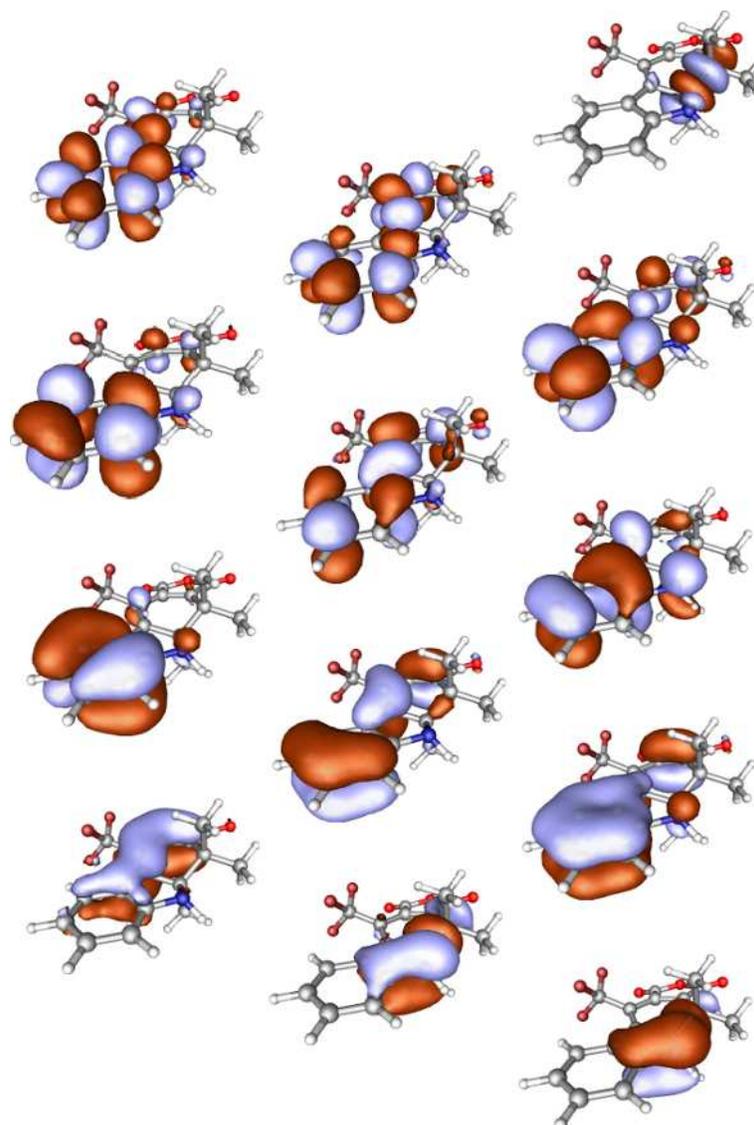
Figure J.1.: (14 electrons/13 orbitals) active space of trifluoromethyl-indolylfulgide. Exemplarily, the active orbitals of the C-form are presented.

List Of Abbreviations

BO   Born-Oppenheimer
BS   Branching Space
CASPT2 Complete–Active–Space–Perturbation–Theory
CASSCF Complete–Active–Space SCF
CHD Cyclohexadiene
CI   Configuration-Interaction
CIS   CI with Singles
CISD CI with Singles and Doubles
CoIn Conical Intersection
CPMCSCF Coupled–Perturbed MCSCF
CSF   Configuration–State–Function
GS   Ground State
ES   Excited State
FC   Franck-Condon
FWHM Full Width at Half Maximum
HF   Hartree–Fock
HOMO Highest Occupied Molecular Orbital
HT   Hexatriene
HTI   Hemithioindigo-Hemistilbene
IR   Infrared
IS   Intersection Space
LUMO Lowest Unoccupied Molecular Orbital
MCSCF Multi–Configuration SCF
MEP Minimum–Energy–Path
MO   Molecular Orbitals
MP2 Møller–Plesset
MRCI Multi–Reference–CI
MS-MR-CASPT2 Multi-State Multi-Reference CASPT2
MS-SR-CASPT2 Multi-State Single-Reference CASPT2
PES   Potential–Energy–Surface
RASSCF Restricted–Active–Space–Self–Consistent–Field
RHS Right–Hand–Side
SA-CASSCF State-Average CASSCF
SCF   Self–Consistent–Field
SS-CASPT2 Single-State CASPT2
SS-CASSCF Single-State CASSCF
UV   Ultraviolet
Vis   Visible
WH   Woodward-Hoffmann

List of Figures

List of Tables

References

[1] M. J. Rosker, M. Dantus and A. H. Zewail, Science **241**, 1200 (1988). 1, 8

[2] A. H. Zewail, Science **242**, 1645 (1988). 1

[3] A. H. Zewail, J. Phys. Chem. A **104**, 5660 (2000). 1, 8

[4] W. Zinth and J. Wachtveitl, <u>Light-triggered peptide dynamics</u>, Springer-Verlag, Berlin (2011). 1, 65

[5] C. G and D. S. S., Rev. Sci. Instrum. **74**, 1 (2003). 1

[6] K. R. A., W. M., R. K., H. P., W. A. M. and W. M., J. Opt. Soc. Am. B **17**, 2086 (2000). 1

[7] E. R. T. Wilhelm, J. Piel, Opt. Lett. **22**, 1494 (1997). 1

[8] S. Lochbrunner, T. Wilhelm, J. Piel, S. Spöerlein and E. Riedle, <u>Sub-20-fs tunable pulses in the visible and NIR by noncollinear optical parametric ampli¿cation (NOPA)</u>, Vol. 26 of <u>Trends in Optics and Photonics</u>, M. Fejer and H. Injeyan and U. Keller, Washington, DC (1999). 1

[9] E. Redle, M. Beutter, J. Piel, S. Schenkl, S. Spörlein and W. Zinth, Appl. Phys. B **71**, 457 (2000). 1

[10] J. Piel, M. Beutter and E. Riedle, Opt. Lett. **25**, 180 (2000). 1

[11] P. Baum, S. Lochbrunner, J. Piel and E. Riedle, Opt. Lett. **28**, 185 (2003). 1

[12] R. Huber, H. Satzger, W. Zinth and J. Wachtveitl, Opt. Commun. **194**, 443 (2002). 1

[13] C. Nagura, A. Suda, H. Kawano, M. Obara and K. Midorikawa, Appl. Opt. **41**, 3735 (2002). 1

[14] P. Farmanara, V. Stert and W. Radloff, Chem. Phys. Lett. **288**, 518 (1998). 1

[15] J. M. Mestdagh, J. P. Visticot, M. Elhanine and B. Soep, J. Chem. Phys. **113**, 237 (2000). 1

[16] S. H. Pullen, L. A. W. II, B. Donovan and R. J. Sension, Chem. Phys. Lett. **242**, 415 (1995). 1, 113

[17] S. H. Pullen, N. A. Anderson, L. A. W. II and R. J. Sension, J. Chem. Phys. **108**, 556 (1998). 1, 113

[18] S. Lochbrunner, W. Fuss, W. E. Schmid and K. L. Kompa, J. Phys. Chem. **102**, 9334 (1998). 1, 113

[19] S. A. Trushin, W. Fuss, T. Schikarski, W. E. Schmid and K. L. Kompa, J. Chem. Phys. **106**, 9386 (1997). 1, 113

[20] W. Fuss, W. E. Schmid and S. A. Trushin, J. Chem. Phys. **112**, 8347 (2000). 1, 113

[21] R. W. Schoenlein, L. A. Peteanu, R. A. Mathies and C. V. Schank, Science **254**, 412 (1991). 1

[22] H. Chosrowjan, N. Mataga, Y. Shibata, S. Tachibanaki, H. Kandori, Y. Shichida, T. Okada and T. Kouyama, J. Am. Chem. Soc. **120**, 9706 (1998). 1

[23] G. Haran, E. A. Morlino, J. Matthess, R. H. Callender and R. M. Hochstrasser, J. Phys. Chem. A **103**, 2202 (1999). 1

[24] E. Teller, Isr. J. Chem. **7**, 227 (1969). 1, 29

[25] H. E. Zimmerman, J. Am. Chem. Soc. **88**, 1566 (1966). 1, 29

[26] J. Michl, J. Mol. Photochem. P. 243 (1972). 1, 29

[27] N. Koga and K. Morokuma, Chem. Phys. Lett. **119**, 371 (1985). 1

[28] A. Farazdel and M. Dupius, J. Comput. Chem. **12**, 276 (1991). 1

[29] I. N. Ragazos, M. A. Robb, F. Bernardi and M. Olivucci, Chem. Phys. Lett. **197**, 217 (1992). 1

[30] M. R. Manaa and D. R. Yarkony, J. Chem. Phys. **99**, 5251 (1993). 1

[31] M. J. Bearpark, M. A. Robb and H. B. Schlegel, Chem. Phys. Lett. **223**, 269 (1994). 1, 12

[32] J. M. Anglada and J. M. Bofill, J. Comput. Chem. **18**, 992 (1997). 1

[33] C. Ciminelli, G. Granucci and M. Persico, Chem. Eur. J. **10**, 2327 (2004). 1

[34] L. D. Vico, M. Olivucci and R. Lindh, J. Chem. Theory Comput. **1**, 1029 (2005). 1

[35] B. G. Levine, C. Ko, J. Quenneville and T. J. Martínez, Mol. Phys. **104**, 1039 (2006). 1

[36] D. R. Yarkony, Rev. Mod. Phys. **68**, 985 (1996). 1, 2

[37] A. Sobolewski and W. Domcke, Phys. Chem. Chem. Phys. **6**, 2763 (2004). 1

[38] S. Perun and A. L. S. und W. Domcke, J. Am. Chem. Soc. **127**, 6257 (2005). 1

[39] S. Perun and A. L. S. und W. Domcke, J. Phys. Chem. A **110**, 13238 (2006). 1

[40] L. S.-A. und M. Merchán, J. Photochem. Photobiol. C **10**, 21 (2009). 1

[41] C. Z. Bisgaard, O. J. Clarkin, G. R. Wu, A. M. D. Lee, O. Gessner, C. C. Hayden and A. Stolow, Science **323**, 1464 (2009). 1

[42] K. Haiser, B. P. Fingerhut, K. Heil, A. Glas, T. T. Herzog, B. M. Pilles, W. J. Schreier, W. Zinth, R. de Vivie-Riedle and T. Carell, Angew. Chem. **124**, 421 (2012). 1, 29

[43] L. M. Frutos, T. Andruniow, F. Santro, N. Ferré and M. Olivucci, Proc. Nat. Acad. Sci. **104**, 7764 (2007). 1, 109, 110

[44] S. Hayashi, E. Taikhorshid and K. Schulten, Biophys. J. **96**, 403 (2009). 1, 106

[45] D. Polli, P. Altoe, O. Weingart, K. M. Spillane, C. Manzoni, D. Brida, G. Tomasello, G. Orlandi, P. Kukura, R. A. Mathies, M. Garavelli and G. Cerullo, Nature **467**, 440 (2010). 1, 114

[46] I. Schapiro, M. N. Ryazantsev, L. M. Frutos, N. Ferré, R. Lindh and M. Olivucci, J. Am. Chem. Soc. **4**, 3354 (2011). 1, 114

[47] P. Celani, S. Ottani, M. Olivucci, F. Bernardi and M. A. Robb, J. Am. Chem. Soc. **116**, 10141 (1994). 1, 8, 45, 113, 117

[48] M. J. Bearpark, M. Deumal, M. A. Robb, T. Vreven, N. Yamamoto, M. Olivucci and F. Bernardi, J. Am. Chem. Soc. **119**, 709 (1997). 1

[49] M. Boggio-Pasqua, M. Ravaglia, M. J. Bearpark, M. Garavelli and M. A. Robb, J Phys. Chem. A **107**, 11139 (2003). 1, 29

[50] G. Tomasello, M. J. Bearpark, M. A. Robb, G. Orlandi and M. Garavelli, Angew. Chem. Int. Ed. **49**, 2913 (2010). 1, 29, 92

[51] D. R. Yarkony, J. Chem. Phys. **104**, 7866 (1996). 1

[52] B. P. Fingerhut, D. Geppert and R. de Vivie-Riedle, Chem. Phys. **343**, 329 (2008). 1

[53] J. S. Lim and S. K. Kim, Nature Chem. **2**, 627 (2010). 1

[54] L. Blancafort, F. Jolibois, M. Olivucci and M. A. Robb, J. Am. Chem. Soc. **123**, 722 (2001). 2

[55] P. Kölle, A. Nenov, U. Megerle, P. Krok, H. Langhals, R. de Vivie-Riedle and E. Riedle, J. Chem. Phys. A **submitted** (2012). 2, 61

[56] G. J. Atchity, S. S. Xantheas and K. Ruedenberg, J. Chem. Phys. **95**, 1862 (1991). 2, 12

[57] M. Desouter-Lecompte, C. Gallow, J. Lorquet and M. Pires, J. Chem. Phys. **71**, 3661 (1979). 2

[58] M. J. Paterson, M. J. Bearpark, M. A. Robb and L. Blancafort, J. Chem. Phys. **121**, 11562 (2004). 2

[59] F. Sicilia, L. Blancafort, M. J. Bearpark and M. A. Robb, J. Phys. Chem. A **111**, 2182 (2007). 2, 11, 119

[60] F. Sicilia, M. J. Bearpark, L. Blancafort and M. A. Robb, Theor. Chem. Acc. **118**, 241 (2007). 2, 11, 119

[61] V. Bonačić-Koutecký, J. Koutecký and J. Michl, Angew. Chem. Int. Ed. Engl. **26**, 170 (1987). 2, 29, 32, 96

[62] N. Regner, T. T. Herzog, K. Haiser, C. Hoppmann, M. Beyermann, J. Sauermann, M. Engelhard, T. Cordes, K. Rück-Braun and W. Zinth, J. Phys. Chem. B **115**, 4181 (2012). 2

[63] S. Malkmus, F. O. Koller, S. Draxler, T. E. Schrader, W. J. Schreier, T. Brust, J. A. DiGirolamo, W. J. Lees, W. Zinth and M. Braun, Adv. Funct. Mat. **17**, 3657 (2007). 2, 65, 83

[64] G. Stock and M. Thoss, Adv. in Chem. Phys. **131** (2005). 2

[65] M. Barbatti, R. Shepard and H. Lischka, <u>Computational and Methodological Elements for Nonadiabatic Trajectory Dynamics Simulations of Molecules</u>, Vol. 17 of <u>Conical Intersections: Theory, Computation and Experiment</u>, World Scientific, Singapore (2011). 2, 104, 109, 110

[66] J. C. Tully, J. Chem. Phys. **93**, 1061 (1990). 2, 104, 106

[67] M. Barbatti, G. Granucci, M. Persico, M. Rueckenbauer, M. Vazdar, M. Eckert-Maksic and H. Lischka, J. Photochem. Photobiol. A **190**, 288 (2007). 3, 110

[68] K. Andersson, P.-A. . Malmqvist, B. O. Roos, A. J. Sadlej and W. K., J. Chem. Phys. **94**, 5483 (1990). 3, 16, 24, 25, 26, 110

[69] K. Andersson, P.-A. . Malmqvist and B. O. Roos, J. Chem. Phys. **96**, 1218 (1992). 3, 16, 24, 110

[70] J. Finley, P.-A. . Malmqvist, B. O. Roos and L. Serrano-Andrés, Chem. Phys. Lett. **288**, 299 (1998). 3, 16, 24, 27, 110

[71] H.-J. Werner, P. J. Knowles, R. Lindh, F. R. Manby, M. Schütz, P. Celani, T. Korona, G. Rauhut, R. D. Amos, A. Bernhardsson, A. Berning, D. L. Cooper, M. J. O. Deegan, A. J. Dobbyn, F. Eckert, C. Hampel, G. Hetzer, A. W. Lloyd, S. J. McNicholas, W. Meyer, M. E. Mura, A. Nicklass, P. Palmieri, R. Pitzer, U. Schumann, H. Stoll, A. J. Stone, R. Tarroni and T. Thorsteinsson, MOLPRO, version 2006.1, a package of ab initio programs (2009), see http://www.molpro.net. 3, 12, 110, 146, 148

[72] M. Klessinger and J. Michl, Excited States and Photochemistry of Organic Molecules, New York, VCH (1995). 3, 8, 70, 112, 113

[73] B. L. Feringa, Molecular Switches, Wiley-VCH, New York (2001). 3, 65, 82

[74] A. Nenov, P. Kölle, M. A. Robb and R. de Vivie-Riedle, J. Org. Chem. **123**, 75 (2010). 3, 11, 29, 45, 114

[75] A. Szabo and N. S. Ostlund, Modern Quantum Chemistry, Dover Publication, inc. Mineooa, New York (1996). 5, 14, 15, 16, 17

[76] I. N. Levine, Quantum Chemistry, Prentice Hall, 5. Edn. (2000). 5, 16

[77] A. Hofmann and R. de Vivie-Riedle, Chem. Phys. Lett. **346**, 299 (2001). 7, 29, 114

[78] J. v. Neumann and E. Wigner, Physik. Zeitschr. **XXX**, 467 (1929). 8, 13

[79] M. Kasha, Discuss. Faraday Soc. P. 14 (1950). 8

[80] F. Bernardi, S. De, M. Olivucci and M. A. Robb, J. Am. Chem. Soc. **112**, 1737 (1990). 8, 45

[81] F. Bernardi, M. Olivucci and M. A. Robb, J. Am. Chem. Soc. **114**, 1606 (1992). 8

[82] F. Bernardi, M. Olivucci, I. Ragazos and M. A. Robb, J. Am. Chem. Soc. **114**, 8211 (1992). 8

[83] M. Olivucci, I. N. Ragazos, F. Bernardi and M. A. Robb, J. Am. Chem. Soc. **115**, 3710 (1992). 8

[84] I. Palmer, I. Ragazos and I. Robb, J. Am. Chem. Soc. **115**, 673 (1993). 8

[85] M. Reguero, M. Olivucci, F. Bernardi and M. A. Robb, J. Am. Chem. Soc. **116**, 2103 (1993). 8

[86] P. Celani, M. Garavelli, S. Ottani, F. Bernardi, M. A. Robb and M. Olivucci, J. Am. Chem. Soc. **117**, 11584 (1995). 8, 45, 49

[87] M. Garavelli, P. Celani, N. Yamamoto, F. Bernardi, M. A. Robb and M. Olivucci, J. Am. Chem. Soc. **118**, 11656 (1996). 8

[88] M. Baer, Chem. Phys. Lett. **35**, 112 (1975). 8

[89] W. Domcke, D. Yarkony and H. E. Köppel (Ed.), Conical Intersections: Electronic Structure, Dynamics and Spectroscopy, Advanced Series in Physical Chemistry, World Scientific Publishing Company, River Edge, NJ (2004). 8, 9, 10, 45

[90] G. Herzberg and H. C. Longuet-Higgins, Trans. Faraday Soc. **35**, 77 (1963). 9

[91] Bentzian and M. Klessiner, J. Org. Chem. **59**, 4887 (1994). 10

[92] F. Sicilia, L. Blancafort, M. J. Bearpark and M. A. Robb, J. Chem. Theor. and Comp. **4**, 257 (2008). 11, 12, 29, 119

[93] M. J. Frisch, G. W. Trucks, H. B. Schlegel, G. E. Scuseria, M. A. Robb, J. R. Cheeseman, G. Scalmani, V. Barone, B. Mennucci, G. A. Petersson, H. Nakatsuji, M. Caricato, X. Li, H. P. Hratchian, A. F. Izmaylov, J. Bloino, G. Zheng, J. L. Sonnenberg, M. Hada, M. Ehara, K. Toyota, R. Fukuda, J. Hasegawa, M. Ishida, T. Nakajima, Y. Honda, O. Kitao, H. Nakai, T. Vreven, J. A. Montgomery, Jr., J. E. Peralta, F. Ogliaro, M. Bearpark, J. J. Heyd, E. Brothers, K. N. Kudin, V. N. Staroverov, R. Kobayashi, J. Normand, K. Raghavachari, A. Rendell, J. C. Burant, S. S. Iyengar, J. Tomasi, M. Cossi, N. Rega, J. M. Millam, M. Klene, J. E. Knox, J. B. Cross, V. Bakken, C. Adamo, J. Jaramillo, R. Gomperts, R. E. Stratmann, O. Yazyev, A. J. Austin, R. Cammi, C. Pomelli, J. W. Ochterski, R. L. Martin, K. Morokuma, V. G. Zakrzewski, G. A. Voth, P. Salvador, J. J. Dannenberg, S. Dapprich, A. D. Daniels, Ö. Farkas, J. B. Foresman, J. V. Ortiz, J. Cioslowski and D. J. Fox, Gaussian 09 Revision A.1, Gaussian Inc. Wallingford CT 2009. 12, 119, 146, 148

[94] P. Celani, M. A. Robb, M. Garavelli, F. Bernardi and M. Olivucci, Chem. Phys. Lett. **243**, 1 (1995). 12

[95] R. B. Woodward and R. Hoffmann, Angew. Chem. Int. Ed. Engl. **8**, 781 (1969). 13, 34, 89, 112

[96] R. B. Woodward and R. Hoffmann, The conservation of orbital symmetry, VCH, Weinheim (1970). 13, 34, 89, 112

[97] H. F. Sherrill, C. D.; Schaefer, Adv. Quantum. Chem. **34**, 142 (1999). 15

[98] C. C. J. Roothaan, Rev. Mod. Phys. **23**, 69 (1951). 15

[99] J. B. Foresman, M. Head-Gordon, J. A. Pople and M. Frish, Phys. Chem. **96**, 135 (1992). 16

[100] J. A. Pople, R. Seeger and R. Krishnan, Int. J. Quantum Chem. **Suppl. Y-11**, 149 (1977). 16

[101] B. O. Roos, Advanced Chemistry and Physics: Ab Initio Methods in Quantum Chemistry II, Wiley, Chicester, UK (1987). 16

[102] H.-J. Werner and P. J. Knowles, J. Chem. Phys. **82**, 5053 (1985). 16

[103] P. J. Knowles and H.-J. Werner, Chem. Phys. Lett. **115**, 259 (1985). 16

[104] P. G. Szalay, T. Müller, G. Gidofalvi, H. Lishka and R. Shepard, Chem. Rev. **112**, 108 (2012). 16, 22, 23, 110

[105] B. Liu, J. Chem. Phys. **58**, 1925 (1973). 16

[106] H. Lischka, R. Shepard, F. Brown and I. Shavitt, Int.J.Quantum Chem. **S15**, 91 (1981). 16

[107] P. A. M. Dirac, The principles of Quantum Mechanics., Claredon Press, Oxford, 4. Edn. (1958). 17

[108] J. Olsen, Lectures, European Summerschool in Quantum Chemistry, Sicily, Italy (2011). 17

[109] J. Olsen, B. O. Roos, P. Jørgensen and H. J. A. Jensen, J. Chem. Phys. **89**, 2185 (1988). 20

[110] P. Knowles, M. Schütz and H.-J. Werner, Ab Initio Methods for Electron Correlation in Molecules, Vol. 3 of Modern Methods and Algorithms of Quantum Chemistry, Proceedings, John von Neumann Institute for Computing, Jülich, 2. Edn. (2000). 20, 110

[111] H.-J. Werner, Adv. Chem. Phys. **69**, 1 (1987). 20

[112] B. Roos, Adv. Chem. Phys. **69**, 399 (1987). 20

[113] G. Chaban, M. W. Schmidt and M. S. Gordon, Theor. Chem. Acc. **97**, 88 (1997). 22

[114] G. B. Bacskay, Chem. Phys. **61**, 385 (1981). 22

[115] T. J. Dudley, R. M. Olson, S. M. W. and G. M. S., J. Comput. Chem. **27**, 352 (2006). 23

[116] A. Nenov, T. Cordes, T. T. Herzog, W. Zinth and R. de Vivie-Riedle, J. Phys. Chem. A **114**, 13016 (2010). 24, 29, 44, 47

[117] C. M. und M. S. Plesset, Phys. Rev. **46**, 618 (1934). 24

[118] R. J. Bartlett, Ann. Rev. Phys. Chem. **32**, 359 (1981). 24

[119] W. D. Laidig, G. Fitzgerald and R. J. Bartlett, Chem. Phys. Lett. **113**, 151 (1985). 24

[120] B. O. Roos and K. Andersson, Chem. Phys. Lett. **245**, 215 (1995). 27, 146, 148

[121] B. O. Roos, K. Andersson, M. P. Fülscher, L. Serrano-Andrés, K. Pierloot, M. Merchán and V. Molina, J. Mol. Struct. Theochem. **257**, 388 (1996). 27, 146, 148

[122] M. Garavelli, Theor. Chem. Acc. **116**, 87 (2006). 29

[123] D. S. Ruiz, A. Cembran, M. Garavelli, M. Olivucci and W. Fuss, Photochem. and Photobiol. **76**, 622 (2002). 29, 45, 49

[124] M. F. Rode and A. L. Sobolewski, J. Phys. Chem. A **114**, 11879 (2010). 29

[125] A. Nenov and R. de Vivie-Riedle, J. Chem. Phys. **135**, 034304 (2011). 29, 34, 35, 45, 83, 120

[126] A. Nenov and R. de Vivie-Riedle, J. Chem. Phys. **137**, 074101 (2012). 29, 44, 56, 83

[127] F. London, Z. Elektrochem. **35**, 552 (1929). 29

[128] F. Bernardi, M. Olivucci, M. A. Robb and G. Tonachini, J. Am. Chem. Soc. **114**, 5805 (1992). 29

[129] M. Garavelli, P. Celani, F. Bernardi, M. A. Robb and M. Olivucci, J. Am. Chem. Soc. **119**, 6891 (1997). 29, 32

[130] M. Garavelli, T. Vreven, P. Celani, F. Bernardi, M. A. Robb and M. Olivucci, J. Am. Chem. Soc. **120**, 1285 (1998). 29, 32

[131] M. Boggio-Pasqua, M. J. Paterson, M. A. Robb, L. Blancafort and A. D. De-Bellis, J. Phys. Chem. A **107**, 7527 (2005). 29

[132] A. Migani, L. Blancafort, M. Robb and A. DeBellis, J. Am. Chem. Soc. **130**, 6932 (2008). 29

[133] A. Nenov, W. J. Schreier, F. O. Koller, M. Braun, R. de Vivie-Riedle, W. Zinth and I. Pugliesi, J. Phys. Chem. A **116**, 10518 (2012). 29

[134] Q. Li, A. Migani and L. Blancafort, J. Phys. Chem. Lett. **3**, 1056 (2012). 29

[135] A. Migani, A. Sinicropi, N. Ferré, A. Cembran, M. Garavelli and M. Olivucci, Faraday Discuss. **127**, 179 (2004). 29

[136] P. A. Hunt and M. A. Robb, J. Am. Chem. Soc. **127**, 5720 (2005). 29

[137] M. Barbatti and H. Lischka, <u>6831</u>, J. Am. Chem. Soc. **130** (2008). 29

[138] O. Weingart, Z. Lan, A. Koslowski and W. Thiel, J. Phys. Chem. Lett. **2**, 1506 (2011). 29

[139] A. Kazaryan, Z. Lan, L. V. Schäfer, W. Thiel and M. Filatov, J. Chem. Theory Comput. **7**, 2189 (2011). 29

[140] M. J. Bearpark, L. Blancafort and M. J. Paterson, Mol. Phys. **104**, 1033 (2006). 29

[141] M. S. O. Takahashi, J. Mol. Struc-THEOCHEM **731**, 173 (2005). 29

[142] M. Sumita and K. Saito, J. Chem. Theory Comput. **4**, 42 (2008). 29, 44

[143] D. R. Yarkony, J. Chem. Phys. **123**, 204101 (2005). 29

[144] L. D. Vico and R. Lindh, J. Chem. Theory Comput. **5**, 186 (2009). 29

[145] L. Salem and C. Rowland, Angew. Chem. **84**, 86 (1972). 30

[146] J. Michl, Mol. Photochem. **4**, 257 (1972). 30

[147] M. Boggio-Pasqua, M. Robb and G. Groenhof, J. Am. Chem. Soc. **131**, 13580 (2009). 32

[148] G. Groenhof, L. V. Schäfer, M. Boggio-Pasqua, H. Grubmller and M. A. Robb, J. Am. Chem. Soc. **130**, 3250 (2008). 32, 109

[149] B. Dick, J. Chem. Theory Comput. **5**, 116 (2009). 44

[150] T. Cordes, B. Heinz, N. Regner, C. Hoppmann, T. E. Schrader, W. Summerer, K. Rück-Braun and W. Zinth, ChemPhysChem **8**, 1713 (2007). 44, 66, 68

[151] T. Cordes, T. Schadendorf, K. Rüück-Braun and W. Zinth, Chem. Phys. Lett. **455**, 197 (2008). 44, 66, 68

[152] T. Brust, S. Draxler, S. Malkmus, C. Schulz, M. Zastrowa, K. Rück-Braun and W. Z. und M. Braun, J. Mol. Liquids **141**, 137 (2008). 44, 83, 89

[153] S. Draxler, T. Brust, S. Malkmus, S. O. Koller, B. Heinz, S. Laimgruber, C. Schulz, S. Dietrich, K. Rück-Braun, W. Zinth and M. Braun, J. Mol. Liquids **141**, 130 (2008). 44, 83

[154] H. Tamura, S. Nanbu, T. Ishida and H. Nakamura, J. Chem. Phys. **124**, 0843131 (2006). 45, 129

[155] M. Olivucci, M. A. Robb and F. Bernardi, Conformational Analysis of Molecules in Excited States, Wiley-VCH, New York (2000). 45, 49

[156] S. Wilsey and K. N. Houk, Photochem. and Photobiol. **76**, 616 (2002). 45, 49

[157] F. Bernardi, M. Olivucci, J. J. W. McDouall and M. A. Robb, J. Phys. Chem. **89**, 6365 (1988). 45

[158] M. Irie, Chem. Rev. **100**, 1685 (2000). 65

[159] H. Dube and J. R. Jr., Angew. Chem. **51**, 3207 (2012). 65

[160] I. Willner and S. Rubin, Angew. Chem. **35**, 367 (1996). 65

[161] P. R. Westmark, J. P. Kelly and B. D. Smith, J. Am. Chem. Soc. **115**, 3416 (1993). 65

[162] K. Komori, K. Yatagai and T. Tatsuma, J. Biotech. **108**, 11 (2004). 65

[163] T. Fehrentz, M. Schöenberger and D. Trauner, Angew. Chem. Int. Ed. **50**, 2 (2011). 65

[164] T. Ikeda and O. Tsutsumi, Science **268**, 1873 (1995). 65

[165] S. Pu, H. Tang, B. Chen, J. Xu and W. Huang, Matter. Lett. **60**, 3553 (2006). 65

[166] A. Perrier, F. Maurel and D. Jacquemin, Acc. Chem. Res. **in press** (2012). 65

[167] T. Hugel, N. B. Holland, A. Cattani, L. Moroder, M. Seitz and H. E. Gaub, science **296**, 1103 (2002). 65

[168] V. Balzani, A. Credi, F. M. Raymo and J. F. Stoddart, Angew. Chem. **39**, 3348 (2000). 65

[169] A. A. Beharry and G. A. Woolley, Chem. Soc. Rev. **40**, 4422 (2011). 65

[170] W. Steinle and K. Rück Braun, Org. Lett **5**, 141 (2003). 66

[171] T. Lougheed, V. Borisenko, T. Hennig, K. Rück-Braun and G. A. Woolley, Org. Biomol. Chem. **2**, 2798 (2004). 66, 67

[172] S. Herre, W. Steinle and K. Rück-Braun, Synthesis **3297**, 3300 (2005). 66

[173] T. Schadendorf, C. Hoppmann and K. Rück-Braun, Tatrahedron Lett. **48**, 9044 (2007). 66, 67

[174] T. Cordes, T. Schadendorf, B. Priewisch, K. Rüück-Braun and W. Zinth, J. Phys. Chem. A **112**, 581 (2008). 66

[175] T. Cordes, C. Elsner, T. T. Herzog, C. Hoppmann, T. Schadendorf, W. Summerer, K. Rück-Braun and W. Zinth, Chem. Phys. **358**, 103 (2009). 66

[176] T. Cordes, D. Weinrich, S. Kemps, K. Reisselmann, S. Herre, C. Hoppmann, K. Rück-Braun and W. Zinth, Chem. Phys. Lett. **428**, 167 (2006). 66, 68

[177] J. Plötner and A. Dreuws, J. Phys. Chem. A **113**, 11882 (2009). 66, 70

[178] T. Cordes, M. Schadendorf, M. Lipp, K. Rück-Braun and W. Zinth, <u>Utrafast Phenomena XVI</u>, Springer-Verlag, Berlin (2009). 68, 69

[179] S. J. Strickler and R. A. Berg, J. Chem. Phys. **37**, 814 (1962). 69

[180] A. D. Becke, J. Chem. Phys. **98**, 5648 (1993). 69

[181] C. Lee, W. Yang and R. G. Parr, Phys. Rev. B **37**, 785 (1988). 69

[182] P. Stephens, F. Delvin, C. F. Chabalowski and M. J. Frish, J. Phys. Chem. **98**, 11623 (1994). 69

[183] M. Merchán and L. Serrano-Andrés, J. Am. Chem. Soc. **125**, 8108 (2003). 71, 146

[184] M. A. Wolak, C. J. Thomas, N. B. Gillespie, R. R. Birge and W. J. Lees, J. Org. Chem. **68**, 319 (2003). 82

[185] I. B. Ramsteiner, A. Hartschuh and H. Port, Chem. Phys. Lett. **343**, 83 (2001). 83

[186] M. Handschuh, M. Seibold, H. Port and H. C. Wolf, J. Phys. Chem. A **101**, 502 (1997). 83

[187] S. Kurita, A. Kashiwagi, Y. Kurita, H. Miyasaka and N. Mataga, Chem. Phys. Lett. **171**, 553 (1990). 83

[188] D. A. Parthenopoulos and P. M. Rentzepis, J. Mol. Struct. **224**, 297 (1990). 83

[189] M. Seibold and H. Port, Chem. Phys. Lett. **252**, 135 (1996). 83

[190] N. Tamai and H. Miyasaka, Chem. Rev. **100**, 1875 (2000). 83

[191] H. Port, P. Gartner, M. Hennrich, I. Ramsteiner and T. Schock, Mol. Cryst. and Liq. Cryst. **430**, 15 (2005). 83

[192] S. R., F. Renth, F. Temps and F. Sönnichsen, Phys. Chem. Chem. Phys. **11**, 5952 (2009). 83

[193] S. R., F. Strübe, J. Mattay, F. Renth and F. Temps, Phys. Chem. Chem. Phys. **13**, 3800 (2011). 83

[194] S. R., F. Strübe, J. Mattay, F. Renth and F. Temps, Phys. Chem. Chem. Phys. **13**, 15699 (2011). 83

[195] B. Heinz, S. Malkmus, S. Laimgruber, S. Dietrich, C. Schulz, K. Rück-Braun, M. Braun, W. Zinth and P. Gilch, J. Am. Chem. Soc. **129**, 8577 (2007). 83

[196] T. Cordes, S. Malkmus, J. Di Girolamo, W. J. Lees, A. Nenov, R. de Vivie-Riedle, M. Braun and W. Zinth, J. Phys. Chem. A **112**, 13364 (2008). 83, 87

[197] T. Brust, S. Draxler, A. Popp, X. Chen, W. J. Lees, W. Zinth and M. Braun, Chem. Phys. Lett. **477**, 298 (2009). 83, 99

[198] T. Brust, S. Malkmus, S. Draxler, S. A. Ahmed, K. Rück-Braun, W. Zinth and M. Braun, J. Photochem. And Photobiol. A: Chemistry **477**, 209 (2009). 83, 99

[199] T. Cordes, T. T. Herzog, S. Malkmus, S. Draxler, T. Brust, J. DiGirolamo, W. J. Lees and M. Braun, Photochem. & Photobiol. Sci. **8**, 528 (2009). 83, 87, 89, 90, 98, 100

[200] Y. Ishibashi, T. Katayama, C. Ota, S. Kobatake, M. Irie, Y. Yokoyama and H. Miyasaka, New J. Chem. **33**, 1409 (2009). 83

[201] F. O. Koller, W. J. Schreier, T. E. Schrader, A. Sieg, S. Malkmus, C. Schulz, S. Dietrich, K. Rück-Braun, W. Zinth and M. Braun, J. Phys. Chem. A **110**, 12769 (2006). 83

[202] F. O. Koller, W. J. Schreier, T. E. Schrader, S. Malkmus, C. Schulz, S. Dietrich, K. Rück-Braun and M. Braun, J. Phys. Chem. A **112**, 210 (2008). 83

[203] P. Hamm, Chem. Phys. **200**, 415 (1995). 85

[204] S. A. Kovalenko, A. L. Dobryakov, J. Ruthmann and N. P. Ernsting, Phys. Rev. A **59**, 2369 (1999). 85

[205] P. Hamm, S. M. Ohline and W. Zinth, J. Chem. Phys. **106**, 519 (1997). 85, 86

[206] T. Schrader, A. Sieg, F. Koller, W. Schreier, Q. An, W. Zinth and P. Gilch, Chem. Phys. Lett. **392**, 358 (2004). 85

[207] W. J. Schreier, I. Pugliesi, F. O. Koller, T. E. Schrader, W. Zinth, M. Braun, S. Kacprzak, S. Weber, W. Ro¿misch-Margl, A. Bacher, B. Illarionov and M. Fischer, J. Phys. Chem. B **115**, 3689 (2011). 93, 94

[208] L. M. Frutos, U. Sancho, M. Garavelli, M. Olivucci and O. Castano, J. Phys. Chem. A **111**, 2830 (2007). 94

[209] B. Sellner, M. Barbatti and H. Lischka, J. Chem. Phys. **131**, 024312 (2009). 94

[210] S. Draxler, T. Brust, S. Malkmus, J. A. DiGirolamo, W. J. Lees, W. Zinth and M. Braun, Phys. Chem. Chem. Phys. **11**, 5019 (2009). 100

[211] M. Baer, <u>Beyond Born-Oppenheimer: Electronic Nonadiabatic Coupling Terms and Conical Intersections</u>, John Wiley & Sons, New Jersey (2006). 103

[212] A. D. McLachlan, Mol. Phys. **8**, 39 (1964). 104

[213] A. Warshel, Nature **260**, 679 (1976). 104, 106

[214] J. C. T. R. K. Preston, J. Chem. Phys. **55**, 562 (1971). 104

[215] J. C. Tully, Faraday Discuss. **110**, 407 (1990). 104

[216] M. Santer, U. Manthe and G. Stock, J. Chem. Phys. **114**, 2001 (2001). 104

[217] P. Pechukas, Phys. Rev. **181**, 174 (1969). 104

[218] I. Burghardt and G. Parlant, J. Chem. Phys. **120**, 3055 (2004). 104

[219] B. F. E. Curchod, I. Tavernelli and U. Rothlisberger, Phys. Chem. Chem. Phys. **8**, 3231 (2011). 104, 109

[220] M. Ben-Nun, J. Quenneville and T. J. Martínez, J. Phys. Chem. A **104**, 5161 (2000). 105

[221] C. Zhu, A. W. Jasper and D. G. Truhlar, J. Chem. Theor. and Comp. **1**, 527 (2005). 105

[222] G. Granucci and M. Persico, Chem. Phys. **126**, 134114 (2007). 105

[223] P. Ehrenfest, Z. Phys. **45**, 455 (1927). 105

[224] L. D. Landau, Phys. Z. **2**, 46 (1932). 106

[225] C. Zener, Proc. R. Soc. Lond. A **137**, 692 (1932). 106

[226] D. F. Coker and L. Xiao, J. Chem. Phys. **102**, 496 (1995). 107

[227] A. W. Jasper, S. N. Stechmann and D. G. Truhlar, J. Chem. Phys. **116**, 5424 (2001). 107

[228] W. C. Swope, H. C. Andersen, P. H. Berens and K. R. Wilson, J. Chem. Phys. **76**, 637 (1982). 107

[229] R. Schinke, Phtodissociation Dynamics: Spectroscopy and Fragmentation of Small Polyatomic Molecules, Cambridge University Press, Cambridge (1995). 108

[230] J. C. Tully, Modern Methods for Multidimensional Dynamics Computations in Chemistry, World Scientific, Singapore (1998). 109

[231] P. Altoe, M. Stenta, A. Bottoni and Garavelli, Theor. Chem. Acc. **118**, 219 (2007). 109

[232] R. Mitrić, J. Petersen and Bonačić-Koutecký, Multistate Nonadiabatic Dynamics "on the fly" in Complex Systems and its Control by Laser Fields, Conical Intersections: Theory, Computation and Experiment, World Scientific, Singapore (2011). 109

[233] P. Celani and H.-J. Werner, to be published . 110

[234] H. Tao, B. G. Levine and T. J. Martínez, J. Phys. Chem. A **113**, 13656 (2009). 110

[235] T. Mori, W. J. Glover, M. Schuurman and T. J. Martínez, J. Phys. Chem. A **116**, 2808 (2012). 110

[236] H.-J. Werner, Mol. Phys. **89**, 645 (1996). 111

[237] D. Simah, B. Hartke and H.-J. Werner, J. Chem. Phys. **111**, 4523 (1999). 111

[238] K. Kosma, S. A. Trushin, W. Fuss and W. E. Schmid, Phys. Chem. Chem. Phys. **11**, 172 (2009). 113, 116, 121, 124

[239] K. Kosma, S. A. Trushin, W. E. Schmid and W. Fuss, Opt. Lett. **33**, 723 (2008). 112

[240] M. Garavelli, C. S. Page, P. Celani, M. Olivucci, W. E. Schmid, S. A. Trushin and W. Fuss, J. Phys. Chem. A **105**, 4458 (2001). 112, 113, 114, 117, 121, 124, 128, 129

[241] W. T. A. M. van der Lugt and L. J. Oosterhoff, J. Chem. Commun. P. 1235 (1968). 112

[242] W. T. A. M. van der Lugt and L. J. Oosterhoff, J. Am. Chem. Soc. **91**, 6042 (1969). 112

[243] N. Kuthirummal, F. M. Rudakov, C. L. Evans and P. M. Weber, J. Chem. Phys. **125**, 133307 (2006). 113

[244] H. Tamura, N. Shinkoh, H. Nakamura and T. Ishida, Chem. Phys. Lett. **401**, 487 (2005). 113, 116, 117

[245] J. J.B.Schönborn and B.Hartke, J. Phys. Chem. A **114**, 4036 (2010). 113

[246] T. Mori and S. Kato, Chem. Phys. Lett. **476**, 97 (2009). 116, 117, 154

[247] N. G. Minnaard and E. Havinga, Recueil **92**, 1179 (1973). 121

[248] M. Merchán, L. Serrano-Andrés, L. S. Slater, B. O. Roos, R. McDiarmid and X. Xing, J. Phys. Chem. A **103**, 5468 (1999). 129

[249] D. Geppert, L. Seyfarth and R. de Vivie-Riedle, Appl. Phys. B **79**, 987 (2004). 129

[250] D. Geppert and R. de Vivie-Riedle, Chem. Phys. Lett. **404**, 289 (2005). 129

[251] D. Geppert and R. de Vivie-Riedle, J. Photochem. Photobiol. A: Chemistry **180**, 282 (2006). 129

[252] M. Kotur, T. Weinacht, B. J. Paerson and S. Matsika, J. Chem. Phys. **130**, 134311 (2009). 129

[253] J. Kim, H. Tao, J. L. White, V. S. Petrovic, T. J. Martínez and P. H. Bucksbaum, J. Phys. Chem. A **116**, 2758 (2012). 129

[254] V. Beltrani, J. Dominy, T.-S. Ho and H. Rabitz, J. Chem. Phys. **126**, 094105 (2007). 132

[255] S. Yamazaki and S. Kato, J. Chem. Phys. **123**, 114510 (2005). 132

[256] H. Rabitz, R. de Vivie-Riedle, M. Motzkus and K. Kompa, Science **288**, 824 (2000). 132

[257] H. Tao, T. K. Allison, T. W. Wright, A. M. Stooke, C. Khurmi, J. van Tilborg, Y. Liu, R. W. Falcone, A. Belkacem and T. J. Martínez, J. Chem. Phys. **134**, 244306 (2011). 133

[258] B. P. Fingerhut, S. Oesterling, K. Haiser, K. Heil, A. Glas, W. J. Schreier, W. Zinth, T. Carell and R. de Vivie-Riedle, J. Chem. Phys. **136**, 204307 (2012). 133

[259] G. Worth, H.-D. Meyer and L. S. Cederbaum, <u>Conical Intersections: Electronic Structure, Dynamics and Spectroscopy</u>, Advanced Series in Physical Chemistry, World Scientific Publishing Company, River Edge, NJ (2004). 134

[260] G. A. Worth, H. P. and R. M. A., J. Phys. Chem. A **107**, 621 (2003). 134

[261] F. Aquilante, L. D. Vico, N. Ferré, G. Ghigo, P.-A. . Malmqvist, P. Neogrády, T. Pedersen, M. Pitonak, M. Reiher, B. Roos, L. Serrano-Andrés, M. Urban, V. Veryazov and R. Lindh, J. Comput. Chem. **31**, 224 (2010). 146, 148

[262] P.-A. . Malmqvist and B. O. Roos, Chem. Phys. Lett. **155**, 189 (1989). 146, 148

[263] R. F. W. Bader, M. T. Carroll, J. R. Cheeseman and C. Chang, J. Am. Chem. Soc. **109**, 7968 (1987). 146

[264] G. Ghigo, B. O. Roos and P.-A. . Malmqvist, Chem. Phys. Lett. **396**, 142 (2004). 146, 148

[265] R. Ditchfield, W. J. Hehre and J. A. Pople, J. Chem. Phys. **54**, 724 (1971). 146, 148

[266] M. M. Francl, W. J. Pietro, W. J. Hehre, J. S. Binkley, D. J. DeFrees, J. A. Pople and M. S. Gordon, J. Chem. Phys. **77**, 3654 (1982). 146, 148

[267] M. E. Casida, C. Jamorski, K. C. Casida and D. R. Salahub, J. Chem. Phys. **108**, 4439 (1998). 148

[268] R. E. Stratmann, G. E. Scuseria and M. J. Frisch, J. Chem. Phys. **109**, 8218 (1998). 148

[269] T. Yanai, D. Tew and N. Handy, Chem. Phys. Lett. **393**, 51 (2004). 148

[270] G. Schaftenaar and J. H. Noordik, J. Comput.-Aided Mol. Design **14**, 123 (2000). 148

Acknowledgement